MINIMIZING CR-EVAPORATION FROM BALANCE OF PLANT COMPONENTS BY UTILIZING COST-EFFECTIVE ALUMINA-FORMING AUSTENITIC STEELS

Award Number: DE- FE0027947

Project Title: MINIMIZING CR-EVAPORATION FROM BALANCE OF PLANT COMPONENTS BY UTILIZING COST-EFFECTIVE ALUMINA-FORMING AUSTENITIC STEELS

Principal Investigator: Dr. Xingbo Liu
(304) 293-3339
Xingbo.Liu@mail.wvu.edu

Recipient Organization: West Virginia University

Submission Date: **October 31, 2021**

DUNS Number: 929332658

Recipient Organization (Name and Address): West Virginia University
Morgantown, West Virginia 26506

Project/Grant Period (Start Date, End Date): April 1, 2018 to September 30, 2021

Reporting Period End Date: September 30, 2021

Report Term or Frequency: Final Technical Report

Signature of Submitting Official (electronic signatures (i.e., Adobe Acrobat) are acceptable)

Executive Summary

A solid oxide fuel cell (SOFC) is a clean and efficient energy conversion device. The development of intermediate-temperature SOFCs has made it preferable to use metallic interconnects (MICs) to greatly reduce the cost and significantly increase the efficiency compared to ceramic interconnect materials. However, gaseous chromium species will evaporate from the chromium-containing layer formed on the surface of commonly used MICs and balance of plant (BoP) components. Volatile chromium species have been shown to form solid deposits which poison the cathodes of SOFCs, causing drastic cell performance degradation and thereby limiting commercialization. In order to alleviate the Cr poisoning and achieve long-term high performance of SOFC stacks, various Al_2O_3-forming austenitic (AFA) stainless steels applied at different temperatures are evaluated in this project.

Based on our Phase I results (500 h operation), it is shown that on the AFAs, an alumina-based protective layer forms under high temperature that is invulnerable to water vapor effects and suppresses the diffusion of chromium and manganese which can prevent the generation of spinels on the alloy surface. Therefore, 310S, OC4 and OC5 at 800 °C and 625, OC11 and OC11LZ at 900 °C are selected to be tested in the Phase II long-term operation. From the results, we find that besides the lower Cr evaporation rates and better oxidation resistance of AFAs than benchmark alloys after short-term (500 h) operation, AFAs also possess the sturdy and compact alumina layer after a long-term operation (5000 h). A protective oxide layer is of great importance for the long-term high-temperature operation of structural materials. The high-temperature oxidation behavior of AFAs and commercial 310S and 625 alloys in Air + 10% H_2O at 800 °C and 900 °C is systematically investigated. Severe breakaway oxidation and minor spallation are observed for the 310S and 625 after the long-term operation, while the AFAs show high oxidation resistance. It is found that the formation of a continuous alumina layer could greatly prevent the volatilization of chromium vapors. In addition, the corresponding evolving models are discussed.

Chromium evaporation from BoP components in high-temperature environment could severely deteriorate the electrochemical performance of SOFC. Several methods were applied to evaluate the Cr evaporation rates of BoP after 500 h exposure at 800 °C to 900 °C in air with 10% H_2O. An optimal method was designed to exclude the effect of silicon (Si) deposits from quartz tube and sodium (Na) deposits from the sodium carbonate on the oxidation process and the chemical interaction between Cr gaseous species and alumina tube which could provide further quantitative correlation of the evaporated Cr species quantities and degradation rates of SOFC.

Based on the great performance of AFAs after long-term operation, AFAs are assembled with Anode-supported cells (ASC) to investigate the the Cr deposition of anode-supported cell under a constant current density of 0.5 A cm^{-2} at 800 °C with AFA alloys compared with commercial alloys. In addition, the anodic and cathodic processes are deconvoluted by distribution of relaxation times (DRT) method which are comprehensively discussed. It is found out that the voltage exhibited a slight decrease of 5.09 % and 1.54 % in the presence of OC11 and OC11LZA alloy, respectively. However, a considerable decrease of 22.14 % and 12.06 % was determined in the presence of 310S and 625 alloy, respectively. AFAs possessing the low-cost, low Cr evaporation rates and the high oxidation resistance will make it of great potential to replace the existing BoP components.

Table of Contents

List of figures

List of tables

1. Milestone Status Report

Milestone Number	Assoc. SOPO Task(s)	Title/ Description	Planned Completion Date	Actual Completion Date	Percent Completed	Verification Method	Comments
1.0		Project Management	03/30/2021		100%	Preparation and publication of reports, project meetings and tracking project milestones	Quarterly report was generated
2.0		Developing and Manufacturing AFAs					
2.1		Lab-scale Manufacturing AFAs	09/30/2019		100%	Oak Ridge National Laboratory(ORNL) develops several AFAs with different alloy addition	
2.2		Industry AFA Manufacturing	09/30/2019		100%	Oak Ridge National Laboratory(ORNL) develops several AFAs with different alloy addition	
3.0		Long-term Cr Evaporation Investigation					
3.1		Cr Evaporation Evaluation	09/30/2020		100%	Obtaining Cr contents evaporated by different AFAs	

3.2		Contribution of partial pressure of different Cr species	12/31/2020		100%	Demonstrating the different partial pressure of different Cr species	
4.0		Quantitative Investigation on Cr-poisoning of SOFC Cathodes					
4.1		Assembly of SOFCs with BOP alloys	03/31/2020		100%	Preparing the electrochemical investigation on the SOFCs coupled with different AFAs.	
4.2		Electrochemical Investigation	06/30/2020		100%	Quantitatively demonstrating the effect of Chromium contents on the poisoning of SOFC Cathodes	
4.3		Post-Mortem Analysis	09/30/2020		100%	Verifying the chromium deposition and poisoning on the cathode and the interface of electrolyte and cathodes.	
5.0		Investigation of AFA's key Properties for BOP Applications					

5.1		Long-term Oxidation Kinetics	09/30/2020		100%	Demonstrating the oxidation properties of different AFAs	
5.2		Characterization of the oxide Scale	09/30/2020		100%	Characterizing the oxide Scale using SEM/EDX	
5.3		AFA high Temp Mechanical Properties	09/30/2020		100%	Demonstrating the high Temp Mechanical properties of different AFAs	
6.0		Manufacturing and Testing BOP Components in Industrial SOFC Systems					
6.1		Investigation on the manufacturability of BOP AFAs	03/31/2020		100%	Applying optimal AFA to the BOP components	
6.2		Testing BOP Components in Industrial SOFC Systems	12/31/2020		100%	Quantitatively demonstrating the effect of Chromium evaporated from AFAs on the poisoning of SOFC Cathodes	
6.3		Post-mortem Analysis	03/31/2021		100%	Verifying the effect of optimal AFA application on the SOFC cathode stability.	

7.0		Preparing the AFA Application for SOFC Industries	03/31/2020				

2. Major Accomplishments

Task 1.0 Project Management and Planning - WVU
During the project, the WVU management team is responsible for project management activities: reporting, organizing and hosting project meeting, tracking project milestones, and substantiating the decision metrics.

Task 2.0 Developing and Manufacturing AFAs – WVU, ORNL, BE, FCE
Based on the results in Phase I, we will chose at least two AFA alloys working at 800 ^{o}C (measurable) and at least two AFA alloys suitable for 900 ^{o}C for long-term oxidation testing up to 5000 hours. In addition, some alloy will continue to be modified, such as doping by Zr, C.

At present, WVU and ORNL had identified AFA samples from the existing material and preliminary decided the test matrix as shown in **Table 1**. The compositions of AFA are shown in **Table 2**.

Table 1 Test matrix of Cr release measurements in air + 10% H_2O for 5000 hours.

Phase II: 10% H_2O, up to 5000 hours							
Sample	MOD	OC4	OC5	OC11	OC11 (LZ)	310S	625
800 ^{o}C	√	√	√	√	√	√	
900 ^{o}C				√	√		√

- **Note**: At 800 ^{o}C, OC4, OC5, and 310S are required running up to 5000 hours with cooling cycle. 500 hours per cycle; OCD, OC11, and OC11-LZ will also probably do depending on the available materials;
- At 900 ^{o}C, OC11 and OC11-LZ are required with alloy 625 as a baseline. All for long-term test for 5000 hours with cooling cycle observation.

Table 2 Nominal compositions of AFA and benchmark commercial Cr_2O_3-forming alloys.

Alloy	Fe	**Ni**	**Cr**	**Al**	**Nb**	Mn	Si	Mo	W	**C**	B	**other**
AFA for ≤ 800-850°C use												
MOD	51	**25**	**14**	**4**	**1**	2	0.15	2	0	**0.15**	0.01	0.5Cu
OC5	51	**25**	**14**	**3**	**1**	2	0.15	2	1	**0.1**	0.01	0.5Cu
OCF	49	**25**	**14**	**4**	**2.5**	2	0.15	2	1	**0.2**	0.01	0.5Cu
OC4	49	**25**	**14**	**3.5**	**2.5**	2	0.15	2	1	**0.1**	0.01	0.5Cu
AFA for ≥ 800-850°C use												
OC11	48	**25**	**15**	**4**	**2.5**	2	0.15	2	0	**0.1**	0.01	0.5Cu **Hf, Y**
OC11LZ	48	**25**	**15**	**4**	**2.5**	2	0.15	2	0	**0.1**	0.01	0.5Cu **Zr, Y**
OC11LZA	49	**25**	**15**	**4**	**2.5**	2	0.15	2	0	**0.1**	0.01	0.5Cu **Zr**
35Ni	39	**35**	**18**	**3.5**	**1**	2	0.15	0	0	**0.15**	0.01	0.5Cu **Hf, Y**
Benchmark commercial Cr_2O_3-forming alloys												
310S	53	20	25	0	0	2	0.75	0.75	0	0.08	0	0.5Cu
625	5	61	22	0.2	3	0.4	0.25	8		0.04	0	0.2Ti

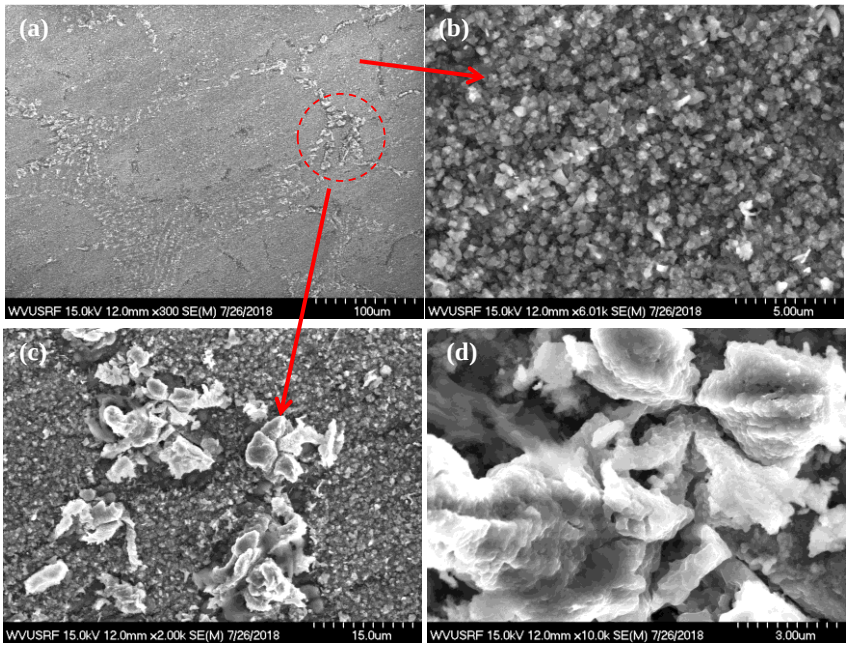

Figure 1 SEM characterization for OCF in 10% H_2O at 850 °C for 500 hours.

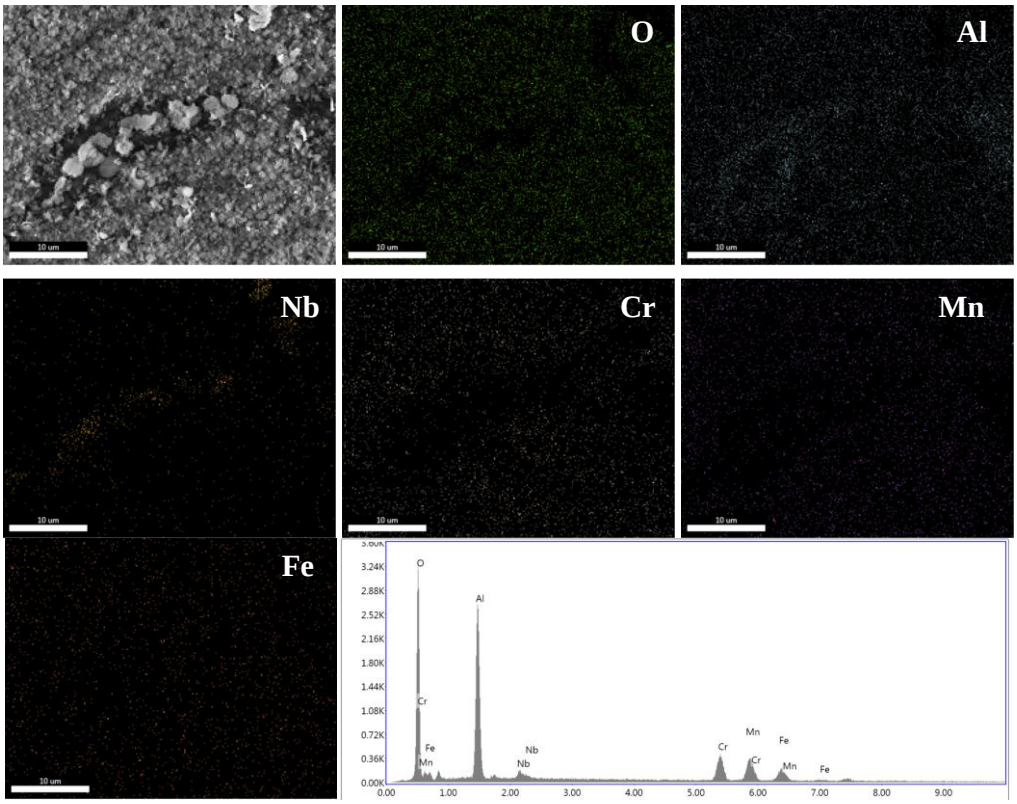

Figure 2 SEM/EDX mapping of the OCF surface tested for 500 h in air + 10% H_2O at 850 °C in quartz tube.

For OCF tested at 850 °C, as we can see from the Figure 1, some Nb-rich oxides could be observed at the grain boundary and some uniform oxides covered majority of the surface which could be ascribed to the Fe-Al-Cr-Mn-rich oxides according to the EDX results.

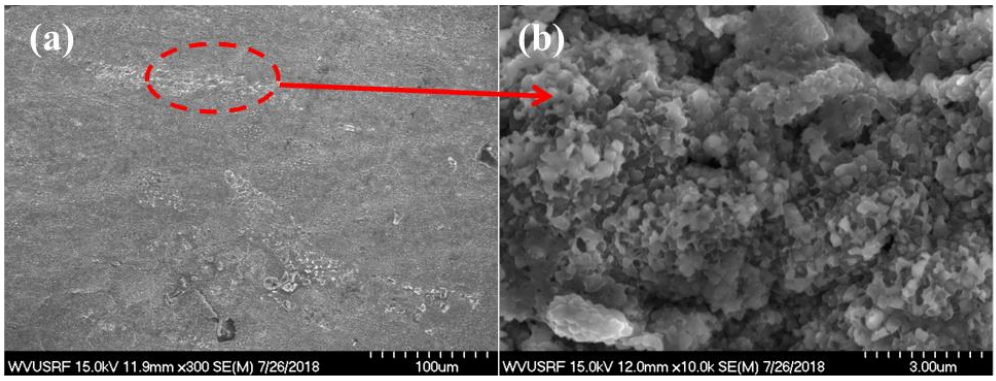

Figure 3 SEM characterization for OC5 in 10% H_2O at 850 °C for 500 hours.

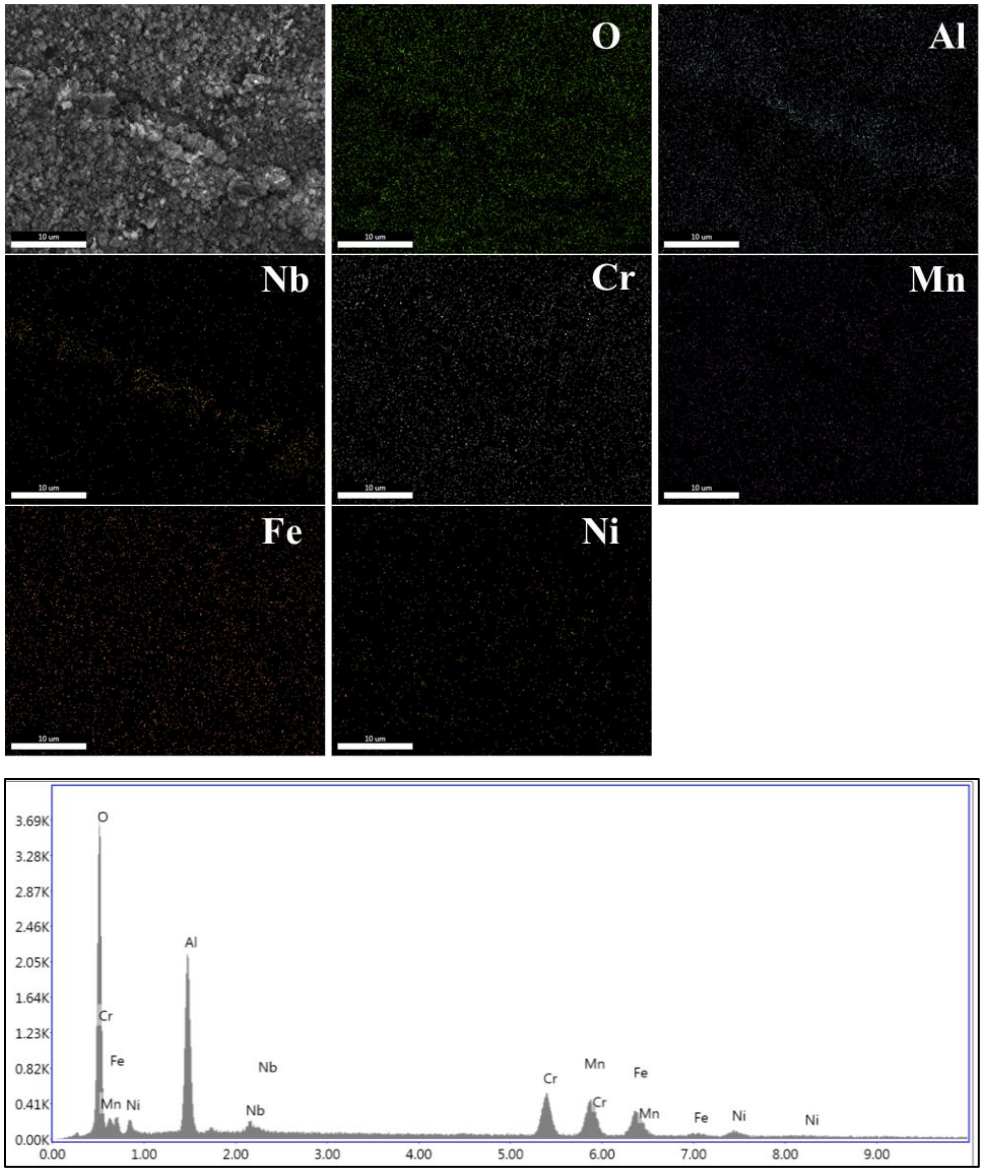

Figure 4 SEM/EDX mapping of the OC5 surface tested for 500 h in air + 10% H_2O at 850 °C in quartz tube.

For OC5 tested at 850 °C, the surface morphology is very similar to that of OCF. Some Nb-rich oxides can also be observed at the grain boundary. The main oxides formed on the surface contains Fe-Al-Cr-Mn-rich oxides based on the EDX mapping results, indicating these two samples might have comparable Cr evaporation rate under this condition.

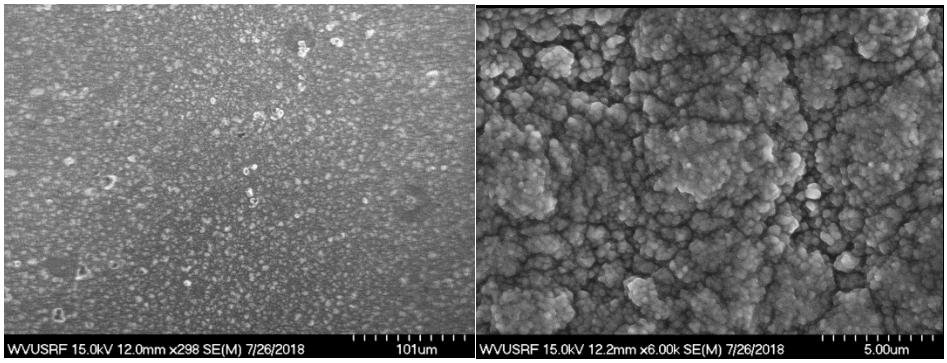

Figure 5 SEM characterization for 625 in 10% H_2O at 850 °C for 500 hours.

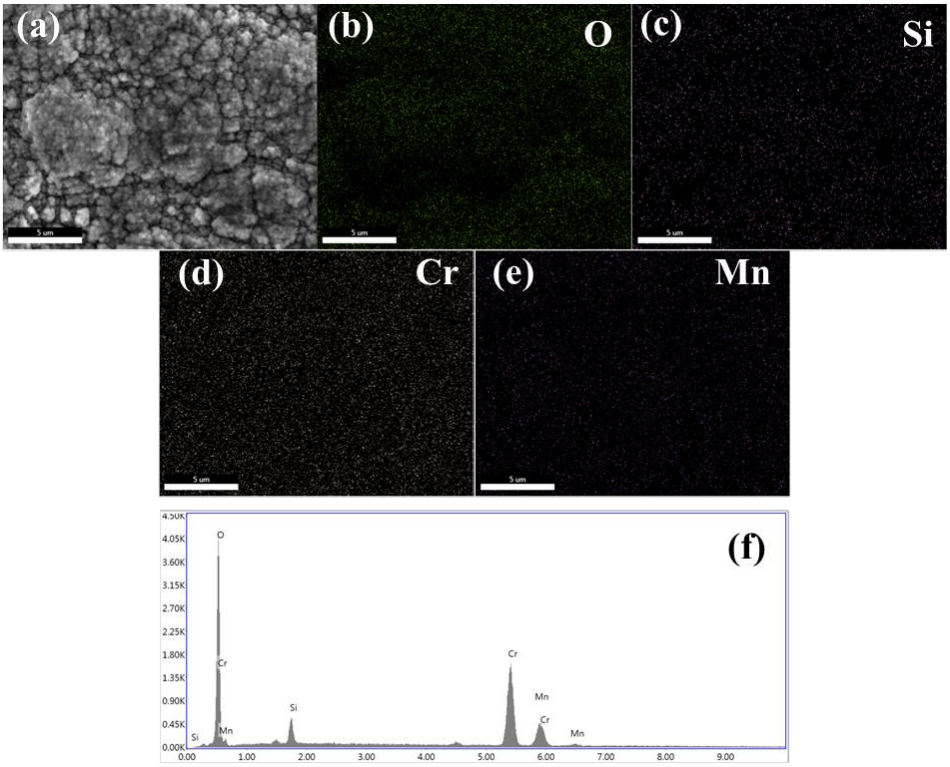

Figure 6 SEM/EDX mapping of the 625 surface tested for 500 h in air + 10% H_2O at 850 °C in quartz tube.

For 625 alloy tested at 850 °C, the uniform oxides formed on the surface are Cr-Mn spinel and chromia based on the EDS results. Moreover, Si contamination from the quartz tube could be also observed.

Task 3.0 Long-term Cr Evaporation Investigations – WVU

During Phase II, WVU will investigate the Cr evaporation rates of AFA alloys from 800 to 900 °C for up to 5000 h. To further understand the Cr-release kinetics, comprehensive and long-term studies are needed to prepare. A counterpart baseline alloy such as 310S and Inconel 625 will also be tested in parallel as listed above.

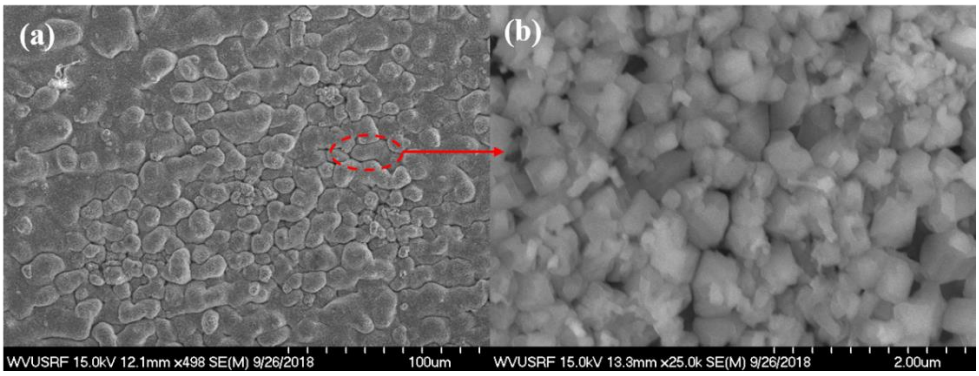

Figure 7 SEM characterization for 625 in 10% H_2O at 900 °C for 500 hours.

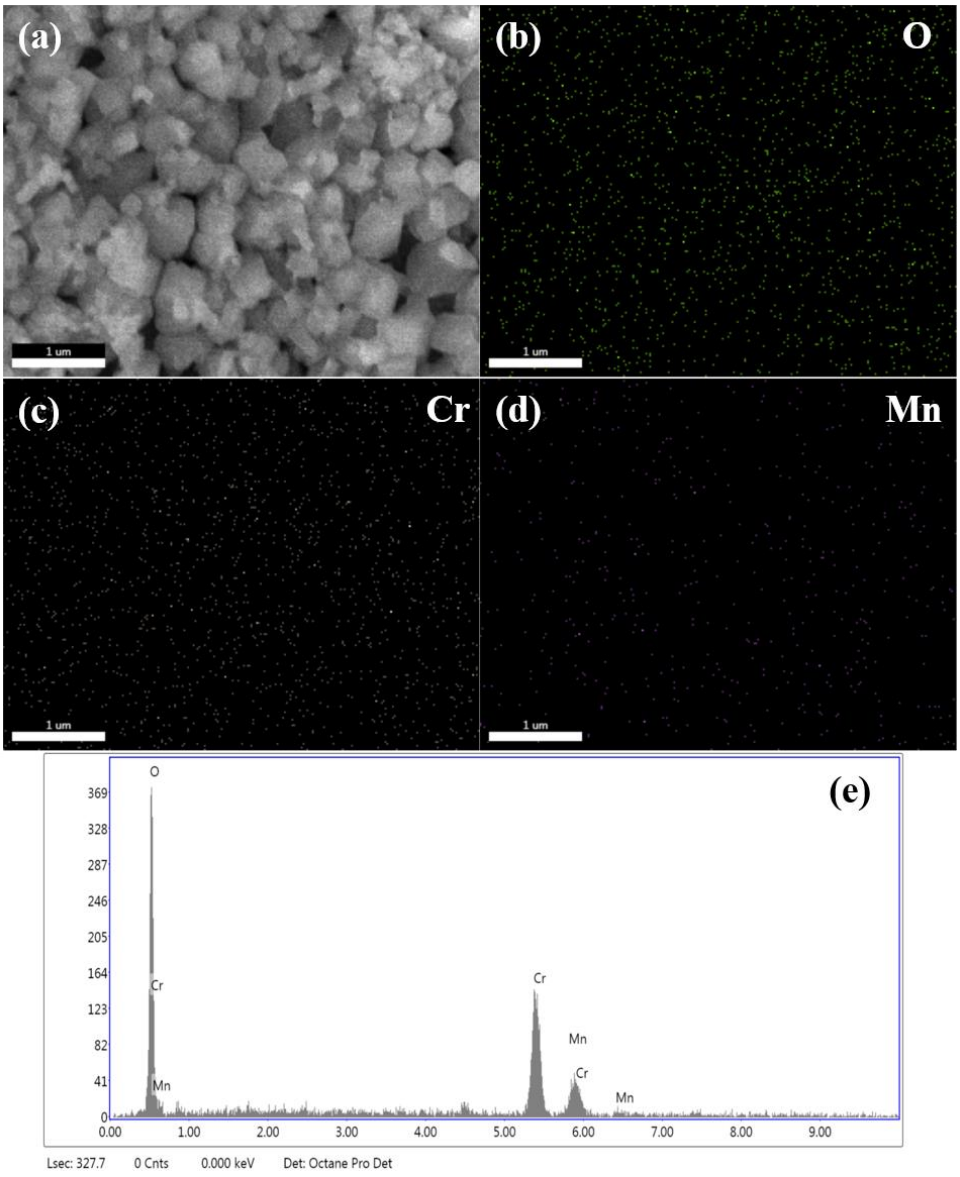

Figure 8 SEM/EDX mapping of the 625 surface tested for 500 h in air + 10% H_2O at 900 °C in quartz tube.

For 625 alloys tested at 900 °C for 500 h which is similar as that tested at 850 °C, diamond-like oxides uniformly formed on the surface are Cr-Mn spinel and chromia based on the EDS results.

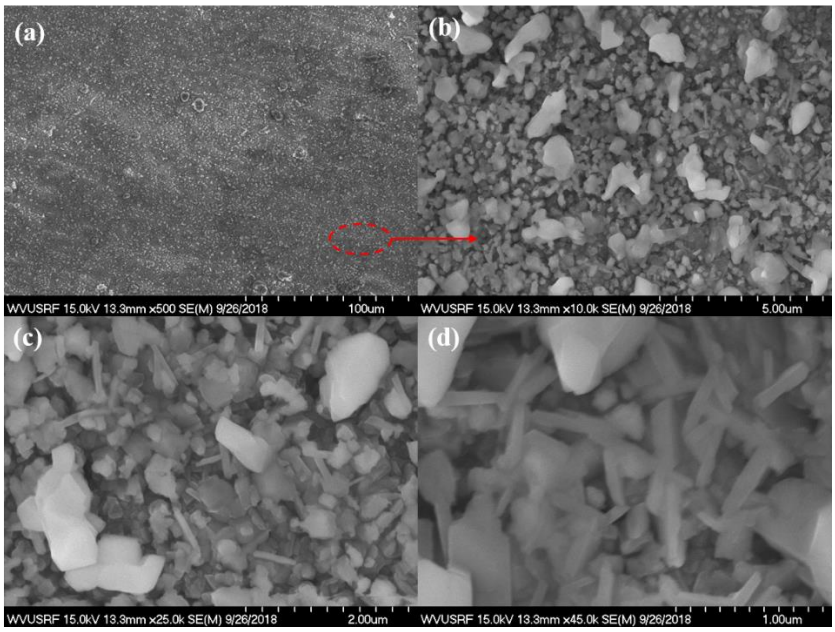

Figure 9 SEM characterization for OC11 in 10% H_2O at 900 °C for 500 hours.

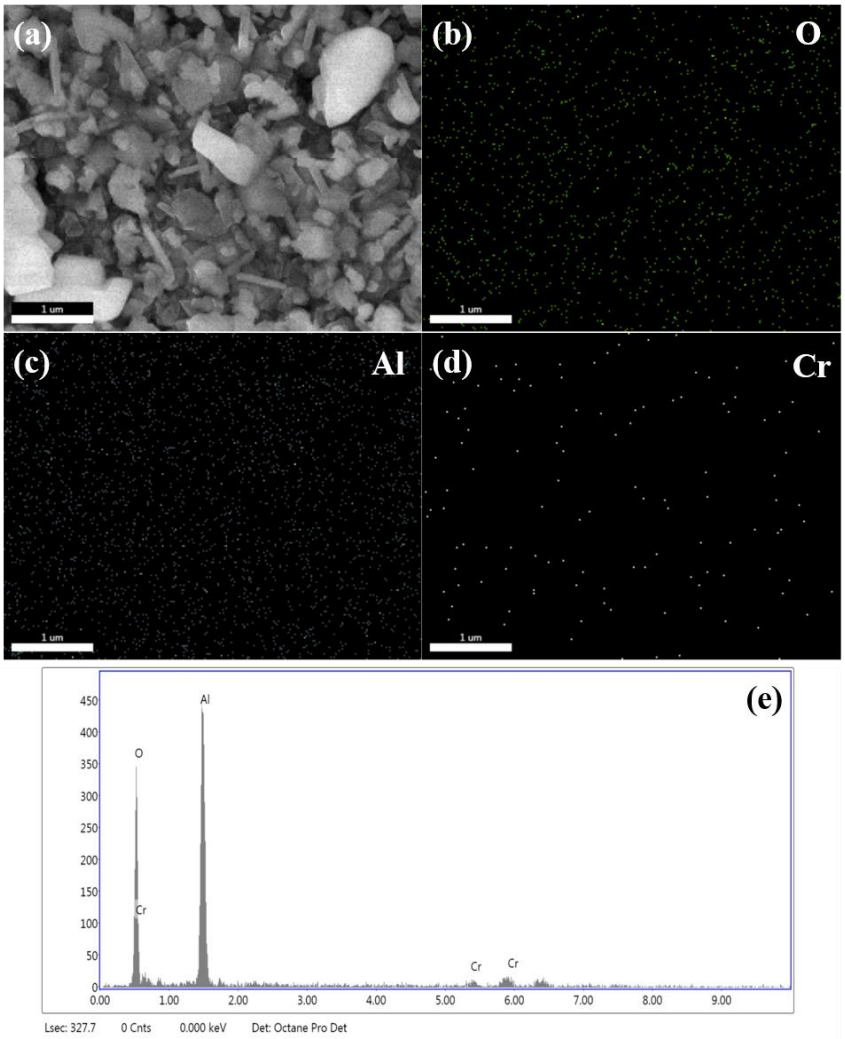

Figure 10 SEM/EDX mapping of the OC11 surface tested for 500 h in air + 10% H_2O at 900 °C in quartz tube.

For OC11 tested at 900 °C for 500 hours, there are some spinel oxides and needle-like oxide on the surface. The main oxide on the surface mainly contains Al according to the EDX mapping results which is corresponding to the needle-like oxide, and the spinel is the Cr-Mn oxide.

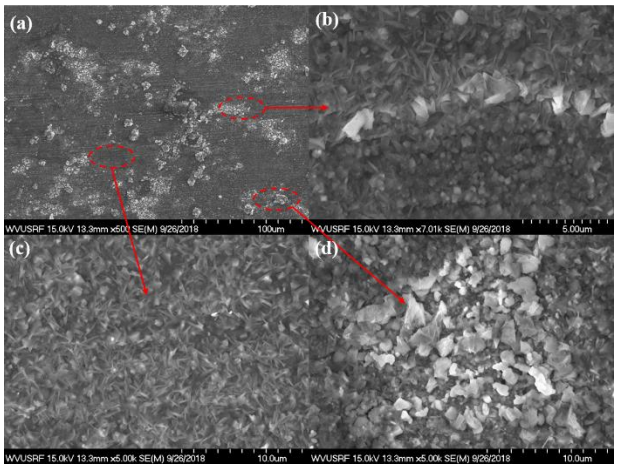

Figure 11 SEM characterization for OC11LZ in 10% H_2O at 900 °C for 500 hours.

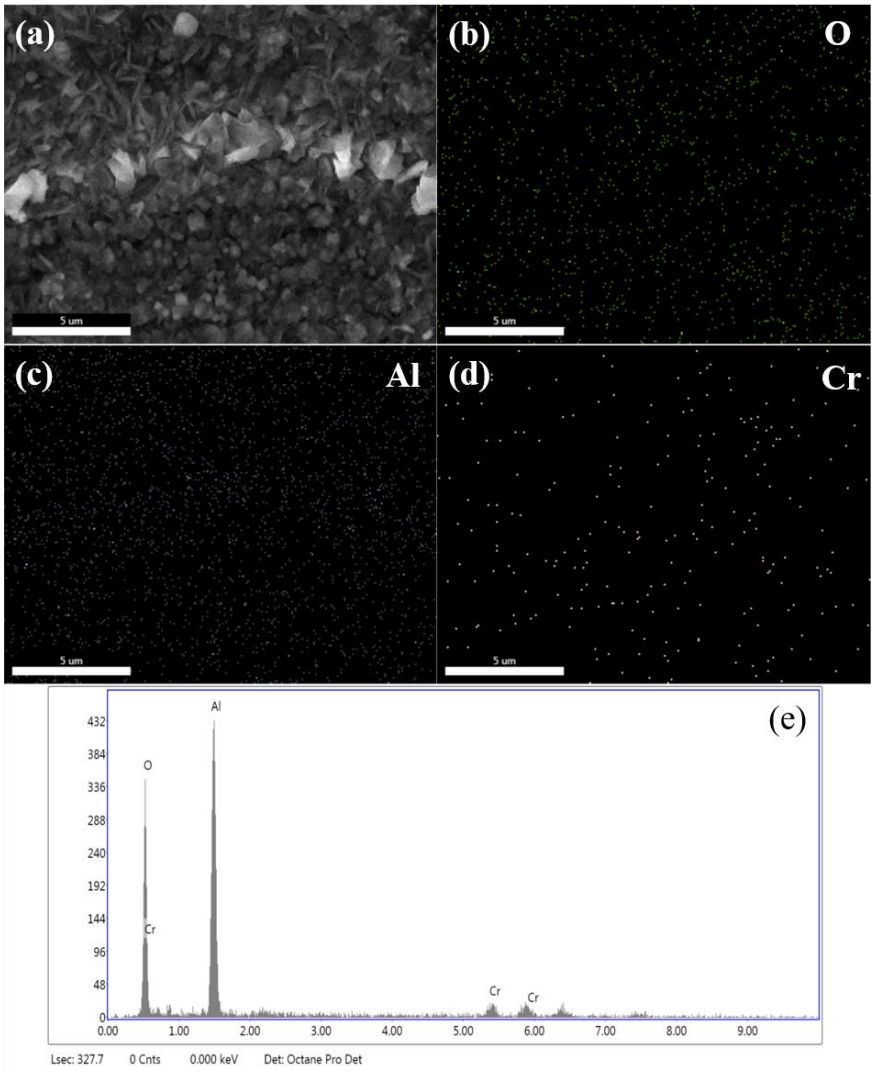

Figure 12 SEM/EDX mapping of the OC11LZ surface tested for 500 h in air + 10% H_2O at 900 °C in quartz tube.

For OC11-LZ tested at 900 °C for 500 hours, the surface morphology is similar to that of OC11. The oxide on the surface mainly contains Al according to the EDX mapping results which is corresponding to the needle-like oxide, and the spinel oxide may be the Cr-Mn oxide which indicates that these two samples may have comparable Cr evaporation rates under this condition.

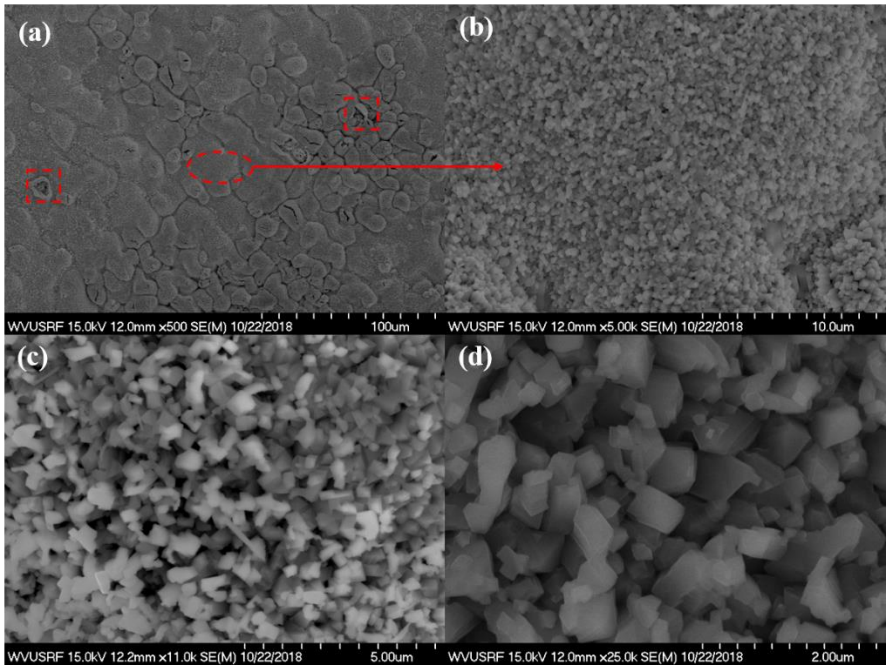

Figure 13 SEM characterization for 625 in 10% H_2O at 900 °C for 1000 hours.

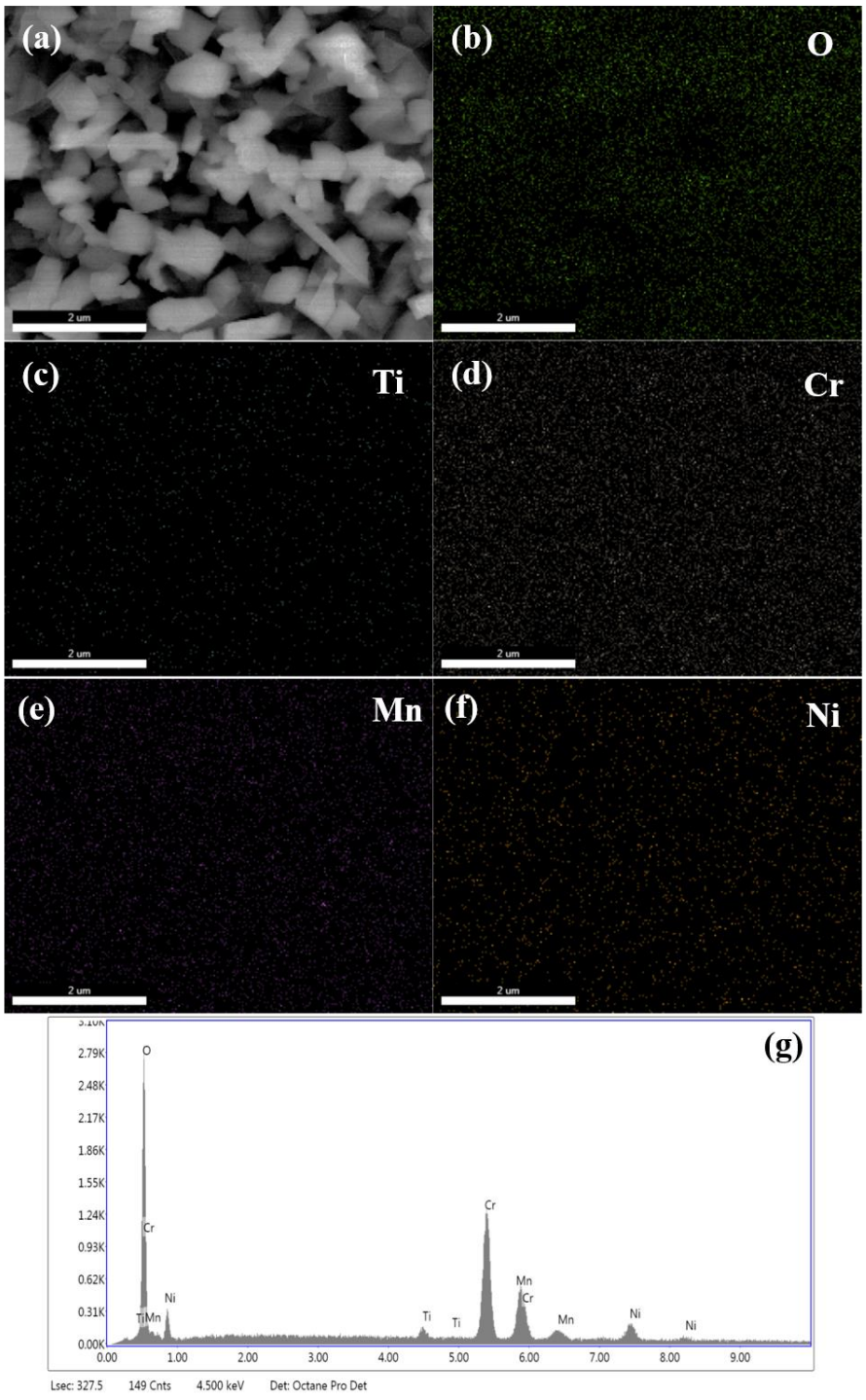

Figure 14 SEM/EDX mapping of the 625 surface tested for 1000 h in air + 10% H_2O at 900 °C in quartz tube.

For 625 alloys tested at 900 °C for 1000 hours, spinel oxide distributes evenly on the surface. And these oxide on the surface contains Cr-Mn oxide based on the EDX mapping results. In addition, there are some spallation on the surface shown in the red square region.

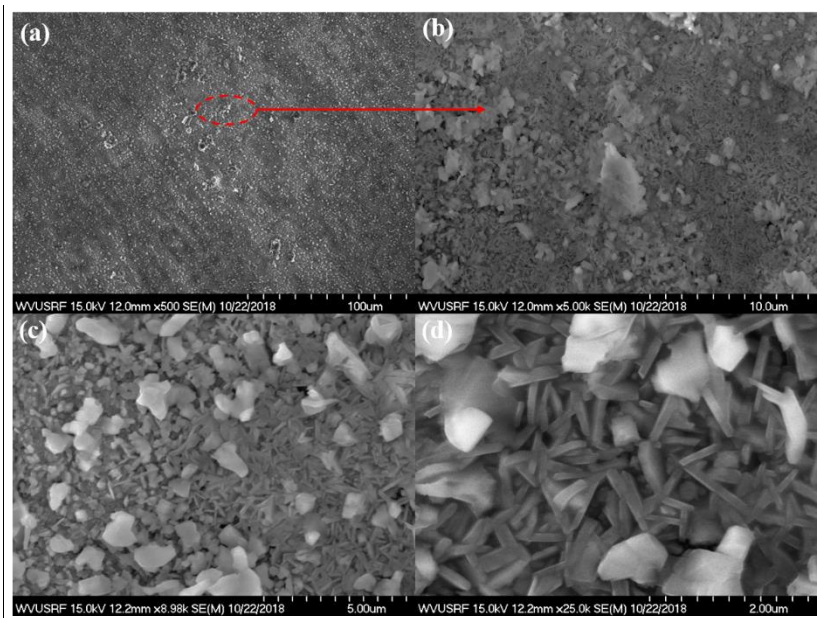

Figure 15 SEM characterization for OC11 in 10% H_2O at 900 °C for 1000 hours.

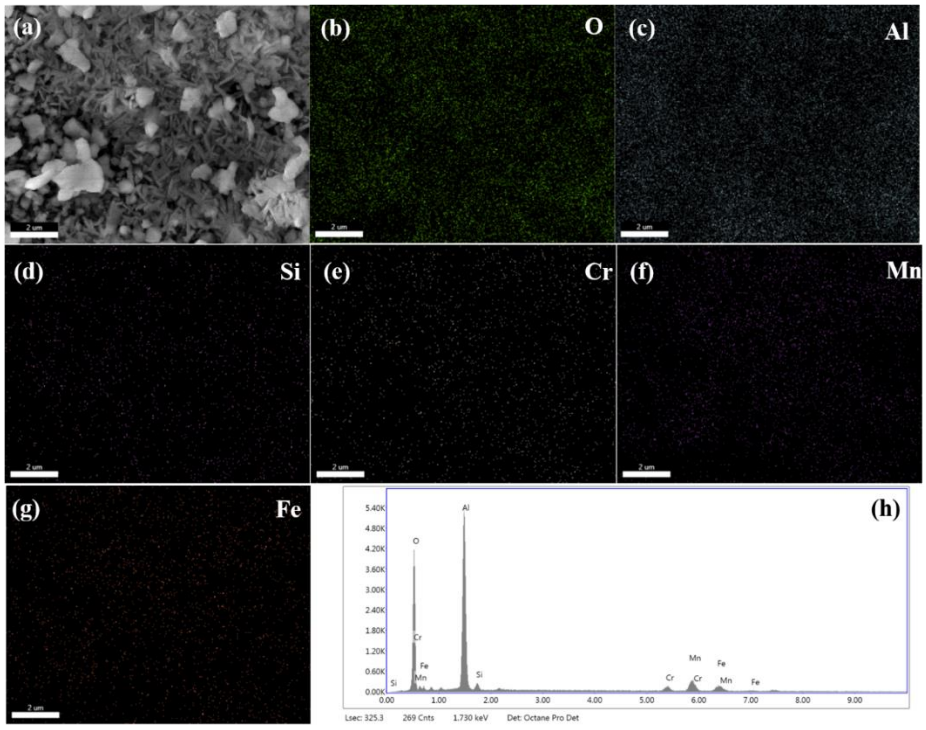

Figure 16 SEM/EDX mapping of the OC11 surface tested for 1000 h in air + 10% H_2O at 900 °C in quartz tube.

For OC11 tested at 900 °C for 1000 hours, the surface morphology is similar to that of 500 hours. The mainly oxide on the surface mainly contains Al according to the EDX mapping results which is corresponding to the needle-like oxide, and the spinel oxide might be the Cr-Mn oxide. In addition, silicon contamination could also be observed on the surface.

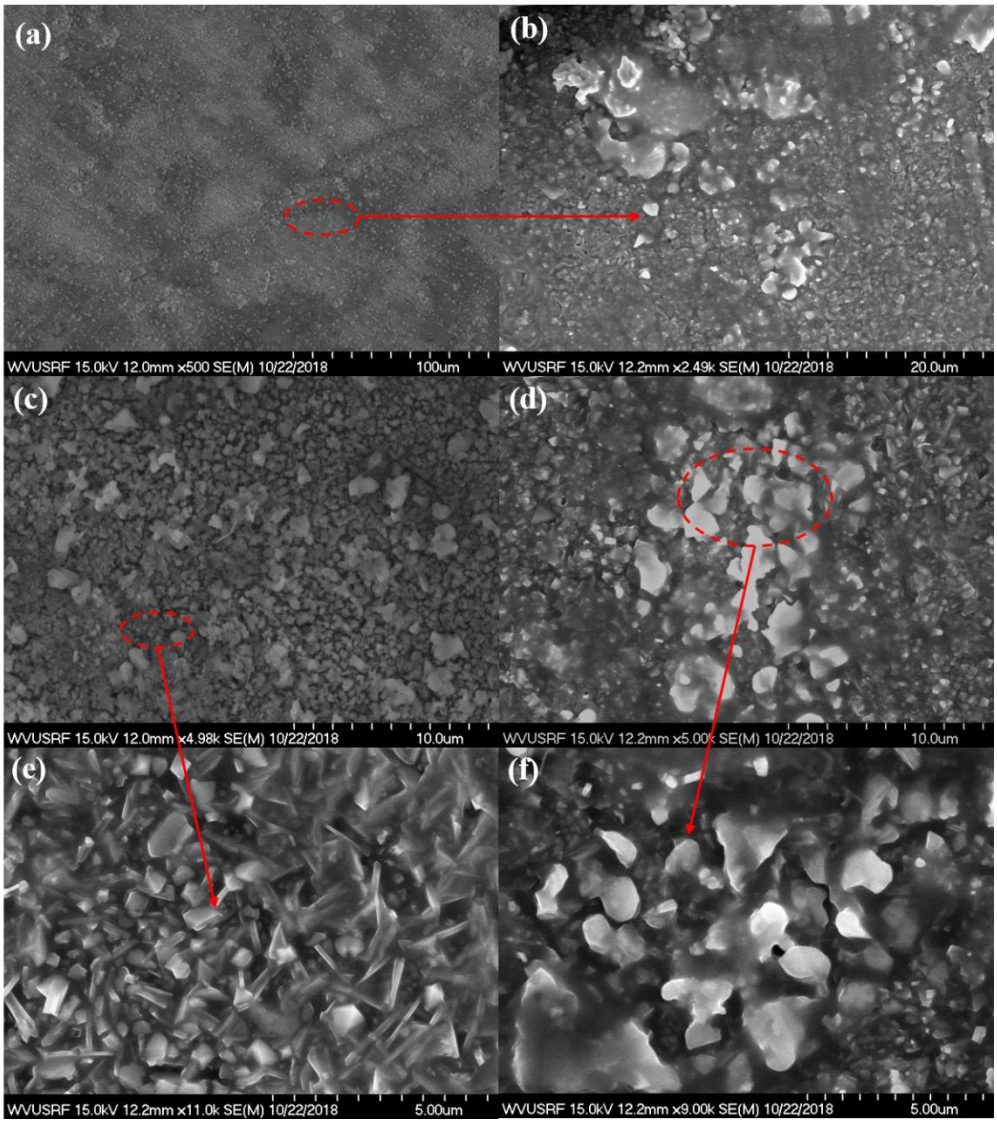

Figure 17 SEM characterization for OC11LZ in 10% H_2O at 900 °C for 1000 hours.

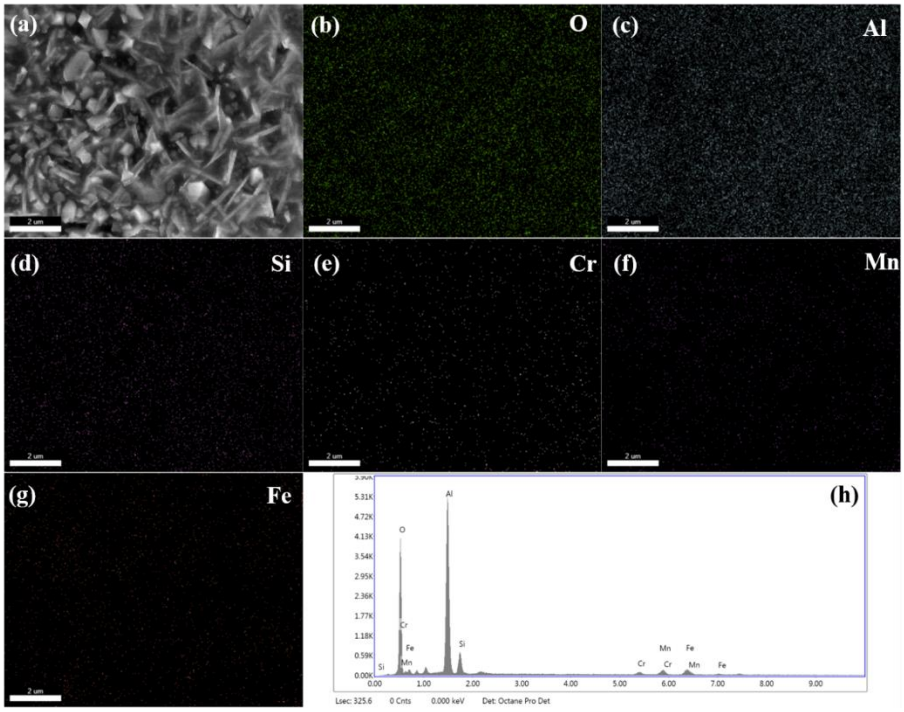

Figure 18 SEM/EDX mapping of the OC11 surface tested for 1000 h in air + 10% H_2O at 900 °C in quartz tube (Area 1).

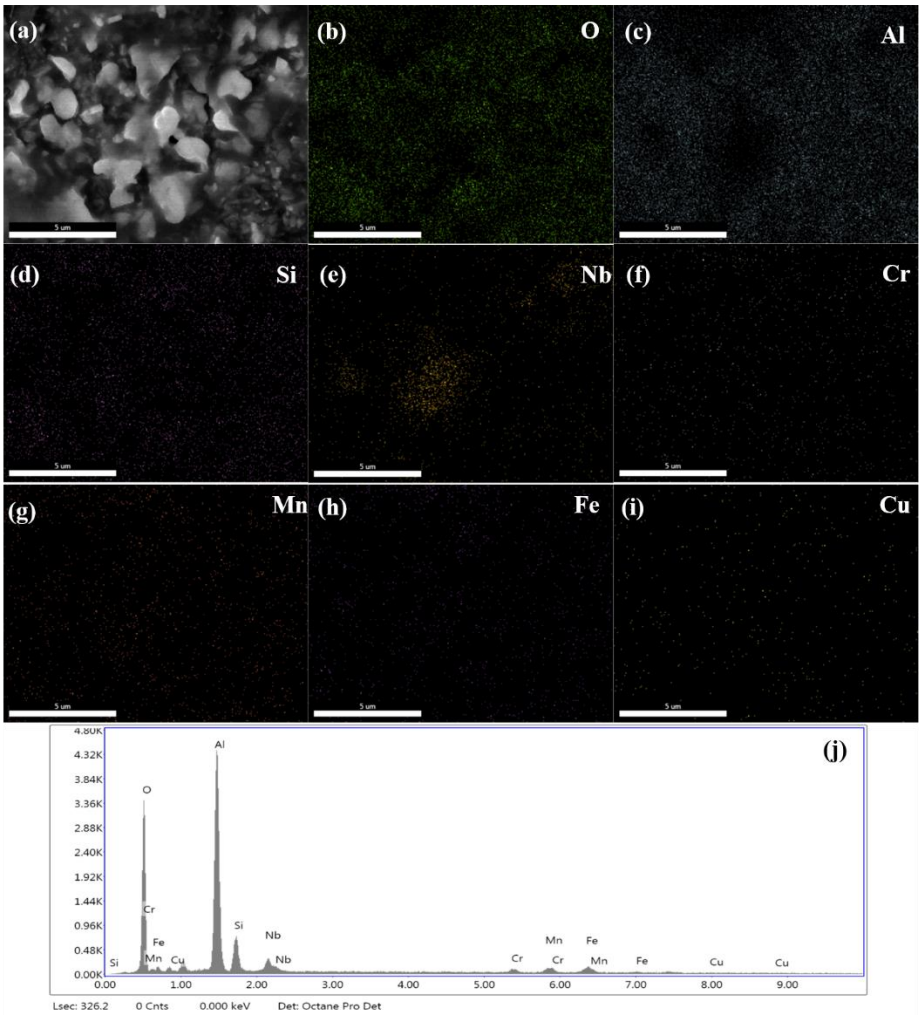

Figure 19 SEM/EDX mapping of the OC11 surface tested for 1000 h in air + 10% H_2O at 900 °C in quartz tube (Area 2).

For OC11LZ tested at 900 °C for 1000 hours, the surface morphology is similar to that of OC11. There are two kinds of oxides on the surface. One is the brighter and bulky oxide which includes the Nb-rich oxide and the other is needle-like oxide. In addition, there are silicon contamination on the surface.

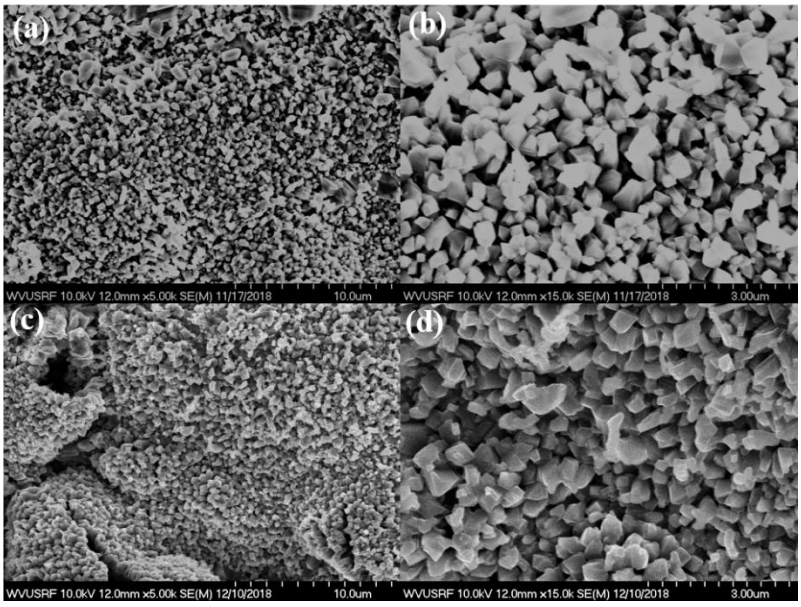

Figure 20 Typical SEM image of 625 samples tested in 10% H_2O at 900 °C with different time (a, b) 1500h and (c, d) 2000h.

A low magnification SEM image reveals a non-uniform surface while the high magnification image reveals three-dimensional crystallites with the dimensions less than the order of 1 μm.

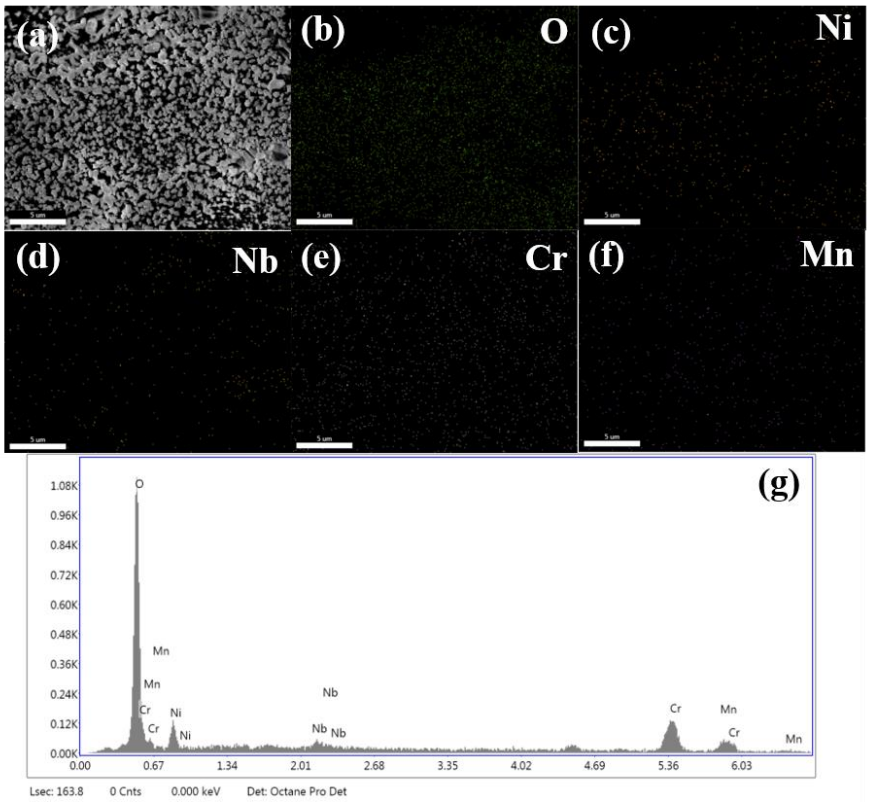

Figure 21 SEM/EDX mapping of the 625 surface tested for 1500 h in air + 10% H_2O at 900 °C in quartz tube.

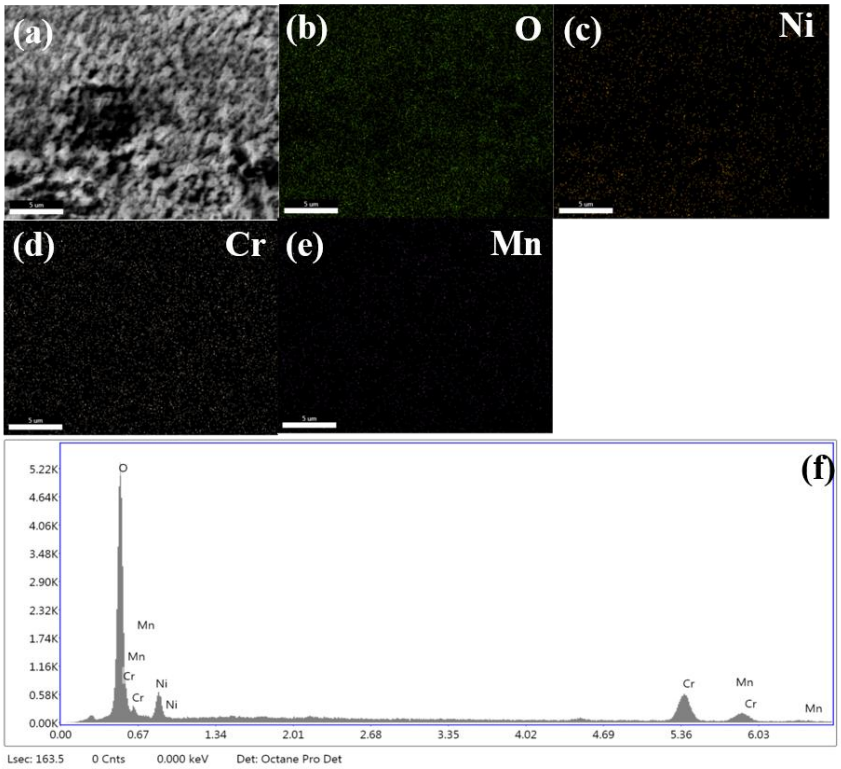

Figure 22 SEM/EDX mapping of the 625 surface tested for 2000 h in air + 10% H_2O at 900 °C in quartz tube.

For 625 alloys tested at 900 °C for 1500 and 2000 hours, spinel oxides dominate at the alloy surface which could be verified by the EDX mapping results.

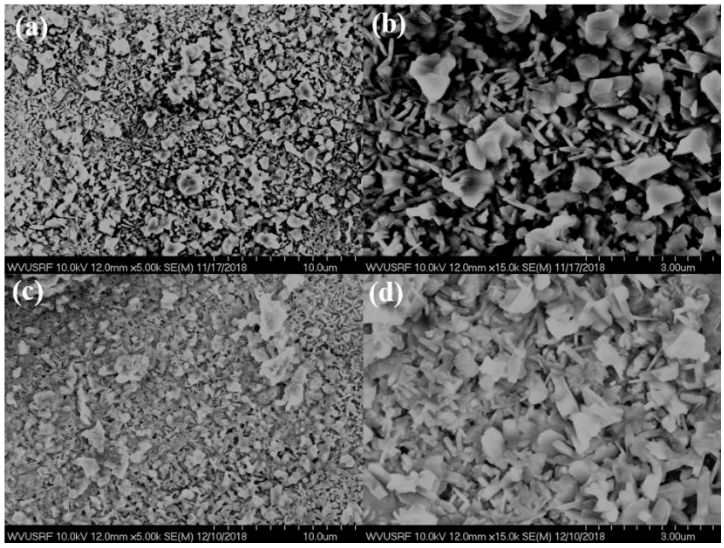

Figure 23 Typical SEM image of OC11 samples tested in 10% H_2O at 900 °C with different time (a, b) 1500h and (c, d) 2000h.

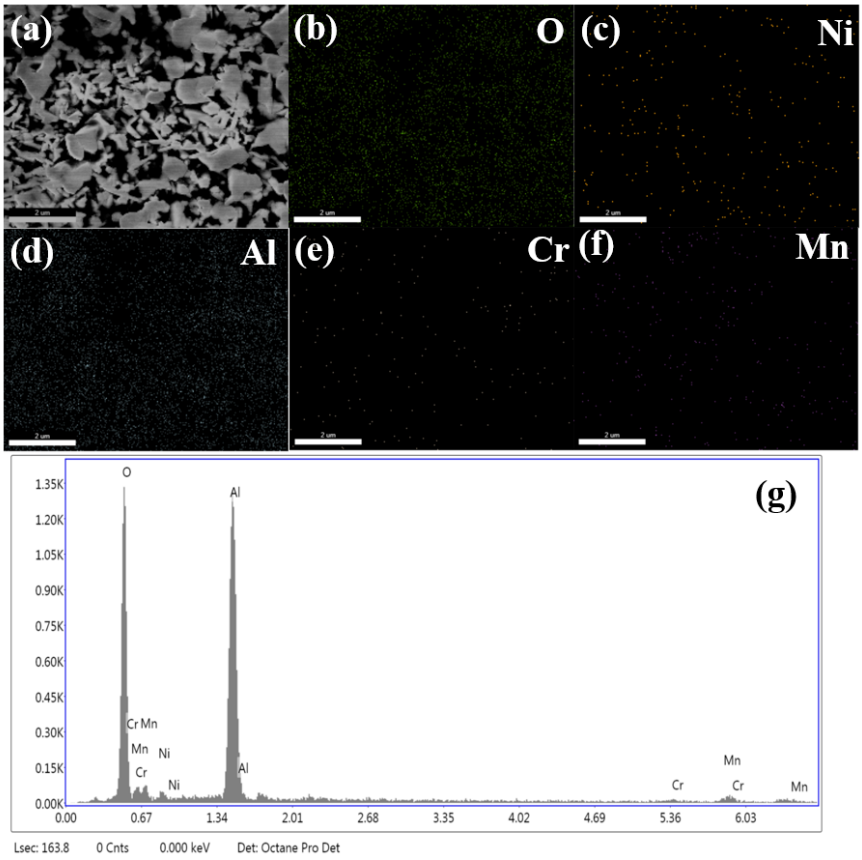

Figure 24 SEM/EDX mapping of the OC11 surface tested for 1500 h in air + 10% H_2O at 900 °C in quartz tube.

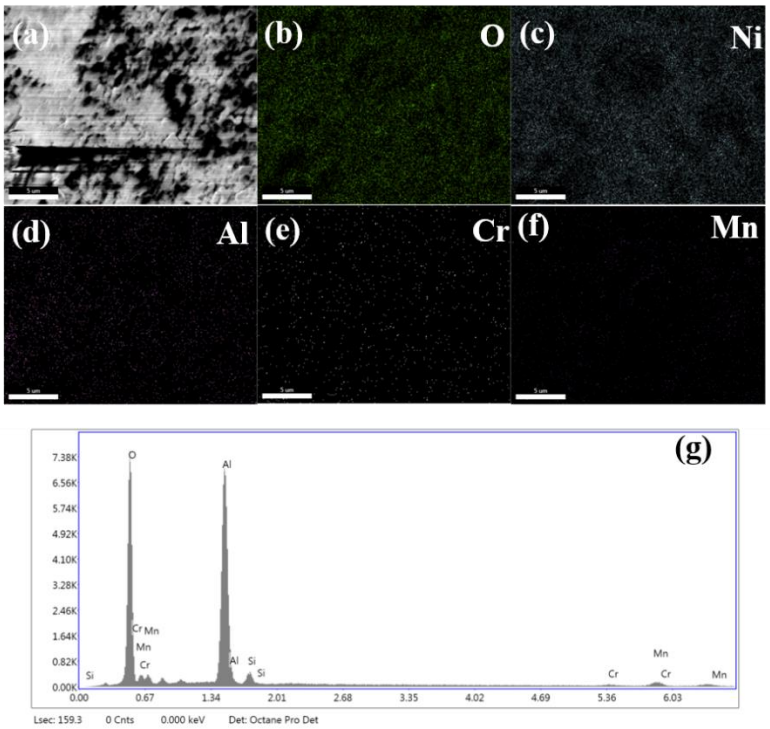

Figure 25 SEM/EDX mapping of the OC11 surface tested for 2000 h in air + 10% H_2O at 900 °C in quartz tube.

For OC11 tested at 900 °C for 1500 and 2000 hours, there are some spinel oxides and needle-like oxide on the surface. The dominant oxide on the surface mainly contains Al according to the EDX mapping results which is corresponding to the needle-like oxide, and the spinel oxide should be the Cr-Mn oxide. EDS mapping measured on the top surface of the sample oxidized for 1500 h is used to verify the formation of the Al_2O_3. It is worth noting that silicon contamination is observed on the 2000h sample.

(1)

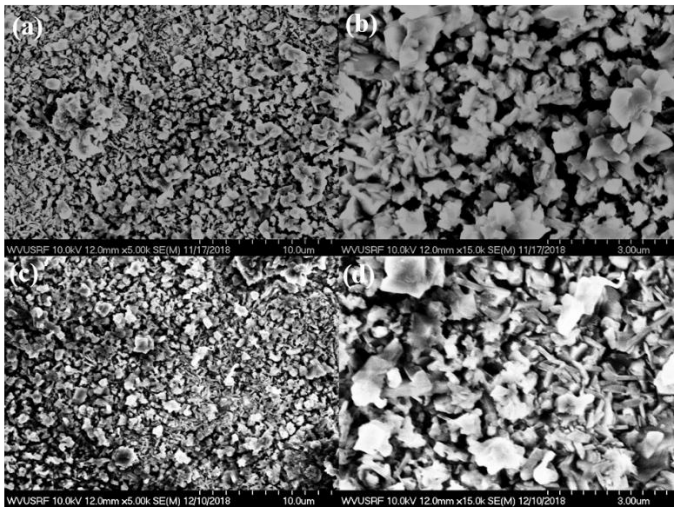

Figure 26 Typical SEM image of OC11LZ samples tested in 10% H_2O at 900 °C with different time (a, b) 1500h and (c, d) 2000h.

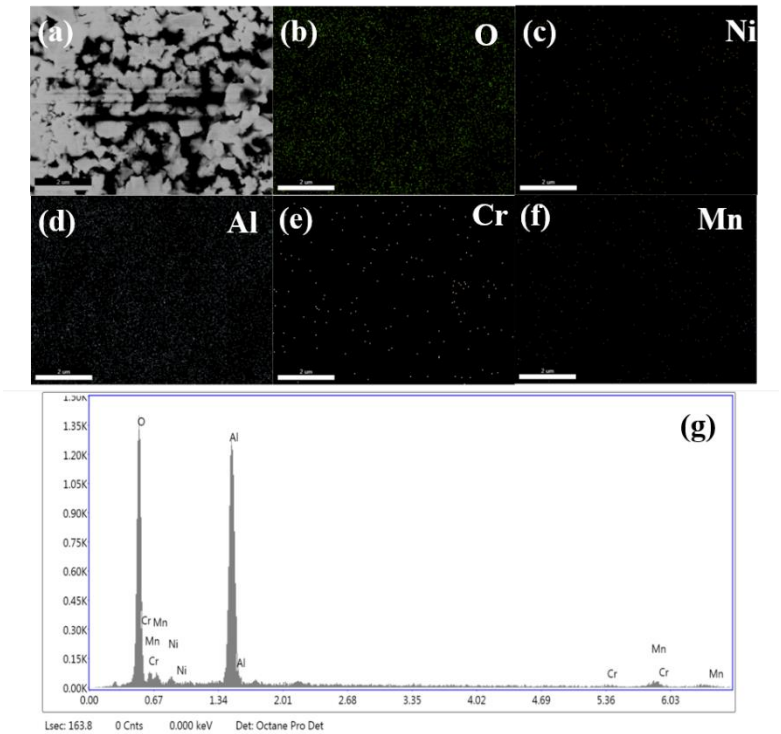

Figure 27 SEM/EDX mapping of the OC11LZ surface tested for 1500 h in air + 10% H_2O at 900 °C in quartz tube.

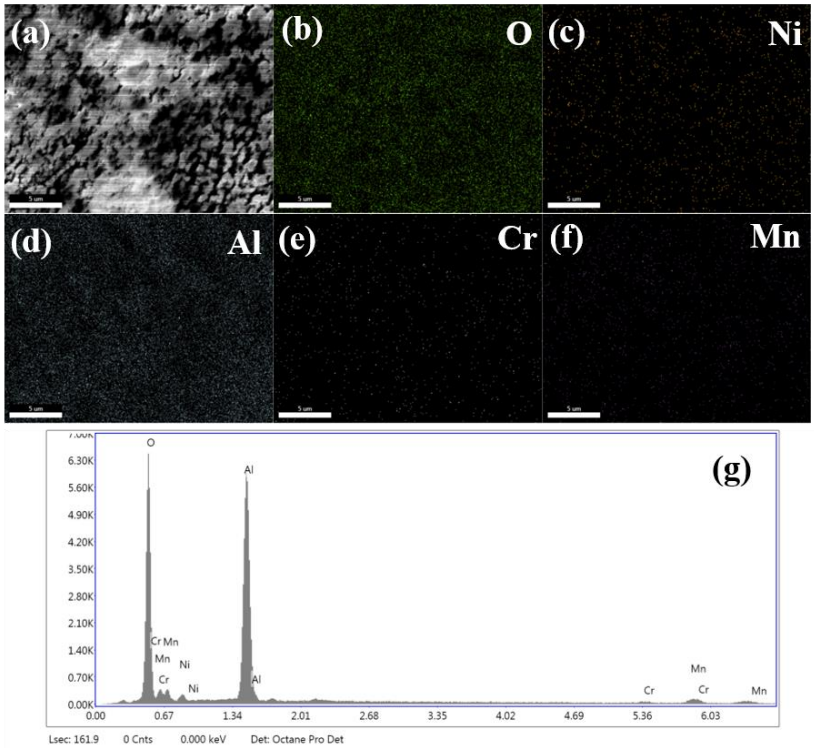

Figure 28 SEM/EDX mapping of the OC11LZ surface tested for 2000 h in air + 10% H_2O at 900 °C in quartz tube.

The surface morphology of OC11LZ is similar to that of OC11. The oxide on the surface mainly contains Al according to the EDX mapping results which is corresponding to the needle-like oxide, and the spinel oxide may be the Cr-Mn oxide. And there is little difference between 1500 and 2000 hours.

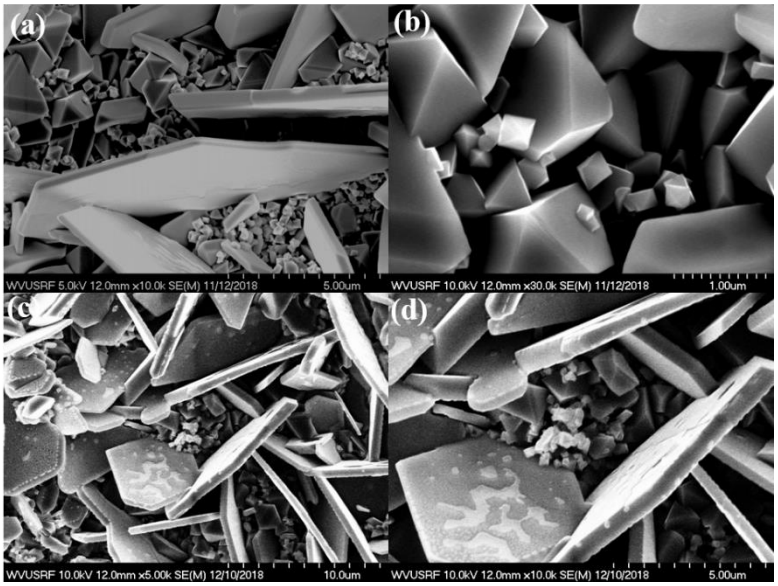

Figure 29 Typical SEM image of 310S samples tested in 10% H_2O at 800 ^oC with different time (a, b) 500 h and (c, d) 1000 h.

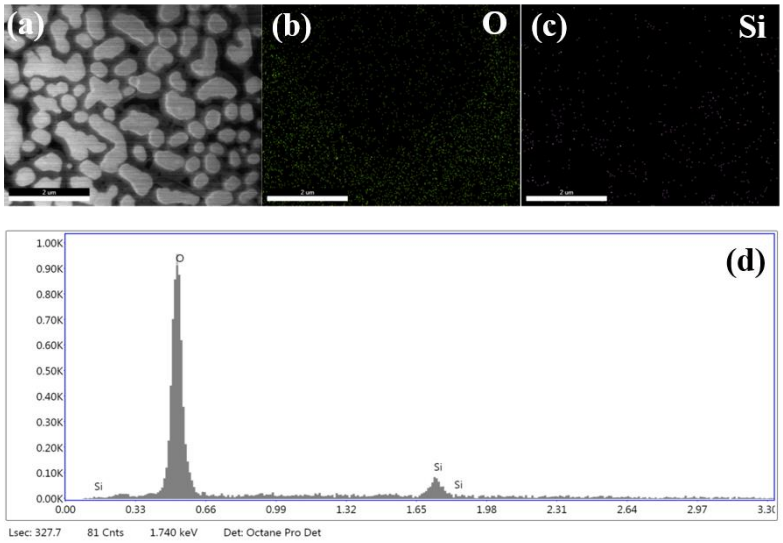

Figure 30 SEM/EDX mapping of the 310S surface tested for 500 h in air + 10% H_2O at 800 °C in quartz tube (Area 1).

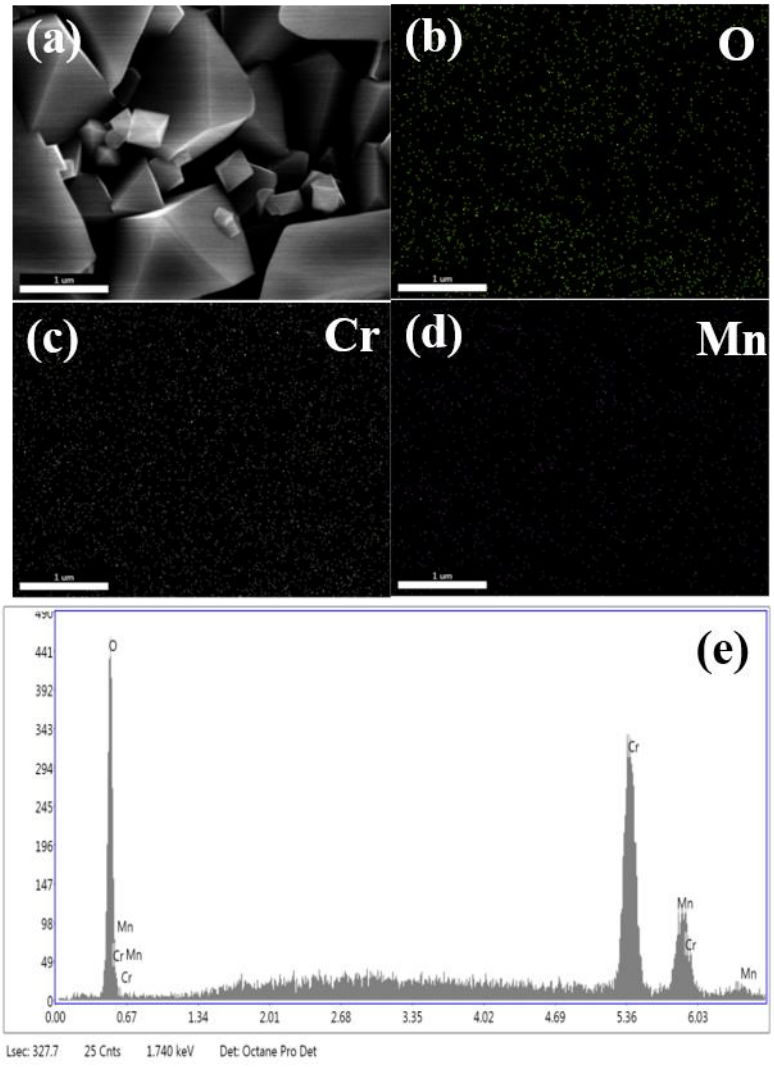

Figure 31 SEM/EDX mapping of the 310S surface tested for 500 h in air + 10% H_2O at 800 °C in quartz tube (Area 2).

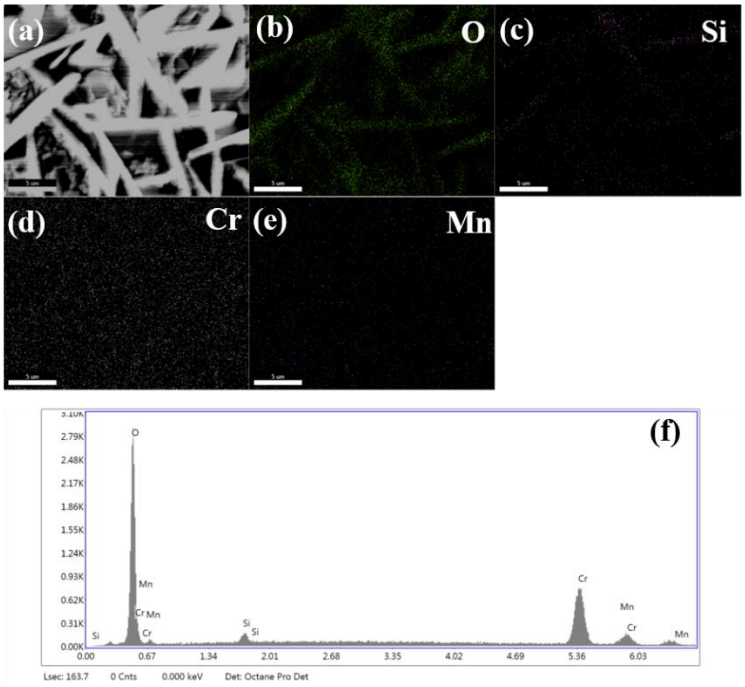

Figure 32 SEM/EDX mapping of the 310S surface tested for 1000 h in air + 10% H_2O at 800 °C in quartz tube.

Oxide scale with polyhedral crystallite particles size less than 1 μm and plate-like oxide where silicon precipitate formed on the exposed surface of the sample. When exposure time was prolonged from 500 h to 1000 h, the oxide layer seemingly does not change. EDS mapping verifies the deposition of the SiO_2 on the plate-like oxide and a large number of formation of Cr-Mn oxide under 500h, there are also formation Cr-Mn oxide and the precipitation of silicon under 1000h.

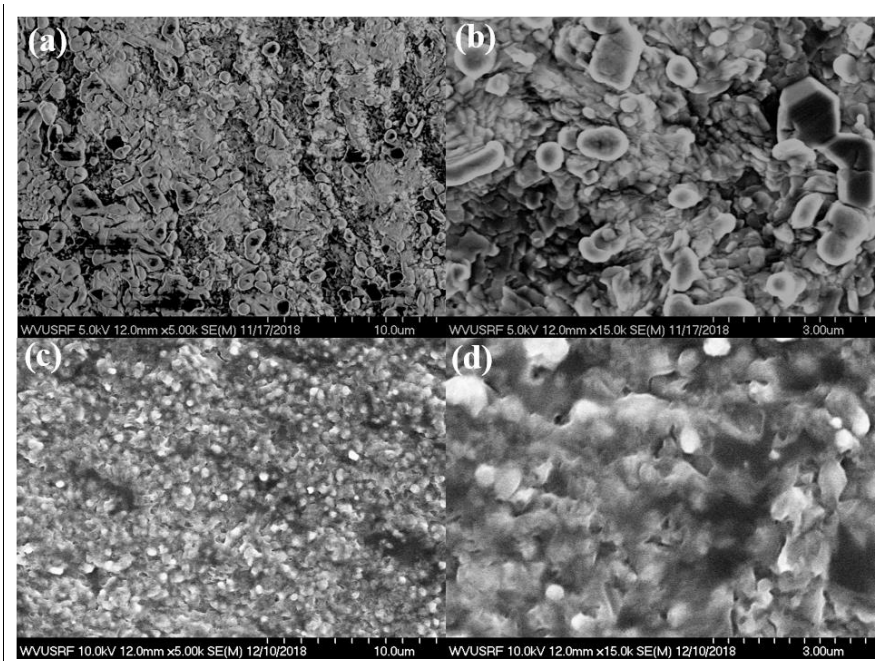

Figure 33 Typical SEM image of OC4 samples tested in 10% H_2O at 800 °C with different time (a, b) 500h and (c, d) 1000h.

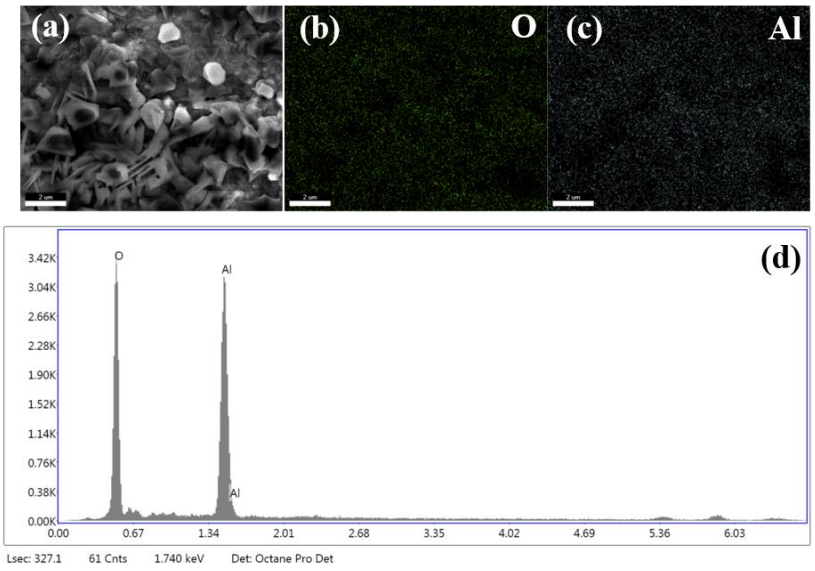

Figure 34 SEM/EDX mapping of the OC4 surface tested for 500 h in air + 10% H_2O at 800 °C in quartz tube.

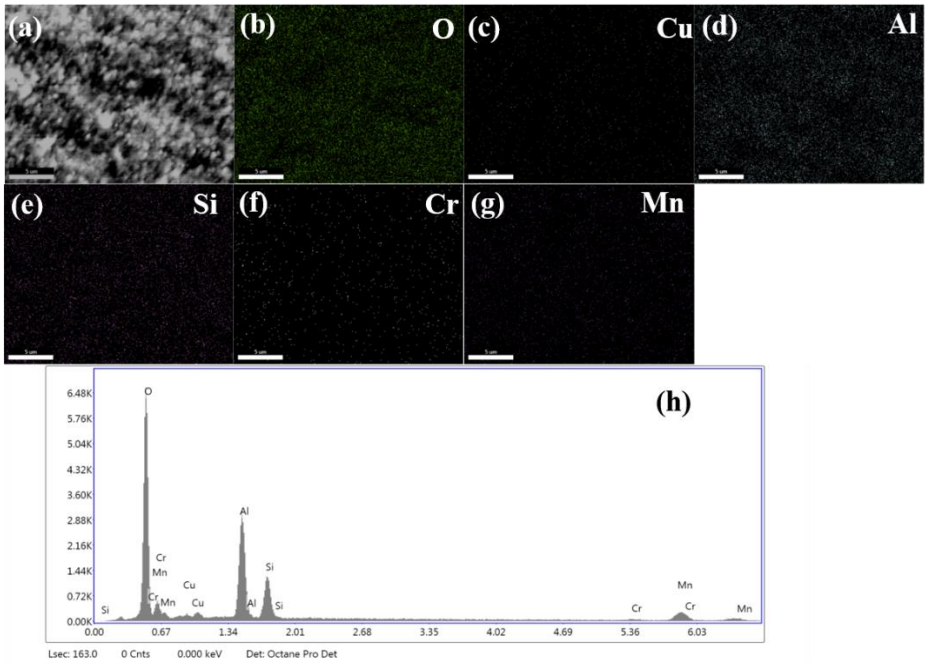

Figure 35 SEM/EDX mapping of the OC4 surface tested for 1000 h in air + 10% H_2O at 800 °C in quartz tube.

For OC4 tested at 800 °C for 1000 hours, the surface morphology is different to that of 500 hours which is attributed to the deposition of silicon from the quartz tube and Cr-Mn-rich oxides. The main oxides on the surface contains Al according to the EDX mapping results which is corresponding to the needle-like oxide under 500 hours. However, the spinel (Cr-Mn-rich oxides) and contamination of silicon appears on the surface under 1000 hours.

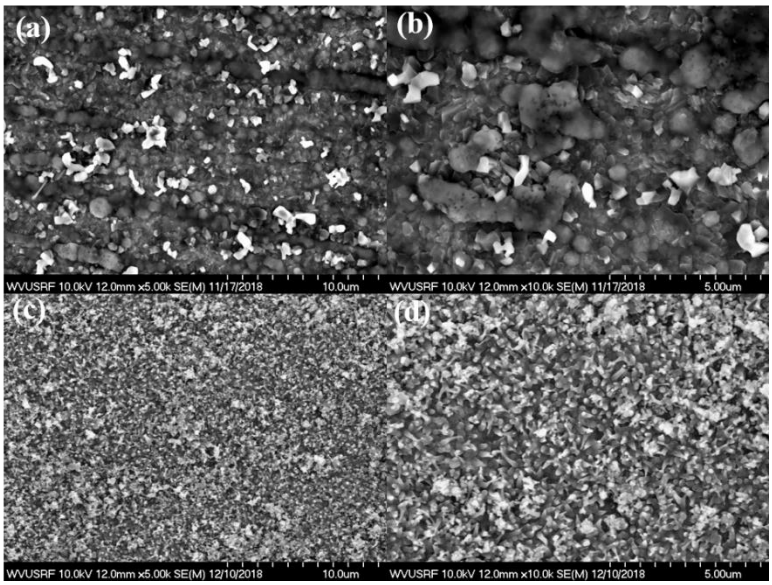

Figure 36 Typical SEM image of OC4 samples tested in 10% H_2O at 800 °C with different time (a, b) 500h and (c, d) 1000h.

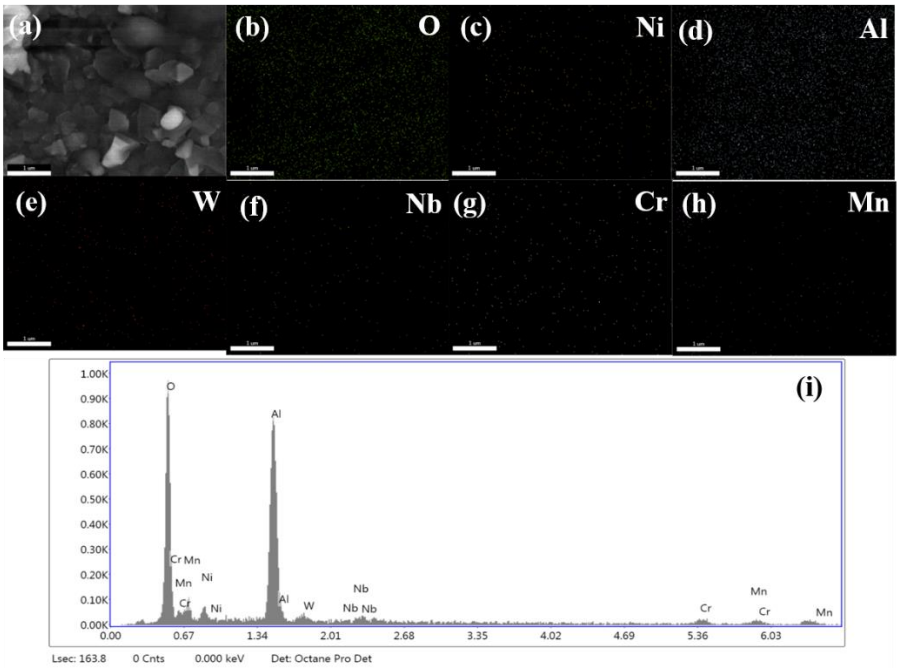

Figure 37 SEM/EDX mapping of the OC5 surface tested for 500 h in air + 10% H_2O at 800 °C in quartz tube.

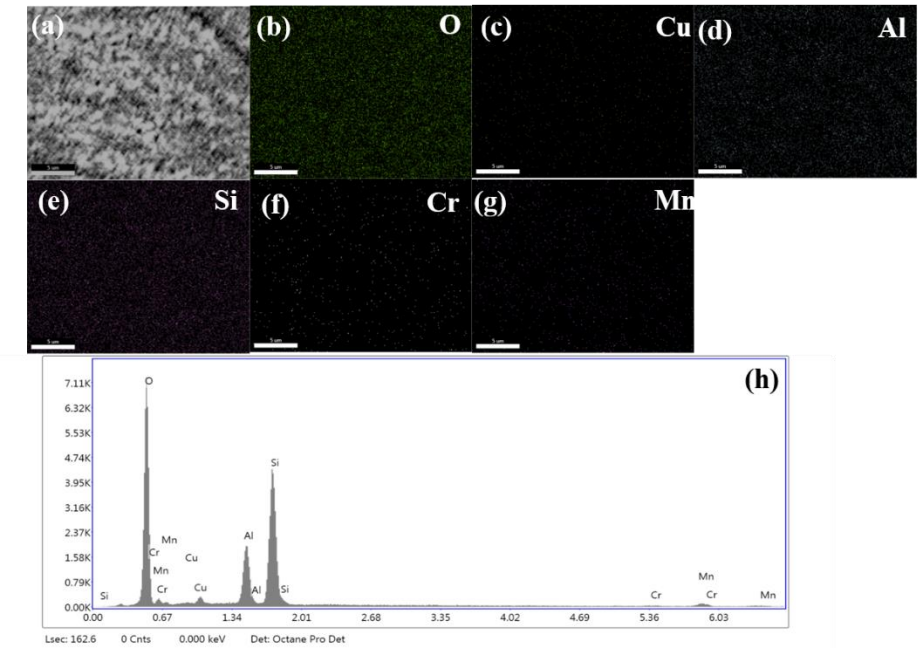

Figure 38 SEM/EDX mapping of the OC5 surface tested for 500 h in air + 10% H_2O at 800 °C in quartz tube.

For OC5 tested at 800 °C for 500 hours, the surface morphology is different to that of 1000 hours. There are also deposition of silicon on the surface under 1000 hours. However, there are not silicon and copper but tungsten and niobium oxides on the surface under 500 hours with a small amount of Cr-Mn oxide.

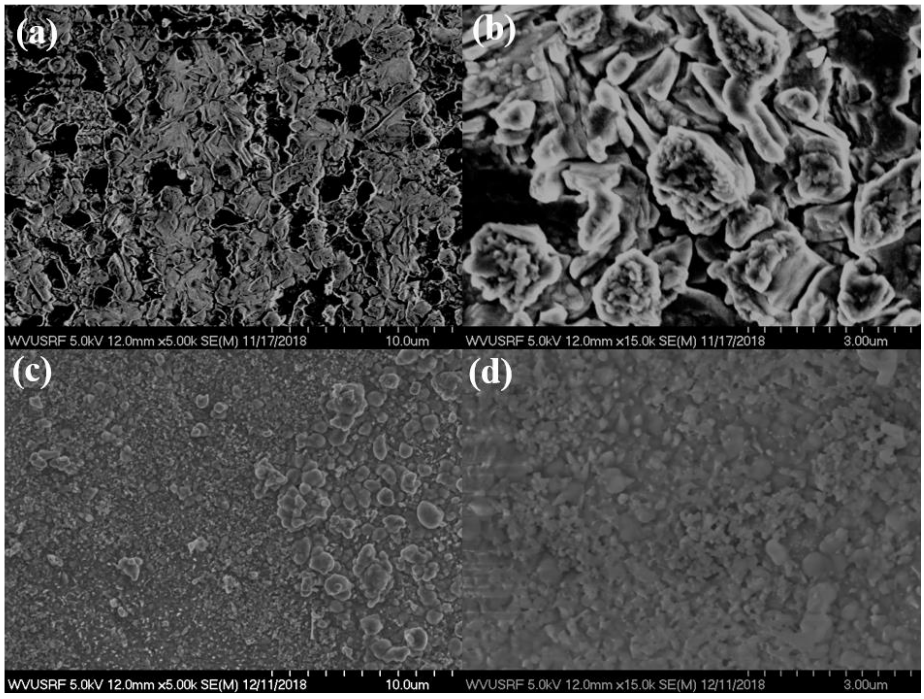

Figure 39 Typical SEM image of MOD samples tested in 10% H_2O at 800 °C with different time (a, b) 500h and (c, d) 1000h.

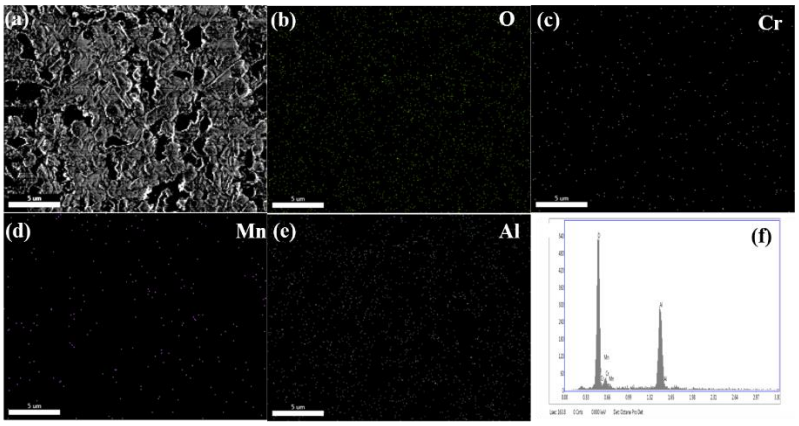

Figure 40 SEM/EDX mapping of the MOD surface tested for 500 h in air + 10% H_2O at 800 °C in quartz tube.

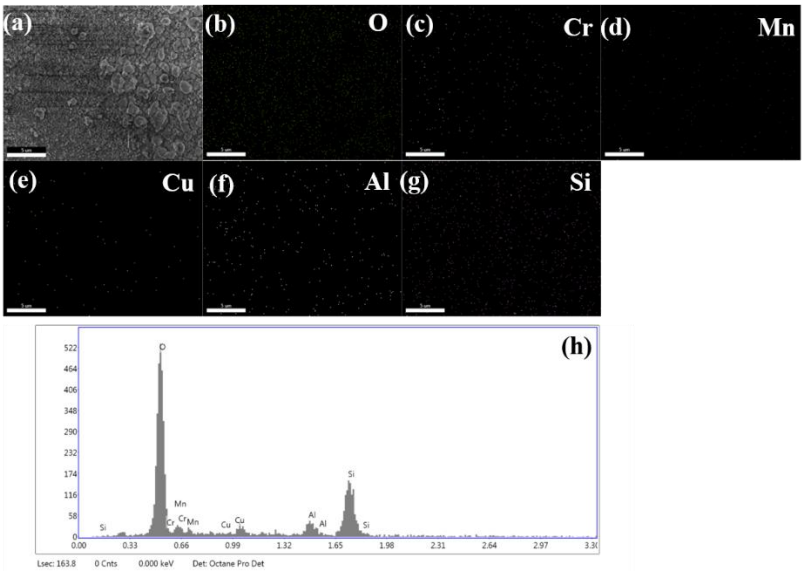

Figure 41 SEM/EDX mapping of the MOD surface tested for 1000 h in air + 10% H_2O at 800 °C in quartz tube.

For MOD tested at 800 °C for 500 and 1000 hours, there are Al_2O_3 on the surface and a small amount of Cr-Mn oxides formed on the surface. However, there was no Si deposition under 500 hours. When the time was prolonged to 1000 hours, there was silicon and copper deposition on the surface.

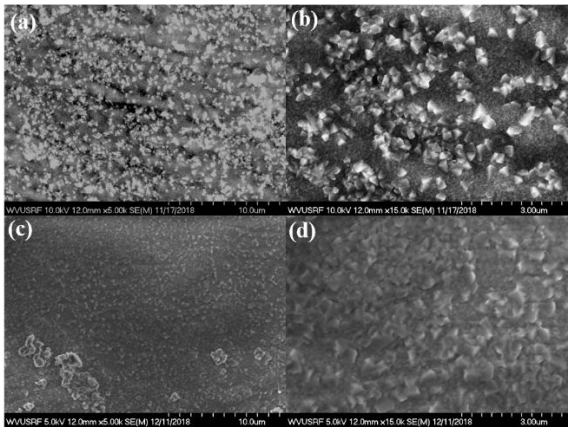

Figure 42 Typical SEM image of OC11 samples tested in 10% H_2O at 800 °C with different time (a, b) 500h and (c, d) 1000h.

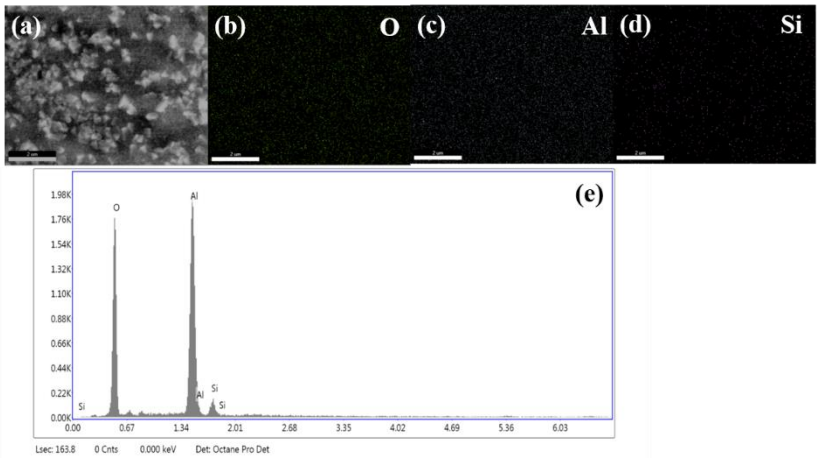

Figure 43 SEM/EDX mapping of the OC11 surface tested for 500 h in air + 10% H_2O at 800 °C in quartz tube.

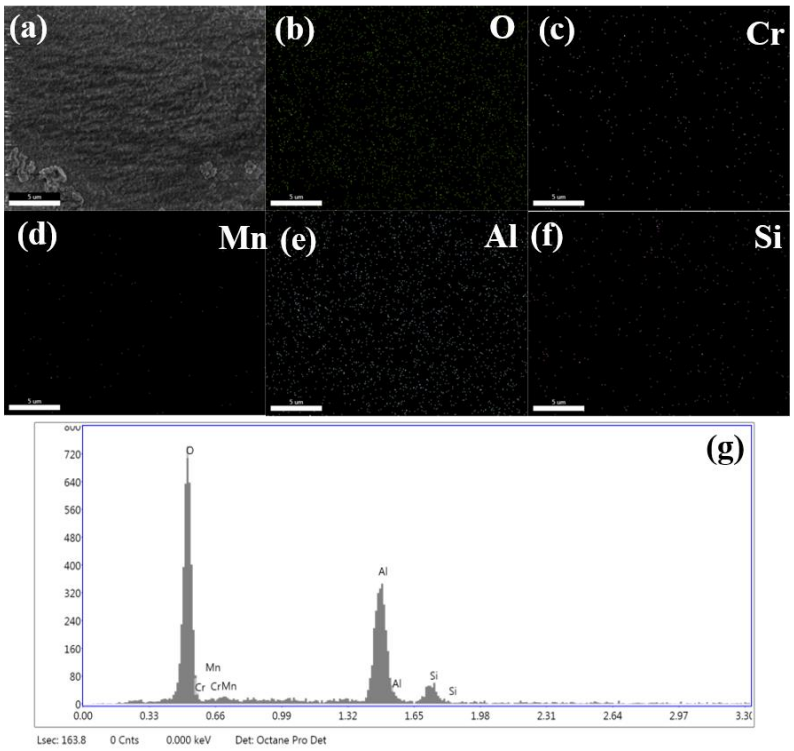

Figure 44 SEM/EDX mapping of the OC11 surface tested for 1000 h in air + 10% H_2O at 800 °C in quartz tube.

For OC11 tested at 800 °C for 500 and 1000 hours, there are oxide uniformly formed on the surface. However, there was almost no Cr-Mn oxide formed under 500 hours. When the time was prolonged to 1000 hours, there was a small amount of Cr-Mn oxides formed on the surface.

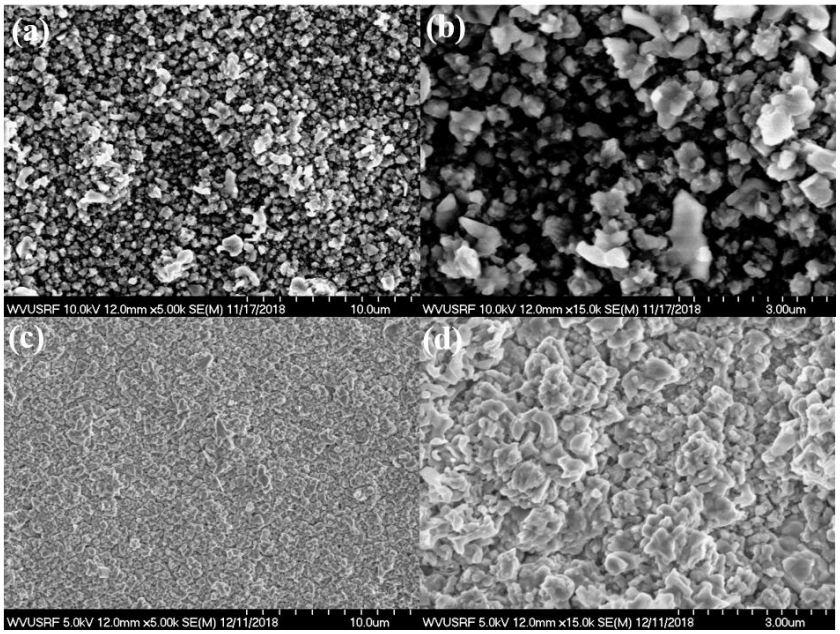

Figure 45 Typical SEM image of OC11LZ samples tested in 10% H_2O at 800 °C with different time (a, b) 500h and (c, d) 1000h.

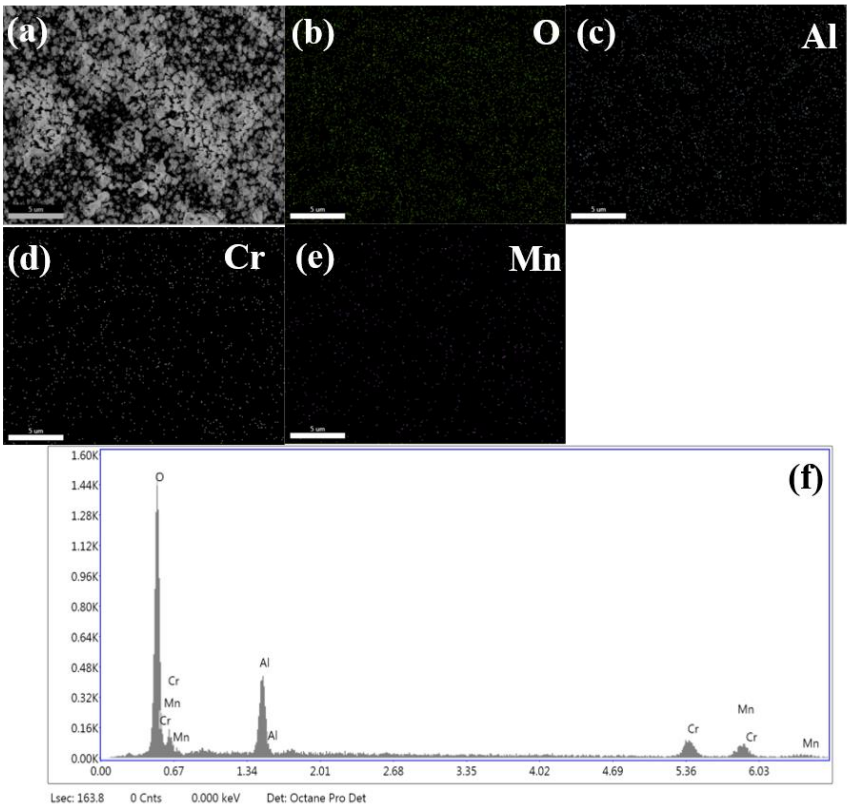

Figure 46 SEM/EDX mapping of the OC11LZ surface tested for 500 h in air + 10% H_2O at 800 °C in quartz tube.

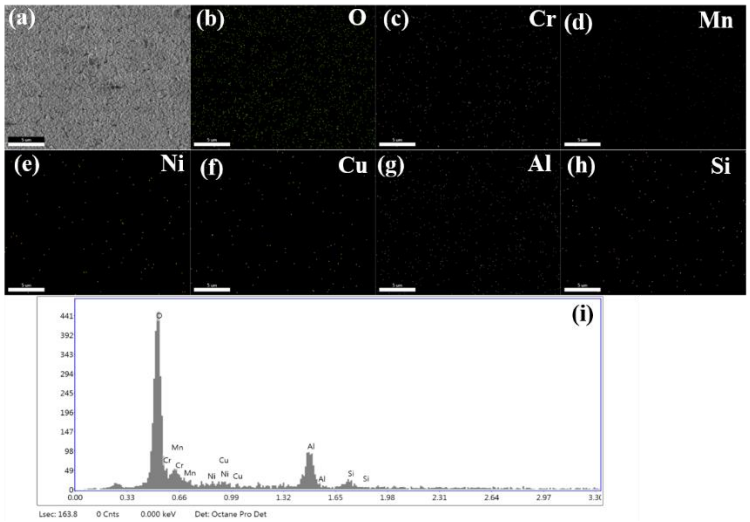

Figure 47 SEM/EDX mapping of the OC11LZ surface tested for 1000 h in air + 10% H_2O at 800 °C in quartz tube.

For OC11LZ tested at 800 °C for 500 and 1000 hours, the morphology almost didn't change, there are Al_2O_3 on the surface and a small amount of Cr-Mn oxides formed on the surface. However, there was no Si deposition at 500 hours. When the time was prolonged to 1000 hours, there was silicon, nickel and copper oxides formed on the surface.

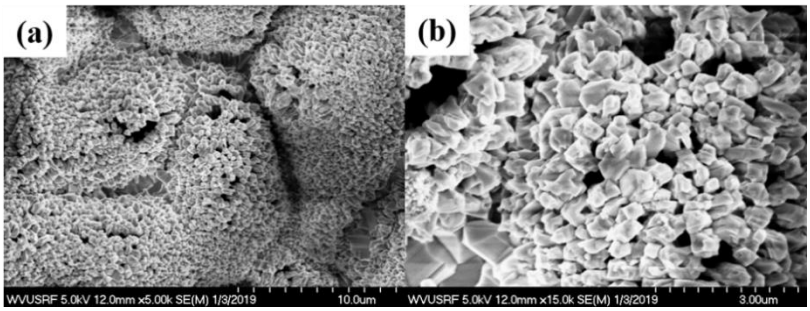

Figure 48 SEM surface morphologies of 625 alloy after exposure to 10% H_2O at 900 °C for 2500h.

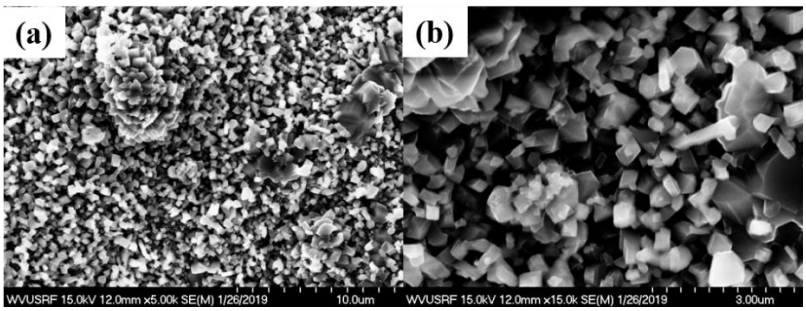

Figure 49 SEM surface morphologies of 625 alloy after exposure to 10% H_2O at 900 °C for 3000h.

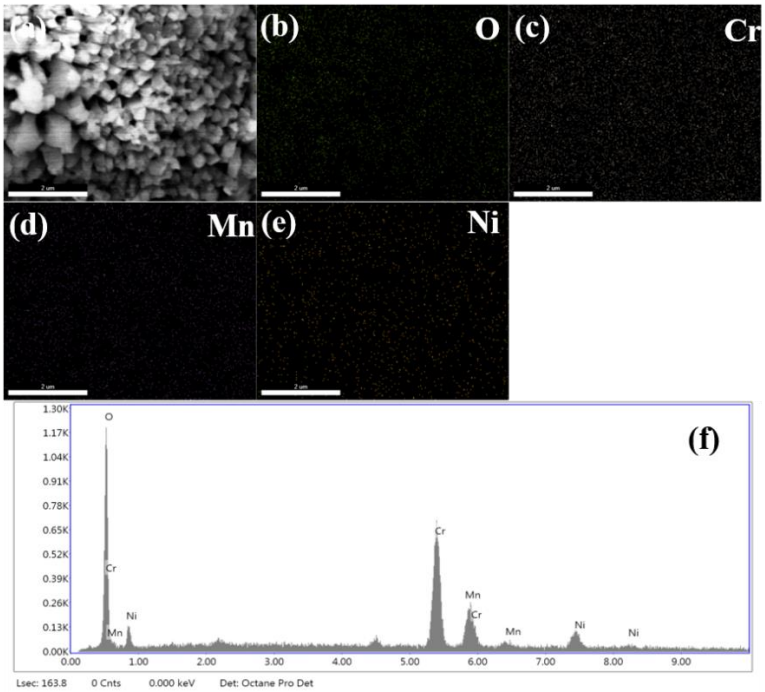

Figure 50 EDX elemental mapping of 625 alloy after exposure to 10% H_2O at 900 °C for 2500h.

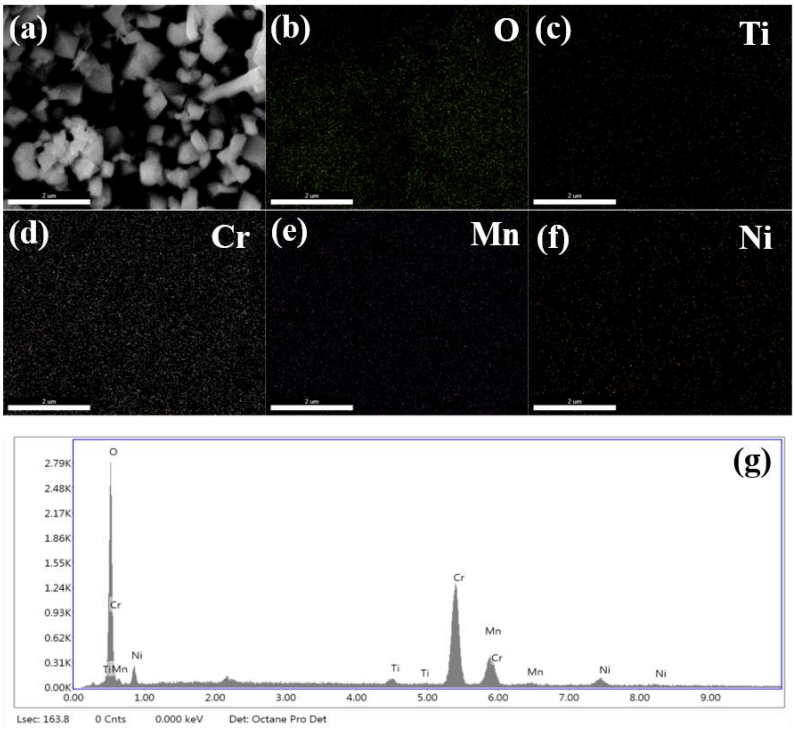

Figure 51 EDX elemental mapping of 625 alloy after exposure to 10% H_2O at 900 °C for 3000h.

Figure 48 and 49 show SEM surface morphologies of 625 alloy after exposure to 10% H_2O at 900 °C for 2500h and 3000h. After 2500 h exposure, the distribution of the oxides on the surface is relatively uniform but small holes are observed in higher magnification images (Figure 48(b)). There is mainly one type of grains of which size is range from 0.3 to 1 μm. These grains are

diamond-shaped which are Cr-Mn-rich oxides confirmed by EDS (Figure 50). As the exposure time increases, both the size and the composition of the oxides do not change much which are revealed in Figure 49 and Figure 51, respectively. However, the Cr-Mn-rich oxide grains accumulate and form big nodules after 2500h exposure (Figure 48(a)), whereas the accumulation of grains reduce after 3000h exposure and a larger number of small holes appear to form after 3000h exposure than 2500h exposure.

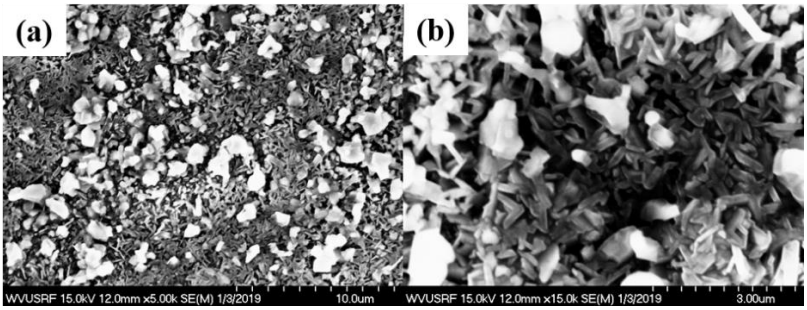

Figure 52 SEM surface morphologies of AFA OC11 after exposure to 10% H_2O at 900 °C for 2500h.

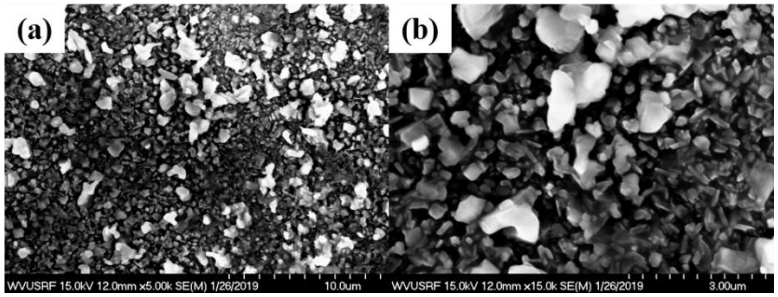

Figure 53 SEM surface morphologies of AFA OC11 after exposure to 10% H_2O at 900 °C for 3000h.

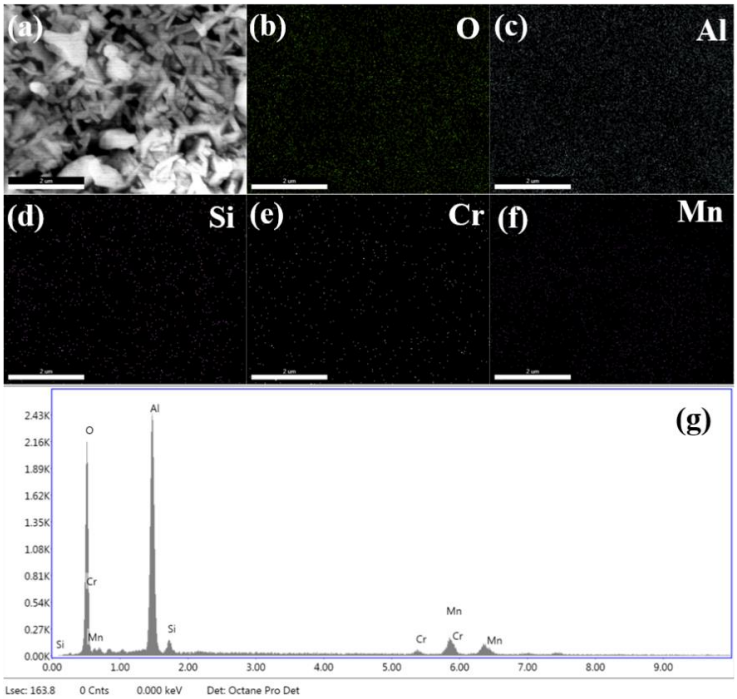

Figure 54 EDX elemental mapping of AFA OC11 after exposure to 10% H_2O at 900 °C for 2500h.

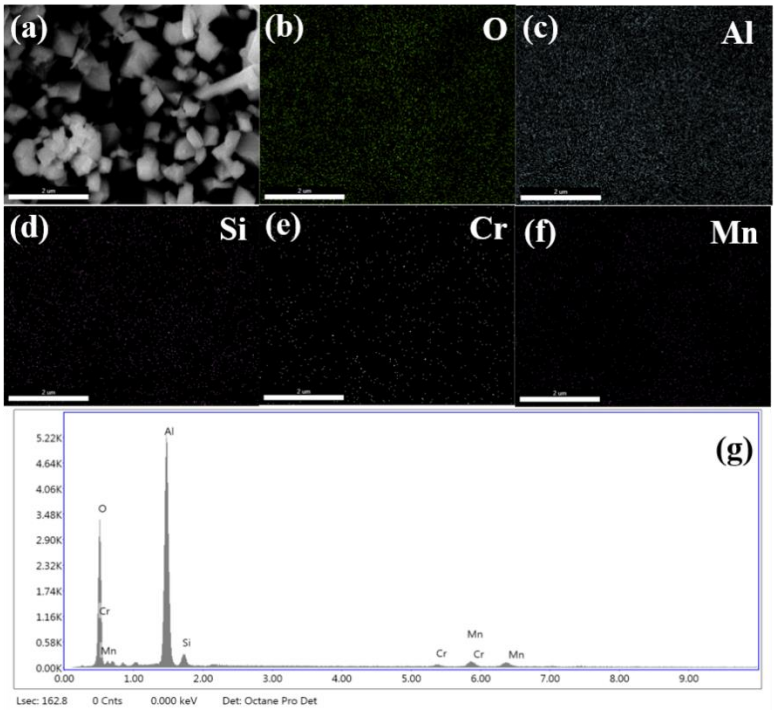

Figure 55 EDX elemental mapping of AFA OC11 after exposure to 10% H_2O at 900 °C for 3000h.

Figure 52 and 53 demonstrate SEM surface morphologies of AFA OC11 after exposure to 10% H_2O at 900 °C for 2500h and 3000h. For the sample operated for 2500h, the surface is non-uniform and there are mainly two types of small grains: one is bar-shaped (length × width: 0.1 μm × 0.5 μm) and the other diamond-shaped (0.3 to 1 μm), which are Al-rich and Cr-Mn-rich oxides confirmed by EDS (Figure 54), respectively. With the increasing of the exposure time to 3000h, the amounts of bar-shaped oxides decrease, and the amounts of diamond-shaped oxides increase (Figure 53). However, the size does not change much for different exposure time. Figure 54 and 55 show that Al-rich oxide is formed on the surface of the AFA OC11 and there are little silicon-related oxides and Cr-Mn-rich oxides on the surface for different expose time.

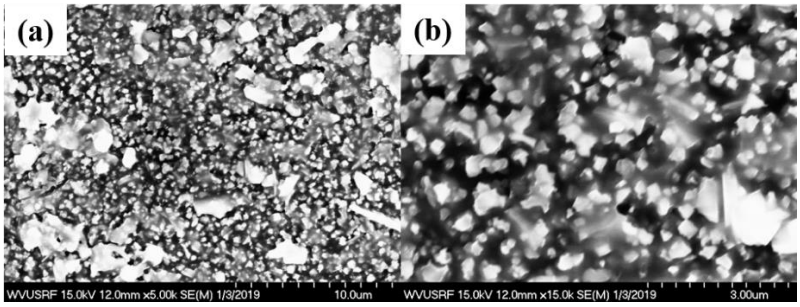

Figure 56 SEM surface morphologies of AFA OC11LZ after exposure to 10% H_2O at 900 °C for 2500h.

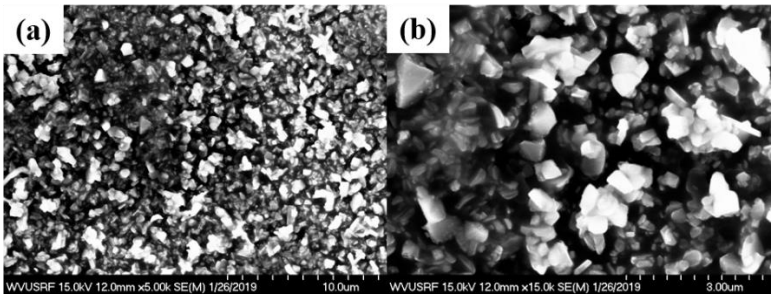

Figure 57 SEM surface morphologies of AFA OC11LZ after exposure to 10% H_2O at 900 °C for 3000h.

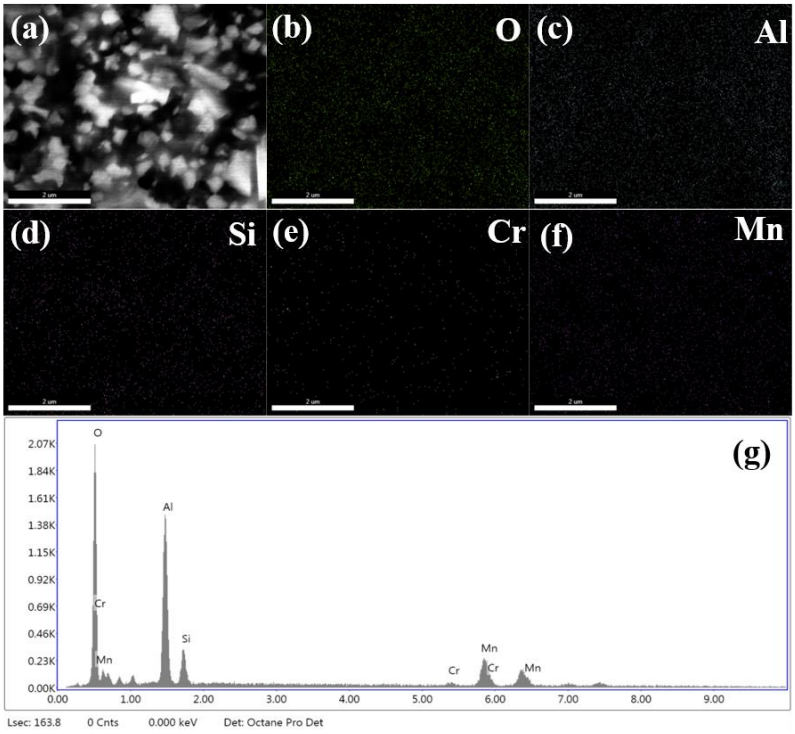

Figure 58 EDX elemental mapping of AFA OC11LZ after exposure to 10% H_2O at 900 °C for 2500h.

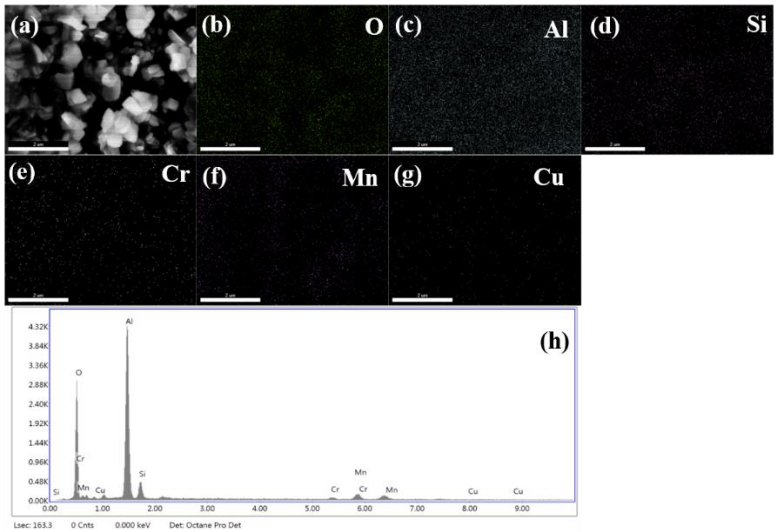

Figure 59 EDX elemental mapping of AFA OC11LZ after exposure to 10% H_2O at 900 °C for 3000h.

Figure 56 and 57 demonstrate SEM surface morphologies of AFA OC11 after exposure to 10% H_2O at 900 °C for 2500h and 3000h. The surface morphology of OC11LZ under different exposure time is similar to that of OC11. After 2500h exposure at 900 °C, the surface is covered by two kinds of small grains: one is bar-shaped and the other diamond-shaped, which are Al-rich and Cr-Mn-rich oxides confirmed by EDS (Figure 58 and 59), respectively. As the exposure time increases, both the size and the composition of the oxides do not change much. However, there is a larger number of oxide grains accumulation for the OC11LZ compared to OC11. Moreover, the quantities of Cr-Mn-rich oxides formed on the surface of OC11LZ appear to be greater than that of OC11.

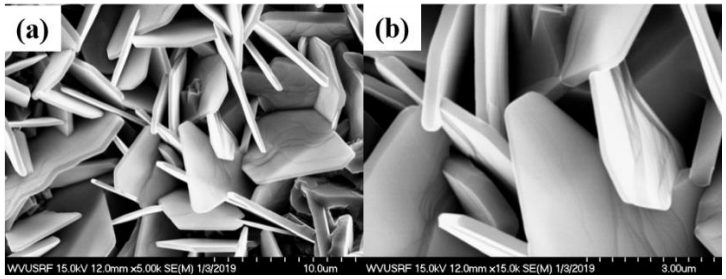

Figure 60 SEM surface morphologies of 310S alloy after exposure to 10% H_2O at 800 °C for 1500h.

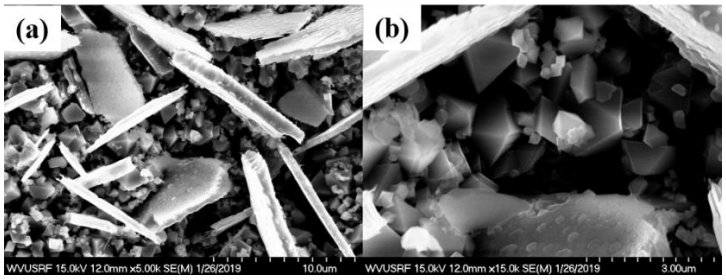

Figure 61 SEM surface morphologies of 310S alloy after exposure to 10% H_2O at 800 °C for 2000h.

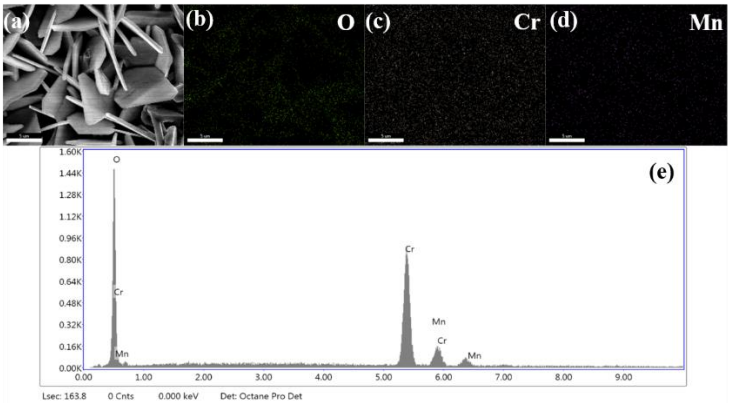

Figure 62 EDX elemental mapping of 310S alloy after exposure to 10% H_2O at 800 °C for 1500h.

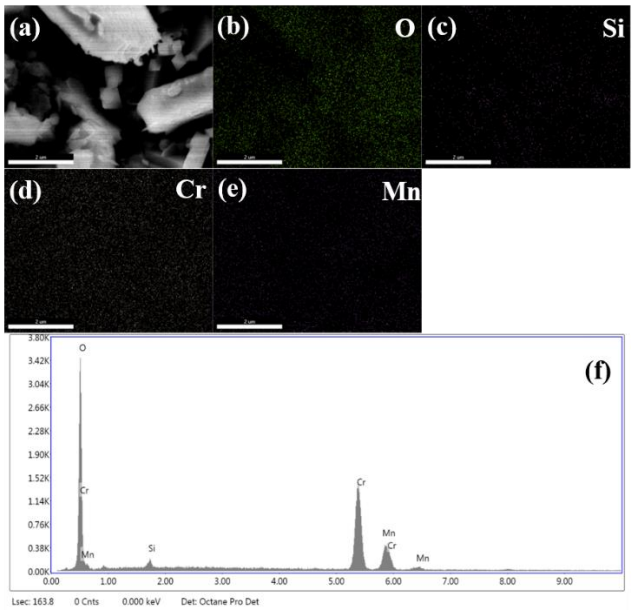

Figure 63 EDX elemental mapping of 310S alloy after exposure to 10% H_2O at 800 °C for 2000h.

Figure 60 and 61 demonstrate SEM surface morphologies of 310S alloy after exposure to 10% H_2O at 800 °C for 1500h and 2000h. Oxide scale after 1500h exposure at 900 °C and 10% H_2O appeared uniform plate-shaped oxides on the surface (Figure 60(a)). At higher magnifications, the small diamond-shaped oxides underneath the plate-shaped oxides are observed (Figure 60(b)). With the increasing of the exposure time, the amounts of plate-shaped oxides [diameter (3 to 10 μm) thickness: 0.3 μm] decrease, and the amounts of diamond-shaped oxides (0.3 to 1 μm) increase (Figure 61). In addition to the quantities of these oxides, the morphology on the plate-shaped oxide is different as well. It's clean for the surface of the plate-shaped oxides under 1500h operation whereas there are oxides circles on the plate-shaped oxides under 2000h operation which can be ascribed to the Si-containing oxides revealed by EDX (Figure 63). These plate-shaped oxides and small diamond-shaped oxides (Figure 60 and 61) were characterized to be the Cr-Mn-rich oxides (Figure 62 and 63).

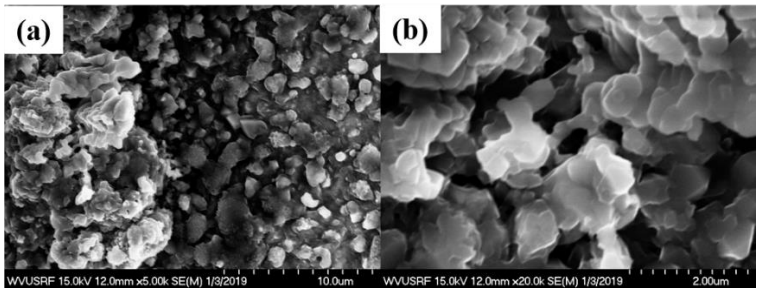

Figure 64 SEM surface morphologies of AFA OC4 after exposure to 10% H_2O at 800 °C for 1500h.

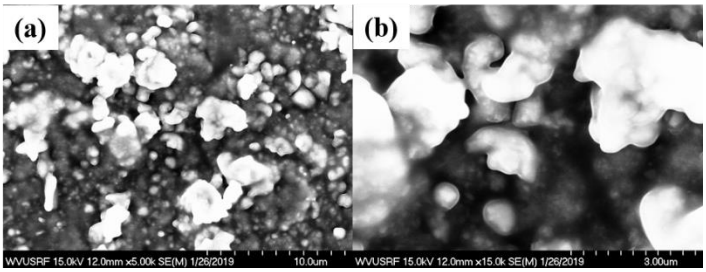

Figure 65 SEM surface morphologies of AFA OC4 after exposure to 10% H_2O at 800 °C for 2000h.

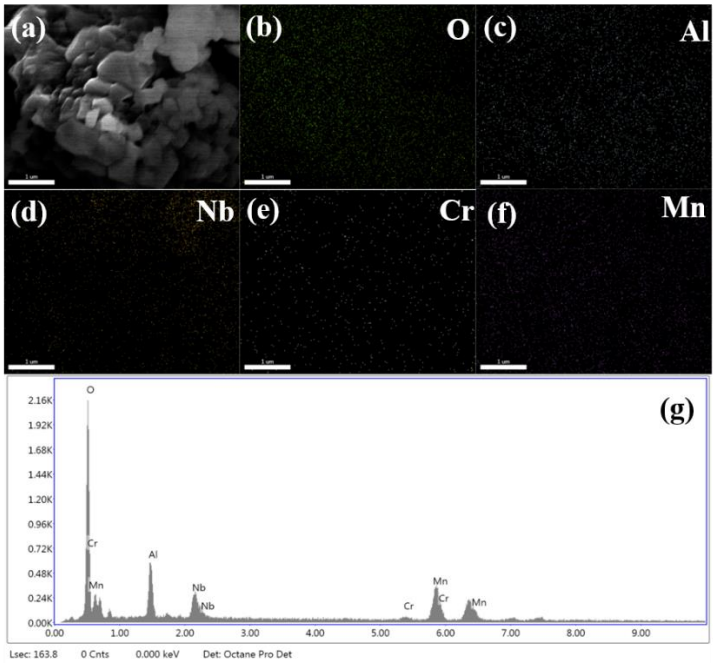

Figure 66 EDX elemental mapping of AFA OC4 after exposure to 10% H_2O at 800 °C for 1500h.

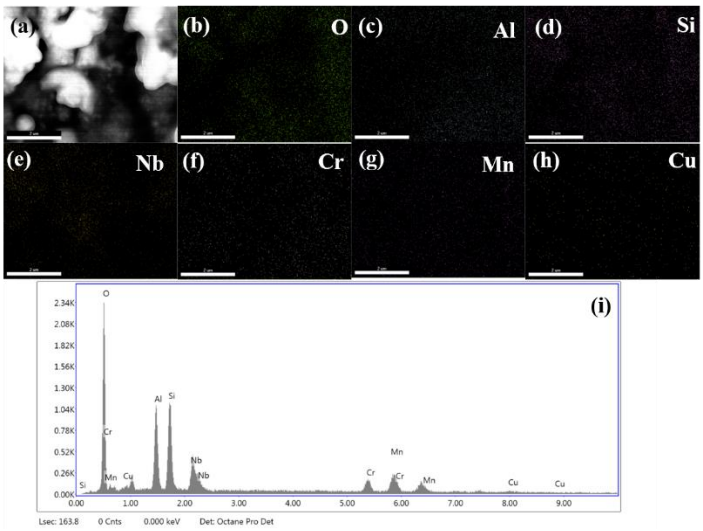

Figure 67 EDX elemental mapping of AFA OC4 after exposure to 10% H_2O at 800 °C for 2000h.

Figure 64 and 65 demonstrate SEM surface morphologies of AFA OC4 after exposure to 10% H_2O at 800 ^oC for 1500h and 2000h. At 800 °C and 1500 h exposure, the surface is relatively coarse and small diamond-shaped oxides are observed in higher magnification images (Figure 64(b)). There are mainly two types of small grains: one is spherical-shaped and the other diamond-shaped, which are Nb-rich and Cr-Mn-rich oxides confirmed by EDS (Figure 67 and 68), respectively. As the exposure time increases to 2000h, Nb-rich oxide grains increase in size for the samples tested for 2000h. Moreover, Al-rich oxides and Cr-Mn-rich oxides are characterized by EDX (Figure 67 and 68). However, Si-containing oxides were revealed by EDX after 2000h exposure.

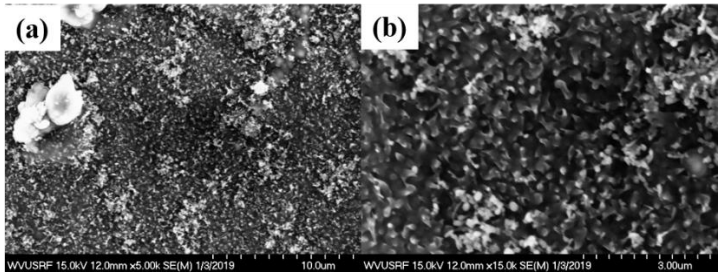

Figure 68 SEM surface morphologies of AFA OC5 after exposure to 10% H_2O at 800 °C for 1500h.

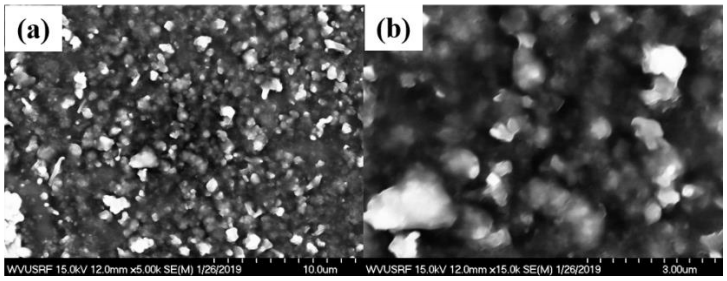

Figure 69 SEM surface morphologies of AFA OC5 after exposure to 10% H_2O at 800 °C for 2000h.

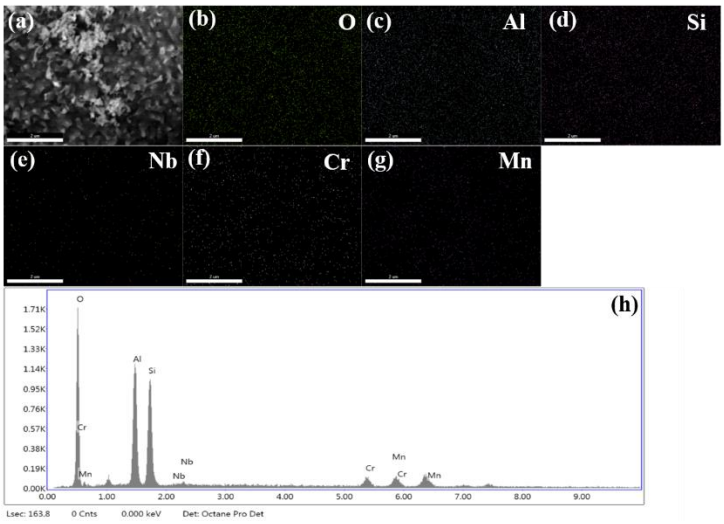

Figure 70 EDX elemental mapping of AFA OC5 after exposure to 10% H_2O at 800 °C for 1500h.

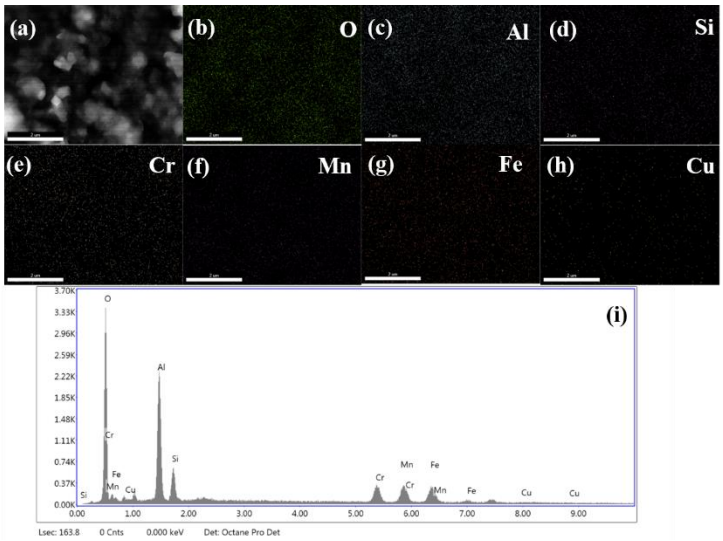

Figure 71 EDX elemental mapping of AFA OC5 after exposure to 10% H_2O at 800 °C for 2000h.

Figure 68 and 69 demonstrate SEM surface morphologies of AFA OC5 after exposure to 10% H_2O at 800 ^oC for 1500h and 2000h. Oxide scale after 1500h exposure at 800 °C and 10% H_2O appeared rounded oxides and some nodules on the surface (Figure 68(a)). At higher magnifications, small amount of diamond-shaped oxides (0.3 to 1 μm) can be observed (Figure 68(b)). With the increasing of the exposure time, the size of rounded oxides (increasing from 0.1 μm to 0.3 μm) increase (Figure 69). In addition to the quantities of these oxides, the Si-containing oxide on the surface is different as well. It exhibits more Si-containing oxides on the surface for the sample under 1500h operation (Figure 70) whereas there are less Si-containing oxides on the surface under 2000h operation (Figure 71). These small amount of diamond-shaped oxides at higher magnification are characterized to be the Cr-Mn-rich oxides (Figure 70 and 71).

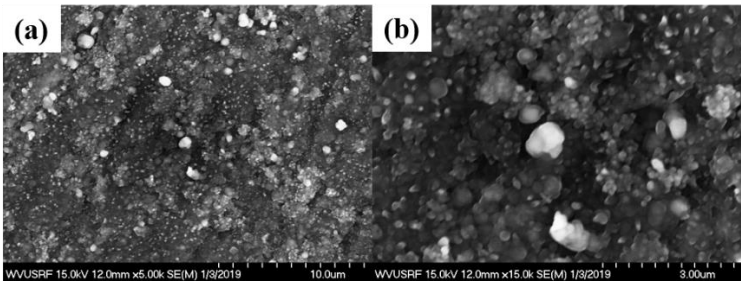

Figure 72 SEM surface morphologies of AFA MOD after exposure to 10% H_2O at 800 °C for 1500h.

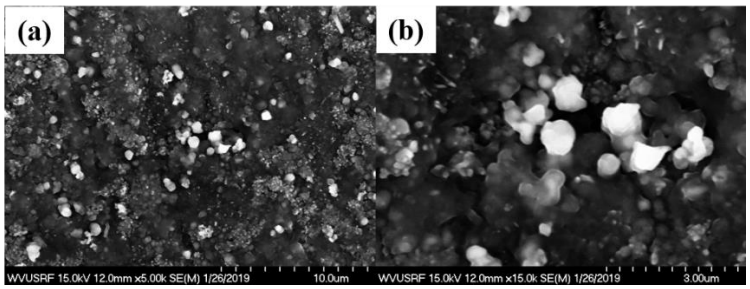

Figure 73 SEM surface morphologies of AFA MOD after exposure to 10% H_2O at 800 °C for 2000h.

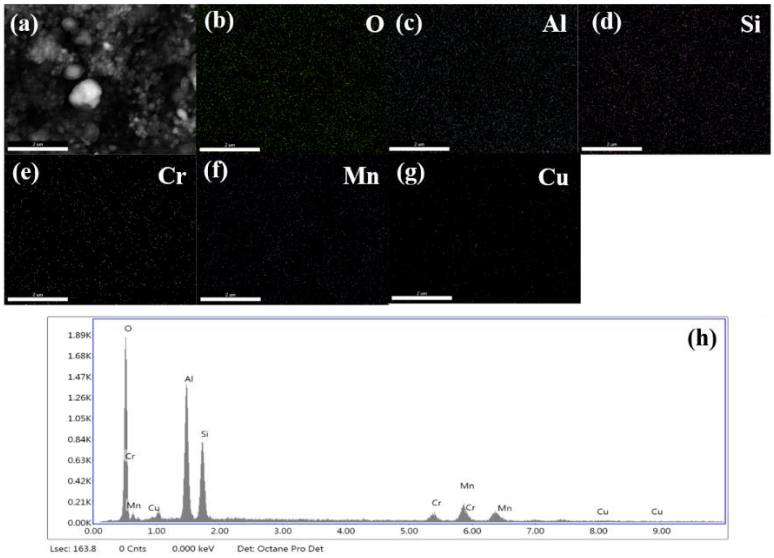

Figure 74 EDX elemental mapping of AFA MOD after exposure to 10% H_2O at 800 °C for 1500h

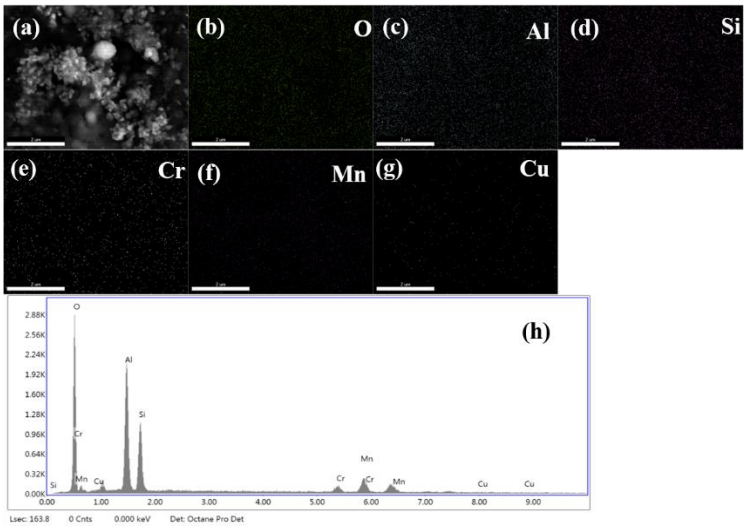

Figure 75 EDX elemental mapping of AFA MOD after exposure to 10% H_2O at 800 °C for 2000h.

Figure 72 and 73 demonstrate SEM surface morphologies of AFA MOD after exposure to 10% H_2O at 800 °C for 1500h and 2000h. For both samples exposed for 1500h and 2000h, there are rounded oxides and some nodules on the surface (Figure 72(a) and 73(a)). At higher magnification (Figure 72(b) and 73(b)), small amount of diamond-shaped oxides (0.3 to 1 μm) can be observed. The morphology of the samples tested for 2000h exposure is similar to that of 1500h. It can be observed from the EDX (Figure 74 and 75) that Si-containing oxides and diamond-shaped Cr-Mn-rich oxides are formed on the surface of the AFA MOD. These small amount of diamond-shaped oxides at higher magnification are characterized to be the Cr-Mn-rich oxides (Figure 74 and 75).

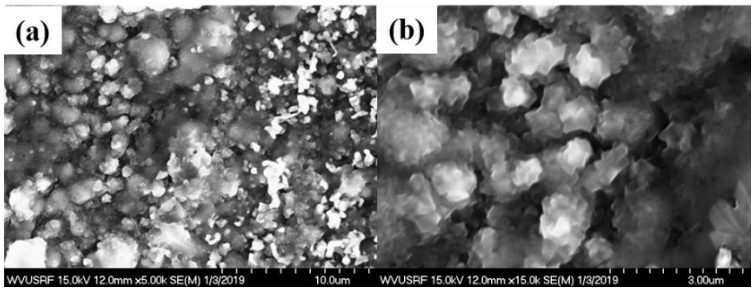

Figure 76 SEM surface morphologies of AFA OC11 after exposure to 10% H_2O at 800 °C for 1500h.

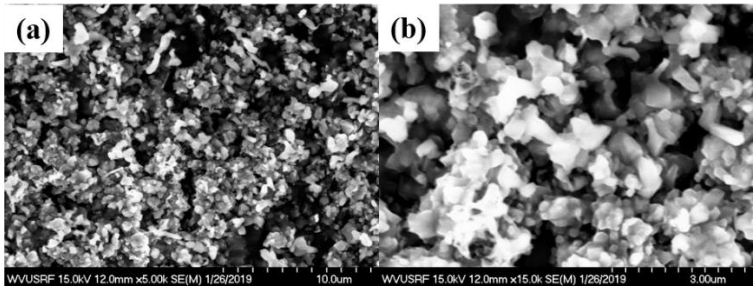

Figure 77 SEM surface morphologies of AFA OC11 after exposure to 10% H_2O at 800 °C for 2000h.

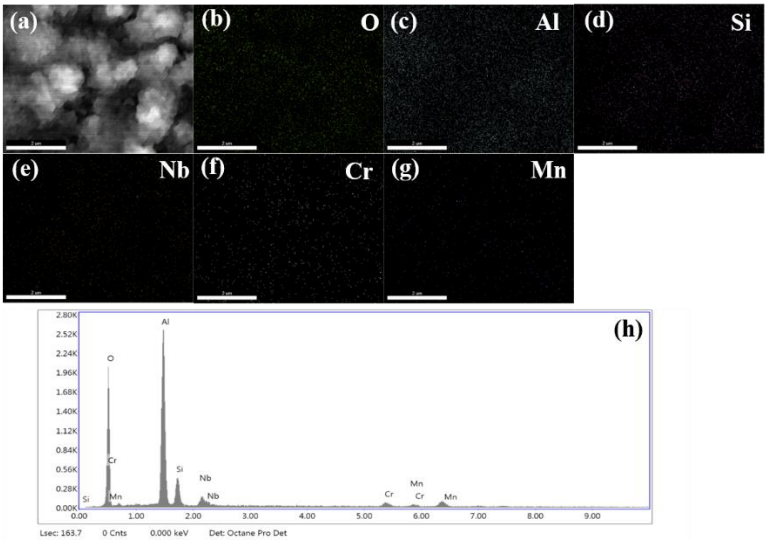

Figure 78 EDX elemental mapping of AFA OC11 after exposure to 10% H_2O at 800 °C for 1500h.

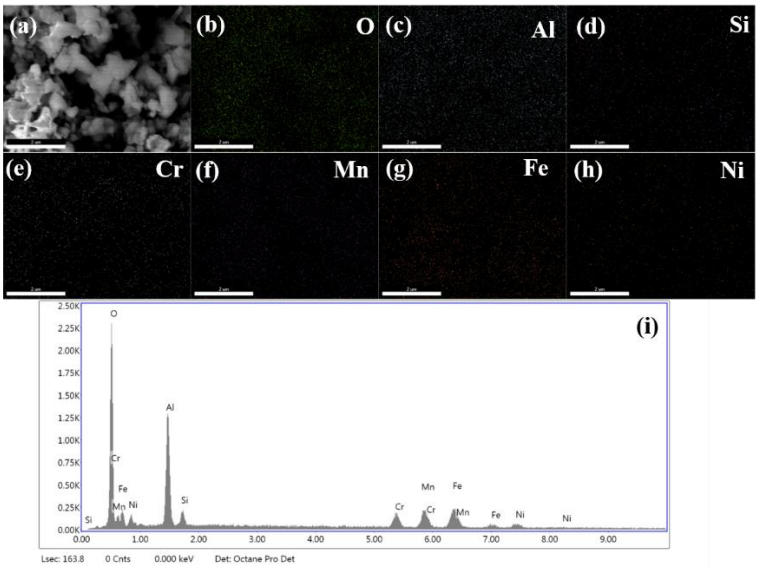

Figure 79 EDX elemental mapping of AFA OC11 after exposure to 10% H_2O at 800 °C for 2000h.

Figure 76 and 77 demonstrate SEM surface morphologies of AFA OC11 after exposure to 10% H_2O at 800 ^oC for 1500h and 2000h. Oxide scale after 1500h exposure at 800 °C and 10% H_2O appeared diamond-shaped oxides and some nodules on the surface (Figure 76(a)). At higher magnifications, these nodules are formed by the accumulation of the small diamond-shaped oxides (Figure 76(b)). With the increasing of the exposure time, the size of small diamond-shaped oxides does not change much (Fig. 77). For the sample tested under 1500h operation, the amount of Si-containing oxide is higher than that of 2000h. However, the amount of Cr-Mn-rich oxides under 2000h is higher than that of 1500h (Figure 78 and 79).

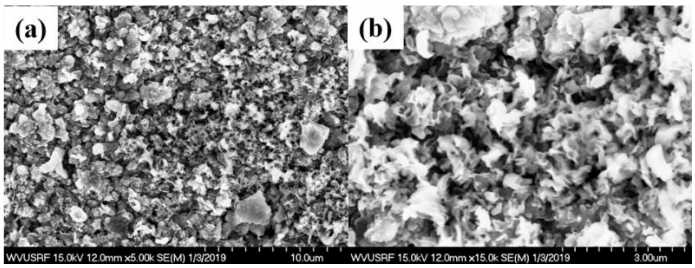

Figure 80 SEM surface morphologies of AFA OC11LZ after exposure to 10% H_2O at 800 °C for 1500h.

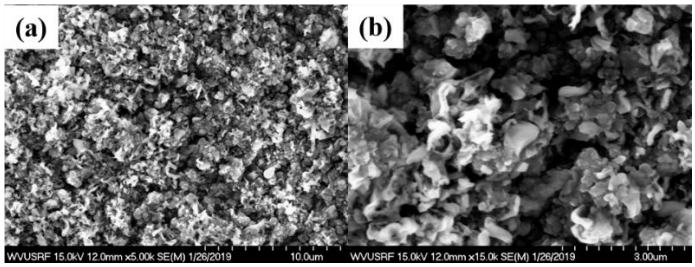

Figure 81 SEM surface morphologies of AFA OC11LZ after exposure to 10% H_2O at 800 °C for 2000h.

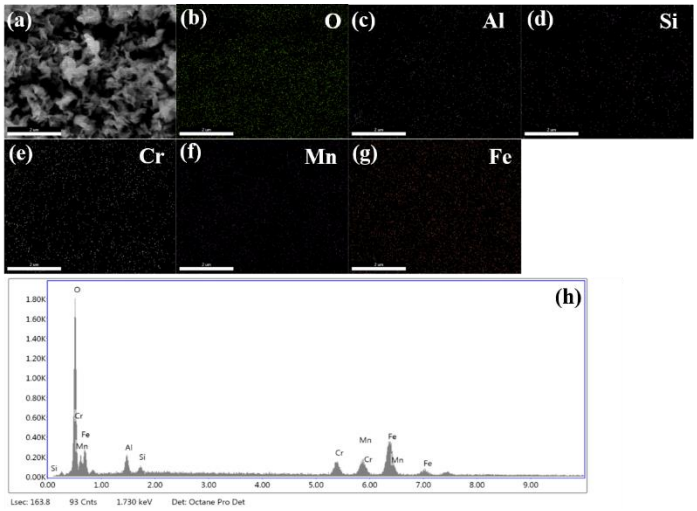

Figure 82 EDX elemental mapping of AFA OC11LZ after exposure to 10% H_2O at 800 °C for 1500h.

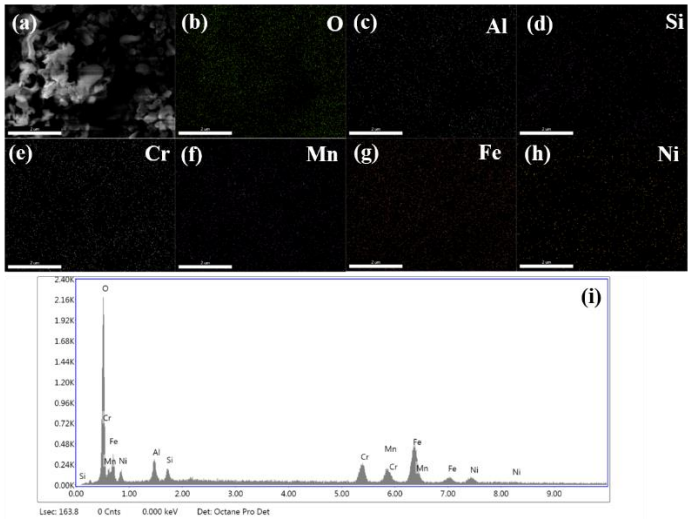

Figure 83 EDX elemental mapping of AFA OC11LZ after exposure to 10% H_2O at 800 °C for 2000h.

Figure 80 and 81 demonstrate SEM surface morphologies of AFA OC11LZ after exposure to 10% H_2O at 800 °C for 1500h and 2000h. For both samples exposed for 1500h and 2000h, there are a large area of fluffy-like oxides and some nodules formed on the surface (Figure 80(a) and 81(a)). At higher magnification (Figure 80(b) and 81(b)), small amount of diamond-shaped oxides (0.3 to 1 μm) underneath the fluffy-like oxides can be observed. The morphology of the samples tested for 2000h exposure is similar to that of 1500h. It can be observed from the EDX (Figure 82 and 83) that Si-containing oxides, Al-rich oxides and diamond-shaped Fe-Cr-Mn-rich oxides are formed on the surface of the alloy surface.

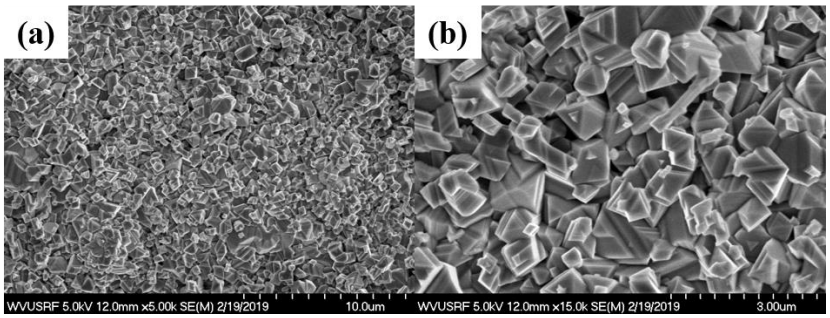

Figure 84 SEM surface morphologies of 625 alloy after exposure to 10% H_2O at 900 °C for 3500h.

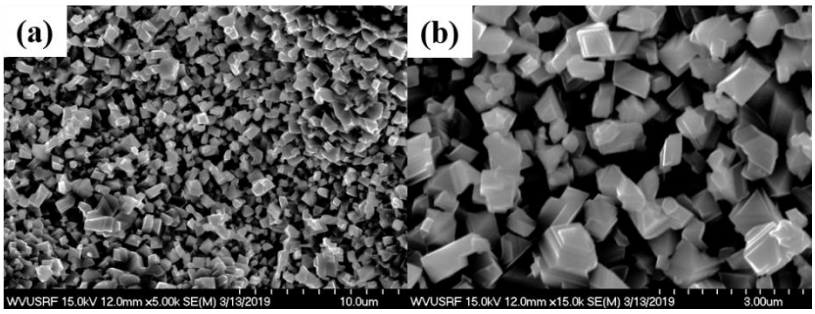

Figure 85 SEM surface morphologies of 625 alloy after exposure to 10% H_2O at 900 °C for 4000h.

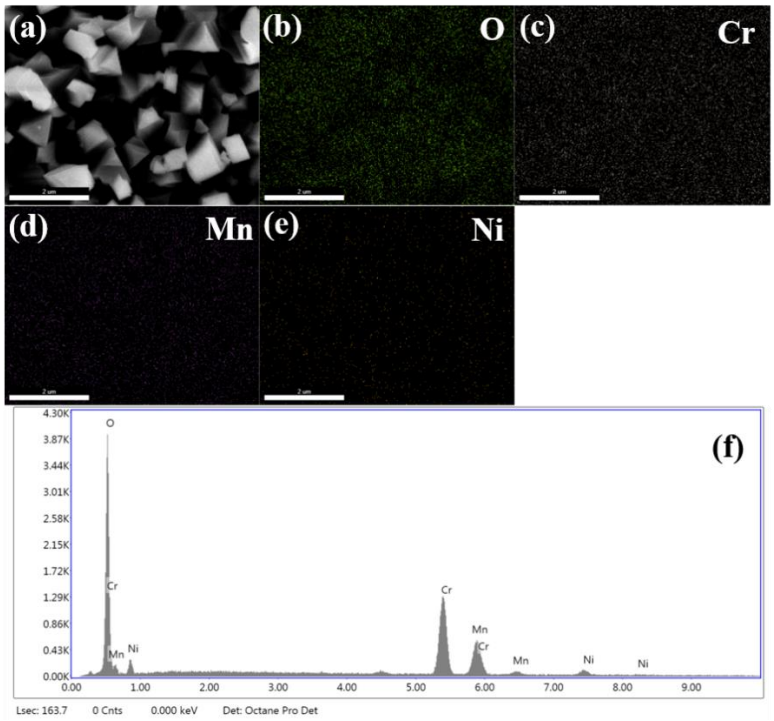

Figure 86 EDX elemental mapping of 625 alloy after exposure to 10% H_2O at 900 °C for 3500h.

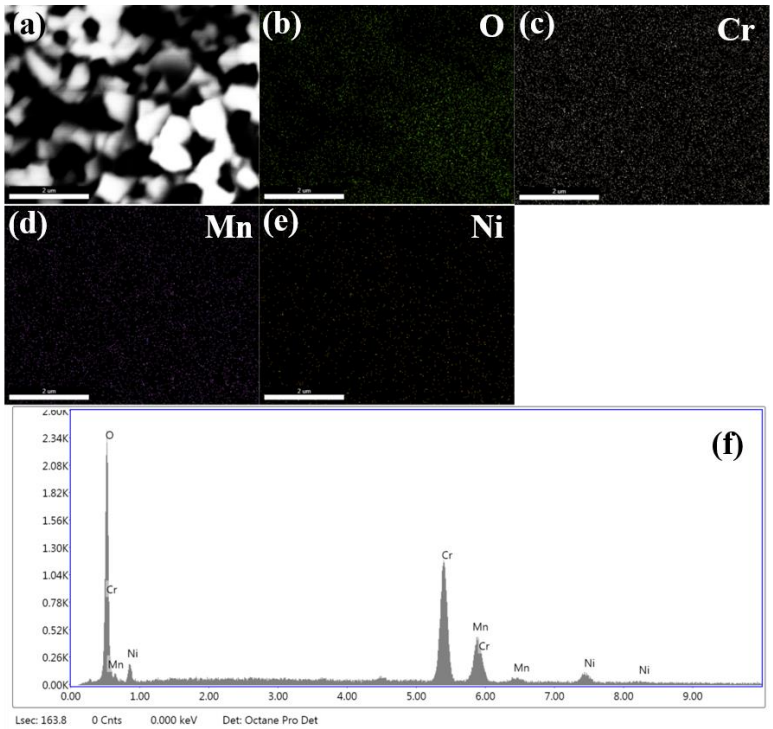

Figure 87 EDX elemental mapping of 625 alloy after exposure to 10% H_2O at 900 °C for 4000h.

Figure 84 and 85 show SEM surface morphologies of 625 alloy after exposure to 10% H_2O at 900 °C for 3500h and 4000h. After 3500 h exposure, 625 alloy formed intact and compact oxide film, without any indication of exfoliation and crack. There is mainly one type of grains of which size is range from 0.3 to 1 μm. These faceted grains are Cr-Mn-rich oxides which are confirmed by

EDS (Figure 86). As the exposure time increases, both the size and the composition of the oxides do not change much which are revealed in Figure 85 and Figure 86, respectively. However, a larger number of small holes appear to form after 4000h exposure than 3500h exposure.

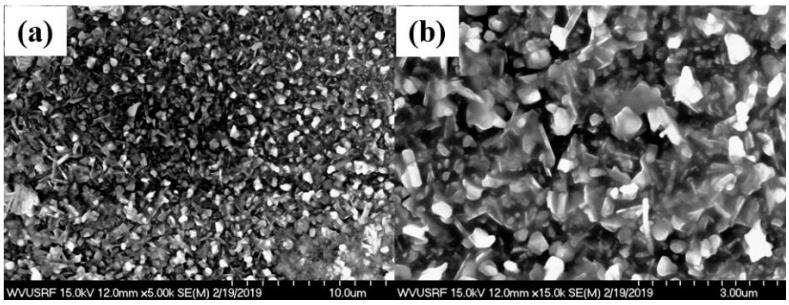

Figure 88 SEM surface morphologies of AFA OC11 after exposure to 10% H_2O at 900 °C for 3500h.

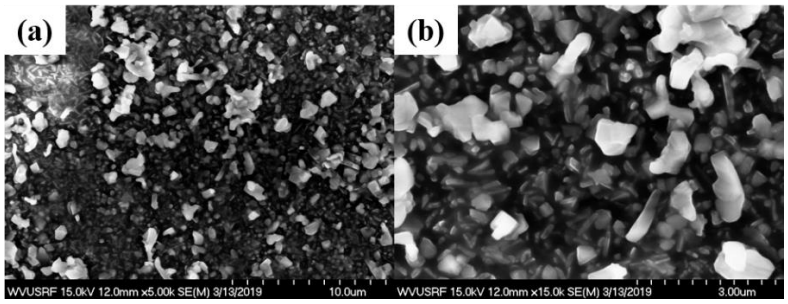

Figure 89 SEM surface morphologies of AFA OC11 after exposure to 10% H_2O at 900 °C for 4000h.

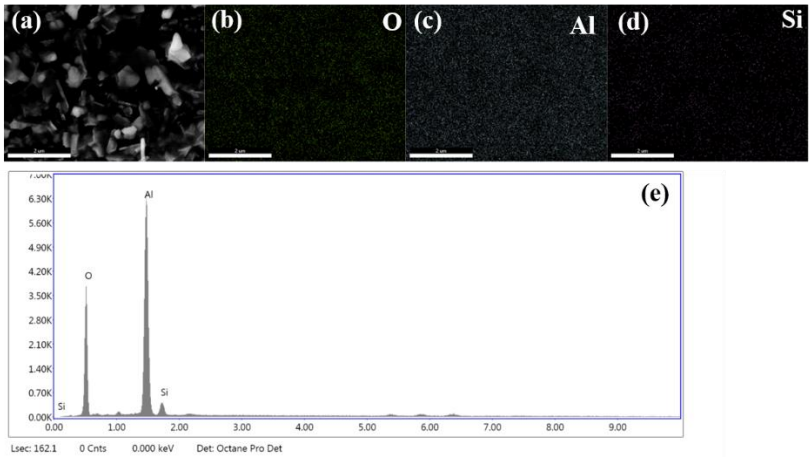

Figure 90 EDX elemental mapping of AFA OC11 after exposure to 10% H_2O at 900 °C for 3500h.

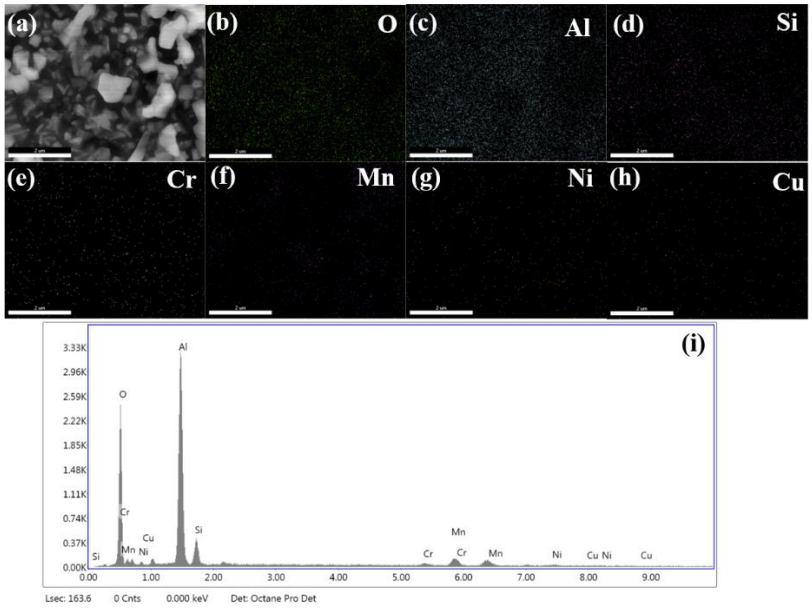

Figure 91 EDX elemental mapping of AFA OC11 after exposure to 10% H_2O at 900 °C for 4000h.

SEM images of AFA OC11 after exposure to 10% H_2O at 900 °C for 3500h and 4000h was demonstrated in Figure 88 and 89. For the sample operated for 3500h, the surface is non-uniform and there are mainly two types of small grains: one is bar-shaped grain (length × width: 0.1 μm × 0.5 μm) and the other is faceted grain (0.3 to 1 μm). With the increasing of the exposure time to 4000h, the amounts and the size of these two grains does not change much for longer exposure time (Figure 89). Figure 90 and 91 show that alumina is largely formed on the surface of the AFA OC11 and there are little silicon-related oxides and Cr-Mn-rich oxides on the surface for different expose time.

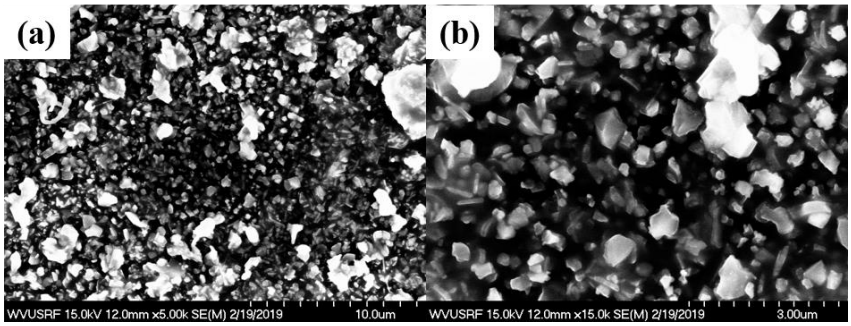

Figure 92 SEM surface morphologies of AFA OC11LZ after exposure to 10% H_2O at 900 °C for 3500h.

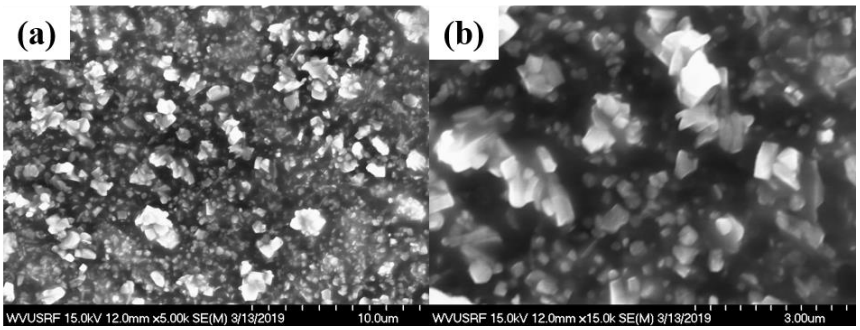

Figure 93 SEM surface morphologies of AFA OC11LZ after exposure to 10% H_2O at 900 °C for 4000h.

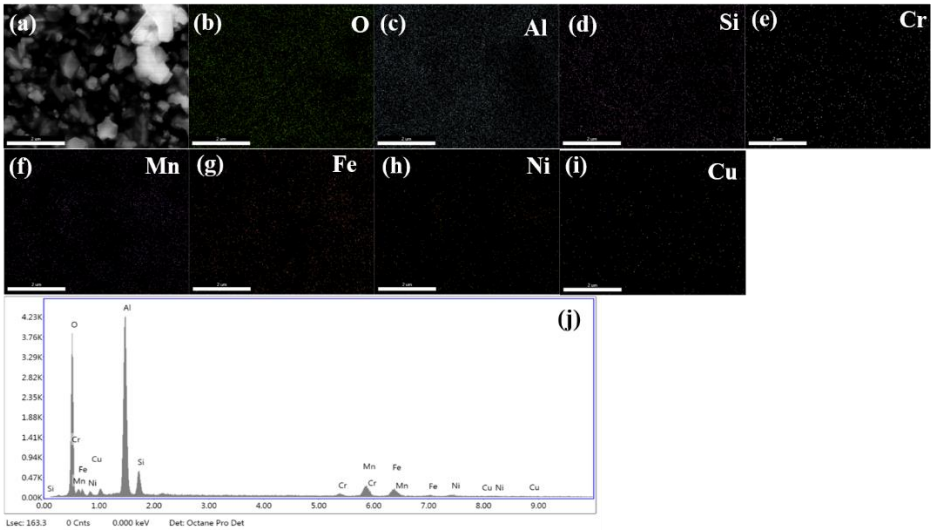

Figure 94 EDX elemental mapping of AFA OC11LZ after exposure to 10% H_2O at 900 °C for 3500h.

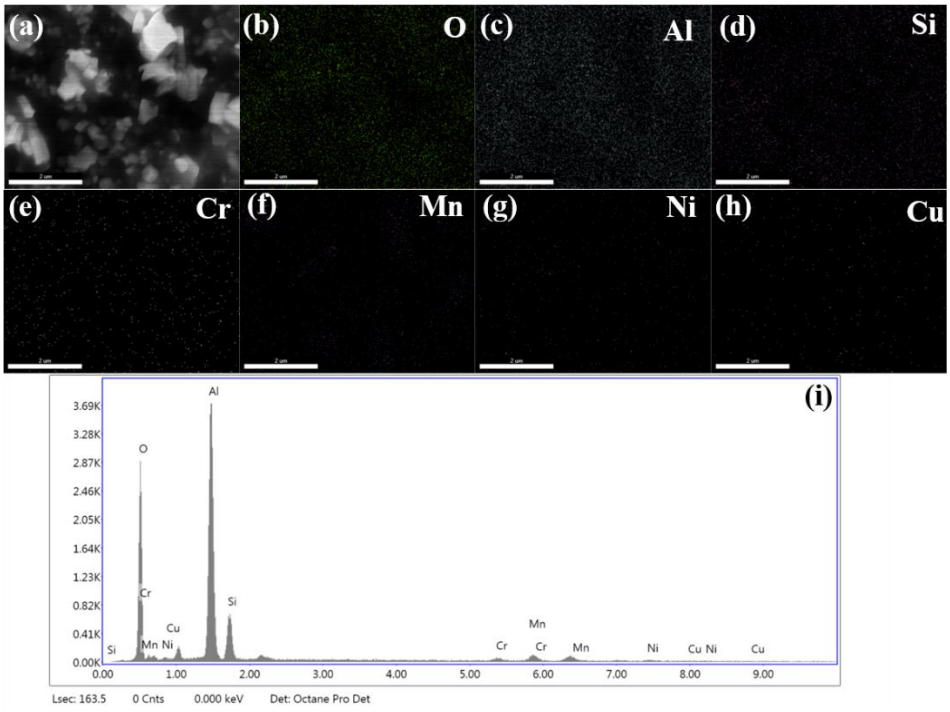

Figure 95 EDX elemental mapping of AFA OC11LZ after exposure to 10% H_2O at 900 °C for 4000h.

Figure 92 and 93 demonstrate SEM surface morphologies of AFA OC11 after exposure to 10% H_2O at 900 °C for 3500h and 4000h. After 2500h exposure at 900 °C, the surface is covered by faceted grains which are Cr-Mn-rich oxides confirmed by EDS (Figure 94 and 95). As the exposure time increases, both the size and the composition of the oxides do not change much. However, there is a larger number of oxide grains accumulation for the OC11LZ compared to OC11. Moreover, the quantities of Cr-Mn-rich oxides formed on the surface of OC11LZ appear to be greater than that of OC11.

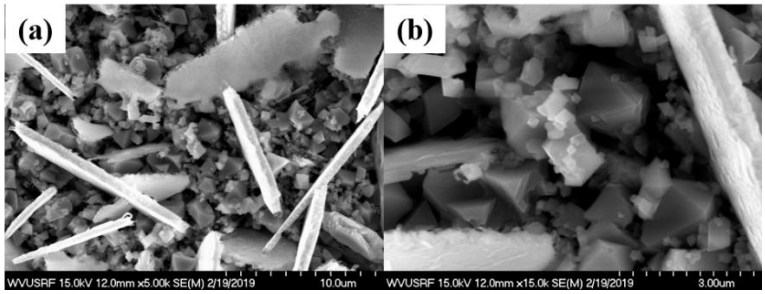

Figure 96 SEM surface morphologies of 310S alloy after exposure to 10% H_2O at 800 °C for 2500h.

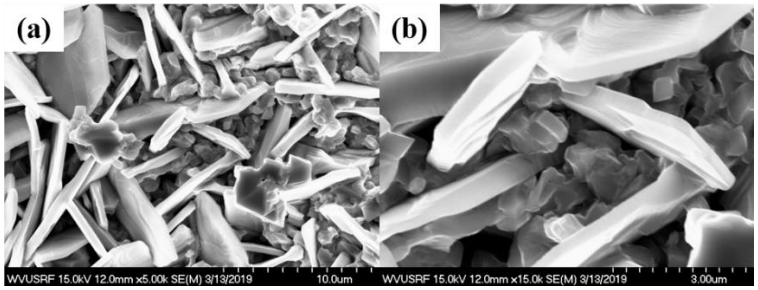

Figure 97 SEM surface morphologies of 310S alloy after exposure to 10% H_2O at 800 °C for 3000h.

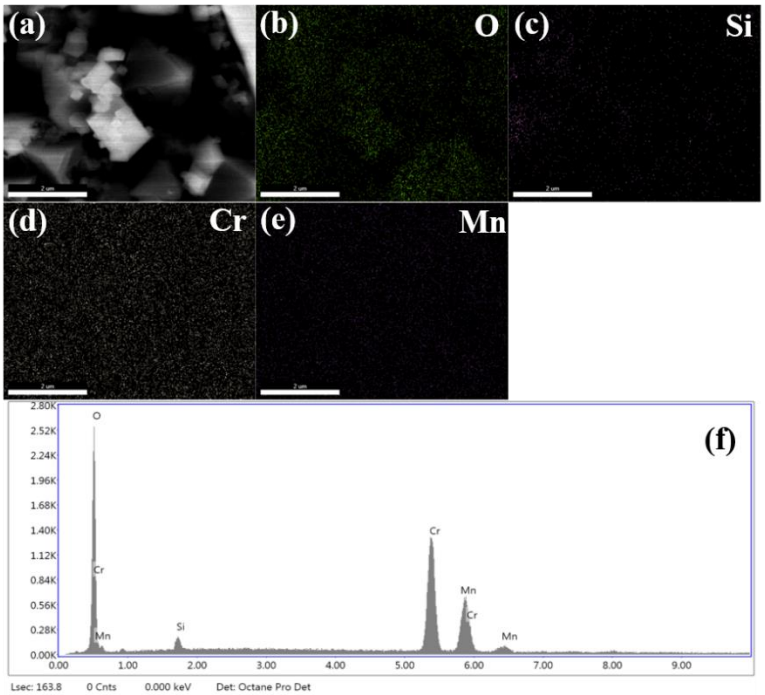

Figure 98 EDX elemental mapping of 310S alloy after exposure to 10% H_2O at 800 °C for 2500h.

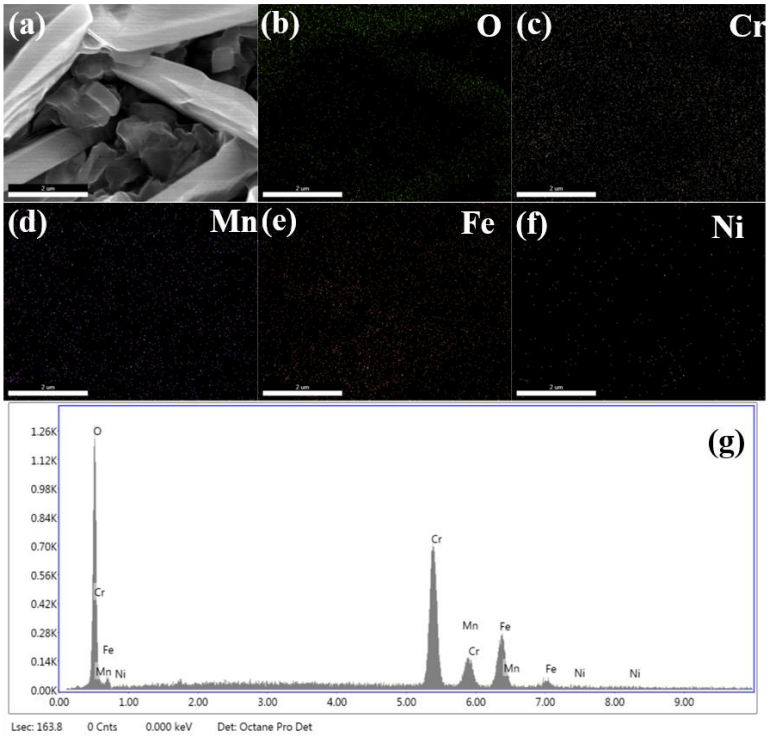

Figure 99 EDX elemental mapping of 310S alloy after exposure to 10% H_2O at 800 °C for 3000h.

Figure 96 and 97 demonstrate SEM surface morphologies of 310S alloy after exposure to 10% H_2O at 800 °C for 2500h and 3000h. For the sample tested at 800 °C and 10% H_2O for 2500h, there are two kinds of grains (plate-shaped oxide and faceted grains) formed on the surface (Figure 96(a)). At higher magnifications, the small diamond-shaped oxides underneath the plate-shaped oxides can be clearly observed (Figure 96(b)). With the increasing of the exposure time, the plate-shaped oxides [diameter (3 to 10 μm) thickness: 0.3 μm] becomes more and more blur and the shape of the oxide grains becomes round-cornered, however, the faceted grains (0.3 to 1 μm) do not change much (Figure 97). These plate-shaped oxides and small faceted grains (Figure 96 and 97) were determined to be the Cr-Mn-rich oxides (Figure 98 and 99).

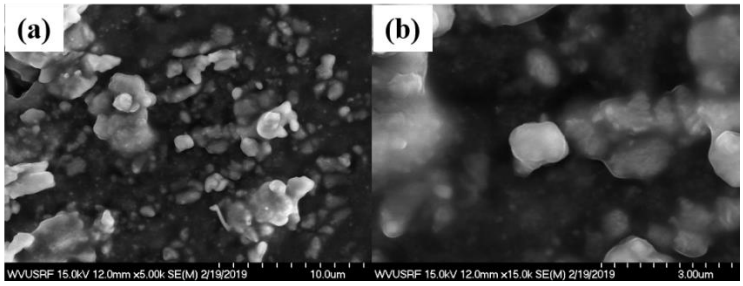

Figure 100 SEM surface morphologies of AFA OC4 after exposure to 10% H_2O at 800 °C for 2500h.

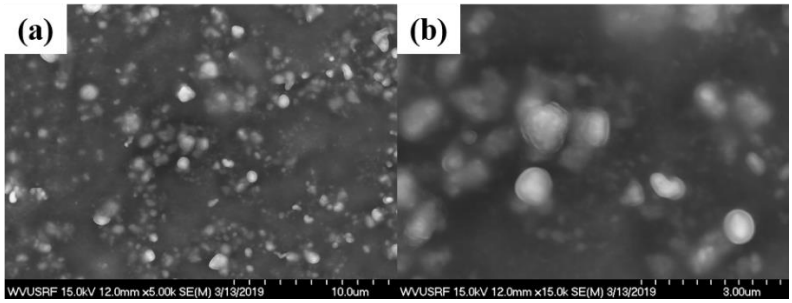

Figure 101 SEM surface morphologies of AFA OC4 after exposure to 10% H_2O at 800 °C for 3000h.

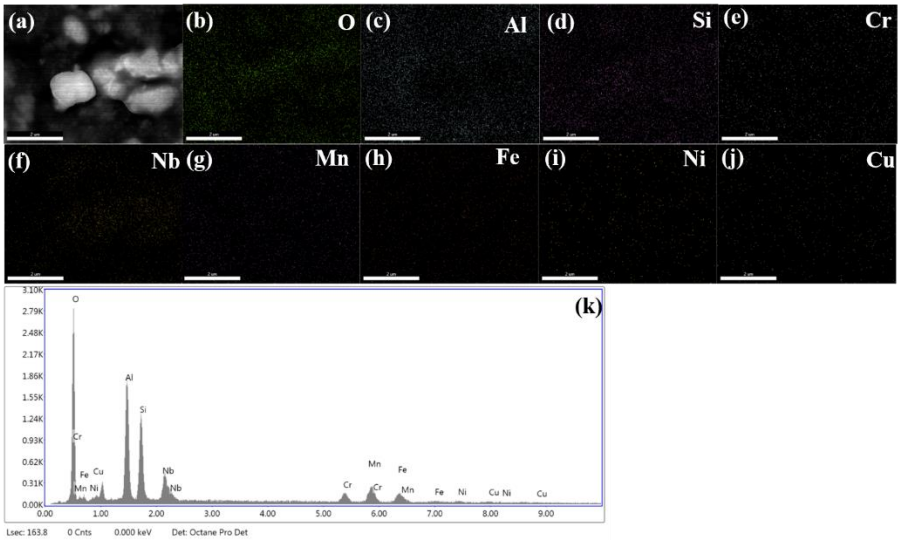

Figure 102 EDX elemental mapping of AFA OC4 after exposure to 10% H_2O at 800 °C for 2500h.

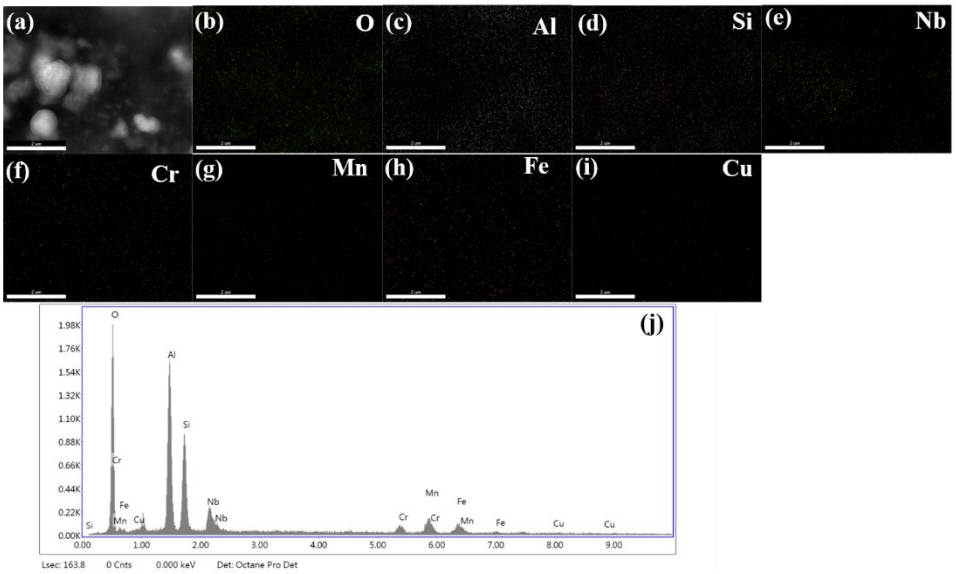

Figure 103 EDX elemental mapping of AFA OC4 after exposure to 10% H_2O at 800 °C for 3000h.

Figure 100 and 101 demonstrate SEM surface morphologies of AFA OC4 after exposure to 10% H_2O at 800 °C for 2500h and 3000h. After the exposure at 800 ºC for 2500 h, the surface is relatively rough and small grains are clearly observed in higher magnification images (Figure

100(b)). There are mainly two types of small grains: one is spherical-shaped and the other facted grains, which could be the Nb-rich and Cr-Mn-rich oxides confirmed by EDS (Figure 102 and 103), respectively. As the exposure time increases to 3000h, the morphology and the EDS does not change much.

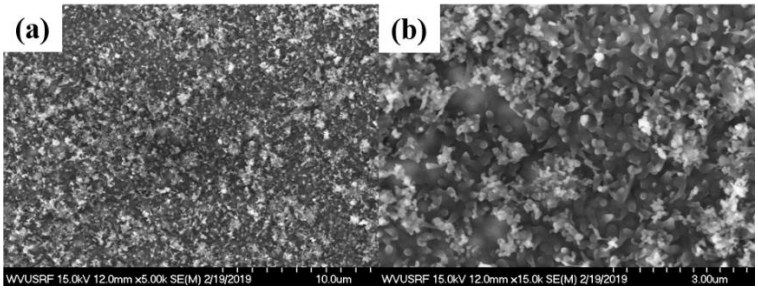

Figure 104 SEM surface morphologies of AFA OC5 after exposure to 10% H_2O at 800 °C for 2500h.

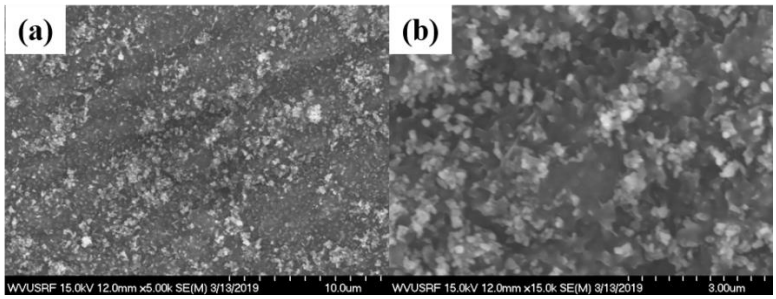

Figure 105 SEM surface morphologies of AFA OC5 after exposure to 10% H_2O at 800 °C for 3000h.

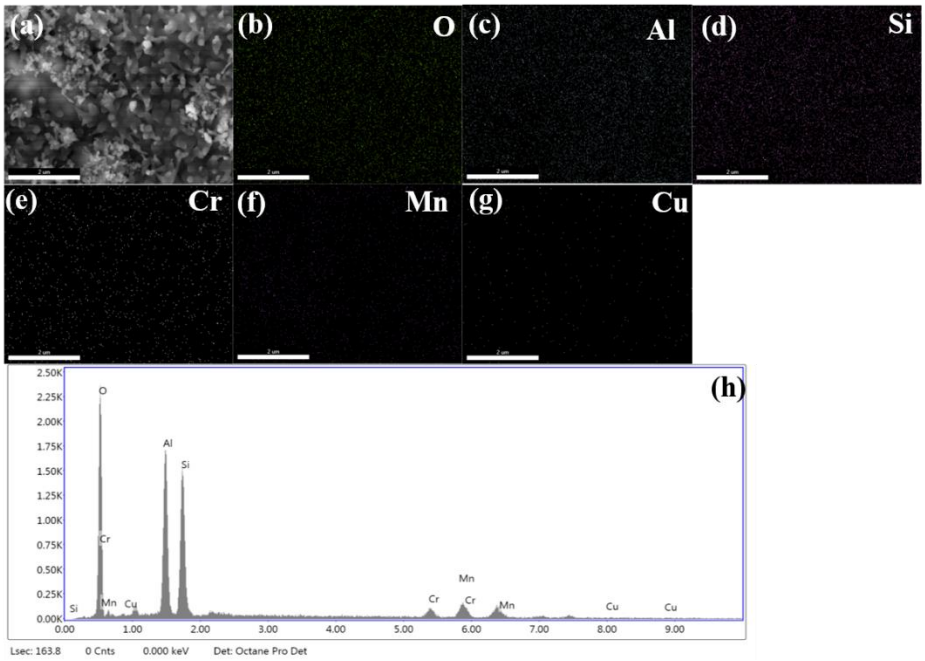

Figure 106 EDX elemental mapping of AFA OC5 after exposure to 10% H_2O at 800 °C for 2500h.

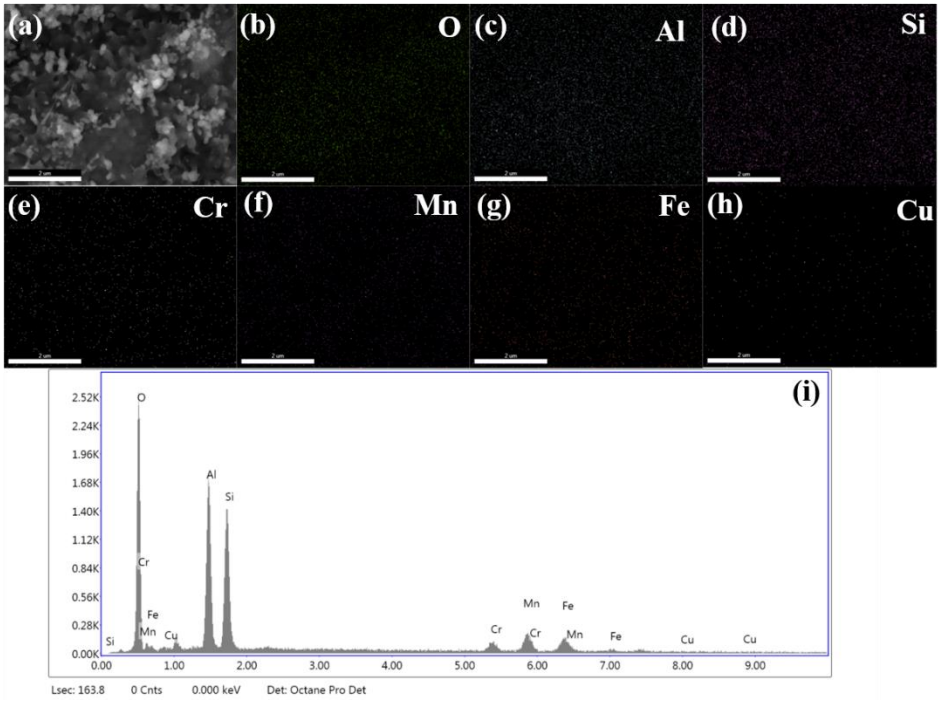

Figure 107 EDX elemental mapping of AFA OC5 after exposure to 10% H_2O at 800 °C for 3000h.

Figure 104 and 105 demonstrate SEM surface morphologies of AFA OC5 after exposure to 10% H_2O at 800 °C for 2500h and 3000h. Oxide scale after 2500h exposure at 800 °C and 10% H_2O appeared rounded oxides and some nodules on the surface (Figure 104(a)). At higher magnifications, small amount of faceted grains (0.3 to 1 μm) can be observed (Figure 104(b)). With the increasing of the exposure time, the morphology does not change much (Figure 105). Moreover, alumina and Si-containing oxides could be easily observed on the surface for the sample under 2500h and 3000h operation (Figure 106 and 107). These small amount of faceted grains at higher magnification are characterized to be the Cr-Mn-rich oxides (Figure 106 and 107).

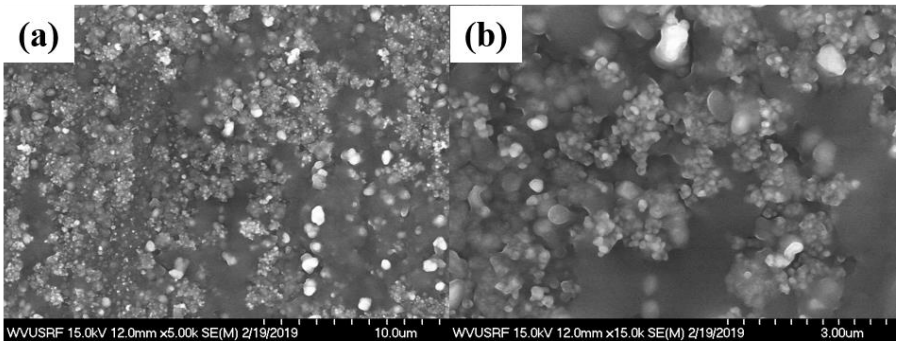

Figure 108 SEM surface morphologies of AFA MOD after exposure to 10% H_2O at 800 °C for 2500h.

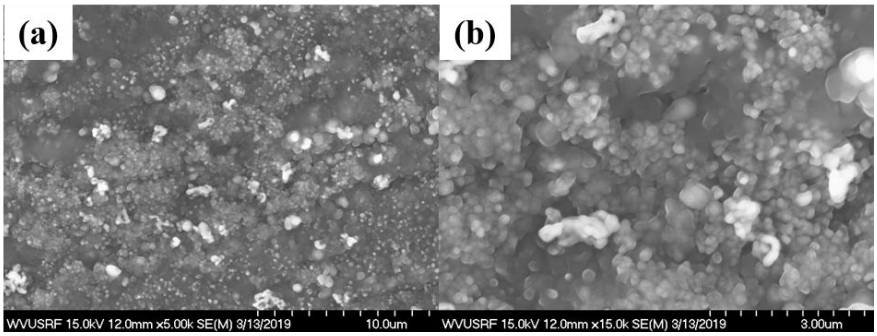

Figure 109 SEM surface morphologies of AFA MOD after exposure to 10% H_2O at 800 °C for 3000h.

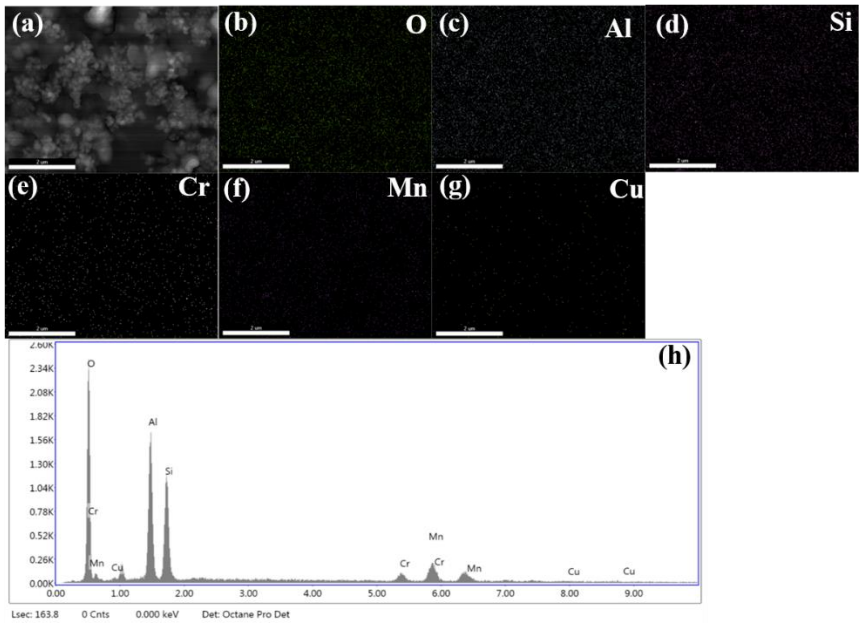

Figure 110 EDX elemental mapping of AFA MOD after exposure to 10% H_2O at 800 °C for 2500h.

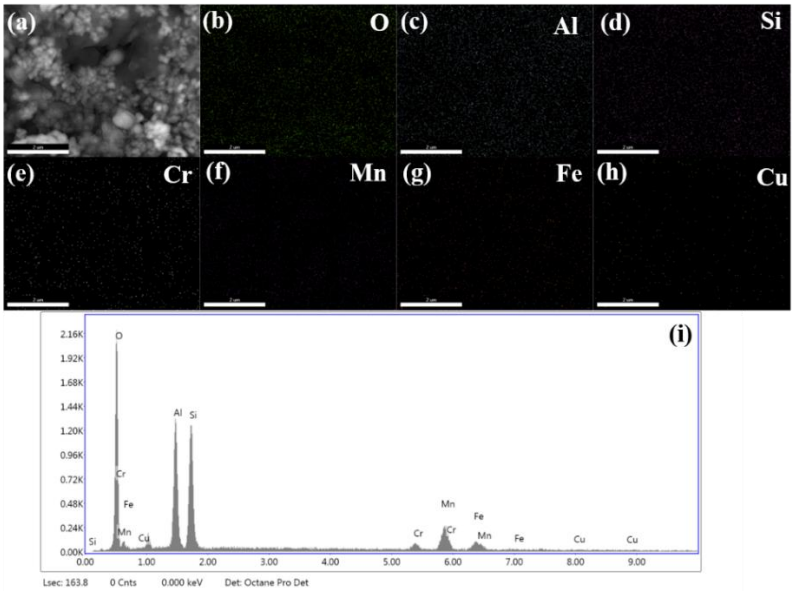

Figure 111 EDX elemental mapping of AFA MOD after exposure to 10% H_2O at 800 °C for 3000h.

Figure 108 and 109 demonstrate SEM surface morphologies of AFA MOD after exposure to 10% H_2O at 800 °C for 2500h and 3000h. For both samples exposed for 2500h and 3000h, there are rounded oxides and some nodules on the surface (Figure 108(a) and 109(a)). At higher magnification (Figure 108(b) and 109(b)), small amount of faceted grains (0.3 to 1 μm) can be observed. With the increasing of the exposure time, the size of the rounded oxides of the samples tested for 3000h exposure is larger than that of 2500h. It can be observed from the EDX (Figure 110 and 111) that Si-containing oxides and faceted grains are formed on the surface of the alloy. These small amount of faceted grains at higher magnification are characterized to be the Cr-Mn-rich oxides (Figure 110 and 111).

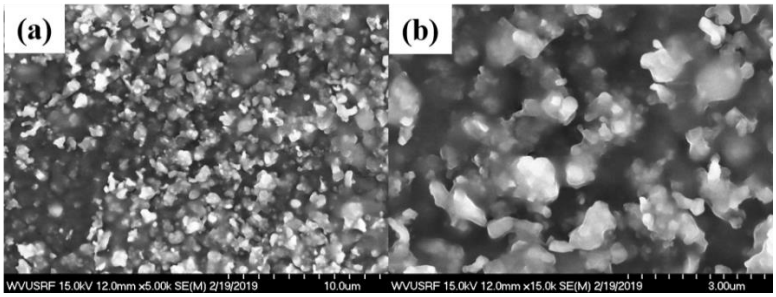

Figure 112 SEM surface morphologies of AFA OC11 after exposure to 10% H_2O at 800 °C for 2500h.

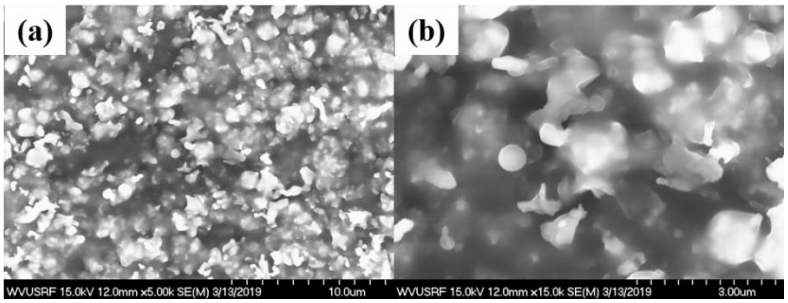

Figure 113 SEM surface morphologies of AFA OC11 after exposure to 10% H_2O at 800 °C for 3000h.

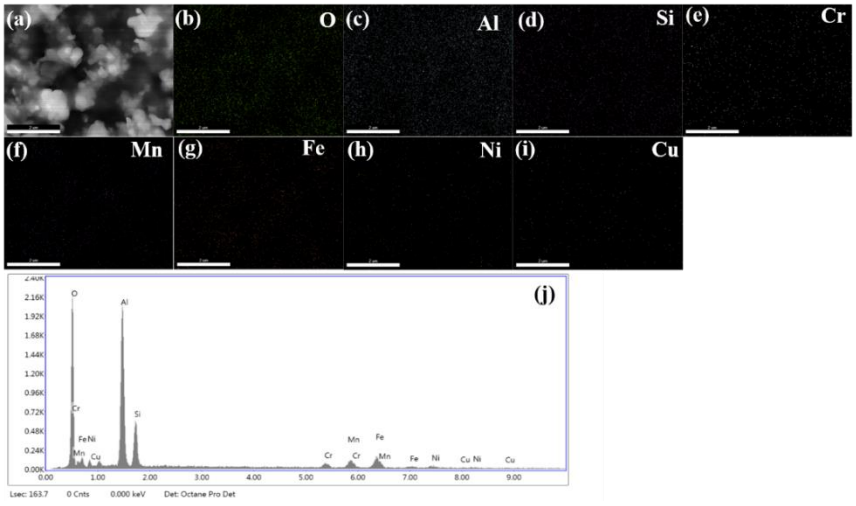

Figure 114 EDX elemental mapping of AFA OC11 after exposure to 10% H_2O at 800 °C for 2500h.

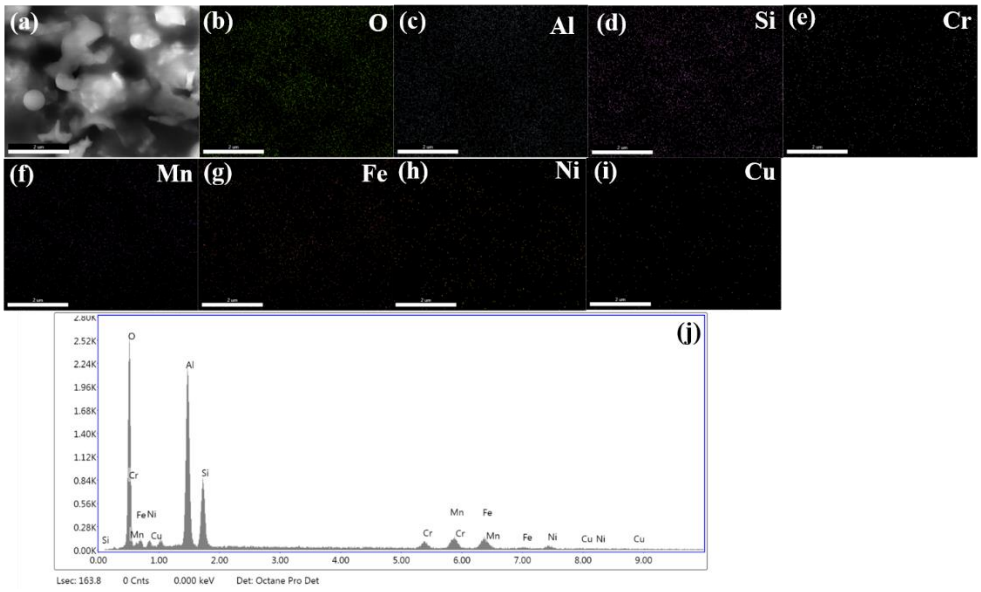

Figure 115 EDX elemental mapping of AFA OC11 after exposure to 10% H_2O at 800 °C for 3000h.

Figure 112 and 113 demonstrate SEM surface morphologies of AFA OC11 after exposure to 10% H_2O at 800 °C for 2500h and 3000h. Oxide scale after 2500h exposure at 800 °C and 10% H_2O appeared faceted grains and some nodules on the surface (Figure 112(a)). At higher magnifications, these nodules are formed by the accumulation of the small faceted grains (Figure 112(b)). With the increasing of the exposure time, the size of small faceted grains of the samples tested for 3000h exposure is larger than that of 2500h. Moreover, the amount of Si-containing oxide and the amount of Cr-Mn-rich oxides under 3000h is similar as that of 2500h (Figure 114 and 115).

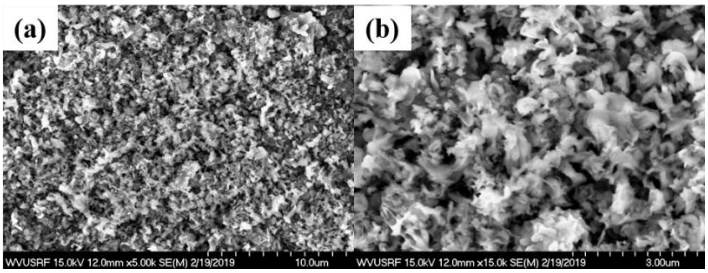

Figure 116 SEM surface morphologies of AFA OC11LZ after exposure to 10% H_2O at 800 °C for 2500h.

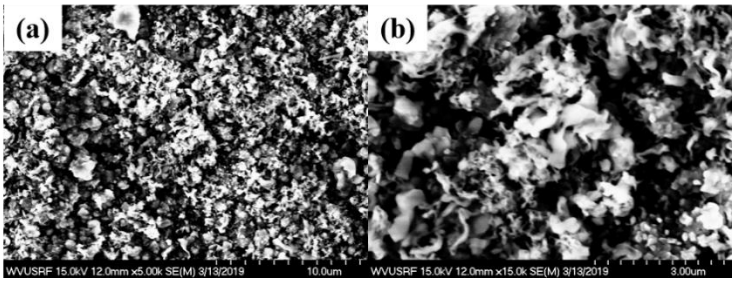

Figure 117 SEM surface morphologies of AFA OC11LZ after exposure to 10% H_2O at 800 °C for 3000h.

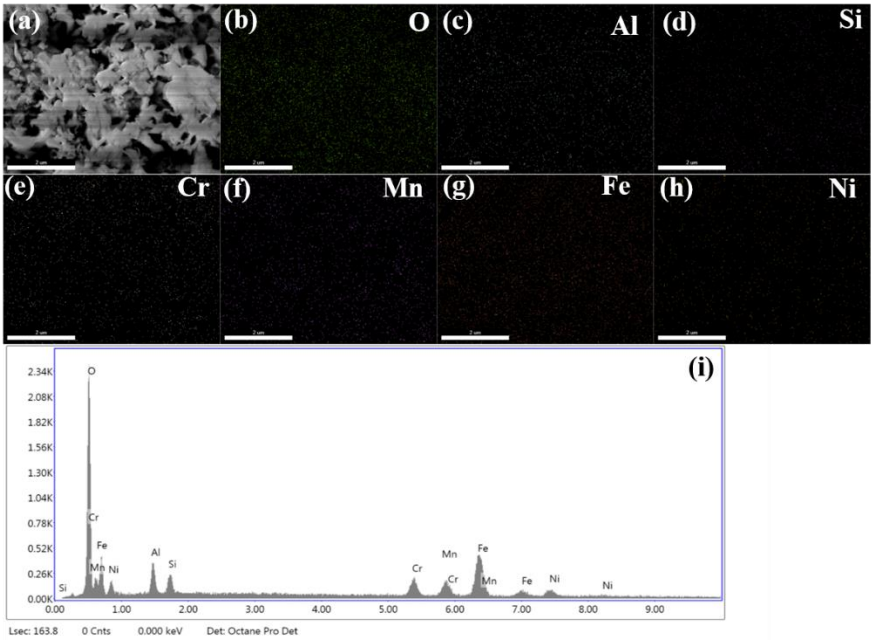

Figure 118 EDX elemental mapping of AFA OC11LZ after exposure to 10% H_2O at 800 °C for 2500h.

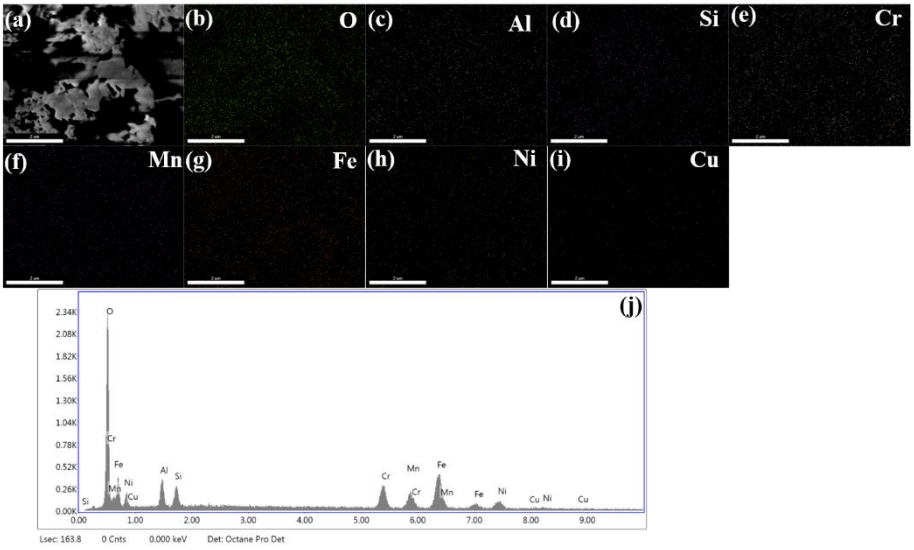

Figure 119 EDX elemental mapping of AFA OC11LZ after exposure to 10% H_2O at 800 °C for 3000h.

Figure 116 and 117 demonstrate SEM surface morphologies of AFA OC11LZ after exposure to 10% H_2O at 800 °C for 2500h and 3000h. For both samples exposed for 2500h and 3000h, there are a large area of fluffy-like oxides and some nodules formed on the surface (Figure 116(a) and 117(a)). At higher magnification (Figure 116(b) and 117(b)), small amount of faceted grains (0.3 to 1 μm) underneath the fluffy-like oxides can be observed. The morphology of the samples tested for 3000h exposure is similar to that of 2500h. It can be observed from the EDX (Figure 118 and 119) that Si-containing oxides, Al-rich oxides and faceted grains are formed on the surface of the alloy.

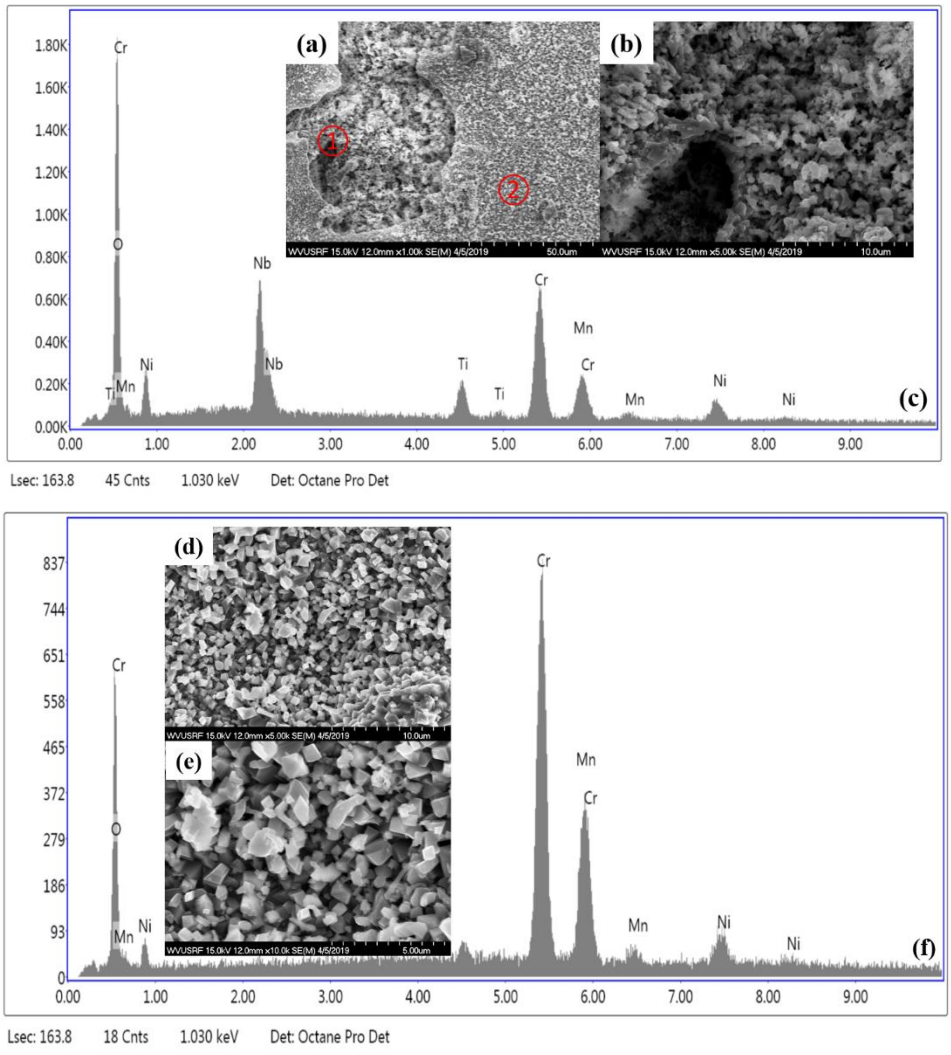

Figure 120 (a) Microstructural analysis of 625 tested in 10% H_2O at 900 °C for 4500 hours, (b) the high-magnification image of area ①, (c) the corresponding EDS spectrum of (b), (d,e) the high-magnification images of area ②, (f) the corresponding EDS spectrum of (d).

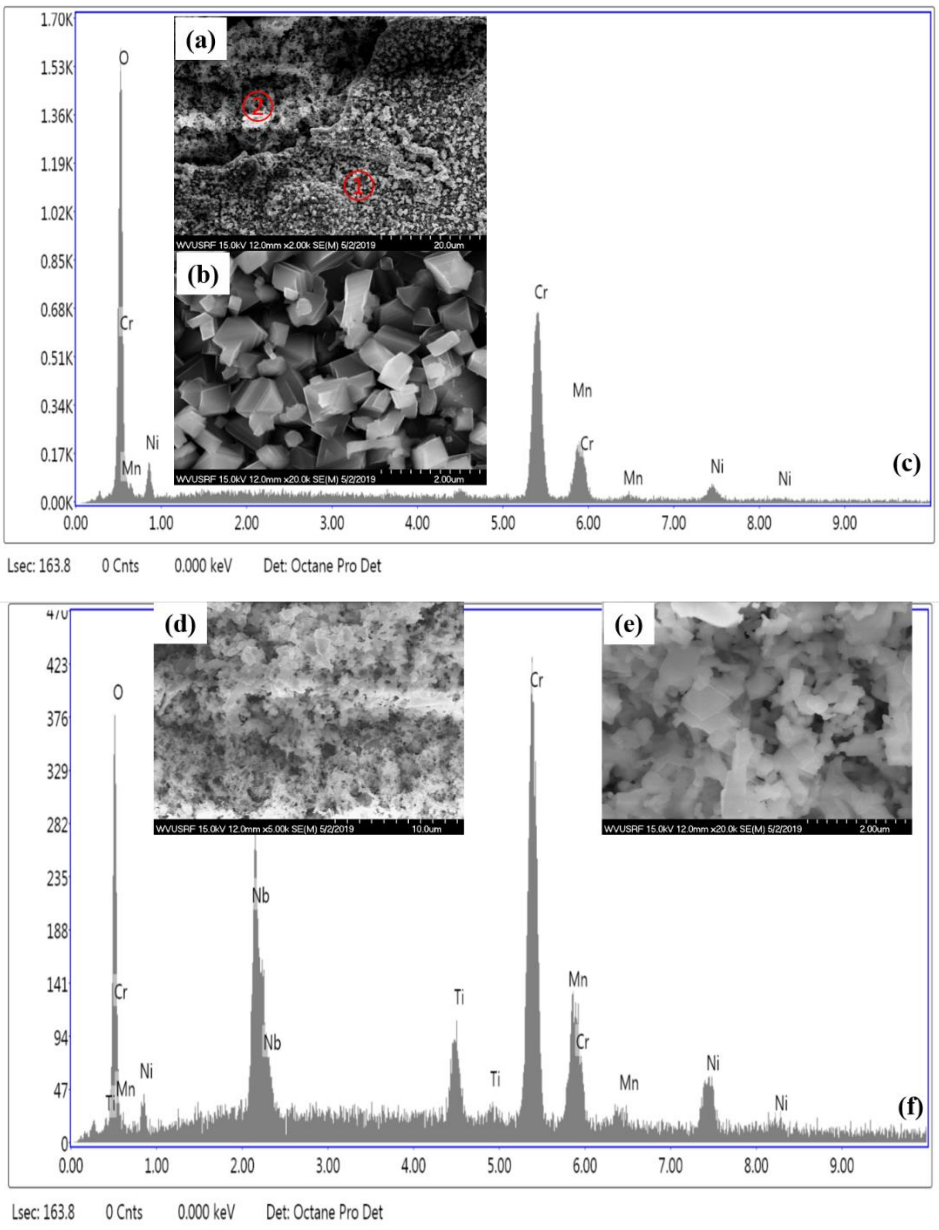

Figure 121 (a) Microstructural analysis of 625 tested in 10% H_2O at 900 °C for 5000 hours, (b) the high-magnification image of area ①, (c) the corresponding EDS spectrum of (b), (d,e) the high-magnification images of area ②, (f) the corresponding EDS spectrum of (d).

Figure 120 and 121 show SEM surface morphologies and related EDS of 625 alloy after exposure to 10% H_2O at 900 °C for 4500 h and 5000 h. After 4500 h and 5000h exposure, the morphology did not change much, it can be easily observed that there were two different kinds of morphologies, spallation area and the area with faceted grains. For the spallation area, the oxides were mainly Cr-Mn-Ti-Ni oxides (Fig. 120f and Fig. 121f). However, for the area with faceted grains, there was mainly one type of grains of which size is range from 0.3 to 1 μm. These faceted grains are Cr-Mn-rich oxides which are confirmed by EDS (Fig. 120c and Fig. 121c).

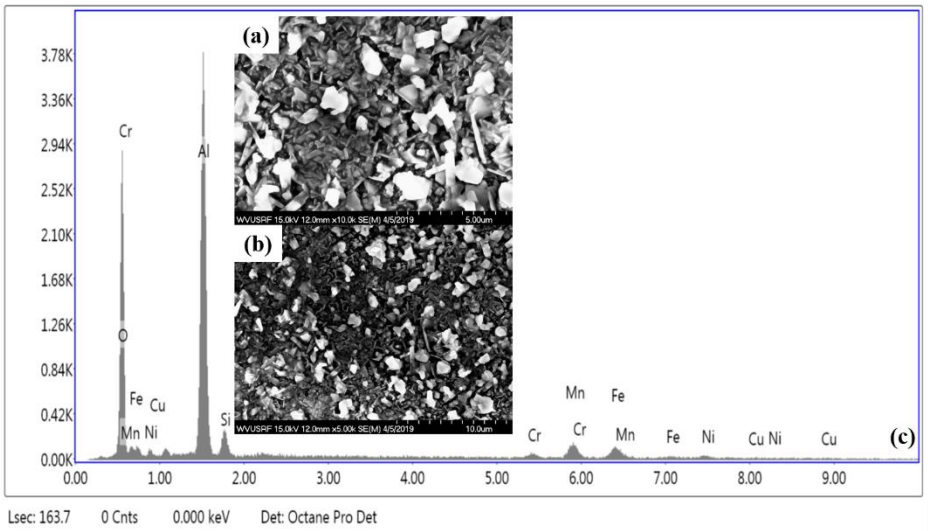

Figure 122 (a) Microstructural analysis of OC11 tested in 10% H_2O at 900 °C for 4500 h, (b) the high-magnification image of area ①, (c) the corresponding EDS spectrum of (b).

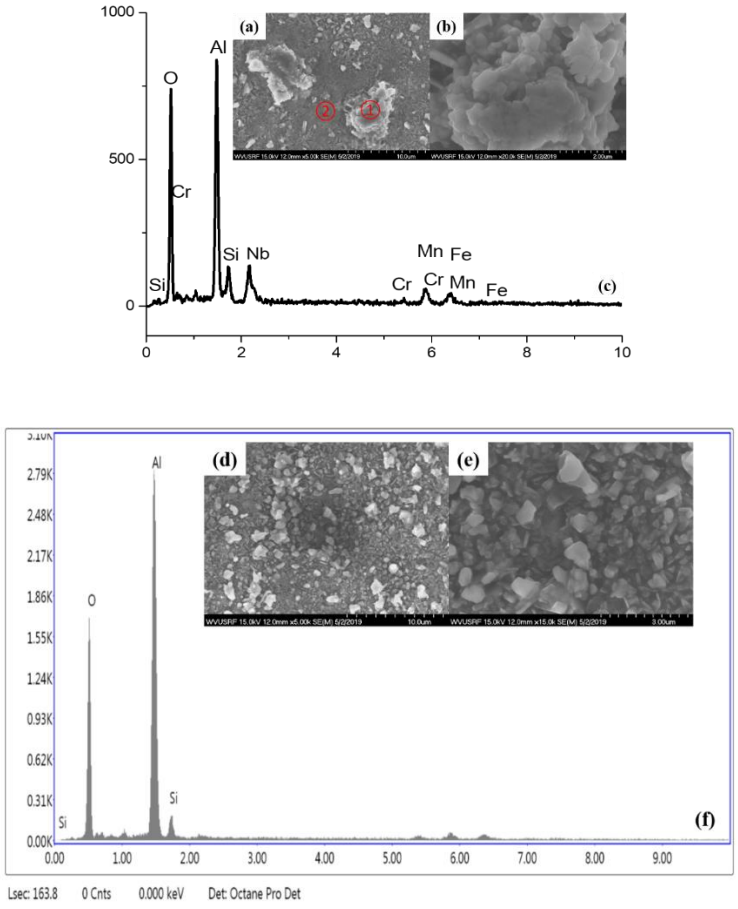

Figure 123 (a) Microstructural analysis of OC11 tested in 10% H_2O at 900 °C for 5000 hours, (b) is the high-magnification image of area ①, (c) is the corresponding EDS spectrum of (b), (d,e) are the high-magnification images of area ②, (g) is the corresponding EDS spectrum of (f).

SEM images of AFA OC11 after exposure to 10% H_2O at 900 °C for 4500 h and 5000 h was demonstrated in Figure 122 and 123. For the sample operated for 4500 h, the surface is non-uniform and there are mainly two types of small grains: one is bar-shaped grain (length × width: 0.1 μm × 0.5 μm) and the other is faceted grain (0.3 to 1 μm). With the increasing of the exposure time to 5000h, the amounts and the size of these two grains does not change much for longer exposure time (Fig. 122a and 122b and Fig. 123d and 123e). However, there was another different morphology for 5000 h exposure sample. For overgrown areas, Cr-Mn-Fe-Si-Nb oxides are the mainly oxides. Figure 122 and 123 both showed that alumina is largely formed on the surface of the AFA OC11 and there are little silicon-related oxides and Cr-Mn-rich oxides on the surface for different expose time.

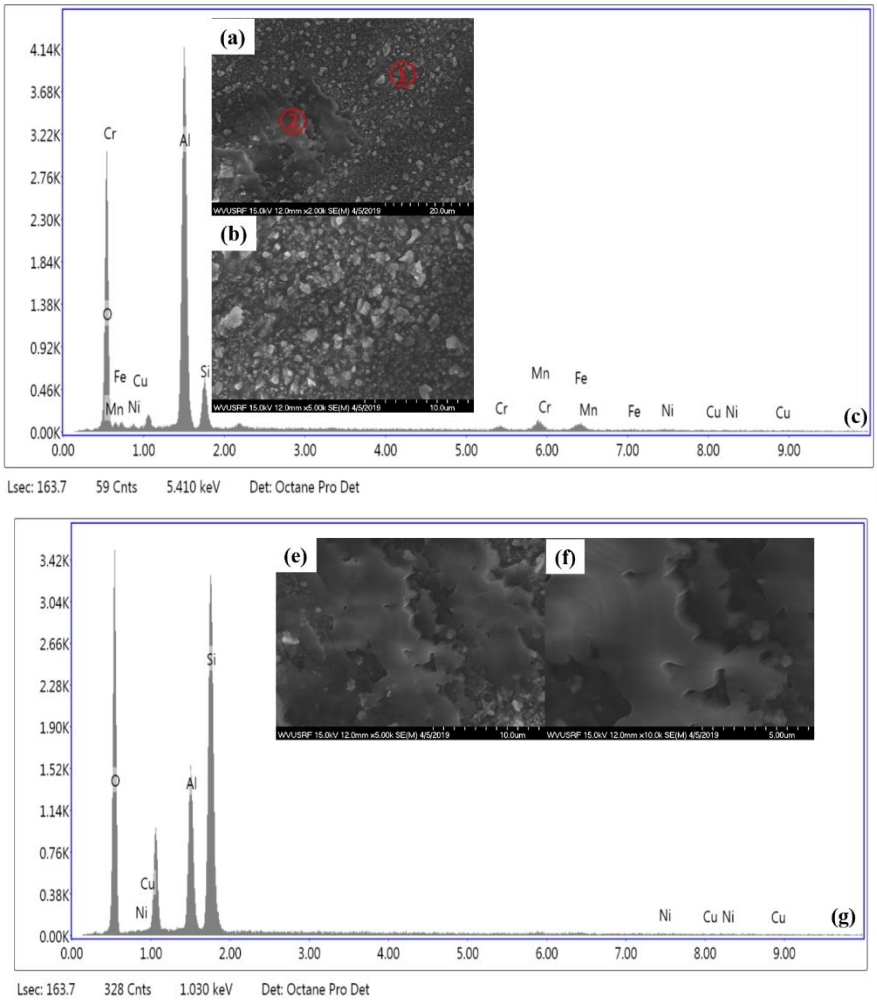

Figure 124 (a) Microstructural analysis of OC11LZ tested in 10% H_2O at 900 °C for 4500 hours, (b) the high-magnification image of area ①, (c) the corresponding EDS spectrum of (b), (d,e) the high-magnification images of area ②, (g) the corresponding EDS spectrum of (f).

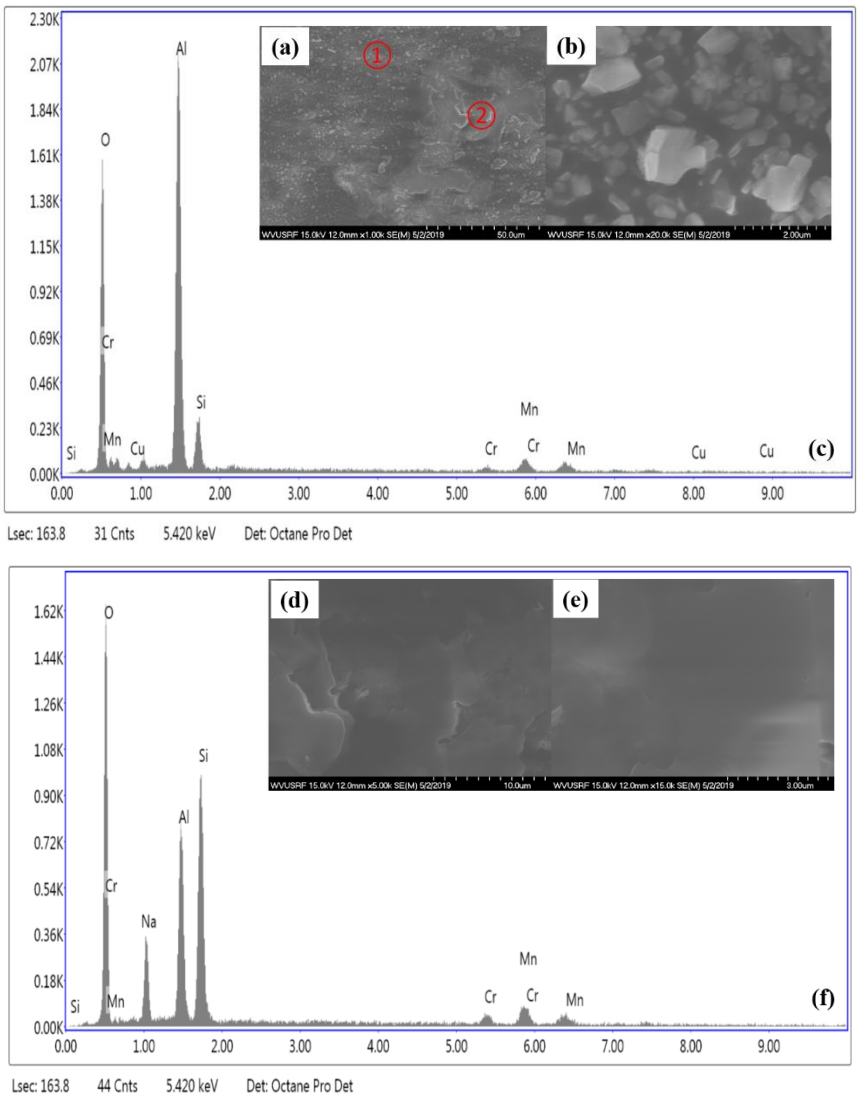

Figure 125 (a) Microstructural analysis of OC11LZ tested in 10% H_2O at 900 °C for 5000 hours, (b) the high-magnification image of area ①, (c) the corresponding EDS spectrum of (b), (d,e) the high-magnification images of area ②, (g) the corresponding EDS spectrum of (f).

Figure 124 and 125 demonstrated SEM surface morphologies of AFA OC11 after exposure to 10% H_2O at 900 °C for 4500h and 5000h. For the sample operated for 4500h, there are mainly two morphologies on the surface of the samples: one is faceted grains (Figure 124b and Figure 125b) and the other is monolithic grains (Figure 124e and Figure 125e). With the increasing of the exposure time to 5000h, the amounts and the size of these two grains does not change much for longer exposure time (Figure 124 and 125). For the areas covered with faceted grains, alumina is the main oxides and a thimbleful of Cr-Mn oxides can also be observed (Figure 124c and Figure 125c). For the areas covered with monolithic grains, silica and alumina are the main oxides and a thimbleful of Cr-Mn oxides can also be observed (Figure 124f and Figure 125f).

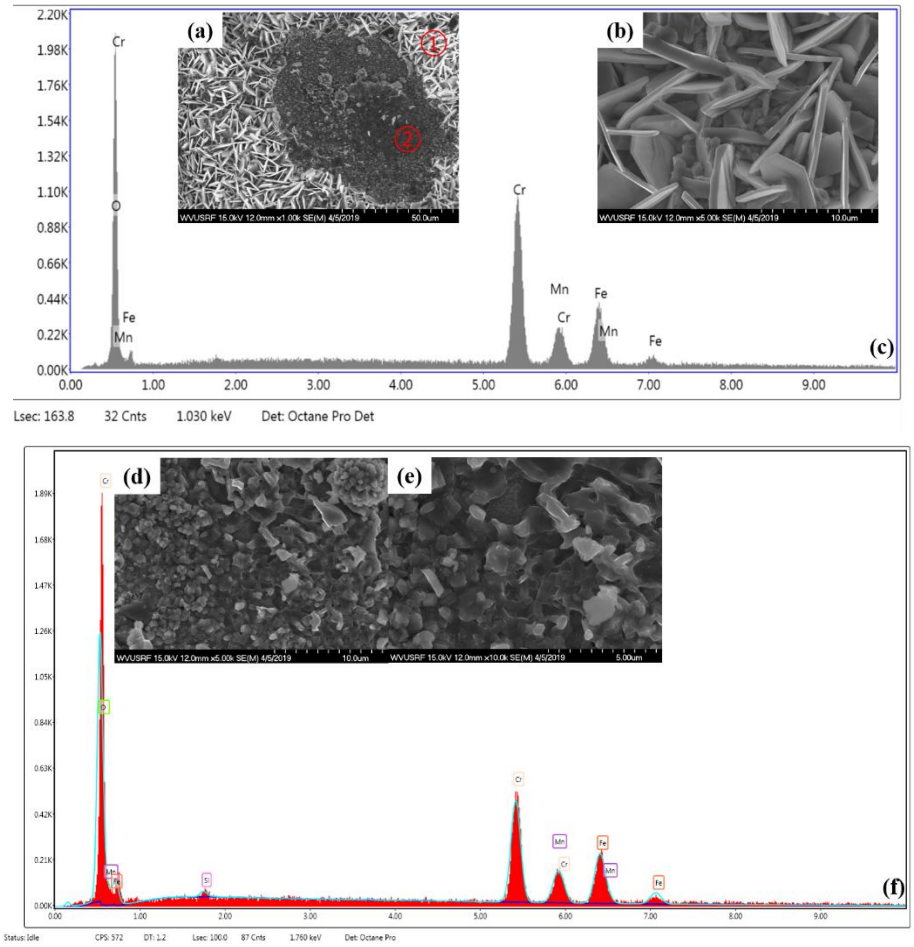

Figure 126 (a) Microstructural analysis of 310S tested in 10% H_2O at 800 °C for 3500 hours, (b) the high-magnification image of area ①, (c) the corresponding EDS spectrum of (b), (d,e) the high-magnification images of area ②, (g) the corresponding EDS spectrum of (f).

Figure 126 and 127 demonstrate SEM surface morphologies of 310S alloy after exposure to 10% H_2O at 800 °C for 3500h and 4000h. There are two different morphology for the samples, however, the composition of oxides from different morphology seemingly the same for each sample. For the sample tested at 800 °C and 10% H_2O for 3500h, there are two kinds of grains (plate-shaped oxide and faceted grains) formed on the surface (Figure 126b). At higher magnifications, the small diamond-shaped oxides underneath the plate-shaped oxides can be clearly observed (Figure 126b). With the increasing of the exposure time, the plate-shaped oxides [diameter (3 to 10 μm) thickness: 0.3 μm] becomes more and more blurred and the shape of the oxide grains becomes round-cornered, however, the faceted grains (0.3 to 1 μm) do not change much (Figure 127d). These plate-shaped oxides and small faceted grains (Figure 126b and 127d) were determined to be the Cr-Mn-rich oxides (Figure 126f and 127f).

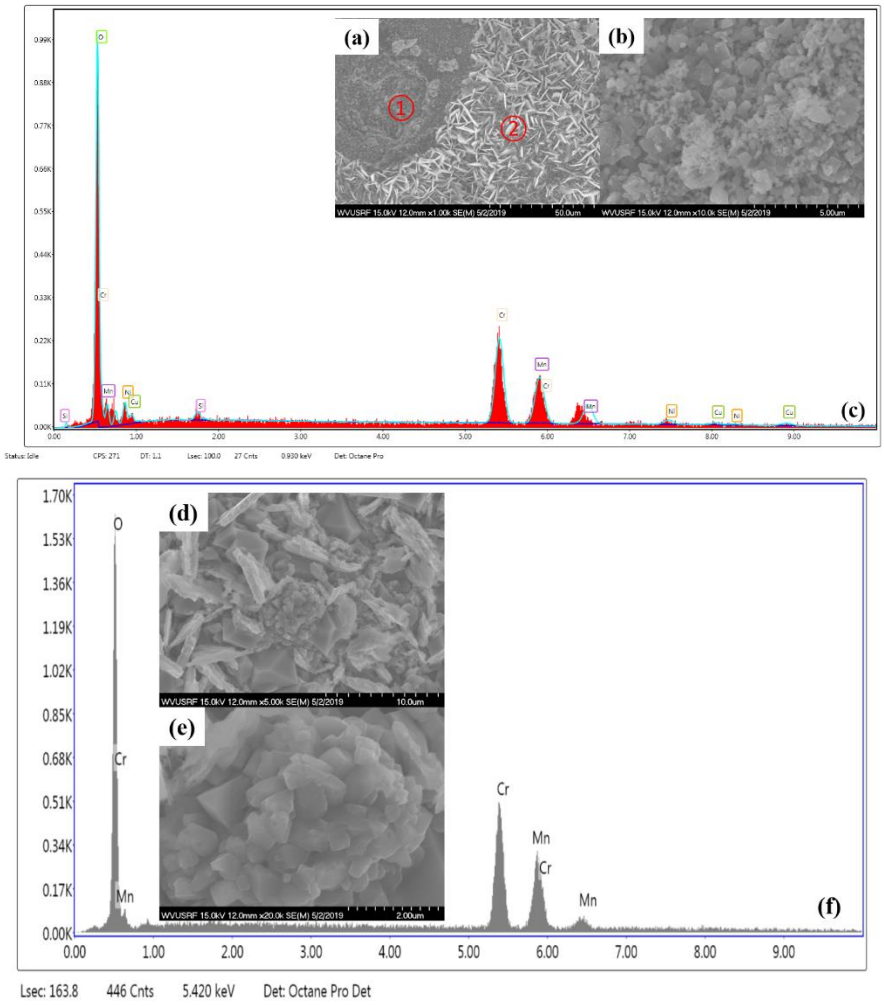

Figure 127 (a) Microstructural analysis of 310S tested in 10% H_2O at 800 °C for 4000 hours, (b) is the high-magnification image of area ①, (c) is the corresponding EDS spectrum of (b), (d,e) are the high-magnification images of area ②, (g) is the corresponding EDS spectrum of (f).

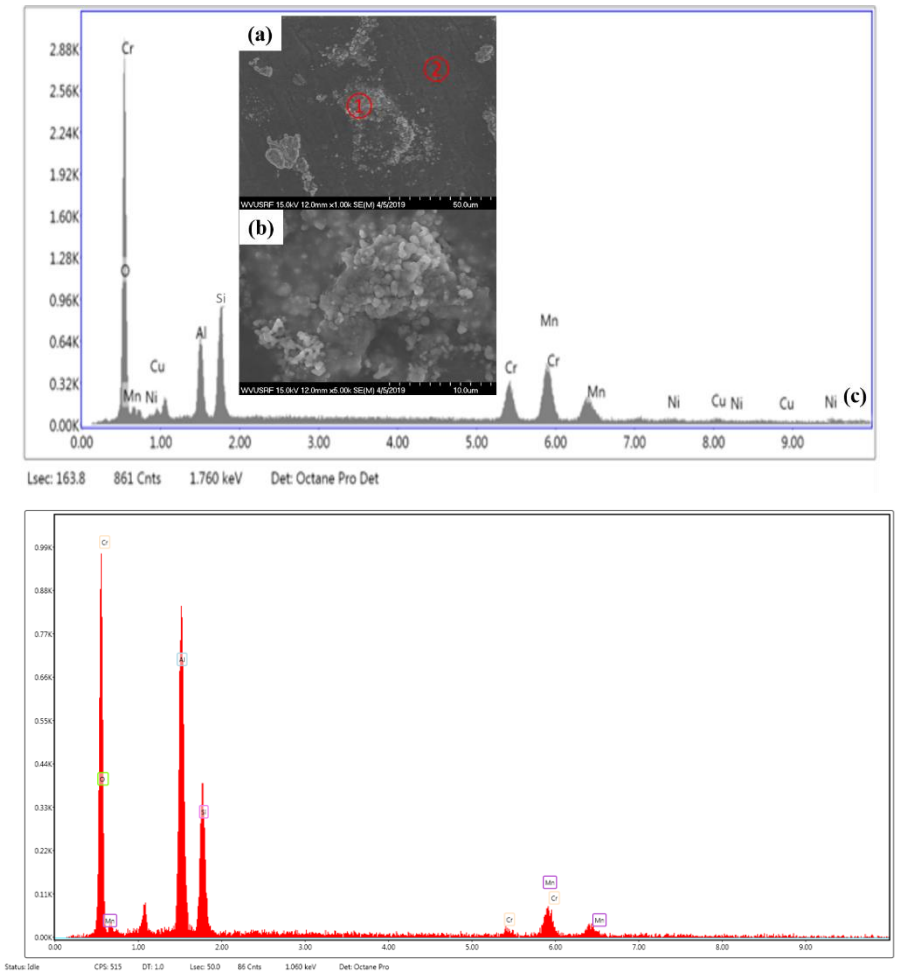

Figure 128 (a) Microstructural analysis of OC4 tested in 10% H_2O at 800 °C for 3500 hours, (b) is the high-magnification image of area ①, (c) is the corresponding EDS spectrum of (b), (d) is the corresponding EDS spectrum of area ②.

Figure 128 and 129 demonstrate SEM surface morphologies of OC4 alloy after exposure to 10% H_2O at 800 °C for 3500h and 4000h. There are two different morphology for the samples, the overgrown areas and the seemingly smooth area. For the overgrown areas, there are two kinds of grains (spherical-shaped oxide and faceted grains) formed on the surface (Figure 128b and 129e), which could be the Nb-Si-rich and Cr-Mn-rich oxides confirmed by EDS (Figure 128c and 129f). However, for the smooth area, alumina and silica oxides are the main oxides, in addition, a thimbleful of Cr-Mn oxides can also be observed (Figure 128d and 129c).

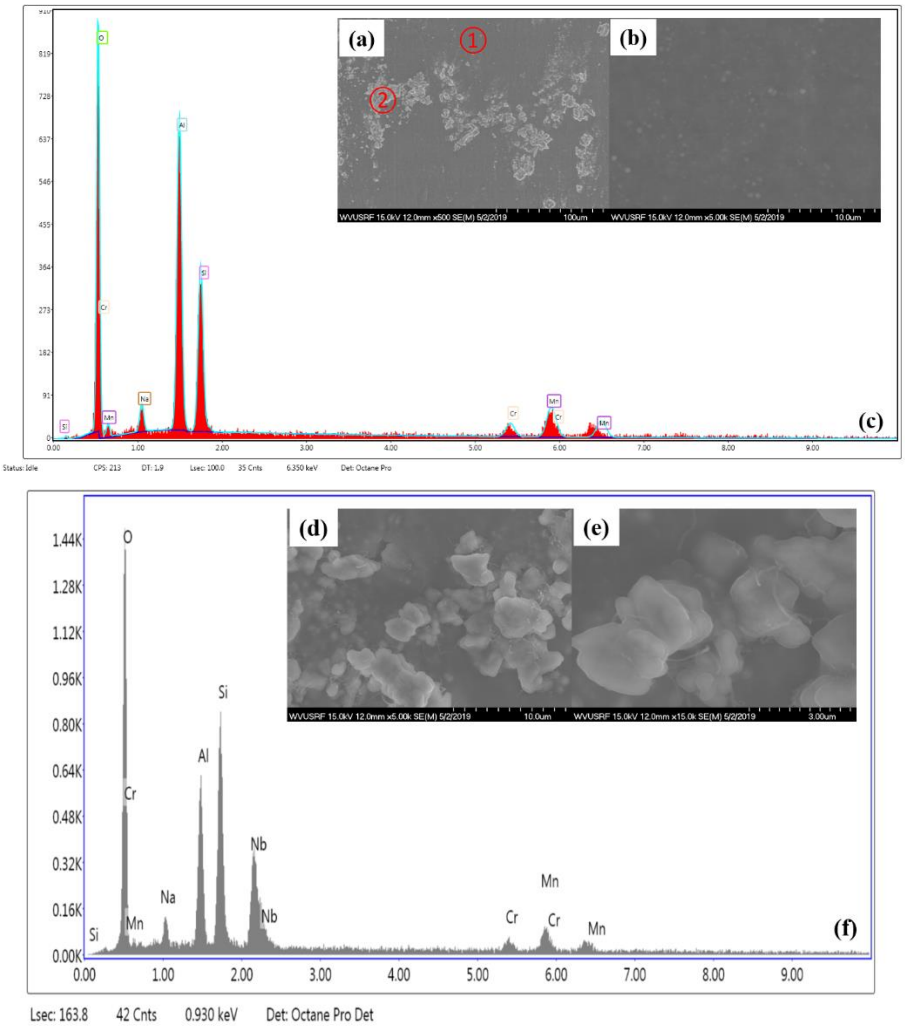

Figure 129 (a) Microstructural analysis of OC4 tested in 10% H_2O at 800 °C for 4000 hours, (b) is the high-magnification image of area ①, (c) is the corresponding EDS spectrum of (b), (d,e) are the high-magnification images of area ②, (f) is the corresponding EDS spectrum of (e).

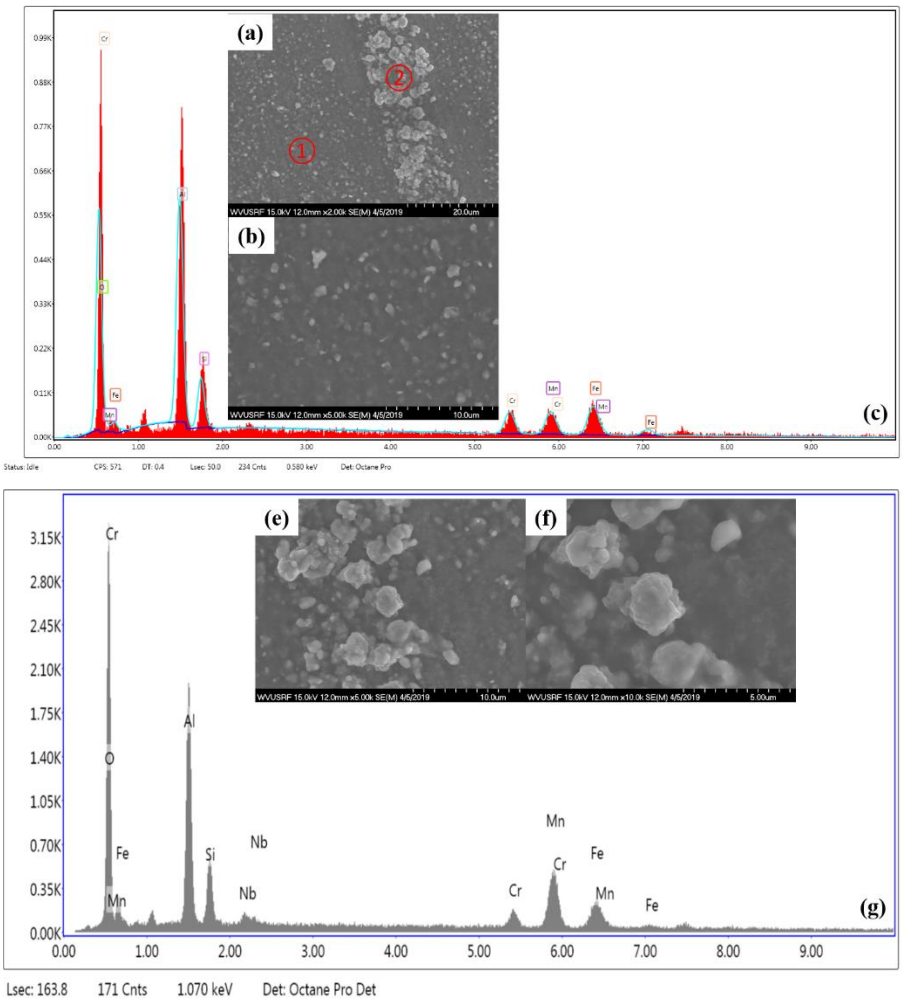

Figure 130 (a) Microstructural analysis of OC5 tested in 10% H_2O at 800 °C for 3500 hours, (b) is the high-magnification image of area ①, (c) is the corresponding EDS spectrum of (b), (d,e) are the high-magnification images of area ②, (g) is the corresponding EDS spectrum of (f).

Figure 130 and 131 demonstrate SEM surface morphologies of OC5 alloy after exposure to 10% H_2O at 800 °C for 3500h and 4000h. The morphology is similar with that of OC4. There are two different morphology for the samples, the overgrown areas and the seemingly smooth area. For the overgrown areas, there are two kinds of grains (spherical-shaped oxide and faceted grains (0.3 to 1 μm)) formed on the surface (Figure 130e and 131b), which could be the Nb-Si-rich and Cr-Mn-Fe rich oxides confirmed by EDS (Figure 130g and 131c). However, for the smooth area, alumina and silica oxides are the main oxides, in addition, a thimbleful of Cr-Mn oxides can also be observed (Figure 130c and 131f).

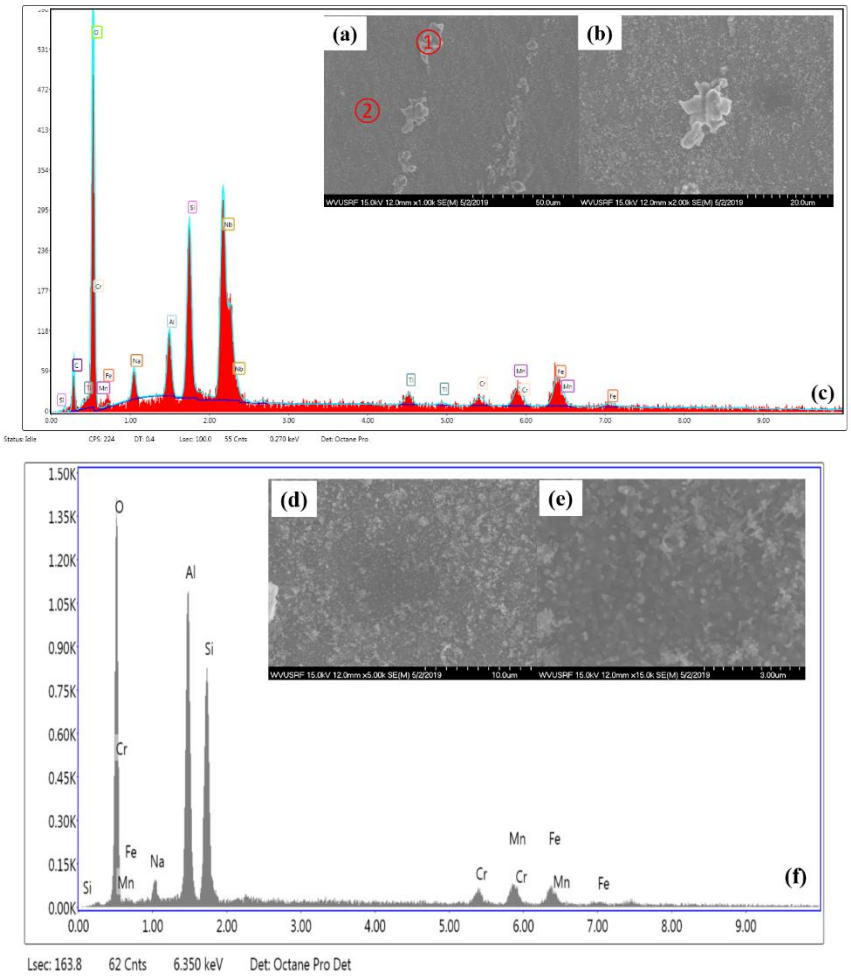

Figure 131 (a) Microstructural analysis of 310S tested in 10% H_2O at 800 °C for 4000 hours, (b) is the high-magnification image of area ①, (c) is the corresponding EDS spectrum of (b), (d,e) are the high-magnification images of area ②, (g) is the corresponding EDS spectrum of (f).

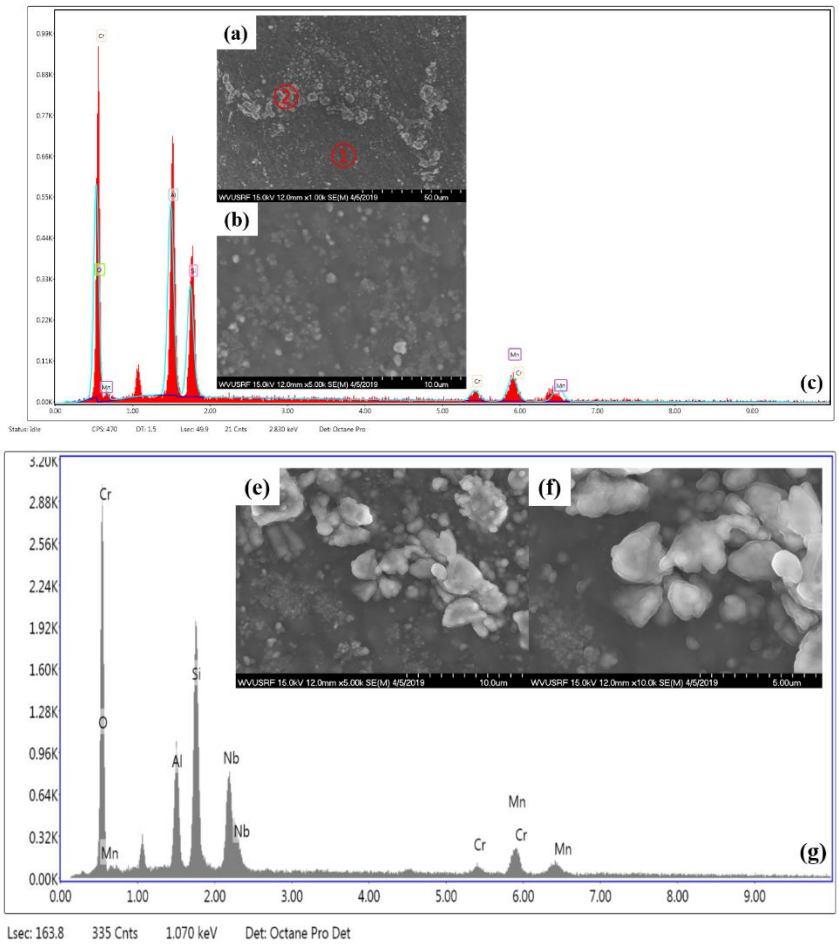

Figure 132 (a) Microstructural analysis of MOD tested in 10% H_2O at 800 °C for 3500 hours, (b) is the high-magnification image of area ①, (c) is the corresponding EDS spectrum of (b), (e,f) are the high-magnification images of area ②, (g) is the corresponding EDS spectrum of (f).

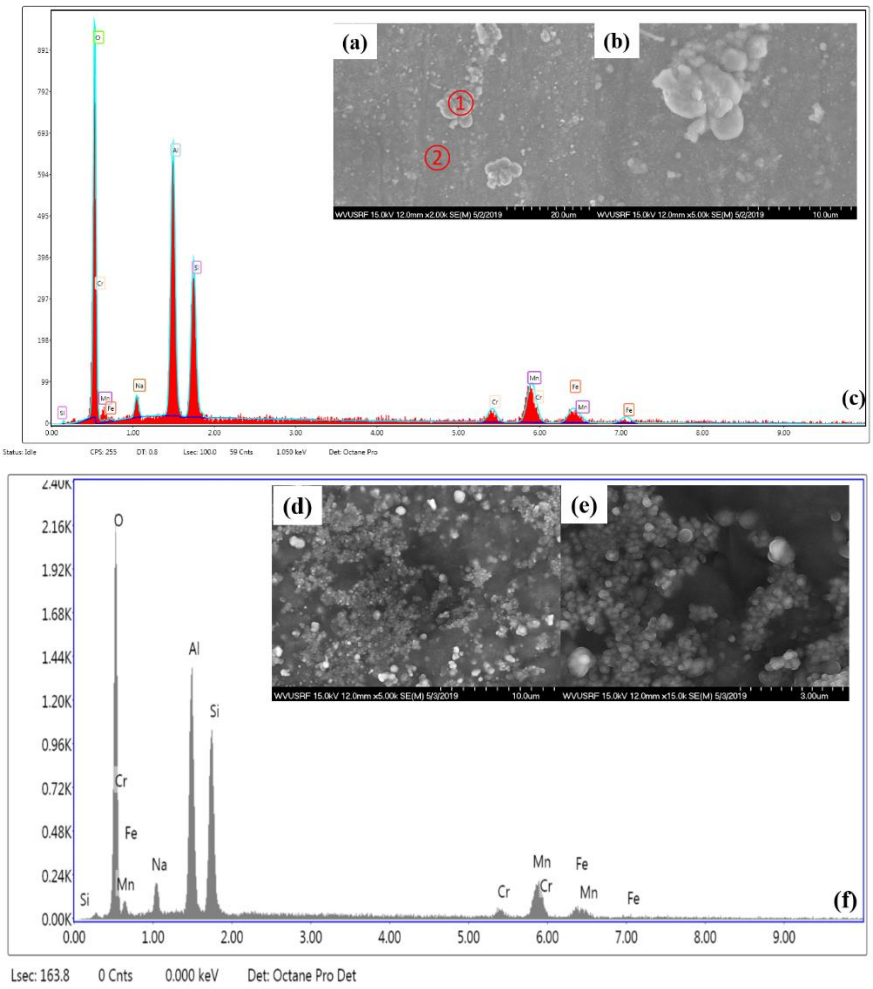

Figure 133 (a) Microstructural analysis of MOD tested in 10% H_2O at 800 °C for 4000 hours, (b) is the high-magnification image of area ①, (c) is the corresponding EDS spectrum of (b), (d,e) are the high-magnification images of area ②, (f) is the corresponding EDS spectrum of (e).

Figure 132 and 133 demonstrate SEM surface morphologies of MOD alloy after exposure to 10% H_2O at 800 °C for 3500h and 4000h. The morphology is similar with that of OC4 and OC5. There are two different morphology for the samples tested for 3500 h and 4000 h, the overgrown areas and the seemingly smooth area. For the overgrown areas of the sample tested for 3500h, there are two kinds of grains (spherical-shaped oxide and faceted grains (0.3 to 1 μm)) formed on the surface (Figure 132a), which could be the Nb-Si-rich and Cr-Mn-Fe rich oxides confirmed by EDS (Figure 132g). However, there was almost no Nb oxides detected for the sample tested for 4000 h. In addition, for the smooth area of both samples, alumina and silica oxides are the main oxides, a thimbleful of Cr-Mn oxides can also be observed (Figure 132c and 133f).

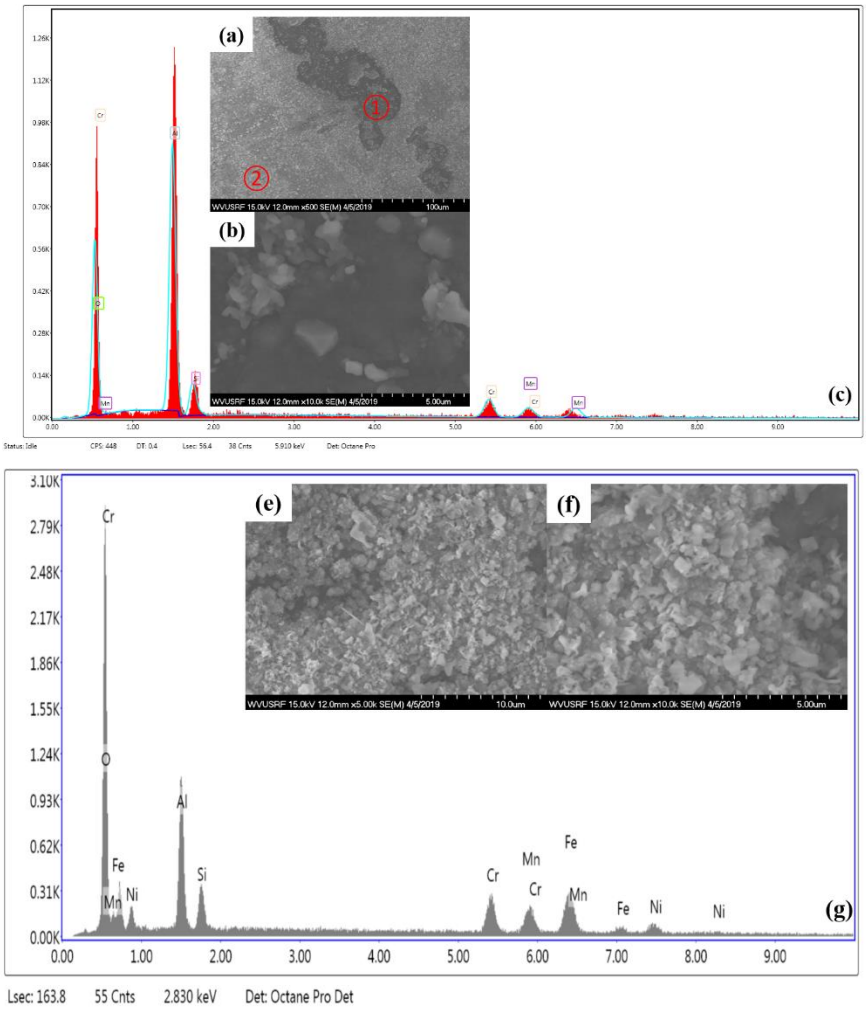

Figure 134 (a) Microstructural analysis of OC11 tested in 10% H_2O at 800 °C for 3500 hours, (b) is the high-magnification image of area ①, (c) is the corresponding EDS spectrum of (b), (e,f) are the high-magnification images of area ②, (g) is the corresponding EDS spectrum of (f).

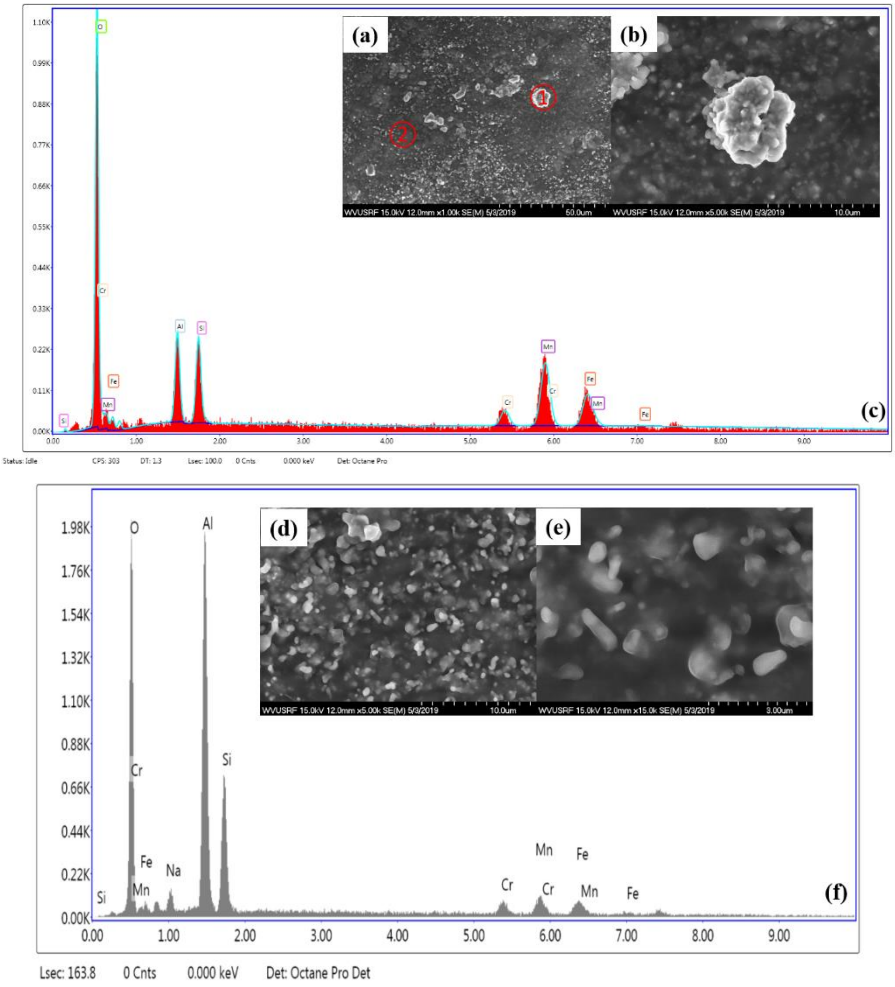

Figure 135 (a) Microstructural analysis of OC11 tested in 10% H_2O at 800 °C for 4000 hours, (b) is the high-magnification image of area ①, (c) is the corresponding EDS spectrum of (b), (d,e) are the high-magnification images of area ②, (g) is the corresponding EDS spectrum of (f).

Figure 134 and 135 demonstrate SEM surface morphologies of AFA OC11 after exposure to 10% H_2O at 800 ºC for 3500h and 4000h. Oxide scale after 3500h exposure at 800 °C and 10% H_2O appeared faceted grains and some nodules on the majority of the sample surface (Figure 134a). At higher magnifications, these nodules are formed by the accumulation of the small faceted grains (Fig. 15f). With the increasing of the exposure time, more nodules formed on the surface of the samples tested for 4000h exposure (Figure 135a). Moreover, the composition of these nodules is characterized to be enriched in Cr-Mn-Fe-Si oxides. (Figure 134f and 135b).

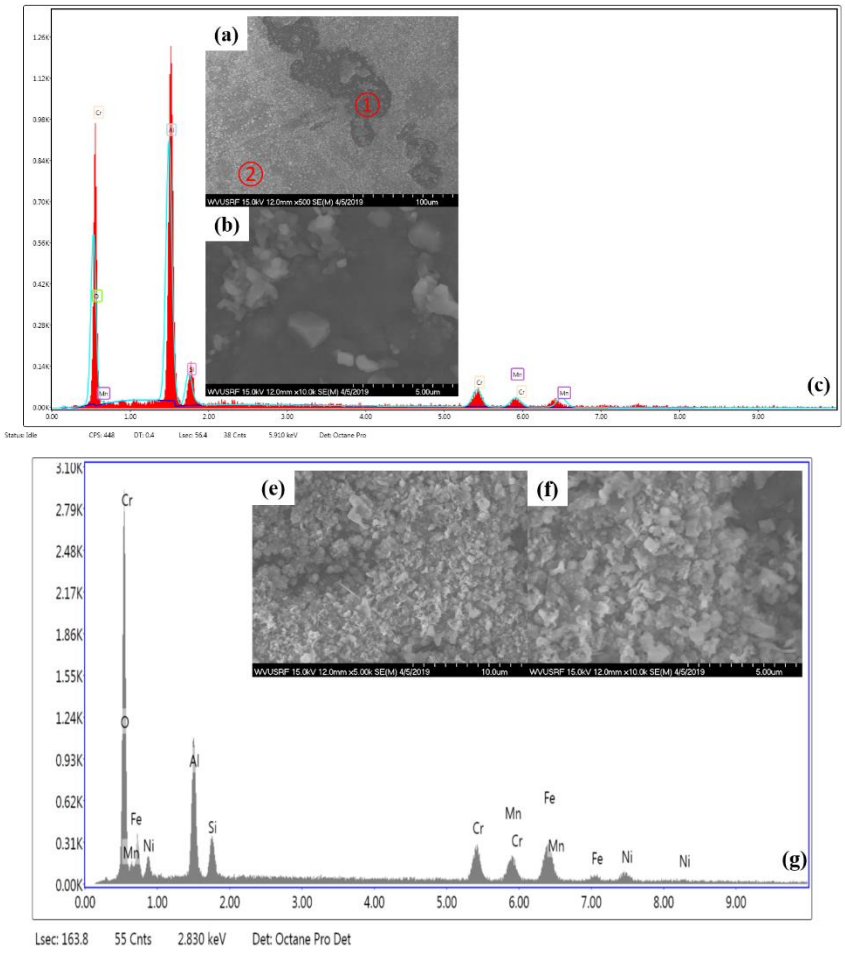

Figure 136 (a) Microstructural analysis of OC11LZ tested in 10% H_2O at 800 °C for 3500 hours, (b) is the high-magnification image of area ①, (c) is the corresponding EDS spectrum of (b), (d,e) are the high-magnification images of area ②, (g) is the corresponding EDS spectrum of (f).

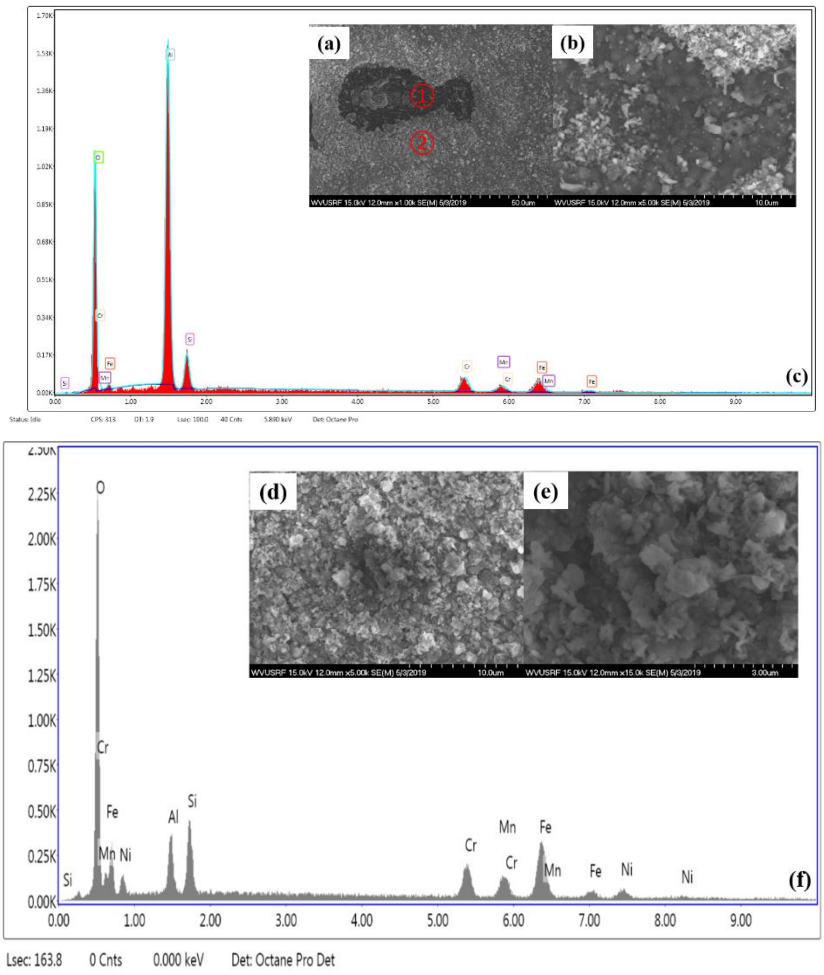

Figure 137 (a) Microstructural analysis of OC11LZ tested in 10% H_2O at 800 °C for 4000 hours, (b) is the high-magnification image of area ①, (c) is the corresponding EDS spectrum of (b), (d,e) are the high-magnification images of area ②, (g) is the corresponding EDS spectrum of (f).

Figure 136 and 137 show the SEM surface morphologies of AFA OC11LZ after exposure to 10% H_2O at 800 °C for 3500h and 4000h. For both samples exposed for 3500h and 4000h, there are a majority area of fluffy-like oxides and some nodules formed on the surface (Figure 136e and 137d), At higher magnification (Figure 136f and 137e), small amount of faceted grains (0.3 to 1 μm) underneath the fluffy-like oxides can be observed. The morphology of the samples tested for 4000h exposure is similar to that of 3500h. It can be observed from the EDX (Figure 136g and 137f) that Si-containing oxides, Al-rich oxides and Cr-Mn oxides are formed on the surface of the alloy. In addition, other areas were covered by faceted grains which can be ascribed to the Cr-Mn oxides and a small number of Si-containing oxides.

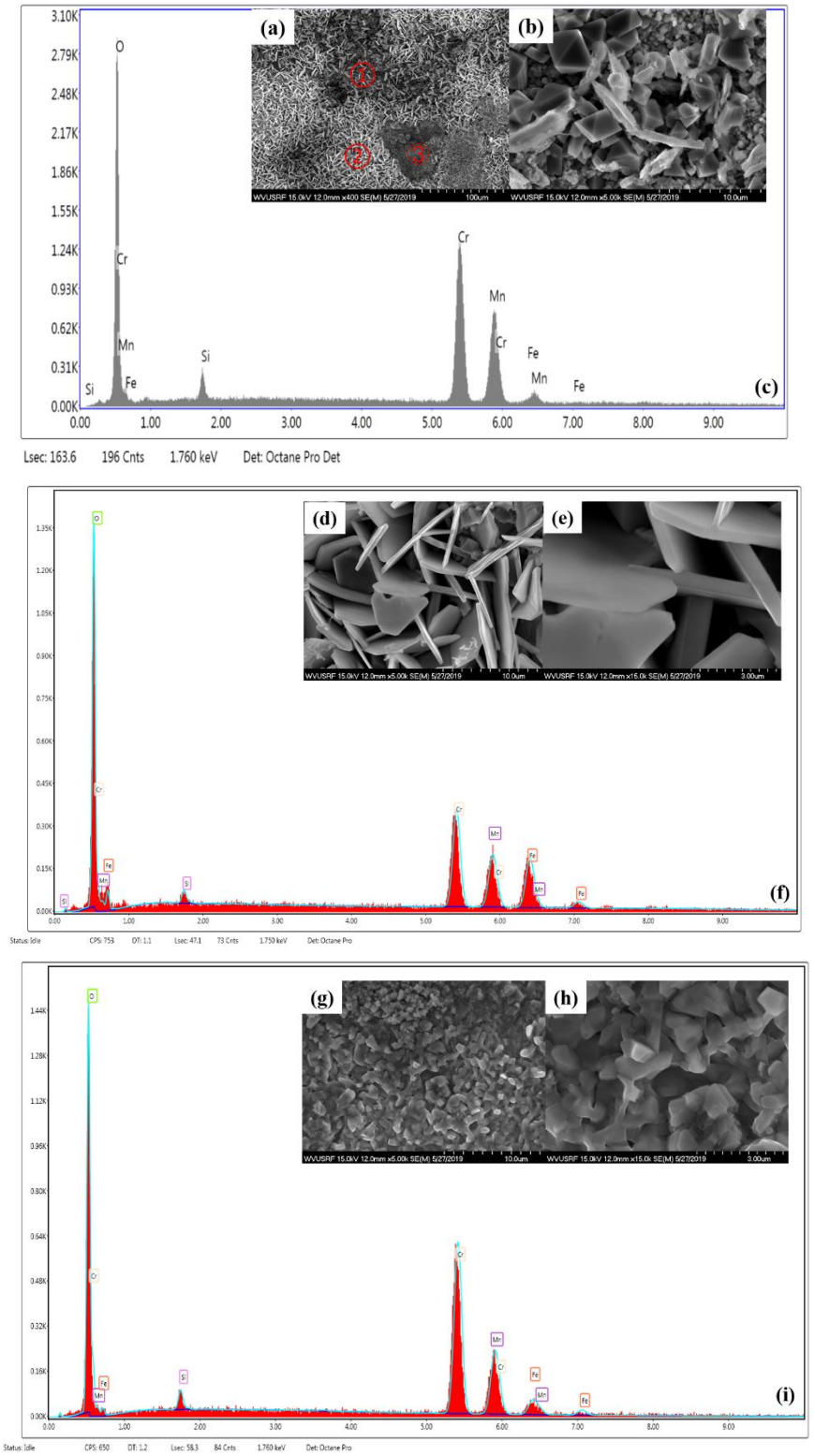

Figure 138 (a) Microstructural analysis of 310S tested in 10% H_2O at 800 °C for 4500 hours, (b) the high-magnification image of area ①, (c) the corresponding EDS spectrum of (b), (d,e) the high-magnification images of area ②, (f) the corresponding EDS spectrum of (e), (g,h) the high-magnification images of area ③, (i) the corresponding EDS spectrum of (h).

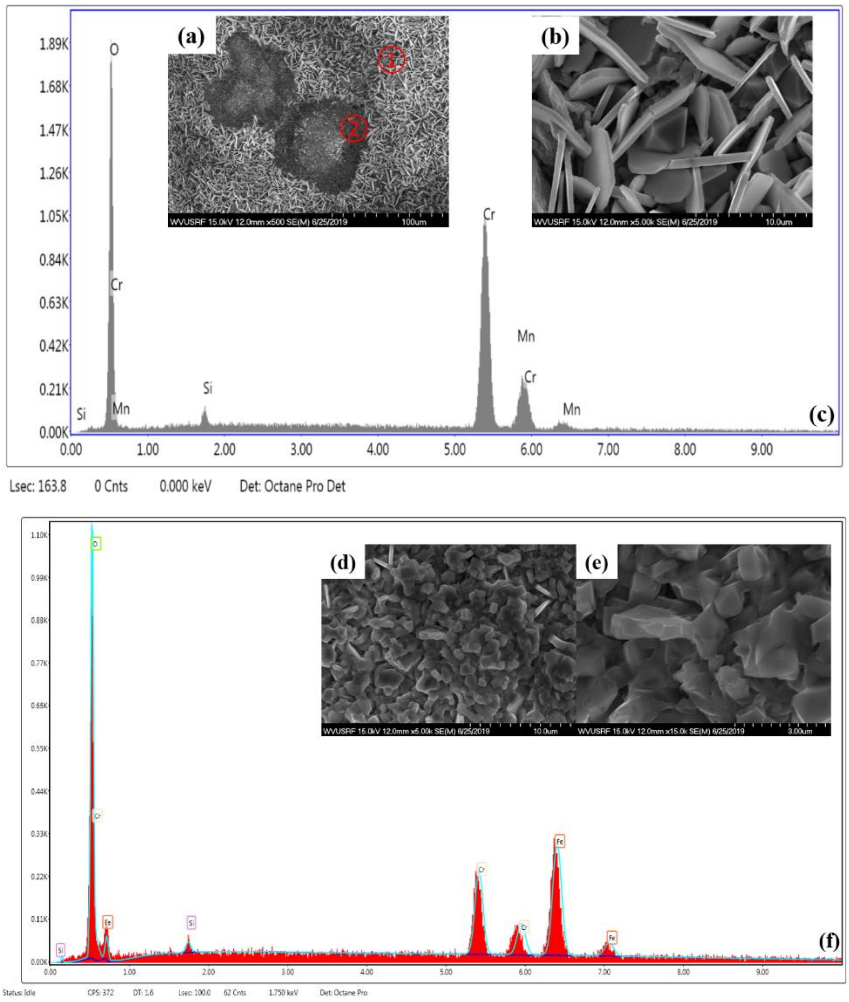

Figure 139 (a) Microstructural analysis of 310S tested in 10% H_2O at 800 °C for 5000 hours, (b) is the high-magnification image of area ①, (c) is the corresponding EDS spectrum of (b), (d,e) are the high-magnification images of area ②, (f) is the corresponding EDS spectrum of (e).

Figure 138 and 139 demonstrate SEM surface morphologies of 310S alloy after exposure to 10% H_2O at 800^{o}C for 4500h and 5000h. Though there are differences in the morphology for the samples, the composition of oxides from different morphology seems the same for each sample. For the sample tested at 800 °C and 10% H_2O for 4500h, there are two kinds of grains (plate-shaped oxide and faceted grains) formed on the surface (Figure 138b, 138e and 138h). At higher magnifications, the small diamond-shaped oxides underneath the plate-shaped oxides can be clearly observed (Figure 138e). With the increase of the exposure time, the plate-shaped oxides [diameter (3 to 10 μm) thickness: 0.3 μm] becomes not that sharp and the shape of the oxide grains becomes round-cornered, however, the faceted grains (0.3 to 1 μm) do not change much (Figure 138d). These plate-shaped oxides (Figure 138d and Figure 139b) and small faceted grains (Figure 138b, 138h and 139d) were determined to be the Cr-Mn-rich oxides (Figure 138c, 138f, 138i and 139c, 139f).

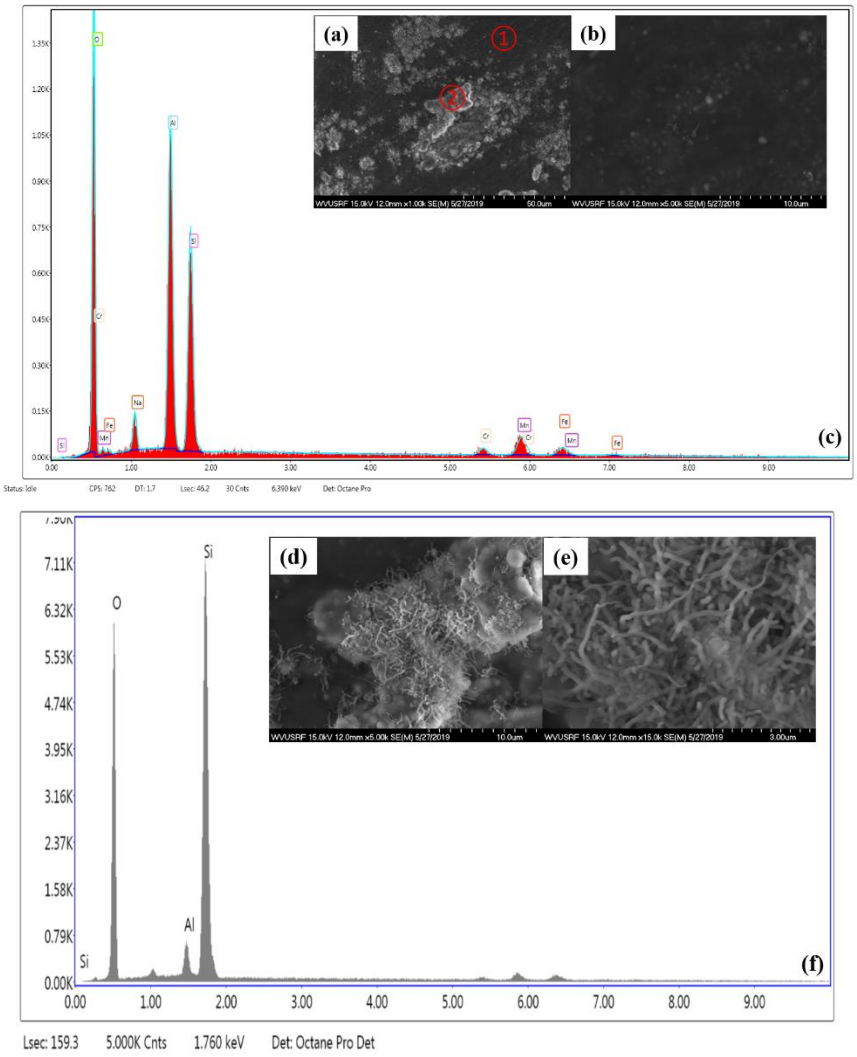

Figure 140 (a) Microstructural analysis of OC4 tested in 10% H_2O at 800 °C for 4500 hours, (b) is the high-magnification image of area ①, (c) is the corresponding EDS spectrum of (b), (d,e) are the high-magnification images of area ②, (f) is the corresponding EDS spectrum of (e).

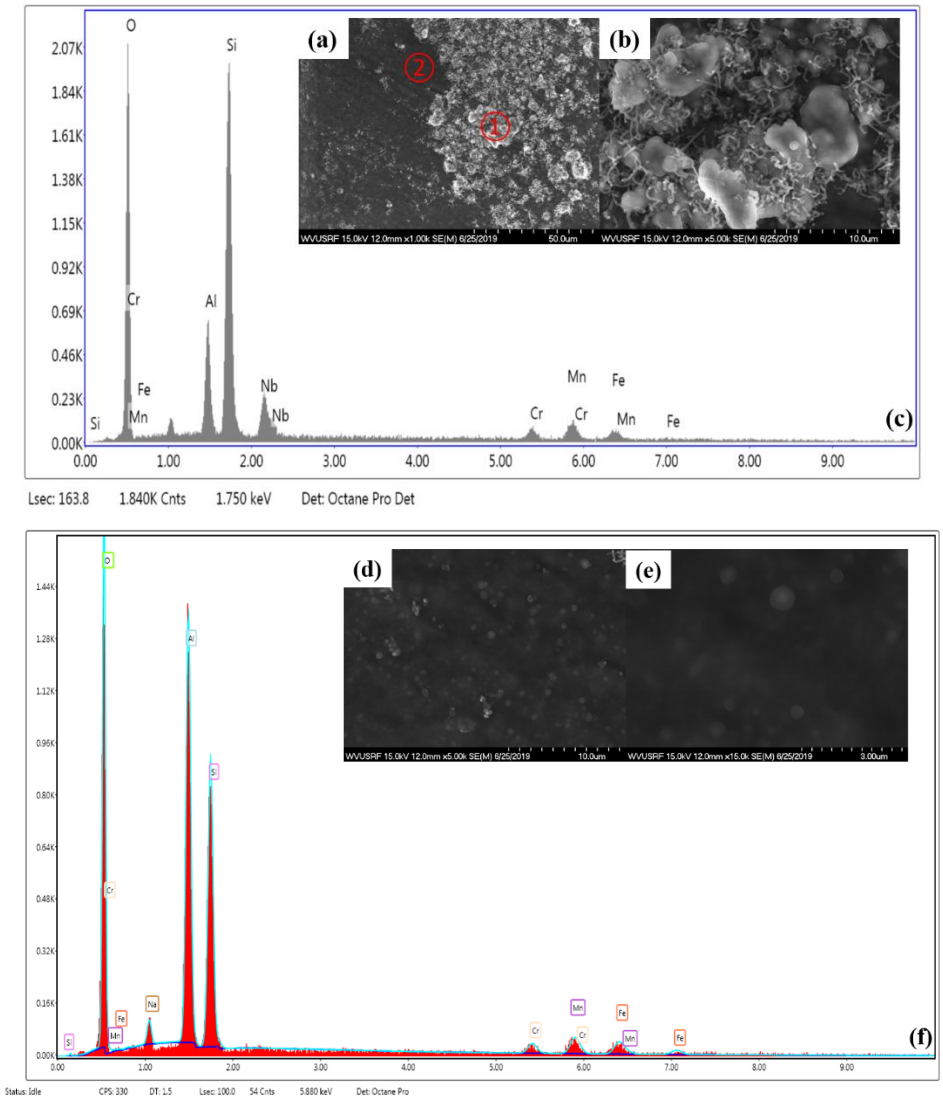

Figure 141 (a) Microstructural analysis of OC4 tested in 10% H_2O at 800 °C for 5000 hours, (b) is the high-magnification image of area ①, (c) is the corresponding EDS spectrum of (b), (d,e) are the high-magnification images of area ②, (f) is the corresponding EDS spectrum of (e).

Figure 140 and 141 demonstrate SEM surface morphologies of OC4 alloy after exposure to 10% H_2O at 800 °C for 4500h and 5000h. There are two different morphology for the samples, the overgrown areas and the smooth area. For the overgrown areas, there are two kinds of grains (whiskers and faceted grains) formed on the surface (Figure 140a and 141a), which could be the Nb-Si-rich and Cr-Mn-rich oxides confirmed by EDS (Figure 140c and 141c). For the smooth area, alumina and silica oxides are the main oxides. In addition, a thimbleful of Cr-Mn oxides can also be observed (Figure 140f and 141f).

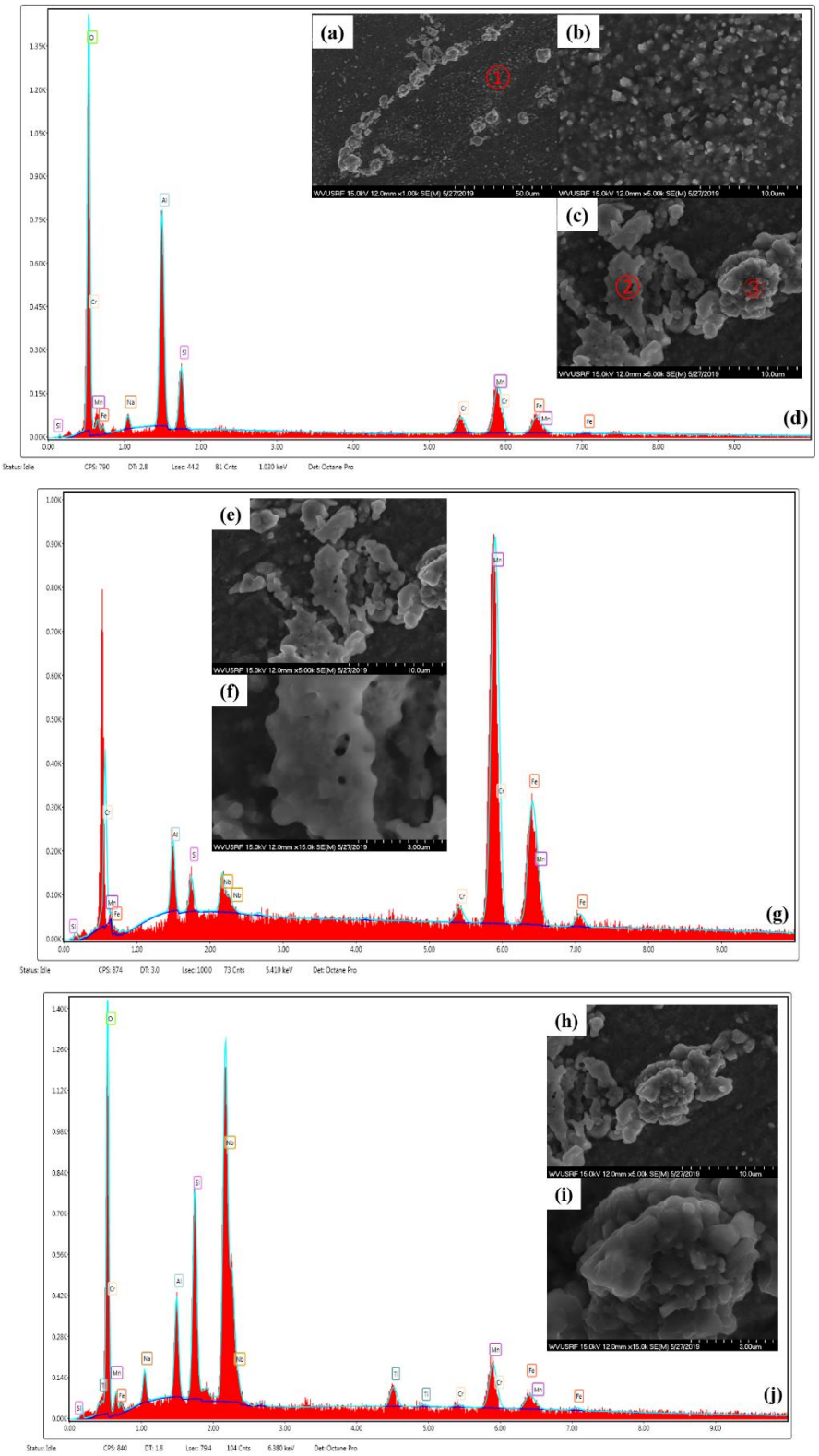

Figure 142 (a) Microstructural analysis of OC5 tested in 10% H_2O at 800 °C for 4500 hours, (b) the high-magnification image of area ①, (c) the corresponding EDS spectrum of (b), (d,e) the high-magnification images of area ②, (f) the corresponding EDS spectrum of (e), (g,h) the high-magnification images of area ③, (i) the corresponding EDS spectrum of (h).

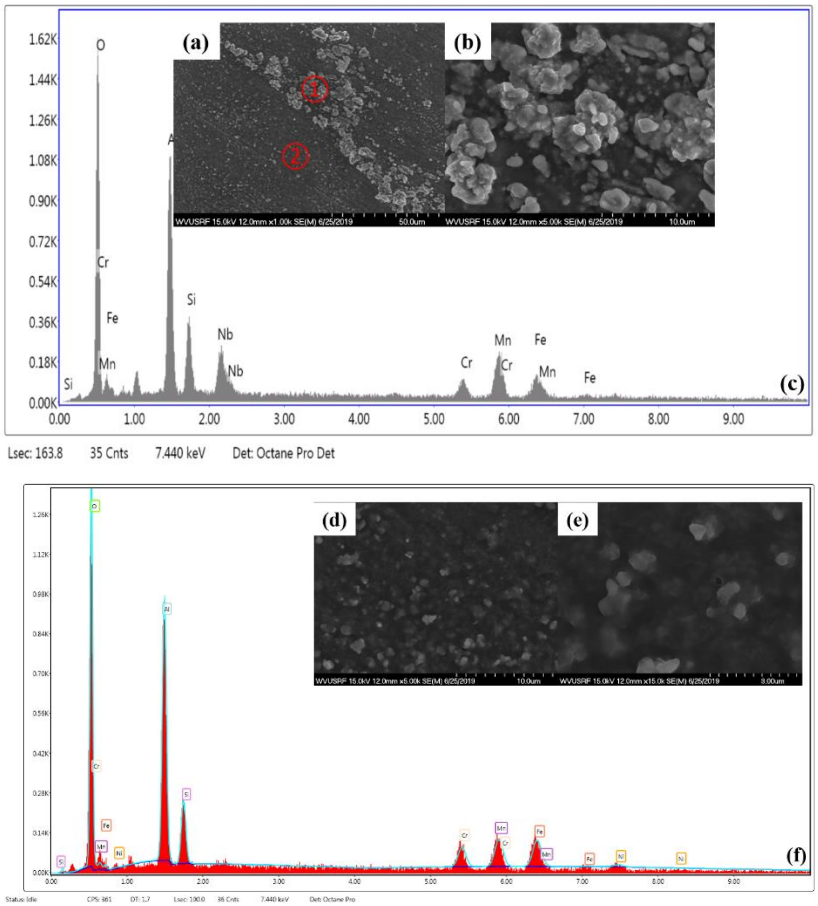

Figure 143 (a) Microstructural analysis of OC5 tested in 10% H_2O at 800 °C for 5000 hours, (b) is the high-magnification image of area ①, (c) is the corresponding EDS spectrum of (b), (d,e) are the high-magnification images of area ②, (f) is the corresponding EDS spectrum of (e).

Figure 142 and 143 demonstrate SEM surface morphologies of OC5 alloy after exposure to 10% H_2O at 800 °C for 4500h and 5000h. The morphology is similar to that of OC4. There are two different morphology for the samples, the overgrown areas and the seemingly smooth area. For the overgrown areas, there are two kinds of grains (spherical-shaped oxide and faceted grains (0.3 to 1 μm)) formed on the surface (Figure 142a and 143a), which could be the Nb-Si-rich and Cr-Mn-Fe rich oxides confirmed by EDS (Figure 142c, 142f and 143c). For the smooth area, alumina and silica oxides are the main oxides. In addition, a thimbleful of Cr-Mn oxides can also be observed (Figure 142d and 143f).

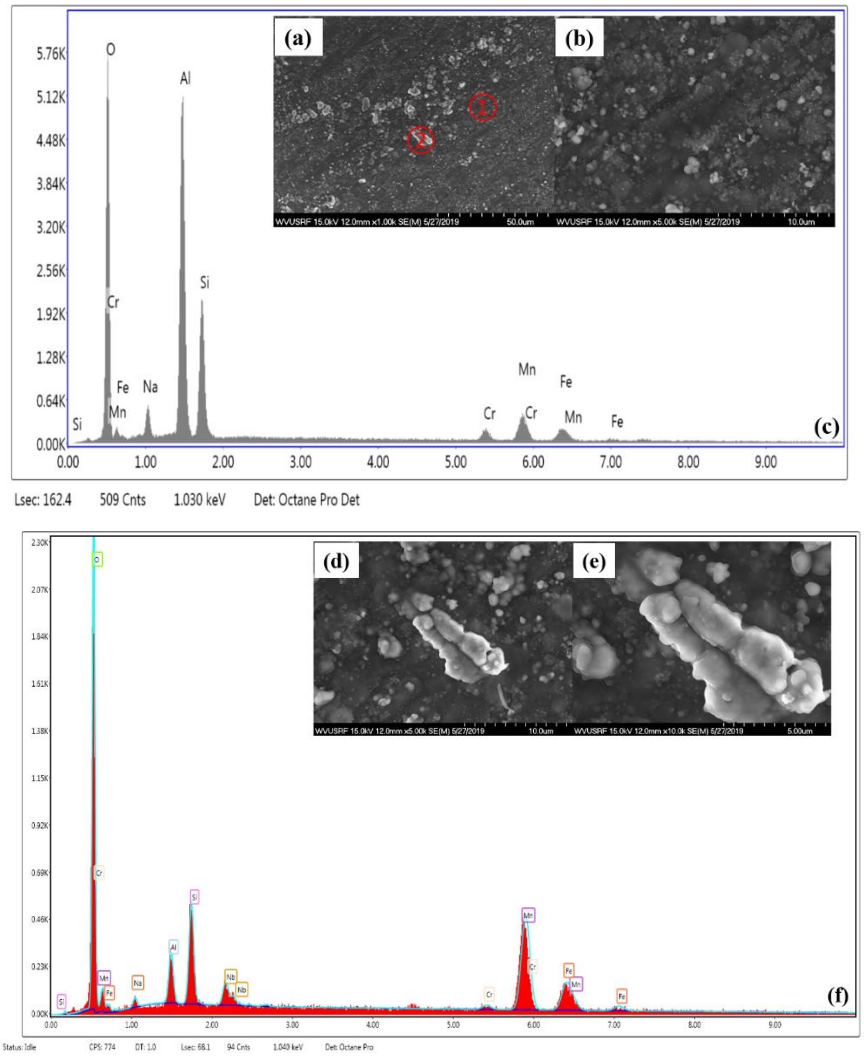

Figure 144 (a) Microstructural analysis of MOD tested in 10% H_2O at 800 °C for 4500 hours, (b) is the high-magnification image of area ①, (c) is the corresponding EDS spectrum of (b), (d,e) are the high-magnification images of area ②, (f) is the corresponding EDS spectrum of (e).

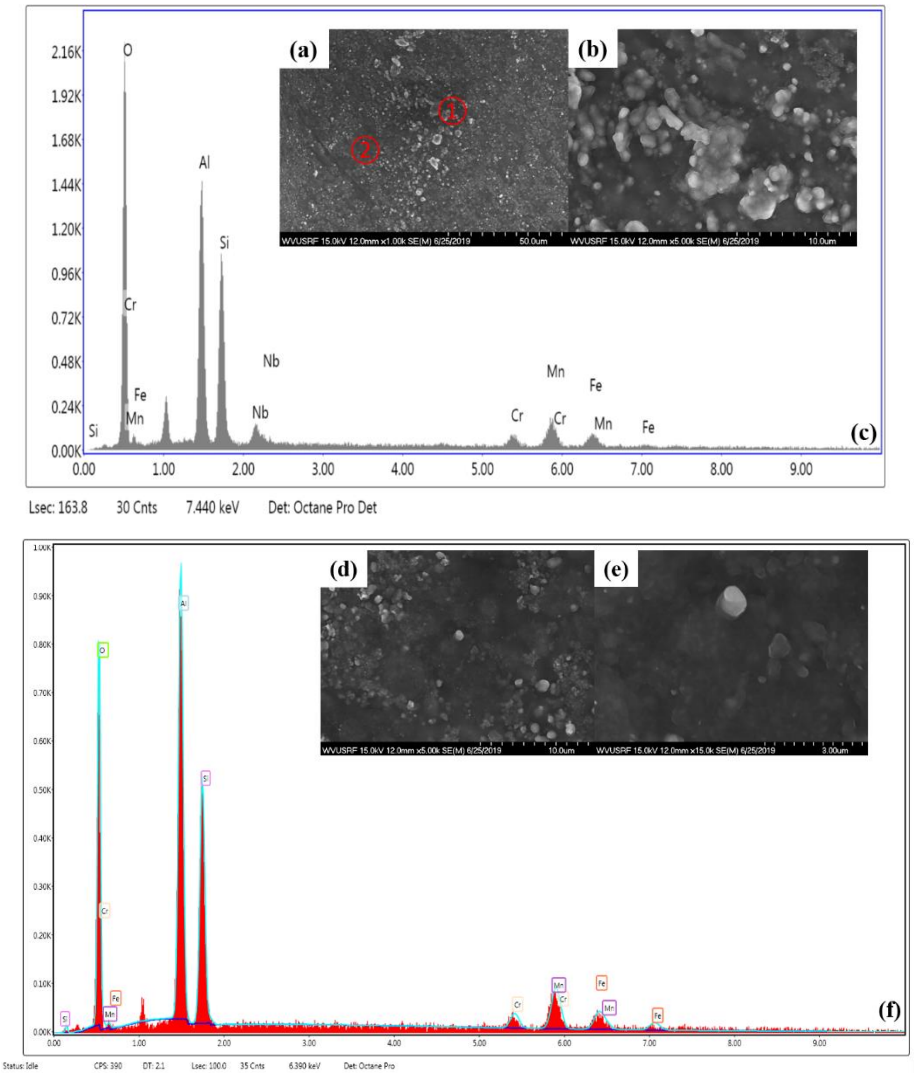

Figure 145 (a) Microstructural analysis of MOD tested in 10% H_2O at 800 °C for 5000 hours, (b) is the high-magnification image of area ①, (c) is the corresponding EDS spectrum of (b), (d,e) are the high-magnification images of area ②, (f) is the corresponding EDS spectrum of (e).

Figure 144 and 145 demonstrate SEM surface morphologies of MOD alloy after exposure to 10% H_2O at 800 °C for 4500h and 5000h. The morphology is similar to that of OC4 and OC5. There are two different morphologies for the samples tested for 4500 h and 5000 h, the overgrown areas and the seemingly smooth area. For the overgrown areas of the sample tested for 4500h, there are two kinds of grains (spherical-shaped oxide and faceted grains (0.3 to 1 μm)) formed on the surface (Figure 144e and 145b), which could be the Nb-Si-rich and Cr-Mn-Fe rich oxides confirmed by EDS (Figure 144f and 145c). However, there was almost no Nb oxides detected for the sample tested for 5000 h. For the smooth area of both samples, alumina and silica oxides are the main oxides, and a thimbleful of Cr-Mn oxides can also be observed (Figure 144c and 145f).

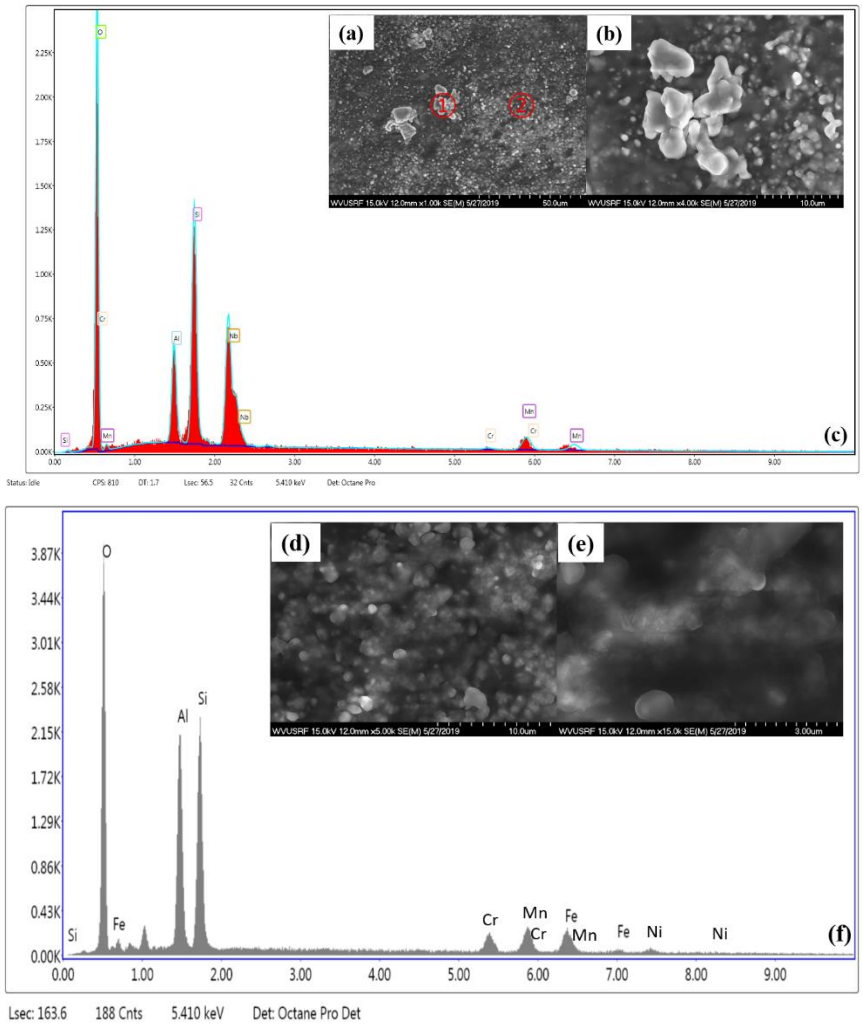

Figure 146 (a) Microstructural analysis of OC11 tested in 10% H_2O at 800 °C for 3500 hours, (b) is the high-magnification image of area ①, (c) is the corresponding EDS spectrum of (b), (d,e) are the high-magnification images of area ②, (f) is the corresponding EDS spectrum of (e).

Figure 146 and 147 demonstrate SEM surface morphologies of AFA OC11 after exposure to 10% H_2O at 800 ^oC for 4500h and 5000h. Oxide scale after 4500h exposure at 800 ^oC and 10% H_2O appeared faceted grains and some nodules on the majority of the sample surface (Figure 146a). At higher magnifications, these nodules are formed by the accumulation of small faceted grains (Figure 146e). With the increase of the exposure time, more nodules formed on the surface of the samples tested for 5000h exposure (Figure 147g). Moreover, the composition of these nodules is characterized to be enriched in Cr-Mn-Fe-Si oxides. (Figure 146f and 147i).

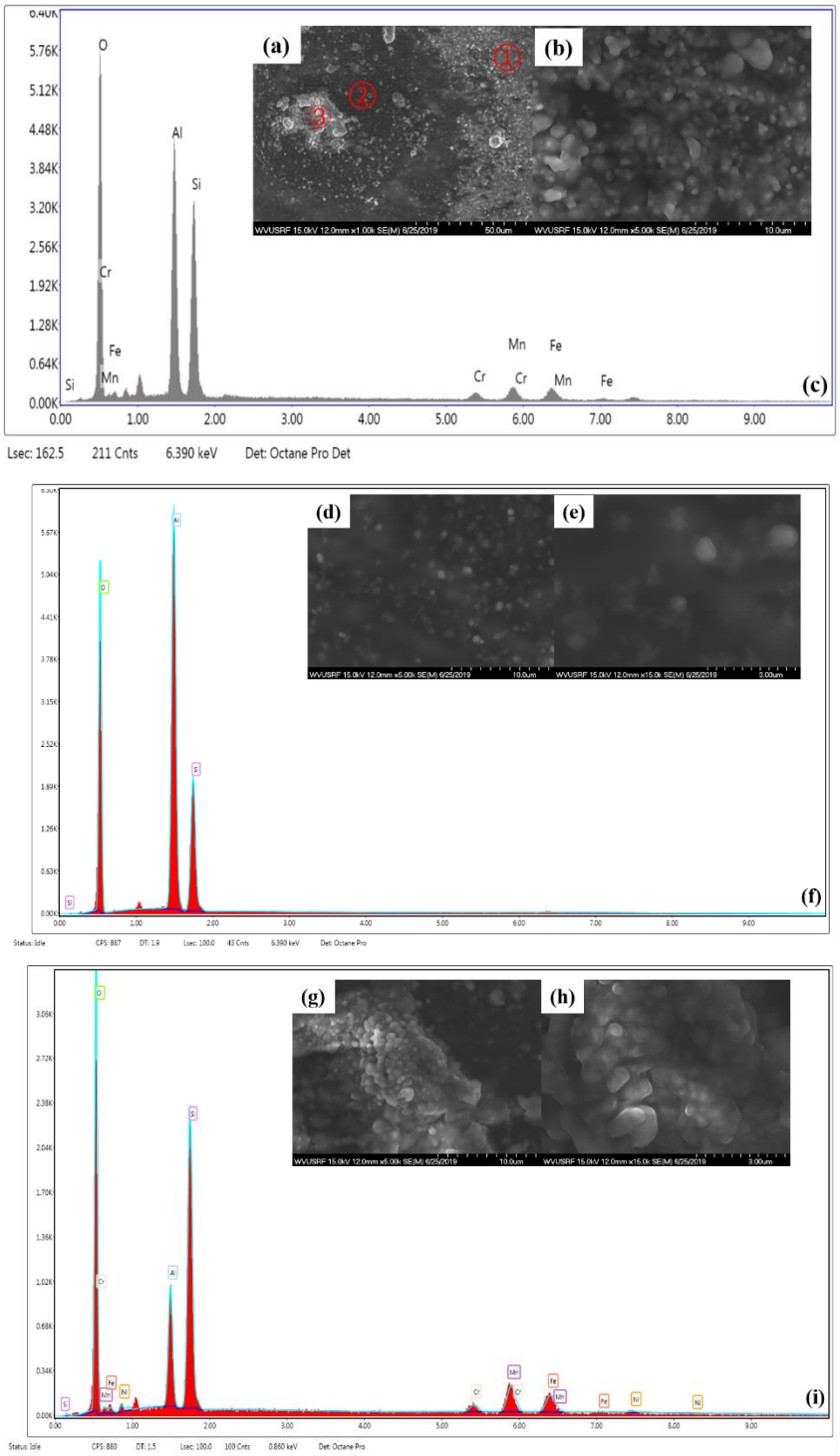

Figure 147 (a) Microstructural analysis of OC11 tested in 10% H_2O at 800 °C for 5000 hours, (b) the high-magnification image of area ①, (c) the corresponding EDS spectrum of (b), (d,e) the high-magnification images of area ②, (f) the corresponding EDS spectrum of (e), (g,h) the high-magnification images of area ③, (i) the corresponding EDS spectrum of (h).

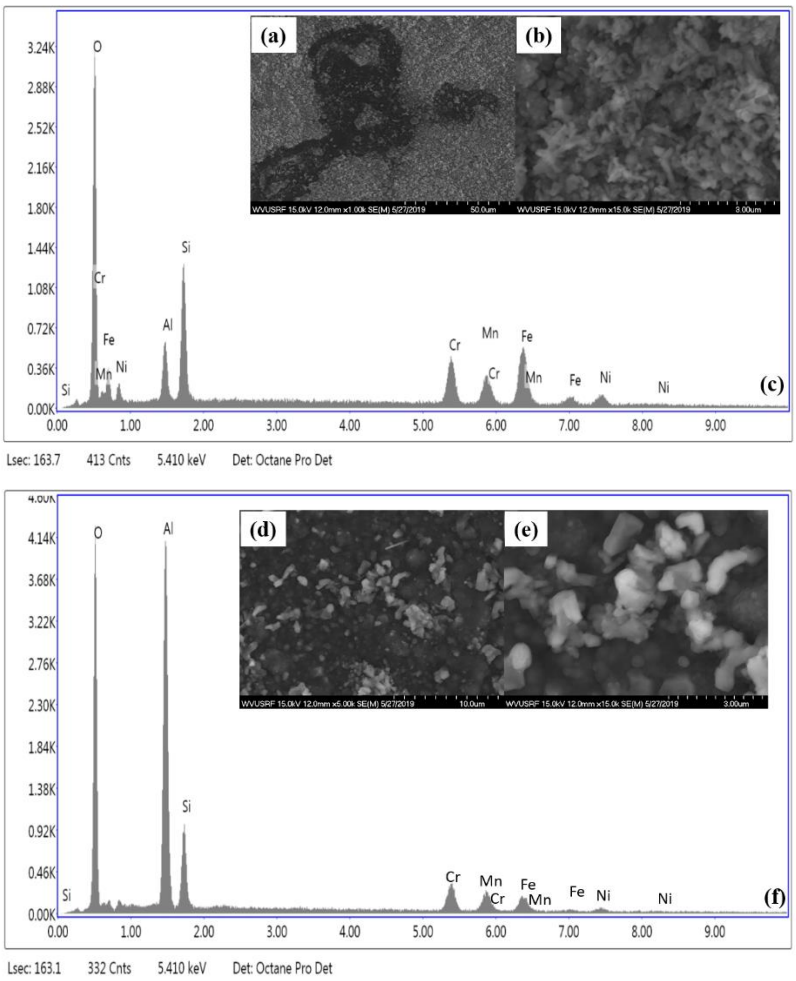

Figure 148 (a) Microstructural analysis of OC11LZ tested in 10% H_2O at 800 °C for 4500 hours, (b) is the high-magnification image of area ①, (c) is the corresponding EDS spectrum of (b), (d,e) are the high-magnification images of area ②, (f) is the corresponding EDS spectrum of (e).

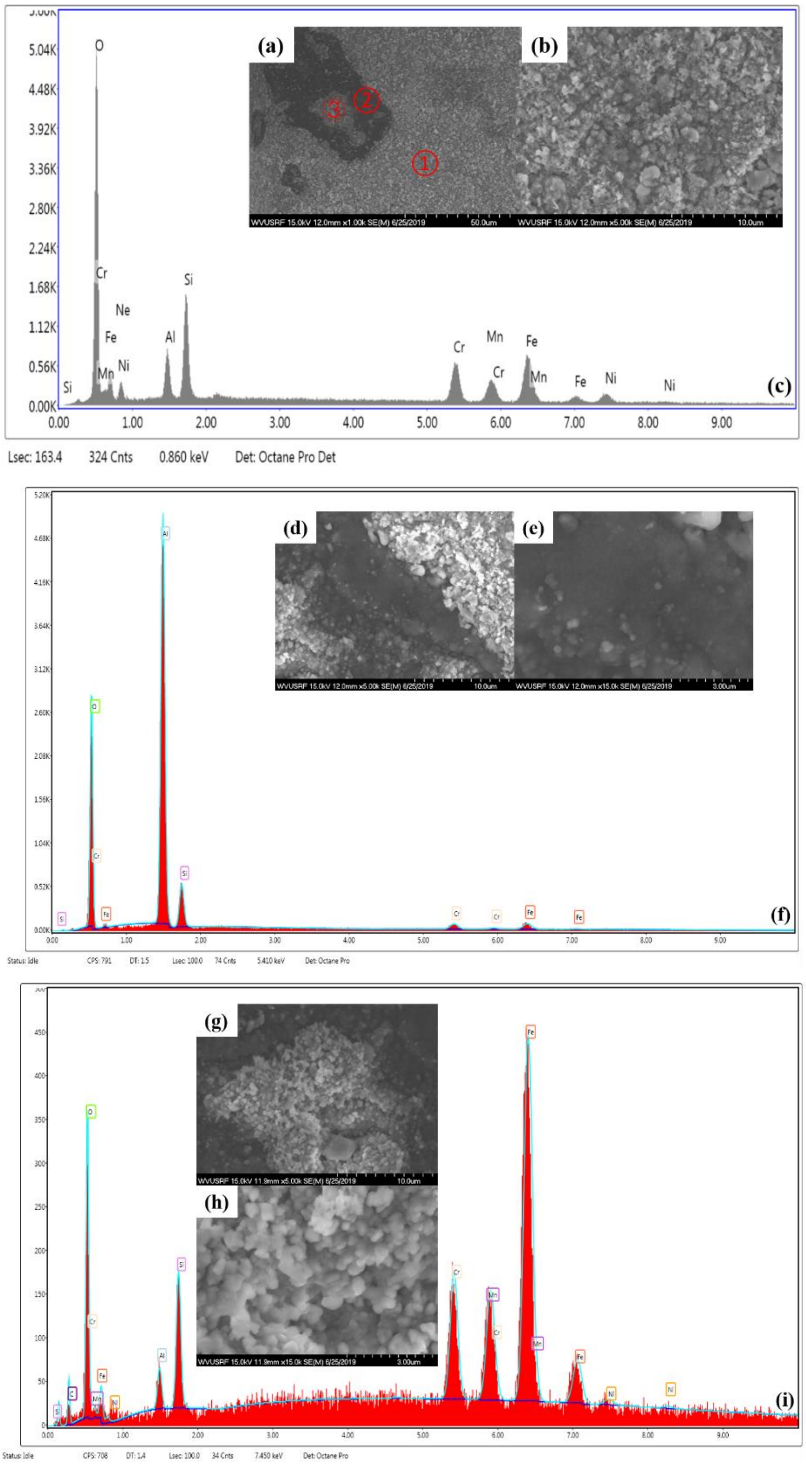

Figure 149 (a) Microstructural analysis of OC11LZ tested in 10% H_2O at 800 °C for 5000 hours, (b) the high-magnification image of area ①, (c) the corresponding EDS spectrum of (b), (d,e) the high-magnification images of area ②, (f) the corresponding EDS spectrum of (e), (g,h) the high-magnification images of area ③, (i) the corresponding EDS spectrum of (h).

Figure 148 and 149 show the SEM surface morphologies of AFA OC11LZ after exposure to 10% H_2O at 800 °C for 4500h and 5000h. For both samples, almost all of the areas are covered with nodules and some delamination areas can also be observed (Figure 148a and 149a), At higher magnification (Figure 148b and 149b), small amount of faceted grains (0.3 to 1 μm) underneath

the nodules can be observed. The morphology of the samples tested for 5000h is similar to that of 4500h. It can be observed from the EDX (Figure 148c and 149c) that Si-containing oxides, Al-rich oxides and Cr-Mn oxides are formed on the surface of the alloy. In addition, other areas were covered by faceted grains which can be identified as the Cr-Mn oxides and a small number of Si-containing oxides (Figure 148f and 149i).

Table 3 For 625, OC11, and OC11LZ alloy samples in 10% H_2O at 900 ^oC for 500 hours (1st cycle).

Analyte		**Cr**
Analysis Date		9/28/18
Method Detection Limit	**Matrix**	**0.009 mg/L**
C11 (625, 500 mL)	**water**	0.115
C12 (625, 500 mL)	**water**	0.58
C13 (625, 500 mL)	**water**	0.405
C14 (625, 500 mL)	**water**	0.415
C15 (625, 500 mL)	**water**	0.403
C16 (625, 505 mL)	**water**	0.35
C21 (OC11, 500 mL)	**water**	0.015
C22 (OC11, 500 mL)	**water**	0.017
C23 (OC11, 500 mL)	**water**	0.018
C24 (OC11, 500 mL)	**water**	0.016
C25 (OC11, 500 mL)	**water**	0.015
C26 (OC11, 715 mL)	**water**	0.014
C31 (OC11-LZ, 500 mL)	**water**	0.013
C32 (OC11-LZ, 500 mL)	**water**	0.038
C33 (OC11-LZ, 500 mL)	**water**	0.039
C34 (OC11-LZ, 500 mL)	**water**	0.033
C35 (OC11-LZ, 500 mL)	**water**	0.027
C36 (OC11-LZ, 598 mL)	**water**	0.039

$$R_{625,900\ oC} = \frac{(0.115 \times 0.5 + 0.58 \times 0.5 + 0.405 \times 0.5 + 0.415 \times 0.5 + 0.403 \times 0.5 + 0.35 \times 0.505)mg \times \frac{10^{-6}kg}{mg}}{21.8\ cm^2 \times \frac{10^{-4}\ m^2}{cm^2} \times 500\ h \times \frac{3600s}{h}}$$

$$= 2.89 \times 10^{-10} \frac{kg}{m^2 \cdot s}$$

$$R_{OC11,9000\ oC} = \frac{[(0.015 + 0.017 + 0.018 + 0.016 + 0.015) \times 0.5 + 0.014 \times 0.715)]mg \times \frac{10^{-6}kg}{mg}}{21.8\ cm^2 \times \frac{10^{-4}\ m^2}{cm^2} \times 500\ h \times \frac{3600s}{h}}$$

$$= 1.29 \times 10^{-11} \frac{kg}{m^2 \cdot s}$$

$$R_{OC11-LZ,900\ oC} = \frac{[(0.013 + 0.038 + 0.039 + 0.033 + 0.027) \times 0.5 + 0.039 \times 0.598]mg \times \frac{10^{-6}kg}{mg}}{21.8\ cm^2 \times \frac{10^{-4}\ m^2}{cm^2} \times 500\ h \times \frac{3600s}{h}}$$

$$= 2.51 \times 10^{-11} \frac{kg}{m^2 \cdot s}$$

Table 4 For 625, OC11, and OC11LZ alloy samples in 10% H_2O at 900 ^oC for 1000 hours(2nd cycle).

Analyte		**Cr**
Analysis Date		10/26/18
Method Detection Limit	**Matrix**	**0.009 mg/L**
C11 (625, 500 mL)	**water**	1.523
C12 (625, 500 mL)	**water**	0.90
C13 (625, 500 mL)	**water**	0.54
C14 (625, 500 mL)	**water**	1.377
C15 (625, 500 mL)	**water**	0.762
C16 (625, 586 mL)	**water**	1.349
C21 (OC11, 500 mL)	**water**	<0.009
C22 (OC11, 500 mL)	**water**	<0.009
C23 (OC11, 500 mL)	**water**	<0.009
C24 (OC11, 500 mL)	**water**	<0.009
C25 (OC11, 500 mL)	**water**	<0.009
C26 (OC11, 814 mL)	**water**	<0.009
C31 (OC11-LZ, 500 mL)	**water**	0.025
C32 (OC11-LZ, 500 mL)	**water**	0.021
C33 (OC11-LZ, 500 mL)	**water**	0.017
C34 (OC11-LZ, 500 mL)	**water**	0.023
C35 (OC11-LZ, 500 mL)	**water**	0.021
C36 (OC11-LZ, 710 mL)	**water**	0.021

$$R_{625,900\ oC}$$

$$= \frac{(1.523 \times 0.5 + 0.90 \times 0.5 + 0.54 \times 0.5 + 1.377 \times 0.5 + 0.762 \times 0.5 + 1.349 \times 0.505)mg \times \frac{10^{-6}kg}{mg}}{21.8\ cm^2 \times \frac{10^{-4}\ m^2}{cm^2} \times 500\ h \times \frac{3600s}{h}}$$

$$= 8.52 \times 10^{-10} \frac{kg}{m^2 \cdot s}$$

$$R_{OC11,900\ oC} < \frac{[(5 * 0.5 + 0.814) \times 0.009]mg \times \frac{10^{-6}kg}{mg}}{21.8\ cm^2 \times \frac{10^{-4}\ m^2}{cm^2} \times 500\ h \times \frac{3600s}{h}} = 7.6 \times 10^{-12} \frac{kg}{m^2 \cdot s}$$

$$R_{OC11-LZ,900\ oC} = \frac{[(0.025 + 0.021 + 0.017 + 0.023 + 0.021) \times 0.5 + 0.021 \times 0.71]mg \times \frac{10^{-6}kg}{mg}}{21.8\ cm^2 \times \frac{10^{-4}\ m^2}{cm^2} \times 500\ h \times \frac{3600s}{h}}$$

$$= 1.74 \times 10^{-11} \frac{kg}{m^2 \cdot s}$$

Table 5 For 625, OC11, and OC11LZ alloy samples in 10% H_2O at 900 °C for 1500 hours(3rd cycle).

Analyte		**Cr**
Analysis Date		11/14/18
Method Detection Limit	**Matrix**	**0.009 mg/L**
C11 (625, 500 mL)	**water**	0.117
C12 (625, 500 mL)	**water**	0.15
C13 (625, 500 mL)	**water**	0.143
C14 (625, 500 mL)	**water**	0.166
C15 (625, 832 mL)	**water**	0.169
C21 (OC11, 500 mL)	**water**	<0.009
C22 (OC11, 500 mL)	**water**	<0.009
C23 (OC11, 700 mL)	**water**	<0.009
C24 (OC11, 600 mL)	**water**	<0.009
C25 (OC11, 1144 mL)	**water**	0.009
C31 (OC11-LZ, 500 mL)	**water**	0.014
C32 (OC11-LZ, 500 mL)	**water**	0.014
C33 (OC11-LZ, 500 mL)	**water**	0.015
C34 (OC11-LZ, 500 mL)	**water**	0.015
C35 (OC11-LZ, 1136 mL)	**water**	0.021

$$R_{625,900\ oC}$$

$$= \frac{[(0.117 + 0.15 + 0.143 + 0.166) \times 0.5 + 0.169 \times 0.832)mg \times \frac{10^{-6}kg}{mg}}{21.8\ cm^2 \times \frac{10^{-4}\ m^2}{cm^2} \times 500\ h \times \frac{3600s}{h}} = 1.09 \times 10^{-10} \frac{kg}{m^2 \cdot s}$$

$$R_{OC11,900\ oC} < \frac{[(0.5 + 0.5 + 0.7 + 0.6 + 1.144) \times 0.009]mg \times \frac{10^{-6}kg}{mg}}{21.8\ cm^2 \times \frac{10^{-4}\ m^2}{cm^2} \times 500\ h \times \frac{3600s}{h}} = 7.9 \times 10^{-12} \frac{kg}{m^2 \cdot s}$$

$$R_{OC11-LZ,900\ oC} = \frac{[(0.014 + 0.014 + 0.015 + 0.015) \times 0.5 + 0.021 \times 1.136]mg \times \frac{10^{-6}kg}{mg}}{21.8\ cm^2 \times \frac{10^{-4}\ m^2}{cm^2} \times 500\ h \times \frac{3600s}{h}}$$

$$= 1.35 \times 10^{-11} \frac{kg}{m^2 \cdot s}$$

Table 6 For 625, OC11, and OC11LZ alloy samples in 10% H_2O at 900 °C for 2000 hours(4th cycle).

Analyte		**Cr**
Analysis Date		12/13/18
Method Detection Limit	**Matrix**	**0.009 mg/L**
C11 (625, 500 mL)	**water**	1.177
C12 (625, 300 mL)	**water**	0.70
C13 (625, 500 mL)	**water**	0.533
C14 (625, 500 mL)	**water**	0.364
C15 (625, 500 mL)	**water**	0.287
C16 (625, 564 mL)	**water**	7.28
C21 (OC11, 500 mL)	**water**	<0.009
C22 (OC11, 500 mL)	**water**	<0.009
C23 (OC11, 500 mL)	**water**	<0.009
C24 (OC11, 500 mL)	**water**	<0.009
C25 (OC11, 500 mL)	**water**	<0.009
C26 (OC11, 719 mL)	**water**	<0.009
C31 (OC11-LZ, 500 mL)	**water**	<0.009
C32 (OC11-LZ, 500 mL)	**water**	0.01
C33 (OC11-LZ, 500 mL)	**water**	0.015
C34 (OC11-LZ, 500 mL)	**water**	0.012
C35 (OC11-LZ, 500 mL)	**water**	0.017
C36 (OC11-LZ, 539 mL)	**water**	0.017

$$R_{625,900\ oC}$$

$$= \frac{(1.177 \times 0.5 + 0.70 \times 0.3 + 0.533 \times 0.5 + 0.364 \times 0.5 + 0.287 \times 0.5 + 7.28 \times 0.564)mg \times \frac{10^{-6}kg}{mg}}{21.8\ cm^2 \times \frac{10^{-4}\ m^2}{cm^2} \times 500\ h \times \frac{3600s}{h}} = 1.4 \times 10^{-9} \frac{kg}{m^2 \cdot s}$$

$$R_{OC11,900\ oC} < \frac{[(5 * 0.5 + 0.719) \times 0.009]mg \times \frac{10^{-6}kg}{mg}}{21.8\ cm^2 \times \frac{10^{-4}\ m^2}{cm^2} \times 500\ h \times \frac{3600s}{h}} = 7.38 \times 10^{-12} \frac{kg}{m^2 \cdot s}$$

$$R_{OC11-LZ,900\ oC} = \frac{[(0.009 + 0.01 + 0.015 + 0.012 + 0.017) \times 0.5 + 0.017 \times 0.539]mg \times \frac{10^{-6}kg}{mg}}{21.8\ cm^2 \times \frac{10^{-4}\ m^2}{cm^2} \times 500\ h \times \frac{3600s}{h}}$$

$$= 1.04 \times 10^{-11} \frac{kg}{m^2 \cdot s}$$

Table 7 For 625, OC11, and OC11LZ alloy samples in 10% H_2O at 900 °C for 2500 hours(5th cycle).

Analyte		**Cr**
Analysis Date		01/08/19
Method Detection Limit	**Matrix**	**0.009 mg/L**
C11 (625, 500 mL)	**water**	0.117
C12 (625, 300 mL)	**water**	0.305
C13 (625, 500 mL)	**water**	0.253
C14 (625, 500 mL)	**water**	0.26
C15 (625, 500 mL)	**water**	0.261
C16 (625, 748 mL)	**water**	0.976
C21 (OC11, 500 mL)	**water**	<0.009
C22 (OC11, 500 mL)	**water**	<0.009
C23 (OC11, 500 mL)	**water**	<0.009
C24 (OC11, 500 mL)	**water**	<0.009
C25 (OC11, 500 mL)	**water**	<0.009
C26 (OC11, 797 mL)	**water**	<0.009
C31 (OC11-LZ, 500 mL)	**water**	<0.009
C32 (OC11-LZ, 500 mL)	**water**	0.012
C33 (OC11-LZ, 500 mL)	**water**	0.013
C34 (OC11-LZ, 500 mL)	**water**	0.012
C35 (OC11-LZ, 500 mL)	**water**	0.017
C36 (OC11-LZ, 744 mL)	**water**	0.018

$$R_{625,900\ oC}$$

$$= \frac{(0.117 + 0.305 + 0.253 + 0.26 + 0.261) \times 0.5 + 0.748 \times 0.976)mg \times \frac{10^{-6}kg}{mg}}{21.8\ cm^2 \times \frac{10^{-4}\ m^2}{cm^2} \times 500\ h \times \frac{3600s}{h}} = 3.38 \times 10^{-10} \frac{kg}{m^2 \cdot s}$$

$$R_{OC11,900\ oC} < \frac{[(5 * 0.5 + 0.797) \times 0.009]mg \times \frac{10^{-6}kg}{mg}}{21.8\ cm^2 \times \frac{10^{-4}\ m^2}{cm^2} \times 500\ h \times \frac{3600s}{h}} = 7.56 \times 10^{-12} \frac{kg}{m^2 \cdot s}$$

$$R_{OC11-LZ,900\ oC} < \frac{[(0.009 + 0.012 + 0.013 + 0.012 + 0.017) \times 0.5 + 0.018 \times 0.744]mg \times \frac{10^{-6}kg}{mg}}{21.8\ cm^2 \times \frac{10^{-4}\ m^2}{cm^2} \times 500\ h \times \frac{3600s}{h}}$$

$$= 1.14 \times 10^{-11} \frac{kg}{m^2 \cdot s}$$

Table 8 For 625, OC11, and OC11LZ alloy samples in 10% H_2O at 900 °C for 3000 hours(6th cycle).

Analyte		**Cr**
Analysis Date		02/04/19
Method Detection Limit	**Matrix**	**0.009 mg/L**
C11 (625, 500 mL)	**water**	0.158
C12 (625, 500 mL)	**water**	0.185
C13 (625, 500 mL)	**water**	0.188
C14 (625, 1383 mL)	**water**	0.579
C21 (OC11, 500 mL)	**water**	<0.009
C22 (OC11, 500 mL)	**water**	<0.009
C23 (OC11, 500 mL)	**water**	<0.009
C24 (OC11, 1843 mL)	**water**	<0.009
C31 (OC11-LZ, 500 mL)	**water**	<0.009
C32 (OC11-LZ, 500 mL)	**water**	0.012
C33 (OC11-LZ, 500 mL)	**water**	0.013
C34 (OC11-LZ, 1526 mL)	**water**	0.017

$$R_{625,900\ oC}$$

$$= \frac{(0.158 + 0.185 + 0.188) \times 0.5 + 0.579 \times 1.383)mg \times \frac{10^{-6}kg}{mg}}{21.8\ cm^2 \times \frac{10^{-4}\ m^2}{cm^2} \times 500\ h \times \frac{3600s}{h}} = 2.72 \times 10^{-10}\ \frac{kg}{m^2 \cdot s}$$

$$R_{OC11,900\ oC} < \frac{[(3 * 0.5 + 1.843) \times 0.009]mg \times \frac{10^{-6}kg}{mg}}{21.8\ cm^2 \times \frac{10^{-4}\ m^2}{cm^2} \times 500\ h \times \frac{3600s}{h}} = 7.67 \times 10^{-12}\ \frac{kg}{m^2 \cdot s}$$

$$R_{OC11-LZ,900\ oC} < \frac{[(0.009 + 0.012 + 0.013) \times 0.5 + 0.017 \times 1.526]mg \times \frac{10^{-6}kg}{mg}}{21.8\ cm^2 \times \frac{10^{-4}\ m^2}{cm^2} \times 500\ h \times \frac{3600s}{h}} = 1.09 \times 10^{-11}\ \frac{kg}{m^2 \cdot s}$$

Table 9 For 625, OC11, and OC11LZ alloy samples in 10% H_2O at 900 °C for 3500 hours(7th cycle).

Analyte		**Cr**
Analysis Date		
Method Detection Limit	**Matrix**	**0.009 mg/L**
C11 (625, 2956 mL)	**water**	0.809
C21 (OC11, 3285 mL)	**water**	<0.009
C31 (OC11-LZ, 2843 mL)	**water**	0.024

$$R_{625,900\ oC}$$

$$= \frac{(0.809 \times 2.956)mg \times \frac{10^{-6}kg}{mg}}{21.8\ cm^2 \times \frac{10^{-4}\ m^2}{cm^2} \times 500\ h \times \frac{3600s}{h}} = 6.09 \times 10^{-10}\ \frac{kg}{m^2 \cdot s}$$

$$R_{OC11,900\ oC} < \frac{(3.285 \times 0.009\text{）}\ mg \times \frac{10^{-6}kg}{mg}}{21.8\ cm^2 \times \frac{10^{-4}\ m^2}{cm^2} \times 500\ h \times \frac{3600s}{h}} = 7.53 \times 10^{-12}\ \frac{kg}{m^2 \cdot s}$$

$$R_{OC11-LZ,900\ oC} = \frac{(2.843 \times 0.024)mg \times \frac{10^{-6}kg}{mg}}{21.8\ cm^2 \times \frac{10^{-4}\ m^2}{cm^2} \times 500\ h \times \frac{3600s}{h}} = 1.74 \times 10^{-11}\ \frac{kg}{m^2 \cdot s}$$

Table 10 For 625, OC11, and OC11LZ alloy samples in 10% H_2O at 900 °C for 4000 hours(8th cycle).

Analyte		**Cr**
Analysis Date		
Method Detection Limit	**Matrix**	**0.009 mg/L**
C11 (625, 3098 mL)	**water**	0.308
C21 (OC11, 3398 mL)	**water**	<0.009
C31 (OC11-LZ, 2528 mL)	**water**	0.011

$$R_{625,900\ oC}$$

$$= \frac{(0.309 \times 3.098)mg \times \frac{10^{-6}kg}{mg}}{21.8\ cm^2 \times \frac{10^{-4}\ m^2}{cm^2} \times 500\ h \times \frac{3600s}{h}} = 2.44 \times 10^{-10}\ \frac{kg}{m^2 \cdot s}$$

$$R_{OC11,900\ oC} < \frac{(3.398 \times 0.009\text{）}\ mg \times \frac{10^{-6}kg}{mg}}{21.8\ cm^2 \times \frac{10^{-4}\ m^2}{cm^2} \times 500\ h \times \frac{3600s}{h}} = 7.79 \times 10^{-12}\ \frac{kg}{m^2 \cdot s}$$

$$R_{OC11-LZ,900\ oC} = \frac{(2.528 \times 0.011)mg \times \frac{10^{-6}kg}{mg}}{21.8\ cm^2 \times \frac{10^{-4}\ m^2}{cm^2} \times 500\ h \times \frac{3600s}{h}} = 7.09 \times 10^{-12}\ \frac{kg}{m^2 \cdot s}$$

Table 11 For 625, OC11, and OC11LZ alloy samples in 10% H_2O at 900 °C for 4500 hours(9th cycle).

Analyte		**Cr**
Analysis Date		
Method Detection Limit	**Matrix**	**0.009 mg/L**
C11 (625, 3252 mL)	**water**	0.357
C21 (OC11, 3446 mL)	**water**	<0.009
C31 (OC11-LZ, 2273 mL)	**water**	0.082

$$R_{625,900\ oC}$$

$$= \frac{(0.357 \times 3.252)mg \times \frac{10^{-6}kg}{mg}}{21.8\ cm^2 \times \frac{10^{-4}\ m^2}{cm^2} \times 500\ h \times \frac{3600s}{h}} = 2.96 \times 10^{-10}\ \frac{kg}{m^2 \cdot s}$$

$$R_{OC11,900\ oC} < \frac{(3.446 \times 0.009\rangle\ mg \times \frac{10^{-6}kg}{mg}}{21.8\ cm^2 \times \frac{10^{-4}\ m^2}{cm^2} \times 500\ h \times \frac{3600s}{h}} = 7.90 \times 10^{-12}\ \frac{kg}{m^2 \cdot s}$$

$$R_{OC11-LZ,900\ oC} = \frac{(2.273 \times 0.082)mg \times \frac{10^{-6}kg}{mg}}{21.8\ cm^2 \times \frac{10^{-4}\ m^2}{cm^2} \times 500\ h \times \frac{3600s}{h}} = 4.75 \times 10^{-11}\ \frac{kg}{m^2 \cdot s}$$

Table 12 For 625, OC11, and OC11LZ alloy samples in 10% H_2O at 900 °C for 5000 hours(10^{th} cycle).

Analyte		**Cr**
Analysis Date		
Method Detection Limit	**Matrix**	**0.009 mg/L**
C11 (625, 3110 mL)	**water**	0.346
C21 (OC11, 3559 mL)	**water**	<0.009
C31 (OC11-LZ, 2148 mL)	**water**	<0.009

$$R_{625,900\ oC}$$

$$= \frac{(0.346 \times 3.110)mg \times \frac{10^{-6}kg}{mg}}{21.8\ cm^2 \times \frac{10^{-4}\ m^2}{cm^2} \times 500\ h \times \frac{3600s}{h}} = 2.74 \times 10^{-10}\ \frac{kg}{m^2 \cdot s}$$

$$R_{OC11,900\ oC} < \frac{(3.559 \times 0.009\rangle\ mg \times \frac{10^{-6}kg}{mg}}{21.8\ cm^2 \times \frac{10^{-4}\ m^2}{cm^2} \times 500\ h \times \frac{3600s}{h}} = 8.16 \times 10^{-12}\ \frac{kg}{m^2 \cdot s}$$

$$R_{OC11-LZ,900\ oC} < \frac{(2.148 \times 0.009)mg \times \frac{10^{-6}kg}{mg}}{21.8\ cm^2 \times \frac{10^{-4}\ m^2}{cm^2} \times 500\ h \times \frac{3600s}{h}} = 4.93 \times 10^{-12}\ \frac{kg}{m^2 \cdot s}$$

Table 13 For 310S, OC4, OC5, MOD OC11 and OC11LZ alloy samples in 10% H_2O at 800 ^oC for 500 hours(1st cycle).

Analyte		**Cr**
Analysis Date		11/14/18
Method Detection Limit	**Matrix**	**0.009 mg/L**
C11 (310S, 464 mL)	**water**	0.630
C21 (OC4, 500 mL)	**water**	<0.009
C22 (OC4, 361 mL)	**water**	0.012
C31 (OC5, 500 mL)	**water**	0.012
C32 (OC5, 387 mL)	**water**	0.013
C41 (MOD, 736 mL)	**water**	0.023
C51 (OC11, 600 mL)	**water**	0.022
C52 (OC11, 562 mL)	**water**	0.021
C61 (OC11LZ, 600 mL)	**water**	0.014
C62 (OC11LZ, 560 mL)	**water**	0.014

$$R_{310s,800\ oC} = \frac{(0.630 \times 0.464)mg \times \frac{10^{-6}kg}{mg}}{21.8\ cm^2 \times \frac{10^{-4}\ m^2}{cm^2} \times 500\ h \times \frac{3600s}{h}} = 7.45 \times 10^{-11} \frac{kg}{m^2 \cdot s}$$

$$R_{OC4,800\ oC} < \frac{(0.5 \times 0.009 + 0.012 \times 0.361)mg \times \frac{10^{-6}kg}{mg}}{21.8\ cm^2 \times \frac{10^{-4}\ m^2}{cm^2} \times 500\ h \times \frac{3600s}{h}} = 2.25 \times 10^{-12} \frac{kg}{m^2 \cdot s}$$

$$R_{OC5,800\ oC} = \frac{(0.012 \times 0.5 + 0.013 \times 0.387)mg \times \frac{10^{-6}kg}{mg}}{21.8\ cm^2 \times \frac{10^{-4}\ m^2}{cm^2} \times 500\ h \times \frac{3600s}{h}} = 2.8 \times 10^{-12} \frac{kg}{m^2 \cdot s}$$

$$R_{MOD,800\ oC} = \frac{(0.736 \times 0.023)mg \times \frac{10^{-6}kg}{mg}}{21.8\ cm^2 \times \frac{10^{-4}\ m^2}{cm^2} \times 500\ h \times \frac{3600s}{h}} = 4.31 \times 10^{-12} \frac{kg}{m^2 \cdot s}$$

$$R_{OC11,800\ oC} = \frac{(0.6 \times 0.022 + 0.562 \times 0.021)mg \times \frac{10^{-6}kg}{mg}}{21.8\ cm^2 \times \frac{10^{-4}\ m^2}{cm^2} \times 500\ h \times \frac{3600s}{h}} = 6.37 \times 10^{-12} \frac{kg}{m^2 \cdot s}$$

$$R_{OC11LZ,800\ oC} = \frac{(0.014 \times 0.6 + 0.014 \times 0.56)mg \times \frac{10^{-6}kg}{mg}}{21.8\ cm^2 \times \frac{10^{-4}\ m^2}{cm^2} \times 500\ h \times \frac{3600s}{h}} = 4.14 \times 10^{-12} \frac{kg}{m^2 \cdot s}$$

Table 14 For 310S, OC4, OC5, MOD OC11 and OC11LZ alloy samples in 10% H_2O at 800 ^oC for 1000 hours(2nd cycle).

Analyte		**Cr**
Analysis Date		11/14/18
Method Detection Limit	**Matrix**	**0.009 mg/L**
C11 (310S, 908 mL)	**water**	0.639
C21 (OC4, 500 mL)	**water**	<0.009
C22 (OC4, 1074 mL)	**water**	<0.009
C31 (OC5, 500 mL)	**water**	<0.009
C32 (OC5, 881 mL)	**water**	<0.009
C41 (MOD, 500 mL)	**water**	<0.009
C42 (MOD, 944 mL)	**water**	<0.009
C51 (OC11, 500 mL)	**water**	<0.009
C52 (OC11, 1041 mL)	**water**	0.028
C61 (OC11LZ, 500 mL)	**water**	<0.009
C62 (OC11LZ, 872 mL)	**water**	<0.009

$$R_{310s,800\ oC} = \frac{(0.639 \times 0.908)mg \times \frac{10^{-6}kg}{mg}}{21.8\ cm^2 \times \frac{10^{-4}\ m^2}{cm^2} \times 500\ h \times \frac{3600s}{h}} = 1.48 \times 10^{-10}\frac{kg}{m^2 \cdot s}$$

$$R_{OC4,800\ oC} < \frac{(0.5 \times 0.009 + 1.074 \times 0.009)mg \times \frac{10^{-6}kg}{mg}}{21.8\ cm^2 \times \frac{10^{-4}\ m^2}{cm^2} \times 500\ h \times \frac{3600s}{h}} = 3.61 \times 10^{-12}\frac{kg}{m^2 \cdot s}$$

$$R_{OC5,800\ oC} < \frac{(0.009 \times 1.381)mg \times \frac{10^{-6}kg}{mg}}{21.8\ cm^2 \times \frac{10^{-4}\ m^2}{cm^2} \times 500\ h \times \frac{3600s}{h}} = 3.17 \times 10^{-12}\frac{kg}{m^2 \cdot s}$$

$$R_{MOD,800\ oC} < \frac{(0.009 \times 1.444)mg \times \frac{10^{-6}kg}{mg}}{21.8\ cm^2 \times \frac{10^{-4}\ m^2}{cm^2} \times 500\ h \times \frac{3600s}{h}} = 3.31 \times 10^{-12}\frac{kg}{m^2 \cdot s}$$

$$R_{OC11,800\ oC} < \frac{(0.5 \times 0.009 + 1.014 \times 0.028)mg \times \frac{10^{-6}kg}{mg}}{21.8\ cm^2 \times \frac{10^{-4}\ m^2}{cm^2} \times 500\ h \times \frac{3600s}{h}} = 8.38 \times 10^{-12}\frac{kg}{m^2 \cdot s}$$

$$R_{OC11LZ,800\ oC} < \frac{(0.009 \times 1.372)mg \times \frac{10^{-6}kg}{mg}}{21.8\ cm^2 \times \frac{10^{-4}\ m^2}{cm^2} \times 500\ h \times \frac{3600s}{h}} = 3.15 \times 10^{-12}\frac{kg}{m^2 \cdot s}$$

Table 15 For 310S, OC4, OC5, MOD OC11 and OC11LZ alloy samples in 10% H_2O at 800 °C for 1500 hours(3rd cycle).

Analyte		**Cr**
Analysis Date		01/08/19
Method Detection Limit	**Matrix**	**0.009 mg/L**
C11 (310S, 500 mL)	**water**	0.324
C12 (310S, 939 mL)	**water**	0.569
C21 (OC4, 500 mL)	**water**	<0.009
C22 (OC4, 1002 mL)	**water**	<0.009
C31 (OC5, 500 mL)	**water**	<0.009
C32 (OC5, 827 mL)	**water**	<0.009
C41 (MOD, 500 mL)	**water**	<0.009
C42 (MOD, 910 mL)	**water**	<0.009
C51 (OC11, 500 mL)	**water**	<0.009
C52 (OC11, 1095 mL)	**water**	<0.009
C61 (OC11LZ, 500 mL)	**water**	<0.009
C62 (OC11LZ, 1037 mL)	**water**	<0.009

$$R_{310s,800\ oC} = \frac{(0.324 \times 0.5 + 0.569 \times 0.939)mg \times \frac{10^{-6}kg}{mg}}{21.8\ cm^2 \times \frac{10^{-4}\ m^2}{cm^2} \times 500\ h \times \frac{3600s}{h}} = 1.77 \times 10^{-10}\ \frac{kg}{m^2 \cdot s}$$

$$R_{OC4,800\ oC} < \frac{(0.5 \times 0.009 + 1.002 \times 0.009)mg \times \frac{10^{-6}kg}{mg}}{21.8\ cm^2 \times \frac{10^{-4}\ m^2}{cm^2} \times 500\ h \times \frac{3600s}{h}} = 3.44 \times 10^{-12}\ \frac{kg}{m^2 \cdot s}$$

$$R_{OC5,800\ oC} < \frac{(0.009 \times 1.327)mg \times \frac{10^{-6}kg}{mg}}{21.8\ cm^2 \times \frac{10^{-4}\ m^2}{cm^2} \times 500\ h \times \frac{3600s}{h}} = 3.04 \times 10^{-12}\ \frac{kg}{m^2 \cdot s}$$

$$R_{MOD,800\ oC} < \frac{(0.009 \times 1.410)mg \times \frac{10^{-6}kg}{mg}}{21.8\ cm^2 \times \frac{10^{-4}\ m^2}{cm^2} \times 500\ h \times \frac{3600s}{h}} = 3.23 \times 10^{-12}\ \frac{kg}{m^2 \cdot s}$$

$$R_{OC11,800\ oC} < \frac{(1.595 \times 0.009)mg \times \frac{10^{-6}kg}{mg}}{21.8\ cm^2 \times \frac{10^{-4}\ m^2}{cm^2} \times 500\ h \times \frac{3600s}{h}} = 3.66 \times 10^{-12}\ \frac{kg}{m^2 \cdot s}$$

$$R_{OC11LZ,800\ oC} < \frac{(0.009 \times 1.537)mg \times \frac{10^{-6}kg}{mg}}{21.8\ cm^2 \times \frac{10^{-4}\ m^2}{cm^2} \times 500\ h \times \frac{3600s}{h}} = 3.53 \times 10^{-12}\ \frac{kg}{m^2 \cdot s}$$

Table 16 For 310S, OC4, OC5, MOD OC11 and OC11LZ alloy samples in 10% H_2O at 800 ^oC for 1500 hours(4^{th} cycle).

Analyte		**Cr**
Analysis Date		02/04/19
Method Detection Limit	**Matrix**	**0.009 mg/L**
C11 (310S, 1356 mL)	**water**	0.419
C21 (OC4, 1670 mL)	**water**	<0.009
C31 (OC5, 1295 mL)	**water**	<0.009
C41 (MOD, 1238mL)	**water**	<0.009
C51 (OC11, 1413 mL)	**water**	<0.009
C61 (OC11LZ, 1413 mL)	**water**	<0.009

$$R_{310s,800\ oC} = \frac{(0.419 \times 1.356)mg \times \frac{10^{-6}kg}{mg}}{21.8\ cm^2 \times \frac{10^{-4}\ m^2}{cm^2} \times 500\ h \times \frac{3600s}{h}} = 1.45 \times 10^{-10}\frac{kg}{m^2 \cdot s}$$

$$R_{OC4,800\ oC} < \frac{(1.67 \times 0.009)mg \times \frac{10^{-6}kg}{mg}}{21.8\ cm^2 \times \frac{10^{-4}\ m^2}{cm^2} \times 500\ h \times \frac{3600s}{h}} = 3.83 \times 10^{-12}\frac{kg}{m^2 \cdot s}$$

$$R_{OC5,800\ oC} < \frac{(0.009 \times 1.295)mg \times \frac{10^{-6}kg}{mg}}{21.8\ cm^2 \times \frac{10^{-4}\ m^2}{cm^2} \times 500\ h \times \frac{3600s}{h}} = 2.98 \times 10^{-12}\frac{kg}{m^2 \cdot s}$$

$$R_{MOD,800\ oC} < \frac{(0.009 \times 1.238)mg \times \frac{10^{-6}kg}{mg}}{21.8\ cm^2 \times \frac{10^{-4}\ m^2}{cm^2} \times 500\ h \times \frac{3600s}{h}} = 2.84 \times 10^{-12}\frac{kg}{m^2 \cdot s}$$

$$R_{OC11,800\ oC} < \frac{(1.413 \times 0.009)mg \times \frac{10^{-6}kg}{mg}}{21.8\ cm^2 \times \frac{10^{-4}\ m^2}{cm^2} \times 500\ h \times \frac{3600s}{h}} = 3.24 \times 10^{-12}\frac{kg}{m^2 \cdot s}$$

$$R_{OC11LZ,800\ oC} < \frac{(0.009 \times 1.413)mg \times \frac{10^{-6}kg}{mg}}{21.8\ cm^2 \times \frac{10^{-4}\ m^2}{cm^2} \times 500\ h \times \frac{3600s}{h}} = 3.24 \times 10^{-12}\frac{kg}{m^2 \cdot s}$$

Table 17 For 310S, OC4, OC5, MOD OC11 and OC11LZ alloy samples in 10% H_2O at 800 ^oC for 2500 hours(5^{th} cycle).

Analyte		**Cr**
Analysis Date		
Method Detection Limit	**Matrix**	**0.009 mg/L**
C11 (310S, 1410 mL)	**water**	0.422
C21 (OC4, 1600 mL)	**water**	<0.009
C31 (OC5, 1373 mL)	**water**	<0.009
C41 (MOD, 1381mL)	**water**	<0.009
C51 (OC11, 1285 mL)	**water**	<0.009
C61 (OC11LZ, 1482 mL)	**water**	<0.009

$$R_{310s,800\ oC} = \frac{(0.422 \times 1.41)mg \times \frac{10^{-6}kg}{mg}}{21.8\ cm^2 \times \frac{10^{-4}\ m^2}{cm^2} \times 500\ h \times \frac{3600s}{h}} = 1.52 \times 10^{-10}\frac{kg}{m^2 \cdot s}$$

$$R_{OC4,800\ oC} < \frac{(1.6 \times 0.009)mg \times \frac{10^{-6}kg}{mg}}{21.8\ cm^2 \times \frac{10^{-4}\ m^2}{cm^2} \times 500\ h \times \frac{3600s}{h}} = 3.67 \times 10^{-12}\frac{kg}{m^2 \cdot s}$$

$$R_{OC5,800\ oC} < \frac{(0.009 \times 1.373)mg \times \frac{10^{-6}kg}{mg}}{21.8\ cm^2 \times \frac{10^{-4}\ m^2}{cm^2} \times 500\ h \times \frac{3600s}{h}} = 3.15 \times 10^{-12}\frac{kg}{m^2 \cdot s}$$

$$R_{MOD,800\ oC} < \frac{(0.009 \times 1.381)mg \times \frac{10^{-6}kg}{mg}}{21.8\ cm^2 \times \frac{10^{-4}\ m^2}{cm^2} \times 500\ h \times \frac{3600s}{h}} = 3.17 \times 10^{-12}\frac{kg}{m^2 \cdot s}$$

$$R_{OC11,800\ oC} < \frac{(1.285 \times 0.009)mg \times \frac{10^{-6}kg}{mg}}{21.8\ cm^2 \times \frac{10^{-4}\ m^2}{cm^2} \times 500\ h \times \frac{3600s}{h}} = 2.95 \times 10^{-12}\frac{kg}{m^2 \cdot s}$$

$$R_{OC11LZ,800\ oC} < \frac{(0.009 \times 1.482)mg \times \frac{10^{-6}kg}{mg}}{21.8\ cm^2 \times \frac{10^{-4}\ m^2}{cm^2} \times 500\ h \times \frac{3600s}{h}} = 3.40 \times 10^{-12}\frac{kg}{m^2 \cdot s}$$

Table 18 For 310S, OC4, OC5, MOD OC11 and OC11LZ alloy samples in 10% H_2O at 800 ^oC for 3000 hours(6^{th} cycle).

Analyte		**Cr**
Analysis Date		
Method Detection Limit	**Matrix**	**0.009 mg/L**
C11 (310S, 1371 mL)	**water**	0.282
C21 (OC4, 1627 mL)	**water**	<0.009
C31 (OC5, 1330 mL)	**water**	<0.009
C41 (MOD, 1407mL)	**water**	<0.009
C51 (OC11, 1373 mL)	**water**	<0.009
C61 (OC11LZ, 1462 mL)	**water**	<0.009

$$R_{310s,800\ oC} = \frac{(0.282 \times 1.371)mg \times \frac{10^{-6}kg}{mg}}{21.8\ cm^2 \times \frac{10^{-4}\ m^2}{cm^2} \times 500\ h \times \frac{3600s}{h}} = 9.85 \times 10^{-11}\frac{kg}{m^2 \cdot s}$$

$$R_{OC4,800\ oC} < \frac{(1.627 \times 0.009)mg \times \frac{10^{-6}kg}{mg}}{21.8\ cm^2 \times \frac{10^{-4}\ m^2}{cm^2} \times 500\ h \times \frac{3600s}{h}} = 3.73 \times 10^{-12}\frac{kg}{m^2 \cdot s}$$

$$R_{OC5,800\ oC} < \frac{(0.009 \times 1.33)mg \times \frac{10^{-6}kg}{mg}}{21.8\ cm^2 \times \frac{10^{-4}\ m^2}{cm^2} \times 500\ h \times \frac{3600s}{h}} = 3.05 \times 10^{-12}\frac{kg}{m^2 \cdot s}$$

$$R_{MOD,800\ oC} < \frac{(0.009 \times 1.407)mg \times \frac{10^{-6}kg}{mg}}{21.8\ cm^2 \times \frac{10^{-4}\ m^2}{cm^2} \times 500\ h \times \frac{3600s}{h}} = 3.23 \times 10^{-12}\frac{kg}{m^2 \cdot s}$$

$$R_{OC11,800\ oC} < \frac{(1.373 \times 0.009)mg \times \frac{10^{-6}kg}{mg}}{21.8\ cm^2 \times \frac{10^{-4}\ m^2}{cm^2} \times 500\ h \times \frac{3600s}{h}} = 3.15 \times 10^{-12}\frac{kg}{m^2 \cdot s}$$

$$R_{OC11LZ,800\ oC} < \frac{(0.009 \times 1.462)mg \times \frac{10^{-6}kg}{mg}}{21.8\ cm^2 \times \frac{10^{-4}\ m^2}{cm^2} \times 500\ h \times \frac{3600s}{h}} = 3.35 \times 10^{-12}\frac{kg}{m^2 \cdot s}$$

Table 19 For 310S, OC4, OC5, MOD OC11 and OC11LZ alloy samples in 10% H_2O at 800 ^oC for 3500 hours(7^{th} cycle).

Analyte		**Cr**
Analysis Date		
Method Detection Limit	**Matrix**	**0.009 mg/L**
C11 (310S, 1293 mL)	**water**	0.297
C21 (OC4, 1626 mL)	**water**	<0.009
C31 (OC5, 1308 mL)	**water**	<0.009
C41 (MOD, 1447mL)	**water**	<0.009
C51 (OC11, 1205 mL)	**water**	<0.009
C61 (OC11LZ, 1271 mL)	**water**	<0.009

$$R_{310s,800\ oC} = \frac{(0.297 \times 1.293)mg \times \frac{10^{-6}kg}{mg}}{21.8\ cm^2 \times \frac{10^{-4}\ m^2}{cm^2} \times 500\ h \times \frac{3600s}{h}} = 9.79 \times 10^{-11}\frac{kg}{m^2 \cdot s}$$

$$R_{OC4,800\ oC} < \frac{(1.626 \times 0.009)mg \times \frac{10^{-6}kg}{mg}}{21.8\ cm^2 \times \frac{10^{-4}\ m^2}{cm^2} \times 500\ h \times \frac{3600s}{h}} = 3.73 \times 10^{-12}\frac{kg}{m^2 \cdot s}$$

$$R_{OC5,800\ oC} < \frac{(0.009 \times 1.308)mg \times \frac{10^{-6}kg}{mg}}{21.8\ cm^2 \times \frac{10^{-4}\ m^2}{cm^2} \times 500\ h \times \frac{3600s}{h}} = 3.00 \times 10^{-12}\frac{kg}{m^2 \cdot s}$$

$$R_{MOD,800\ oC} < \frac{(0.009 \times 1.447)mg \times \frac{10^{-6}kg}{mg}}{21.8\ cm^2 \times \frac{10^{-4}\ m^2}{cm^2} \times 500\ h \times \frac{3600s}{h}} = 3.32 \times 10^{-12}\frac{kg}{m^2 \cdot s}$$

$$R_{OC11,800\ oC} < \frac{(1.205 \times 0.009)mg \times \frac{10^{-6}kg}{mg}}{21.8\ cm^2 \times \frac{10^{-4}\ m^2}{cm^2} \times 500\ h \times \frac{3600s}{h}} = 2.76 \times 10^{-12}\frac{kg}{m^2 \cdot s}$$

$$R_{OC11LZ,800\ oC} < \frac{(0.009 \times 1.271)mg \times \frac{10^{-6}kg}{mg}}{21.8\ cm^2 \times \frac{10^{-4}\ m^2}{cm^2} \times 500\ h \times \frac{3600s}{h}} = 2.92 \times 10^{-12}\frac{kg}{m^2 \cdot s}$$

Table 20 For 310S, OC4, OC5, MOD OC11 and OC11LZ alloy samples in 10% H_2O at 800 ^oC for 4000 hours(8^{th} cycle).

Analyte		**Cr**
Analysis Date		
Method Detection Limit	**Matrix**	**0.009 mg/L**
C11 (310S, 1365 mL)	**water**	0.238
C21 (OC4, 1626 mL)	**water**	<0.009
C31 (OC5, 1347 mL)	**water**	<0.009
C41 (MOD, 1415mL)	**water**	<0.009
C51 (OC11, 1327 mL)	**water**	<0.009
C61 (OC11LZ, 1415 mL)	**water**	<0.009

$$R_{310s,800\ oC} = \frac{(0.238 \times 1.365)mg \times \frac{10^{-6}kg}{mg}}{21.8\ cm^2 \times \frac{10^{-4}\ m^2}{cm^2} \times 500\ h \times \frac{3600s}{h}} = 8.28 \times 10^{-11}\frac{kg}{m^2 \cdot s}$$

$$R_{OC4,800\ oC} < \frac{(1.626 \times 0.009)mg \times \frac{10^{-6}kg}{mg}}{21.8\ cm^2 \times \frac{10^{-4}\ m^2}{cm^2} \times 500\ h \times \frac{3600s}{h}} = 3.73 \times 10^{-12}\frac{kg}{m^2 \cdot s}$$

$$R_{OC5,800\ oC} < \frac{(0.009 \times 1.347)mg \times \frac{10^{-6}kg}{mg}}{21.8\ cm^2 \times \frac{10^{-4}\ m^2}{cm^2} \times 500\ h \times \frac{3600s}{h}} = 3.09 \times 10^{-12}\frac{kg}{m^2 \cdot s}$$

$$R_{MOD,800\ oC} < \frac{(0.009 \times 1.415)mg \times \frac{10^{-6}kg}{mg}}{21.8\ cm^2 \times \frac{10^{-4}\ m^2}{cm^2} \times 500\ h \times \frac{3600s}{h}} = 3.25 \times 10^{-12}\frac{kg}{m^2 \cdot s}$$

$$R_{OC11,800\ oC} < \frac{(1.327 \times 0.009)mg \times \frac{10^{-6}kg}{mg}}{21.8\ cm^2 \times \frac{10^{-4}\ m^2}{cm^2} \times 500\ h \times \frac{3600s}{h}} = 3.04 \times 10^{-12}\frac{kg}{m^2 \cdot s}$$

$$R_{OC11LZ,800\ oC} < \frac{(0.009 \times 1.415)mg \times \frac{10^{-6}kg}{mg}}{21.8\ cm^2 \times \frac{10^{-4}\ m^2}{cm^2} \times 500\ h \times \frac{3600s}{h}} = 3.25 \times 10^{-12}\frac{kg}{m^2 \cdot s}$$

Table 21 For 310S, OC4, OC5, MOD OC11 and OC11LZ alloy samples in 10% H_2O at 800 ^oC for 4500 hours(9^{th} cycle).

Analyte		**Cr**
Analysis Date		
Method Detection Limit	**Matrix**	**0.009 mg/L**
C11 (310S, 1350 mL)	**water**	0.131
C21 (OC4, 1551mL)	**water**	<0.009
C31 (OC5, 1410 mL)	**water**	<0.009
C41 (MOD, 1451mL)	**water**	<0.009
C51 (OC11, 1412 mL)	**water**	<0.009
C61 (OC11LZ, 1495 mL)	**water**	<0.009

$$R_{310s,800\ oC} = \frac{(0.131 \times 1.35)mg \times \frac{10^{-6}kg}{mg}}{21.8\ cm^2 \times \frac{10^{-4}\ m^2}{cm^2} \times 500\ h \times \frac{3600s}{h}} = 4.5 \times 10^{-11}\frac{kg}{m^2 \cdot s}$$

$$R_{OC4,800\ oC} < \frac{(1.551 \times 0.009)mg \times \frac{10^{-6}kg}{mg}}{21.8\ cm^2 \times \frac{10^{-4}\ m^2}{cm^2} \times 500\ h \times \frac{3600s}{h}} = 3.56 \times 10^{-12}\frac{kg}{m^2 \cdot s}$$

$$R_{OC5,800\ oC} < \frac{(0.009 \times 1.41)mg \times \frac{10^{-6}kg}{mg}}{21.8\ cm^2 \times \frac{10^{-4}\ m^2}{cm^2} \times 500\ h \times \frac{3600s}{h}} = 3.23 \times 10^{-12}\frac{kg}{m^2 \cdot s}$$

$$R_{MOD,800\ oC} < \frac{(0.009 \times 1.415)mg \times \frac{10^{-6}kg}{mg}}{21.8\ cm^2 \times \frac{10^{-4}\ m^2}{cm^2} \times 500\ h \times \frac{3600s}{h}} = 3.33 \times 10^{-12}\frac{kg}{m^2 \cdot s}$$

$$R_{OC11,800\ oC} < \frac{(1.327 \times 0.009)mg \times \frac{10^{-6}kg}{mg}}{21.8\ cm^2 \times \frac{10^{-4}\ m^2}{cm^2} \times 500\ h \times \frac{3600s}{h}} = 3.24 \times 10^{-12}\frac{kg}{m^2 \cdot s}$$

$$R_{OC11LZ,800\ oC} < \frac{(0.009 \times 1.415)mg \times \frac{10^{-6}kg}{mg}}{21.8\ cm^2 \times \frac{10^{-4}\ m^2}{cm^2} \times 500\ h \times \frac{3600s}{h}} = 3.43 \times 10^{-12}\frac{kg}{m^2 \cdot s}$$

Table 22 For 310S, OC4, OC5, MOD OC11 and OC11LZ alloy samples in 10% H_2O at 800 ^oC for 5000 hours(10^{th} cycle).

Analyte		**Cr**
Analysis Date		
Method Detection Limit	**Matrix**	**0.002 mg/L**
C11 (310S, 1324 mL)	**water**	0.124
C21 (OC4, 1503mL)	**water**	<0.002
C31 (OC5, 1377 mL)	**water**	<0.002
C41 (MOD, 1368mL)	**water**	<0.002
C51 (OC11, 1615 mL)	**water**	<0.002
C61 (OC11LZ, 1502 mL)	**water**	<0.002

$$R_{310s,800\ oC} = \frac{(0.124 \times 1.324)mg \times \frac{10^{-6}kg}{mg}}{21.8\ cm^2 \times \frac{10^{-4}\ m^2}{cm^2} \times 500\ h \times \frac{3600s}{h}} = 4.18 \times 10^{-11} \frac{kg}{m^2 \cdot s}$$

$$R_{OC4,800\ oC} < \frac{(1.503 \times 0.002)mg \times \frac{10^{-6}kg}{mg}}{21.8\ cm^2 \times \frac{10^{-4}\ m^2}{cm^2} \times 500\ h \times \frac{3600s}{h}} = 7.66 \times 10^{-13} \frac{kg}{m^2 \cdot s}$$

$$R_{OC5,800\ oC} < \frac{(0.002 \times 1.377)mg \times \frac{10^{-6}kg}{mg}}{21.8\ cm^2 \times \frac{10^{-4}\ m^2}{cm^2} \times 500\ h \times \frac{3600s}{h}} = 7.02 \times 10^{-13} \frac{kg}{m^2 \cdot s}$$

$$R_{MOD,800\ oC} < \frac{(0.002 \times 1.368)mg \times \frac{10^{-6}kg}{mg}}{21.8\ cm^2 \times \frac{10^{-4}\ m^2}{cm^2} \times 500\ h \times \frac{3600s}{h}} = 6.97 \times 10^{-13} \frac{kg}{m^2 \cdot s}$$

$$R_{OC11,800\ oC} < \frac{(1.615 \times 0.002)mg \times \frac{10^{-6}kg}{mg}}{21.8\ cm^2 \times \frac{10^{-4}\ m^2}{cm^2} \times 500\ h \times \frac{3600s}{h}} = 8.23 \times 10^{-13} \frac{kg}{m^2 \cdot s}$$

$$R_{OC11LZ,800\ oC} < \frac{(0.002 \times 1.502)mg \times \frac{10^{-6}kg}{mg}}{21.8\ cm^2 \times \frac{10^{-4}\ m^2}{cm^2} \times 500\ h \times \frac{3600s}{h}} = 7.66 \times 10^{-13} \frac{kg}{m^2 \cdot s}$$

As a summary, the Cr evaporation rates for all the tested samples at the corresponding environment and listed in **Table 23**.

Table 23 500 hours (10 cycle) Cr release measurements in air + 10% H_2O to date (Unit: kg/(m^2·s)).

Cycle		**1**	**2**	**3**	**4**	**5**	**6**	**7**	**8**	**9**	**10**
800 °C	310S	7.45 $\times 10^{-11}$	1.48 $\times 10^{-10}$	1.77 $\times 10^{-10}$	1.45 $\times 10^{-10}$	1.52 $\times 10^{-10}$	9.85 $\times 10^{-11}$	9.79 $\times 10^{-11}$	8.28 $\times 10^{-11}$	4.5 $\times 10^{-11}$	4.18 $\times 10^{-11}$
	OC4	<2.25 $\times 10^{-12}$	<3.61 $\times 10^{-12}$	<3.44 $\times 10^{-12}$	<3.83 $\times 10^{-12}$	<3.67 $\times 10^{-12}$	<3.73 $\times 10^{-12}$	<3.73 $\times 10^{-12}$	<3.73 $\times 10^{-12}$	<3.56 $\times 10^{-12}$	<7.66 $\times 10^{-13}$
	OC5	2.8 $\times 10^{-12}$	<3.17 $\times 10^{-12}$	<3.04 $\times 10^{-12}$	<2.98 $\times 10^{-12}$	<3.15 $\times 10^{-12}$	<3.05 $\times 10^{-12}$	<3.00 $\times 10^{-12}$	<3.09 $\times 10^{-12}$	<3.23 $\times 10^{-12}$	<7.02 $\times 10^{-13}$
	MOD	4.31 $\times 10^{-12}$	<3.31 $\times 10^{-12}$	<3.23 $\times 10^{-12}$	<2.84 $\times 10^{-12}$	<3.17 $\times 10^{-12}$	<3.23 $\times 10^{-12}$	<3.32 $\times 10^{-12}$	<3.25 $\times 10^{-12}$	<3.33 $\times 10^{-12}$	<6.97 $\times 10^{-13}$
	OC11	6.37 $\times 10^{-12}$	<8.38 $\times 10^{-12}$	<3.66 $\times 10^{-12}$	<3.24 $\times 10^{-12}$	<2.95 $\times 10^{-12}$	<3.15 $\times 10^{-12}$	<2.76 $\times 10^{-12}$	<3.04 $\times 10^{-12}$	<3.24 $\times 10^{-12}$	<8.23 $\times 10^{-13}$
	OC11LZ	4.14 $\times 10^{-12}$	<3.15 $\times 10^{-12}$	<3.53 $\times 10^{-12}$	<3.24 $\times 10^{-12}$	<3.40 $\times 10^{-12}$	<3.35 $\times 10^{-12}$	<2.92 $\times 10^{-12}$	<3.25 $\times 10^{-12}$	<3.43 $\times 10^{-12}$	<7.66 $\times 10^{-13}$
900 °C	625	2.89 $\times 10^{-10}$	8.52 $\times 10^{-10}$	1.09 $\times 10^{-10}$	1.4 $\times 10^{-9}$	3.38 $\times 10^{-10}$	2.72 $\times 10^{-10}$	6.09 $\times 10^{-10}$	2.44 $\times 10^{-10}$	2.96 $\times 10^{-10}$	2.74 $\times 10^{-10}$
	OC11	1.29 $\times 10^{-11}$	<7.6 $\times 10^{-12}$	<7.9 $\times 10^{-12}$	<7.38 $\times 10^{-12}$	<7.56 $\times 10^{-12}$	<7.67 $\times 10^{-12}$	<7.53 $\times 10^{-12}$	<7.79 $\times 10^{-12}$	<7.90 $\times 10^{-12}$	<8.16 $\times 10^{-12}$
	OC11LZ	2.51 $\times 10^{-11}$	1.74 $\times 10^{-11}$	1.35 $\times 10^{-11}$	1.04 $\times 10^{-11}$	<1.14 $\times 10^{-11}$	<1.09 $\times 10^{-11}$	1.74 $\times 10^{-11}$	7.09 $\times 10^{-12}$	4.75 $\times 10^{-11}$	<4.93 $\times 10^{-12}$

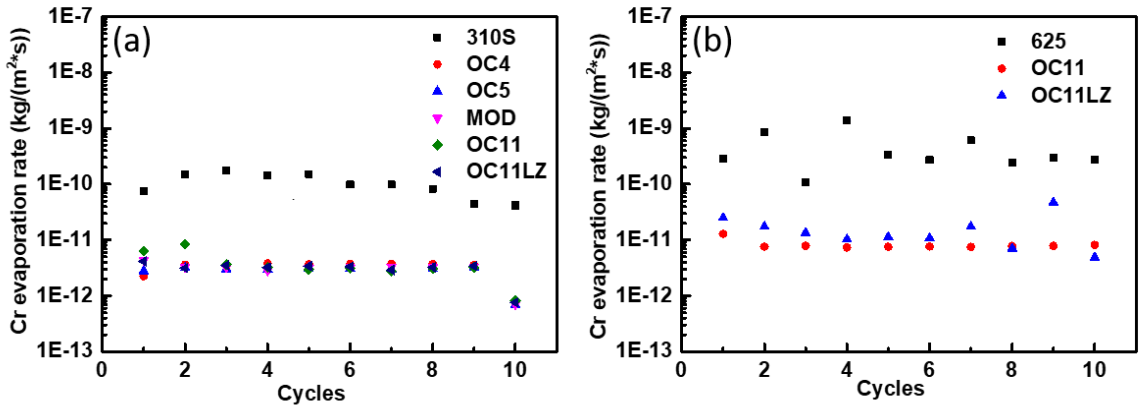

Figure 150 Chromium evaporation rates of each cycle for commercial alloys and AFA alloys in 10% H_2O at (a) 800 °C and (b) 900 °C.

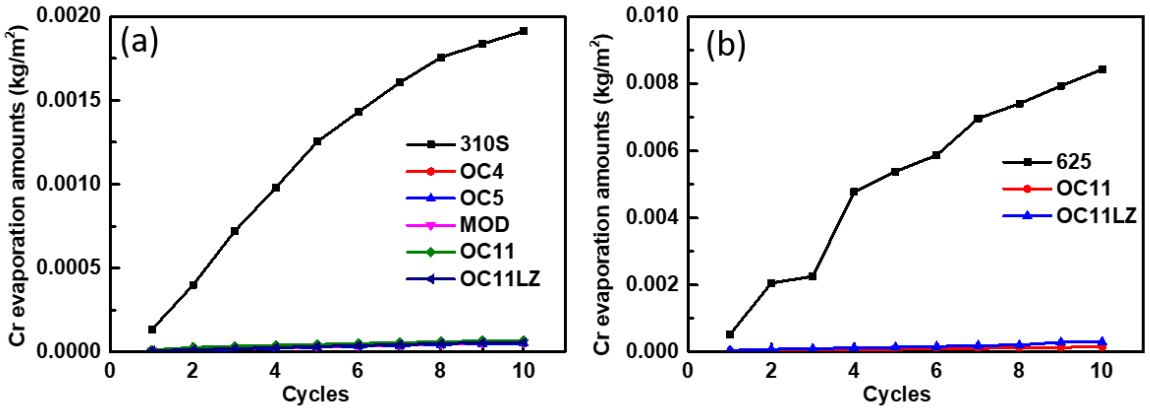

Figure 151 Accumulated evaporated Cr amounts for commercial alloys and AFA alloys in 10% H2O at (a) 800 °C and (b) 900 °C.

To intuitively demonstrate the Cr evaporation rates difference between commercial alloys and AFA alloys, the Cr evaporation rates resulting from 5000 h exposures (10 cycles) at 800 °C to 900 °C in air with 10% H_2O are summarized in Figure 150. The Cr evaporation rates from the AFA alloys were generally over an order of magnitude lower than the chromia-forming alloys 310S and 625 at 800 and 900 °C, respectively, which exhibited roughly comparable Cr evaporation rates. For example, at 800 °C, the Cr evaporation rate of AFA alloys was 20~35 times lower than 310S, although only 10~20 times lower at 900 °C. The Cr evaporation rates increased with increasing temperatures for OC11 and OC11LZ alloys with about 1 magnitude increases. The large Cr evaporation rates difference between commercial alloys and AFA alloys was likely related to the formation of a protective alumina scale on AFA alloys.It is also worth noting that the Cr evaporation rates of OC11LZ oscillates during the 5000h operation which is not the case with OC11, likely attributed to the different reactive elements in these two alloys.

To clearly demonstrate the difference between AFA alloys and commercial alloys , the accumulated Cr amounts of all alloys were plotted in Figure 151. A 35 and 20 times higher amounts of evaporated Cr of 310S than AFA alloys could be observed after the long-term operation, thus verifying the viability of AFA application in SOFC BoP components.

Newly developed methods for the Cr evaporation evaluations

Chromium evaporation from Cr_2O_3 and MICs has been studied widely in the past decades, however, researches on the BoP components are scarce and scattered. All Cr evaporation tests in these papers were conducted in quartz tube from which Si vapors evaporated and deposited on the alloy surface and furtherly resulted in altering the oxidation process of the alloys that might contributed to the error of the accurate evaporated Cr quantities in the long-term operation of SOFC stacks. In addition, Thomann and Froitzheim applied denuder technique to accurately quantify the evaporated Cr quantities, however, the sodium carbonate they used were quite expensive. Taking into the consideration of the above-mentioned problems, we had designed to investigate the Cr evaporation rates of the Al_2O_3-forming austenitic stainless steels in an atmosphere with 10% water vapor at 800 °C and 900 °C in comparison with commercial alloys and to figure out a reliable and accurate method to replace quartz tube with alumina tubes that coated with sodium bicarbonate which is much cheaper than sodium carbonate to exclude the Si deposits effect.

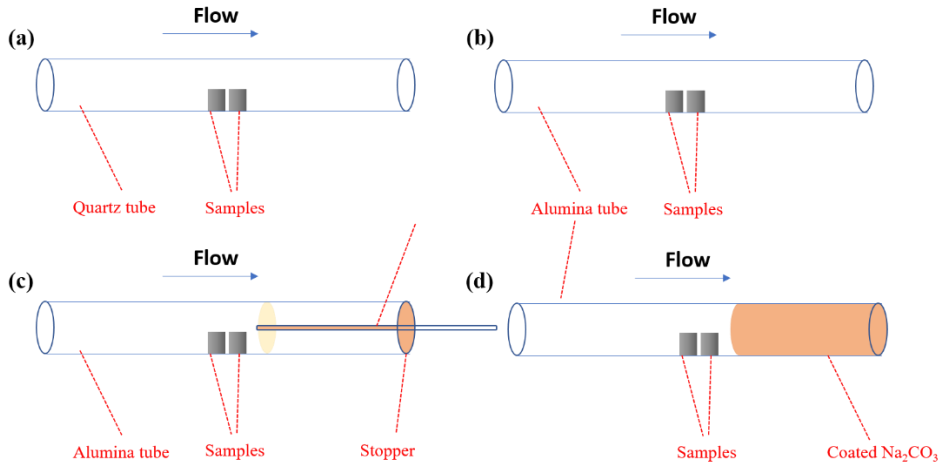

Figure 152 Schematic of the Cr evaporation test of different alloys in a) alumina tube, b) quartz tube, c) sodium carbonate coated thin alumina tube and d) sodium carbonate coated alumina tube.

Chromium Evaporation from different alloys using different methods

At the beginning of Cr evaporation experiments, the specimens were heated to the designated temperature (800 °C and 900 °C) at a heating rate of 3 °C/min. The tests were performed at atmospheric pressure for 500 h and the specimens were finally cooled down to room temperature at a rate of 3 °C/min after the test. Based on our previous research, deposited Si species from quartz tubes (Figure 152a, method 1) on the samples will probably affect the oxidation process of alloys, therefore herein we use alumina tubes to replace quartz tubes to exclude the effect of Si deposits. Several different methods were used to figure out the most reliable and accurate testing method. The optimal testing method using thinner alumina tubes (Figure 152c, method 3) which were firstly coated with $NaHCO_3$ and pre-heated at 250 °C for 2 h to ensure their transformation to Na_2CO_3 were fitted in the hole of the alumina disk which could prevent the backflow of Na species observed in test using sodium carbonate coated alumina tube (Figure 152d, method 4).

The volatility of chromium compounds is a well-known phenomenon which limits the use of chromia-forming alloys to service temperatures below 1100 °C. In the presence of humidity, the dominant species is chromium oxyhydroxide which is formed according to Equation.

$$1.5O_2(g)+Cr_2O_3(s)+2H_2O = 2CrO_2(OH)_2(g) \quad (1)$$

And the absorption reaction between Sodium carbonate and chromium volatile species which is according to Equation.

$$CrO_2(OH)_2(g) + Na_2CO_3(s)= Na_2CrO_4(s) + H_2O(g) + CO_2(g) \quad (2)$$

Cr transpiration tests were operated to accurately evaluate the Cr evaporation rates from different selected AFA alloys compared to commercial alloys for 500 h in air + 10% H_2O which simulates a SOFC cathode operating condition. Cr evaporation rates of various alloys after 500 h test using different methods are shown in Figure 153. In general, for all the testing methods, it is clearly observed that 310S and 625 exhibits a comparatively higher Cr evaporation rate than OC4 and OC5 under 800 °C and OC11 and OC11LZ under 900 °C, respectively, which can be attributed to the formed thick chromia scale on 310S and 625. Among the two alumina forming alloys at 800 °C, OC4 exhibits the lowest evaporation rate. Whereas the OC11 exhibits the lowest evaporation rate at 900 °C. The reason why these Cr evaporation rates vary to a great extent with each other will be discussed later.

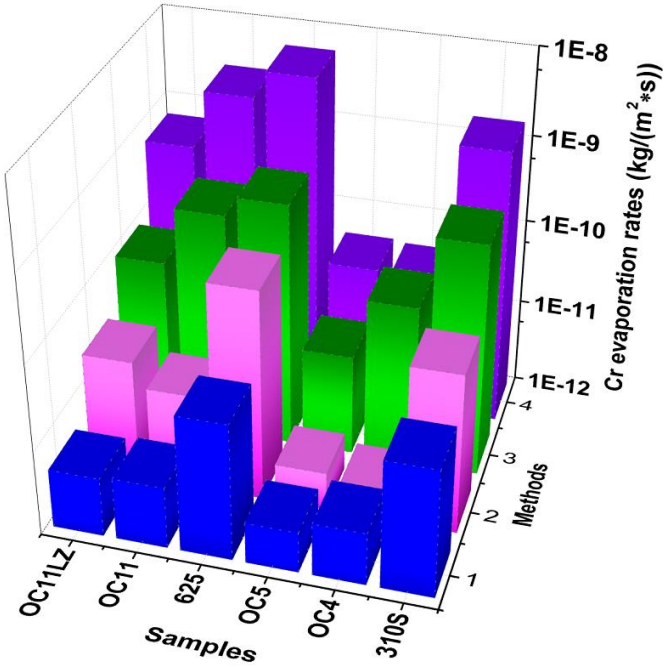

Figure 153 Cr evaporation rates of 310S, OC4 and OC5 800 °C and 625, OC11 and OC11LZ at 900 °C tested in 1) alumina tube, 2) quartz tube, 3) sodium carbonate coated thin alumina tube and 4) sodium carbonate coated alumina tube for 500 h in air with 10% H_2O.

Oxide Phase characterization

X-ray diffraction (XRD) profiles from commercial alloys and selected AFA alloys tested under 800 °C and 900 °C are demonstrated in Figure 154. It is clearly observed that 310S and 625 forms an oxide scale predominantly rich in Cr_2O_3, along with the presence of minor peaks related to spinel. Significant differences in the peak intensities of Cr_2O_3 scales appear for OC4 and OC5 alloys at 800 °C and OC11 and OC11LZ under 900 °C, respectively. This obviously indicates different kinetics of scale formation for different alloys. Relative peak intensity of Cr_2O_3 is smaller compared to the peak of substrate, suggesting thinner scale formation at 800 °C. However, the peak of Cr_2O_3 is even larger than the substrate peak for 625 at 900 °C.

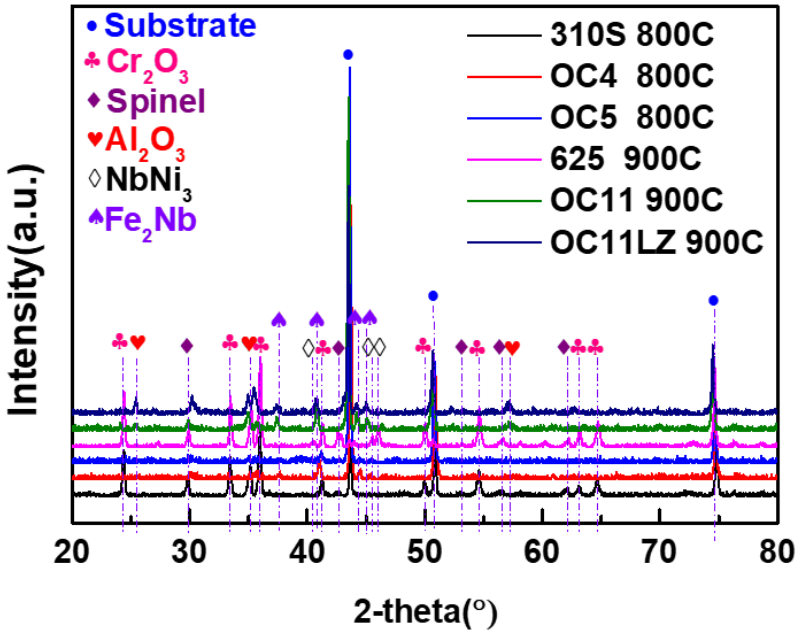

Figure 154 XRD profiles of the oxide scales developed on 310S, OC4 and OC5 at 800 °C and 625, OC11 and OC11LZ after 500 h chromium evaporation test in sodium carbonate coated thin alumina tube.

Oxidation of OC4 and OC5 at 800 °C in humidified air shows similar peaks. As can be seen from the XRD profiles, formation of Cr_2O_3 scale is observed along with large peaks from the substrate, while minor peaks from Cr_2O_3 and spinel are also observed.

The oxidation behavior of OC11 and OC11LZ demonstrates significantly different as compared to commercial alloys and AFA alloys at 800 °C. Oxidation of OC11 and OC11LZ at 900 °C results in the formation of mixed oxide scales. Large intensities from Al_2O_3 and Cr_2O_3 appear on the alloy surface. In addition, spinel peaks with smaller intensities could also be observed.

Oxide Scale Morphology

Alloy specimens were oxidized in air + 10% H_2O air at 800 °C and 900 °C for 500 h to observe the oxide growth behavior and its morphologies after the Cr evaporation test (Figure 155 and 156). The microstructure of 310S sample oxidized under 800 °C is shown in Figure 155a and 155b. A fully porous oxide scale is observed to cover the alloy surface which is uniform. Elemental analysis of the surface indicates formation of a mixed oxide scale under 800 °C with a subscale that is rich in Cr-Mn containing scale at the surface which indicates formation of mostly chromia scale and some $(Cr, Mn)_3O_4$ spinel.

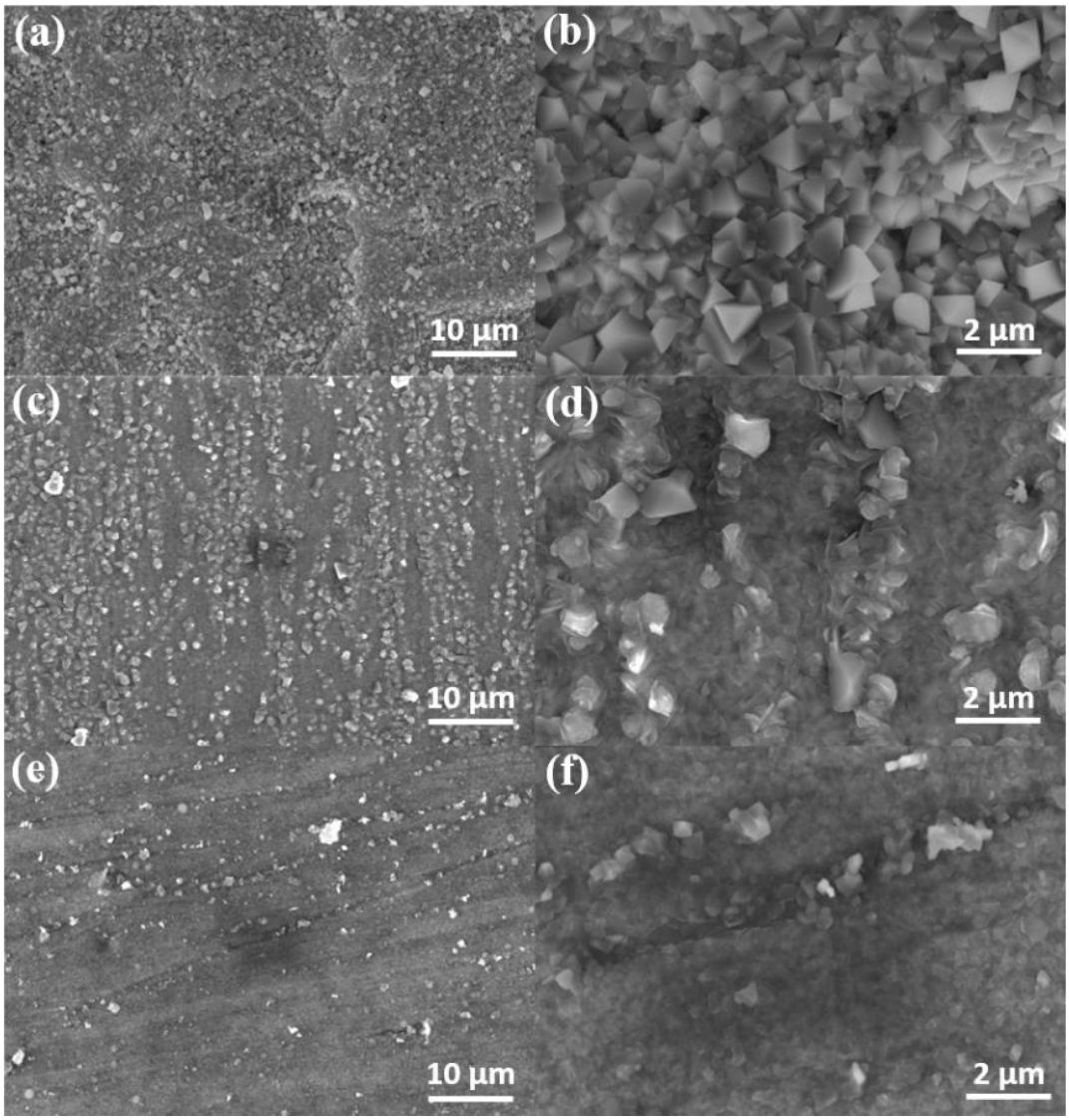

Figure 155

Fig. 4. Oxide scale morphologies developed on (a, b) 310S, (c, d) OC4 and (e, f) OC5 tested for 500 h in air + 10% H_2O at 800 °C in sodium carbonate coated thin alumina tube.

Distinct morphologies of the surface scale formed on OC4 samples are shown in Figure 155c and 155d. Uniform scale formation with minor overgrown areas could be observed on the OC4 samples surface. Surface elemental analyses using EDS reveal that the overgrown areas are highly rich in Fe, Cr and Mn. The subscale, however, appears to have a high concentration of Al. The Al-dominant scale appears to be very uniform and dense as compared to the Fe-Cr-Mn-rich microstructure. Whereas there are less overgrown areas for the OC5 sample whose scale are uniform Fe-Cr-Mn-rich scales which validated in the EDS analysis, in addition, the uniform Al-dominant scale can also be observed (Figure 155e and 155f).

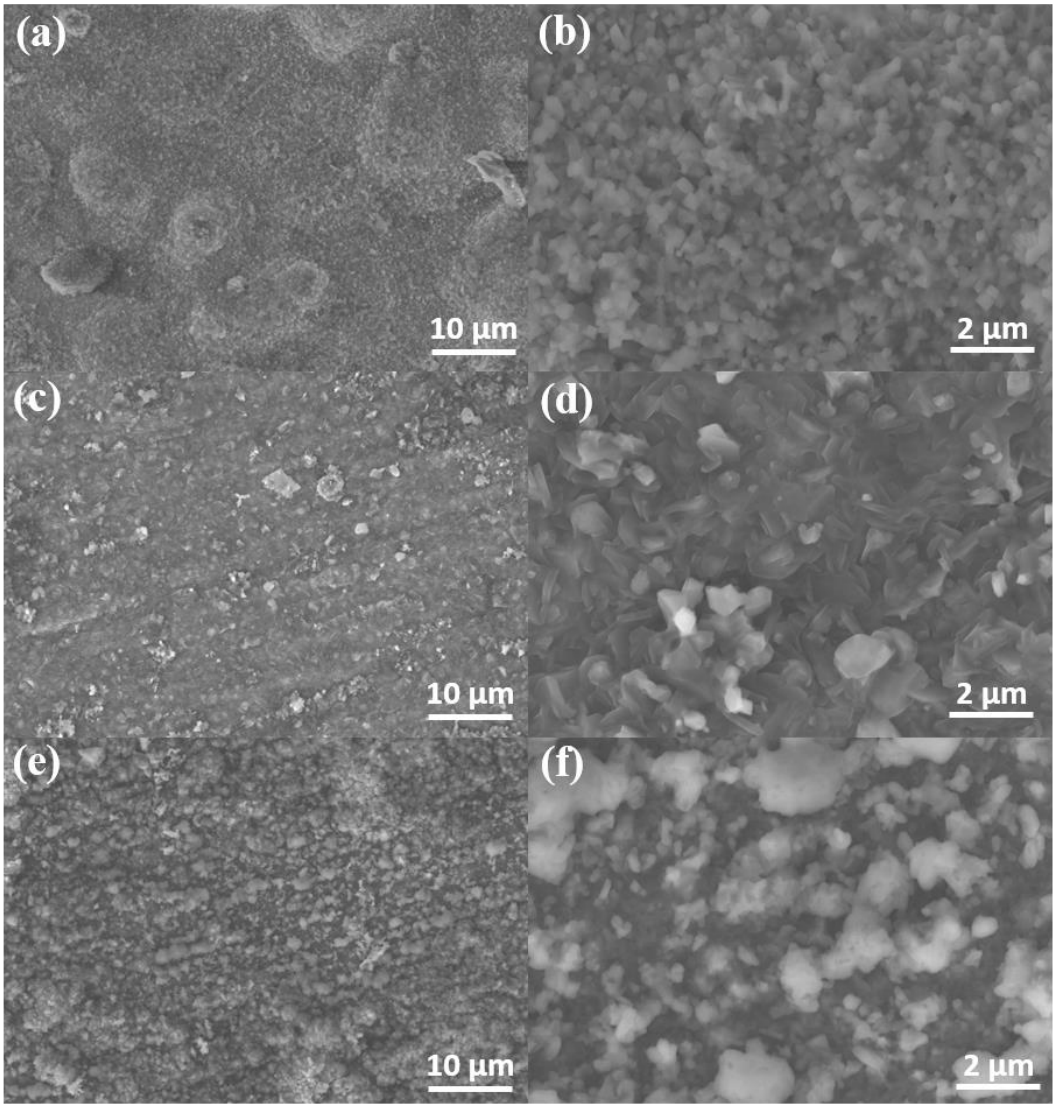

Figure 156 Oxide scale morphologies developed on (a, b) 625, (c, d) OC11 and (e, f) OC11LZ tested for 500 h in air + 10% H_2O at 900 °C in sodium carbonate coated thin alumina tube.

The morphology of 625 sample oxidized at 900 °C is shown in Figure 156a and 156b. A uniform oxide scale is observed to cover the alloy surface which is similar as 310S. However, some minor spallation could be observed on the morphology (Figure 156a). Elemental analysis of the surface indicates formation of a mixed oxide scale at 900 °C with a top layer that is rich in Cr and Mn and a chromia subscale. Oxidation behavior of OC11 at 900 °C is shown in Figure 156c and 156d. OC11has almost the same oxide scales as compared to OC4 under 800 °C. Higher magnification images reveal crystalline overgrown structures and a smooth surface underneath at 900C. Oxide scale analyses indicate the formation of an Al-rich surface as a sublayer with surface oxides rich in Fe, Cr and Mn. Oxidation of OC11LZ under 900 °C (Figure 156e and 156f) shows a more overgrown area than OC11. The faceted grains on the surface could be attributed to the Fe-Cr-Mn-rich oxides and the dense subscale is Al-rich scales which is indicated by EDS analysis.

Cross-sectional images
310S, OC4 and OC5 at 800 °C

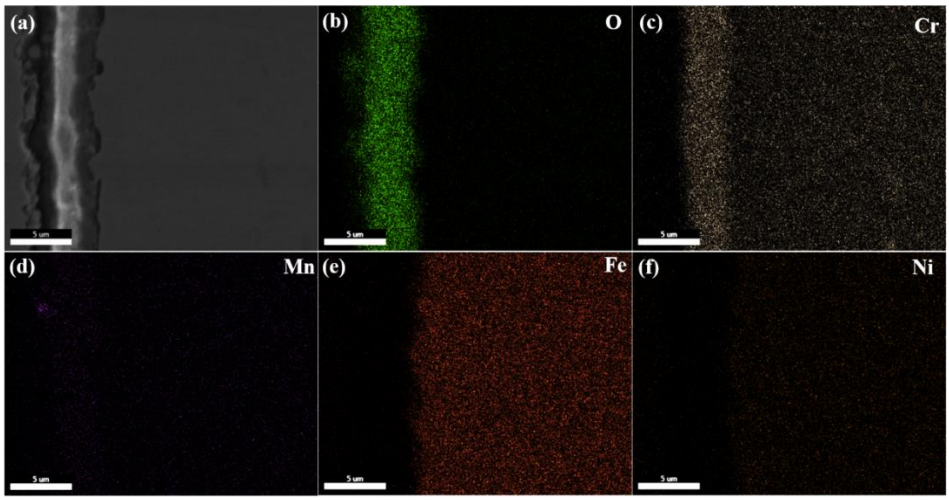

Figure 157 SEM/EDX mapping of the cross-sectional of the 310S tested for 500 h in air + 10% H_2O at 800 °C in sodium carbonate coated thin alumina tube.

In order to analyze the chemical composition across the depth of the oxide scales, a cross section of alloy 310S tested for 500 h in air + 10% H_2O at 800 °C was characterized by SEM/EDS mapping. It can be seen from Figure 157. that the outmost oxide layer which is about 2 μm thickness and the inner oxide layer which is about 2 μm thickness are assigned to $(Cr, Mn)_3O_4$ spinel and Cr_2O_3, respectively. In addition, plenty of voids can be easily observed at the interface of the oxide scales and the alloy substrate. The highest chromium evaporation rate of alloy 310S among the three tested alloys at 800 °C is assigned to the formation of a chromium-rich scale which can react with oxygen and water to form chromium oxyhydroxide. The alloy addition of manganese in alloy 310S contributed to the formation of the outmost layer of $(Cr, Mn)_3O_4$ spinel, whereas the inner scale was Cr_2O_3. There were researchers reporting that the presence of the protective $(Cr, Mn)_3O_4$ spinel can lower the chromium evaporation by an order of magnitude when compared to pure chromia. However, it is reported that the outmost $(Cr, Mn)_3O_4$ spinel layer not covering the entire alloy surface and the loose $(Cr, Mn)_3O_4$ spinel layer resulted in the exposure of Cr_2O_3 to humid air for alloy 310S which accounted for the higher chromium evaporation rate. However, the cross-sectional SEM/EDX mapping images in Figure 158 and 159 show the chemical analysis of oxide scales formed on OC4 and OC5 tested for 500 h in air + 10% H_2O at 800 °C. It can be seen that the outmost layer is enriched in Fe, Cr, Mn and Al and the inner layer is a continuous alumina layer for OC4 and OC5. Moreover, there are no voids observed at the interface between the oxide scales and the alloy substrate. The continuous alumina layer formed on OC4 and OC5 remains dense and uniform in thickness of which is about 500nm and 400nm, respectively. The continuous alumina layer can prevent the diffusion of chromium and manganese which contributes to lower Cr evaporation rates.

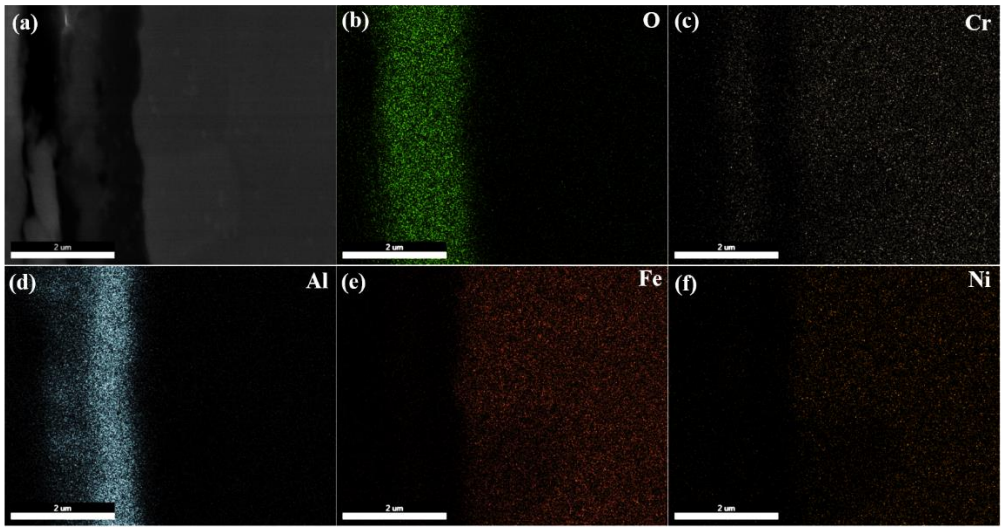

Figure 158 SEM/EDX mapping of the cross-sectional of the OC4 tested for 500 h in air + 10% H_2O at 800 °C in sodium carbonate coated thin alumina tube.

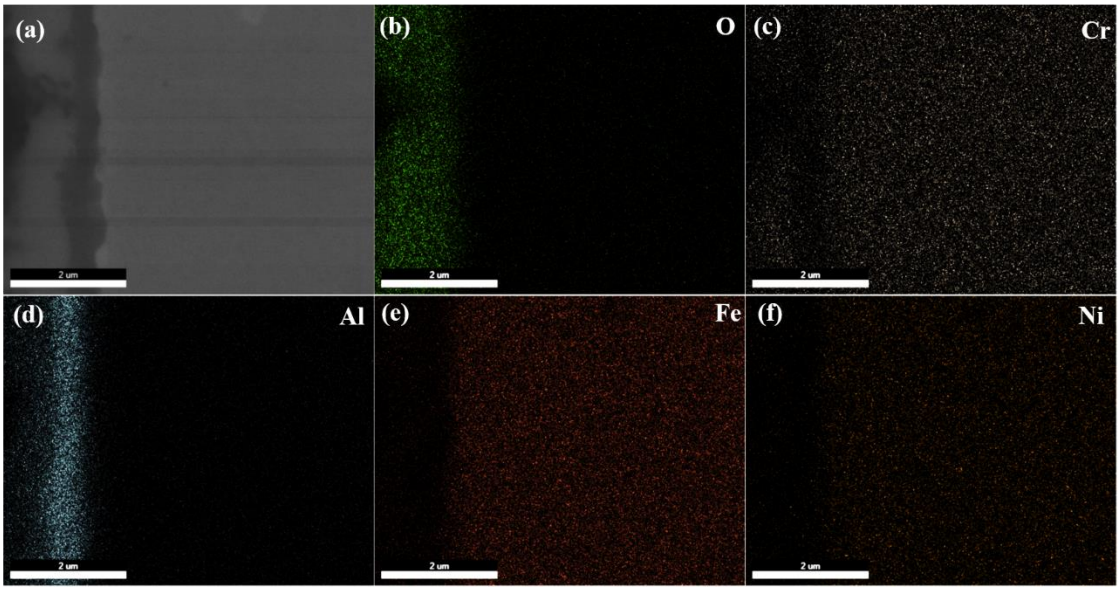

Figure 159 SEM/EDX mapping of the cross-sectional of the OC5 tested for 500 h in air + 10% H_2O at 800 °C in sodium carbonate coated thin alumina tube.

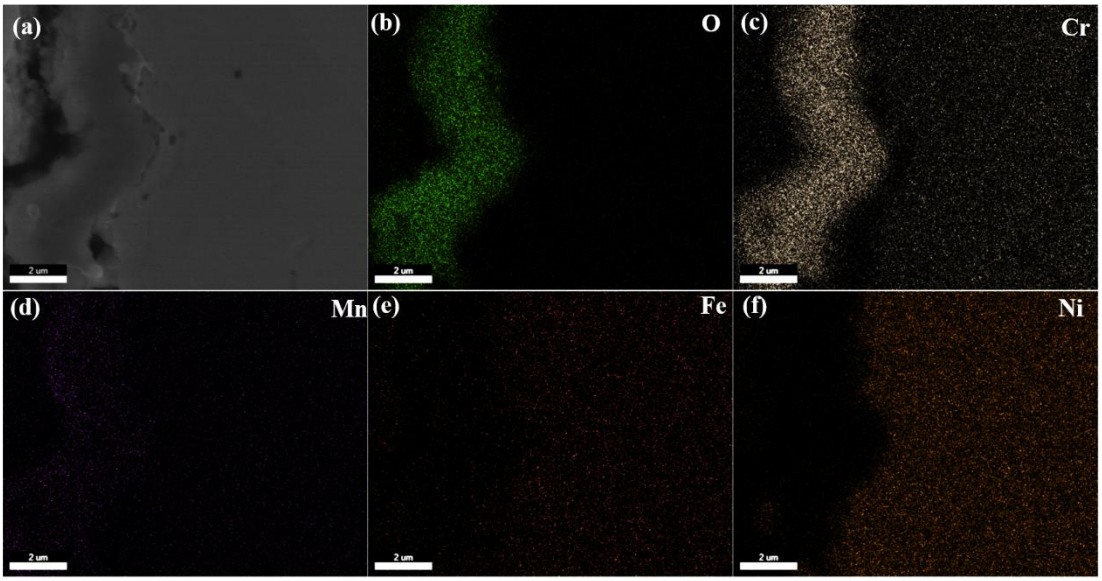

Figure 160 SEM/EDX mapping of the cross-sectional of the 625 tested for 500 h in air + 10% H_2O at 900 °C in sodium carbonate coated thin alumina tube.

625, OC11 and OC11LZ at 900 °C

The SEM/EDS cross-sectional images of the oxide scales of 625, OC11 and OC11LZ are shown in Figures 160, 161 and 162. It can be seen from Figure 160 that the outmost layer is $(Cr, Mn)_3O_4$ spinel of which thickness is ~500 nm and the inner layer is Cr_2O_3 of which thickness is 2.5 μm. The spallation of the outmost $(Cr, Mn)_3O_4$ spinel layer and the direct exposure of Cr_2O_3 inner layer to humified air reasonably accounted for the high Cr evaporation rate of 625 in these three alloys tested at 900 °C. Whereas for the OC11 and OC11LZ, an outmost layer enriched in Fe, Cr, Mn and Al, an intermediate layer consisted of Cr_2O_3 and an inner continuous alumina layer could be observed from the SEM/EDS mapping analysis (Figure 161 and 162). The layers of Cr_2O_3 and Al_2O_3 confirm by XRD are also consistent with the reported nature of the oxide scales developed on a similar steel in steam.

The formation of thick Cr_2O_3 layer which can react with oxygen and water to form chromium oxyhydroxide (Figure 157 and 160) accounts for the higher chromium evaporation of alloy 310S and 625 that OC4 and OC5 at 800 °C and OC11 and OC11LZ at 900 °C. The formation of a continuous alumina layer on AFA alloys can effectively decrease the diffusion of chromium, thus decreasing the Cr evaporation rates of AFA alloys which makes it potential for the application of BoP components in SOFC industry.

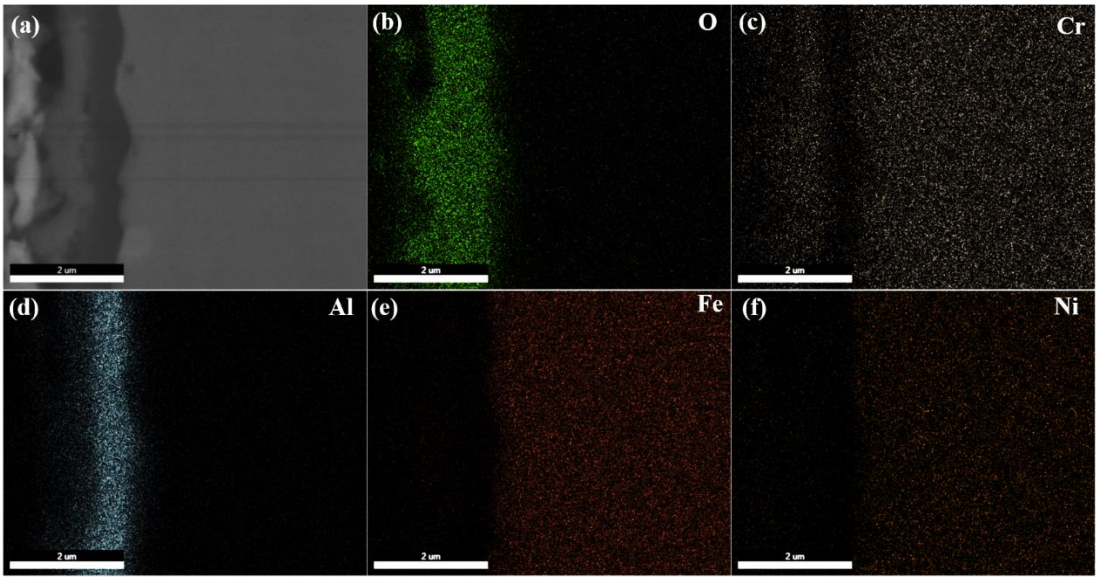

Figure 161 SEM/EDX mapping of the cross-sectional of the OC11 tested for 500 h in air + 10% H_2O at 900 °C in sodium carbonate coated thin alumina tube.

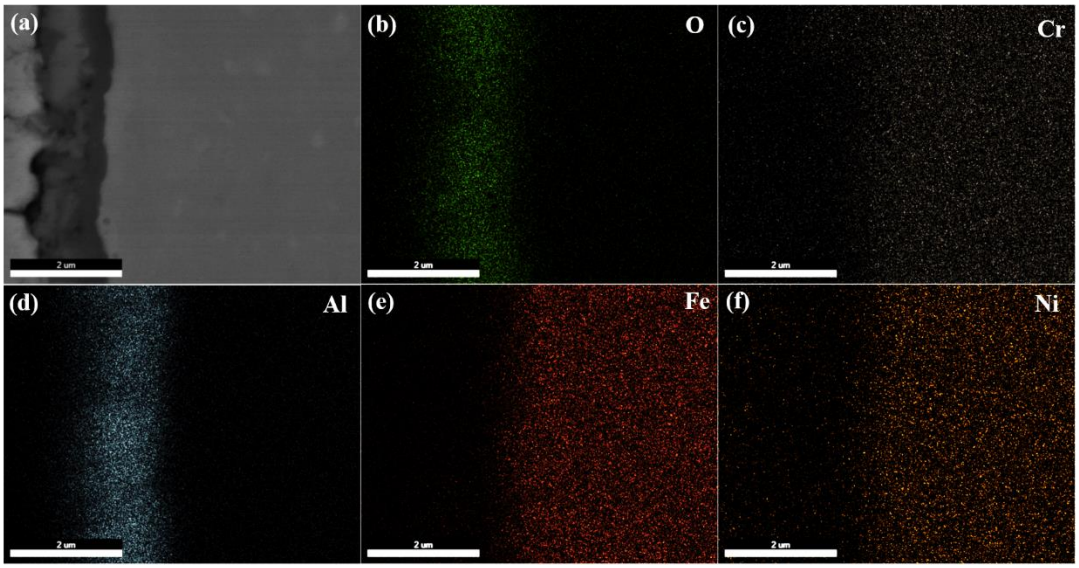

Figure 162 SEM/EDX mapping of the cross-sectional of the OC11LZ tested for 500 h in air + 10% H_2O at 900 °C in sodium carbonate coated thin alumina tube.

Comparison of these testing methods

Testing in quartz tubes (method 2)

Many researchers had evaluated the Cr evaporation rates of chromia-forming alloys and alumina-forming alloys using quartz tubes with different humidity at different temperatures with different flow rate in the last decades. It was unanimous that the Cr evaporation rates of alumina-forming alloys were much lower than that of chromia-forming alloys which can be attributed to the formed continuous alumina layer that could prevent the diffusion of chromium, thus greatly reducing the corresponding Cr evaporation rates. However, some problems could occur in this testing method which we used in our previous paper to check the feasibility to replace chromia-forming alloys with AFA alloys for the application of balance of plant in SOFC industry. One is the Cr deposits on the quartz tubes, and the other one is the Si deposits on the alloy surface. The former problem could be solved by cleaning the quartz tubes after every test. However, in the case of the latter problem which might affect the long-term Cr evaporation rate of alloy even though we figured out that the Si deposits after 500 h test was not enough to severely influence the Cr evaporation rates in comparison with many studies. The Si deposits on the alloy surface at the range of 800-900 °C were characterized by XPS in the previous research. Moreover, the Si deposits on the alloy surface may affect the establishment of oxide scales and the diffusion of chromium which might lead to the imprecise tested Cr evaporation rates of various alloys in the long-term operation. The long-term operation of 310S, OC4 and OC5 at 800 °C and 625, OC11 and OC11LZ at 900°C for 4500 h using quartz tubes had been conducted in this paper. The SEM images of alloy surfaces and the corresponding EDS after 4500 h test were demonstrated in Fig. S3 and S4. It could be clearly observed that there were Si deposits for the all the alloys except 625. The Cr deposits on 625 alloy surfaces after 500 h test had been validated even though there were no Si deposits for the 4500 h sample of which reason had not been figured out. In addition, the Cr evaporation rates of alloys using quartz tubes were about one magnitude lower than that tested with sodium carbonate coated thin alumina tubes, implying that the Si deposits on the surface might have some effects to reduce the Cr evaporation rates. The effect of Si deposits on the Cr evaporation rates and the establishment of oxide scales will be studied in the future. In a word, there could be plenty of Si deposits on the alloy surface after the long-term test using the quartz tubes which could contribute to the lower Cr evaporation rates.

Testing in alumina tubes

Si deposits on the alloy using quartz tubes were characterized by SEM and XPS in our previous research. And it was also reported that the Si deposits would not undermine the oxidation process of these alloys which validated by XRD. The only problem is that the Si deposits on the alloy surface would reduce the Cr evaporation rates. Up to now, almost all studies were using quartz tubes to investigate the Cr evaporation rates of alloys. Researchers might neglect the effect of Si deposits on the Cr evaporation rates and oxidation process of alloys in the short-term operation. However, there could be a great number of Si deposits on the alloy surface after 4500 h operation (Fig. S3c). In order to exclude the effect of Si deposits, alumina tubes were used to replace the quartz tubes. The phase determination of oxide scales was characterized by XRD and SEM and the problems occurred in these testing methods were discussed below.

Testing in alumina tubes (no coating, method 1)

Herein, we applied alumina tubes to evaluate the Cr evaporation rates of these alloys. It could be seen that the Cr evaporation rates tested in were even lower than that of quartz tubes which could be attributed to the chemical interaction between Cr gaseous species and alumina tubes. Many researchers had reported the reaction mechanism of alumina/chromia solid solution. The

evaporated Cr species could react with alumina tube to form the solid solution on alumina tubes which could be extremely difficult to be fully cleaned. The phase determination of oxide scales tested in alumina tubes was shown in Fig. S5. These peaks were quite similar as the samples tested in the sodium carbonate coated thin alumina tube and no other secondary phases could be observed which verified that the oxidation process would not be undermined in alumina tubes. In addition, morphologies of samples after the Cr evaporation test in alumina tube were shown in Fig. S6 and S7. The morphologies were almost the same as that tested in the sodium carbonate coated thin alumina tube, and no spallation could be observed.

Testing in sodium carbonate coated alumina tubes (method 4)

As there were solid solutions formed resulted from the chemical reaction between gaseous Cr species and alumina tube at the high temperature region which contributed to the lower Cr evaporation rates, we managed to coat the inner wall of alumina tube to alleviate the chemical reaction. The Cr evaporation rates of 310S at 800 °C and 625, OC11 and OC11LZ at 900 °C were much higher than that tested with method 3, however, the Cr evaporation rates of OC4 and OC5 at 800 °C were in the same magnitude as method 3. In order to figure out this abnormal phenomenon, the XRD profiles of these alloys tested with method 4 were shown in Fig. S8. It could be seen that hematite (Fe_2O_3) and magnetite (Fe_3O_4) were formed on 310S at 800 °C, OC11 and OC11LZ at 900 °C and nickel oxide (NiO) were formed on after the test with method 4 which could contribute to the abnormal higher Cr evaporation rates. EDS analysis of these alloys were shown in Fig. S9 to examine the integrity of the oxide scales. It could be seen that the morphologies of these alloys were totally different compared to that tested with method 3. Sodium pollution on the 310S surface (Fig. S9b) and the breakaway oxidation of 625, OC11 and OC11LZ at 900 °C could be obviously observed (Fig. S9d, f, h). The thermal decomposition of sodium carbonate had been studied by many researchers, the backflow of the sodium species could deposit on the alloy surface and result in the breakaway of these alloys which contributed to the abnormal higher Cr evaporation rates. However, the Cr evaporation rates of OC4 and OC5 were in the same magnitude as method 3 that did not suffer from sodium pollution which was in agreement with the Cr evaporation rates data and XRD profiles.

In summary, using method 1 will result in the Si deposits on the alloy surface which may influence the oxidation process and reduces the Cr evaporation rates of alloys. Method 2 is applied to exclude the effect of Si deposits, however, the alumina/chromia solid solution resulted from chemical interaction between gaseous Cr species and alumina tube also reduces the Cr evaporation rates of alloys. And the Cr deposits using method 1 and 2 are extremely difficult to be cleaned. Thus, method 4 is invented to absorb the evaporated Cr species and alleviate the Si deposits on the alloy surface and the chemical interaction. However, the backflow of the sodium species on the alloy surface results in the breakaway oxidation of the alloys, thus contributing to the abnormal high Cr evaporation rates. Based on these problems, method 3 with thin alumina tube is applied to prevent the backflow of the sodium species which evaluates the Cr evaporation rates more accurate. However, there is also a problem that some solid solution formed in the high temperature region cannot be avoided.

Discussion

1. **Effect of temperature on the Cr evaporation rate**

Basically, the Cr evaporation rates increase with the increasing of temperature, for instance, the evaporation rate under 900 ^oC is higher than that under 800 ^oC for the OC11LZ alloy at all time. Moreover, the Cr evaporation rate of OC11 under 900 ^oC is higher than that under 800 ^oC in the first 500h cycle. Other Cr evaporation rates of OC11 after 500h cannot be detected which can be attributed to the formed continuum Al_2O_3 layer which can suppress the evaporation and diffusion

of chromium. Ebbinghaus, Graham and Stearns investigated the kinetics of oxidation of materials with Cr_2O_3 scales to analyze the evaporation of fifteen gaseous chromium species several decades ago. They found that $CrO_3(g)$ was the species which accounted for the evaporation of chromium oxide when Cr_2O_3 was heated in dry air (lower water partial pressure). Furthermore, subsequent researchers substantiated $CrO_2(OH)_2(g)$ was the predominant gaseous species existing over solid Cr_2O_3 in a humid oxidizing environment (higher water partial pressure). Hilpert particularly studied the temperature dependence of the evaporation of $Cr_2O_3(s)$ in moist air, it was shown that $CrO_2(OH)_2(g)$ was the amplest vapor species and the partial pressure of $CrO_3(g)$ exhibited larger temperature dependence compared to the partial pressure of $CrO_2(OH)_2(g)$. However, both the partial pressure of $CrO_3(g)$ and $CrO_2(OH)_2(g)$ increased with the increasing of the temperature which verified the higher Cr evaporation rate under higher temperature.

2. Effect of alloy composition on the Cr evaporation rate

The transpiration experiments with AFA alloy show that the continuum formation of Al_2O_3 layer offers a superior protection against Cr evaporation than chromia-forming alloys such as 310S and 625 alloy. The measured Cr evaporation rates of 5 samples of the AFA alloys under 800 ºC are comparable with each other. After operation at 800 °C for 2000 h, the Cr evaporation rate of 310S is 2 orders of magnitude higher than AFA alloys. With increasing oxidation time, the Cr evaporation rates flatten and after 2000 h of oxidation at 800 °C the Cr evaporation rate of 310S surface is larger by about a factor of 100 than after 500 h which could be attributed to the incompletely formed Cr_2O_3 layer on the alloys surface. However, for the AFA alloys, the decrease of the Cr evaporation rates after 500 h of oxidation can be explained by the decrease of the scale thickening rate of the alumina scale with increasing time and thickness of the scale. The evaporation rates of Cr are then flattened by the slower diffusion transport. In terms of the samples tested under 900 °C, the Cr_2O_3 layer could be formed quickly on the 625-alloy surface and resulted in a comparable Cr evaporation rates with other cycles. The drastic increasing of Cr evaporation rate of fourth cycle could be ascribed to the Cr-containing liquid in the quartz tube mixed with the liquid in the condenser. OC11 exhibited the superior Cr evaporation rate than OC11LZ which can be attributed to the minor additions of Y suppressing the formation of θ-alumina and encourage the formation of α-alumina. The faster growth of the alumina scale OC11 can therefore be explained by the slower phase transformation from rapid-growing metastable γ- and θ-aluminas to slowly-growing stable α-alumina. Another explanation might be, that the rate of nucleation of α-Al_2O_3 depends on the underlying metallic matrix.

Task 4.0 Quantitative Investigation of Cr-poisoning of the SOFC Cathode – WVU

Subtask 4.1 Assembly of SOFCs with BOP Alloys

Anode-supported cells (ASC) were used to study the degradation processes by Cr poisoning. The cells consist of a 300 μm thickness NiO/8YSZ anode substrate and an 10-20 μm thickness 8YSZ electrolyte. Subsequently, a double-layered GDC (10 μm thickness barrier layer)/60-70 μm thickness LSCF cathode was applied by screen-printing and sintering. The active area of the working cathode was 0.45 cm^2. The cells were tested in a single-cell test bench and characterized by EIS measurements.

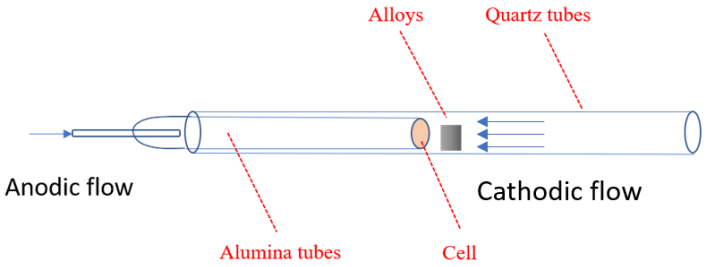

Figure 163 Schematic of the Cr poisoning test of ASC cells with different alloys.

Figure 163 displays the single cell test setup. Silver paste and Pt mesh was applied to the anode and cathode as current collector, respectively. Silver wire was used as lead wire in the anode atmosphere; and gold wire was used as lead wire in the cathode atmosphere to prevent the reaction between silver wire and gaseous Cr species. At the cathode, four different alloys were place 10 mm away from the cathode. Different alloys were applied in this study to investigate the degradation of ASC performance by Cr poisoning via gaseous Cr species.

The cells were operated under ambient pressure with air at the cathode side and 3% H_2O + H_2 mixtures at the anode side. The fuel and air flow rates were maintained at 50 and 200 ml min^{-1} during all experiments, respectively. The cells were tested at an operating temperature of 800 °C. The cell performance was evaluated by a galvanostatic test. Impedance was collected over the frequency range from 1 MHz to 0.1 Hz with an AC perturbation of 10 mV at open-circuit voltage condition (OCV). The galvanostatic test was carried out with a constant current density of 0.5 A/cm^2 for 500 h. The galvanostatic test was interrupted to do the EIS measurements at several specific dates.

Subtask 4.2 Electrochemical Investigations

Electrochemical properties of NiO-YSZ/YSZ/GDC/LSCF-GDC anode-supported fuel cells

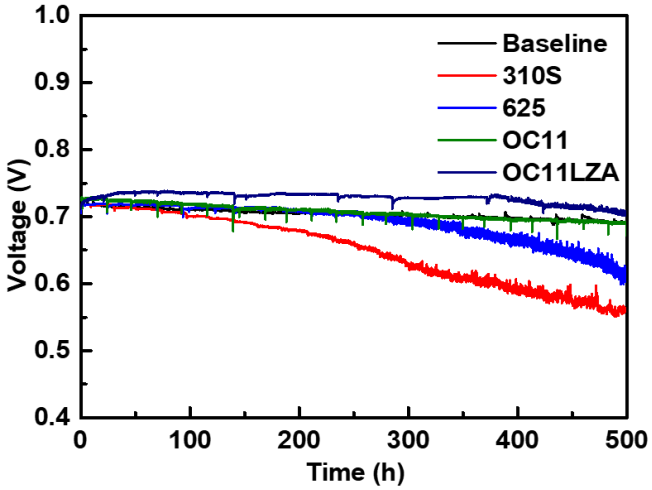

Figure 164 Voltage versus time of ASC during the galvanostatic test at 0.5 A/cm^2 at 800 °C w/wo alloys.

Figure 164 shows the time course of cell voltage during the galvanostatic test of the ASC in the presence of different alloys at the cathode region. During the galvanostatic test the cell voltage decreases about 8.84%/kh ($V_{baseline,\ t = 0\ h}$ = 724 mV, $V_{baseline,\ t = 500\ h}$ = 692 mV) in the absence of alloys. However, a considerable decrease of 44.28%/kh ($V_{310S,\ t = 0\ h}$ = 718 mV, $V_{310S,\ t = 500\ h}$ = 559 mV) and 24.12%/kh ($V_{625,\ t = 0\ h}$ = 705 mV, $V_{baseline,\ t = 500\ h}$ = 620 mV) was determined in the presence of 310S and 625 alloy, respectively. It can be deduced that gaseous Cr species evaporated from chromia-forming 310S and 625 vastly deteriorate the performance of the cells. However, slight decrease of 10.18%/kh % ($V_{OC11,\ t = 0\ h}$ = 727 mV, $V_{OC11,\ t = 500\ h}$ = 690 mV) and 3.08%/kh % ($V_{OC11LZA,\ t = 0\ h}$ = 712 mV, $V_{OC11LZA,\ t = 500\ h}$ = 701 mV) was determined in the presence of OC11 and OC11LZA alloy, respectively. These results demonstrate that the continuous alumina layer formed on the alumina-forming alloys greatly reduced the diffusion and evaporation of Cr from the substrate. Moreover, it can be seen that all cells tested w/wo alloys are affected by the electrode activation more or less, which can influence the electrochemical performance.

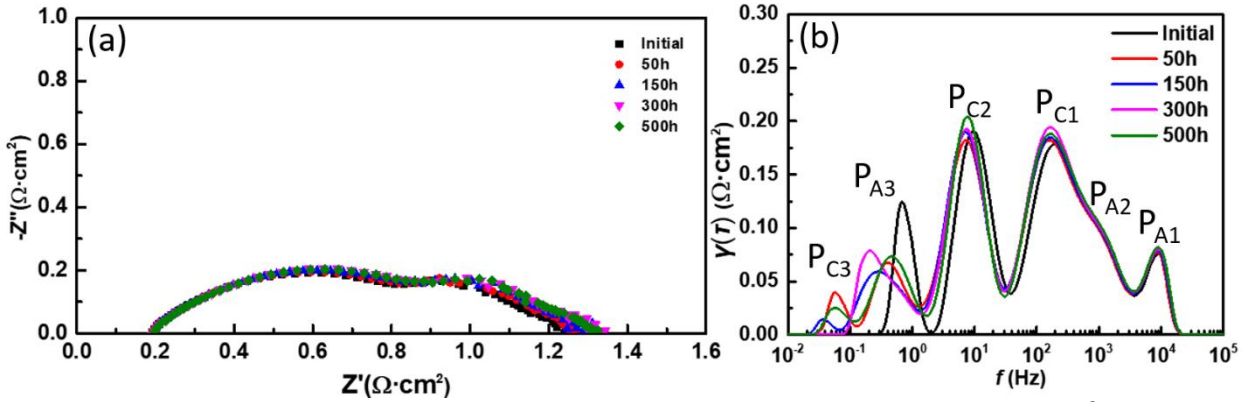

Figure 165 (a) EIS and (b) the corresponding DRT spectra under OCV during the galvanostatic test at 0.5 A/cm^2 under 800 °C for cell tested without alloy.

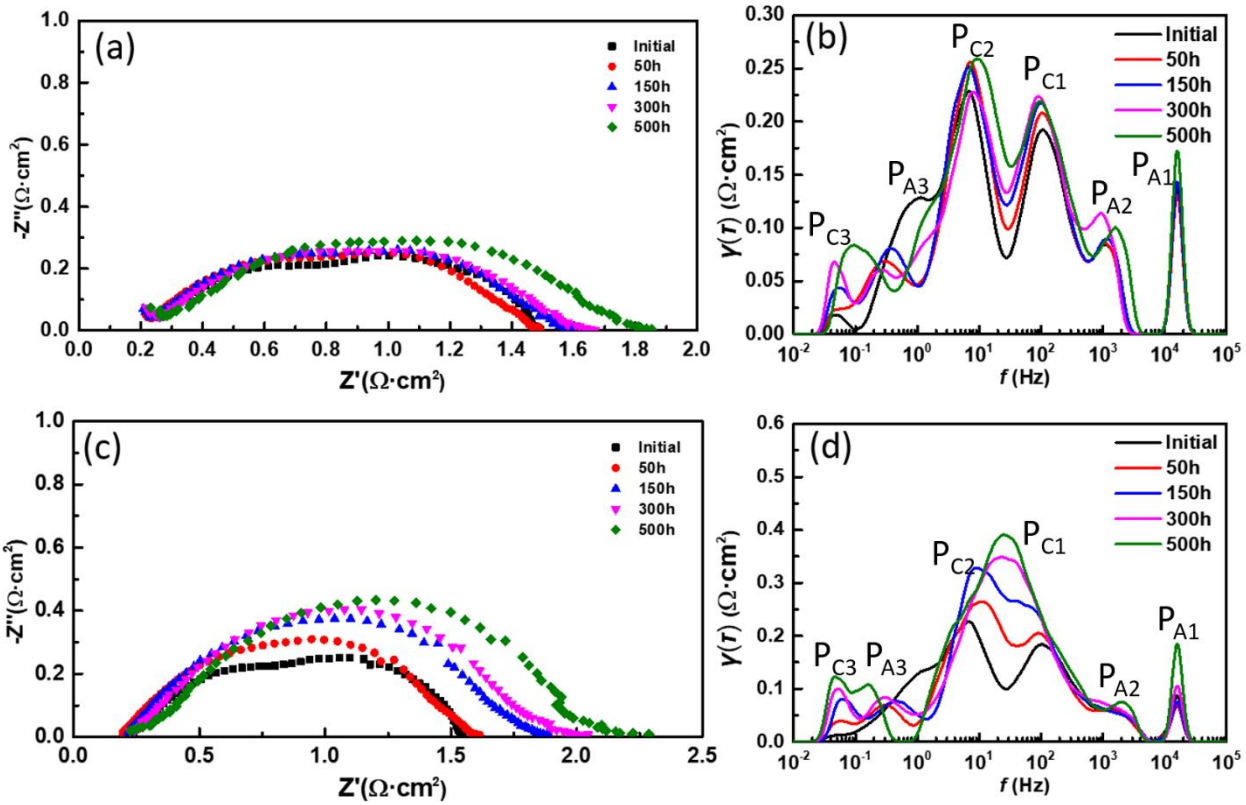

Figure 166 (a, c) EIS and (b, d) the corresponding DRT spectra under OCV during the galvanostatic test at 0.5 A/cm^2 under 800 °C for cell tested with 310S (a, b) and 625 (c, d).

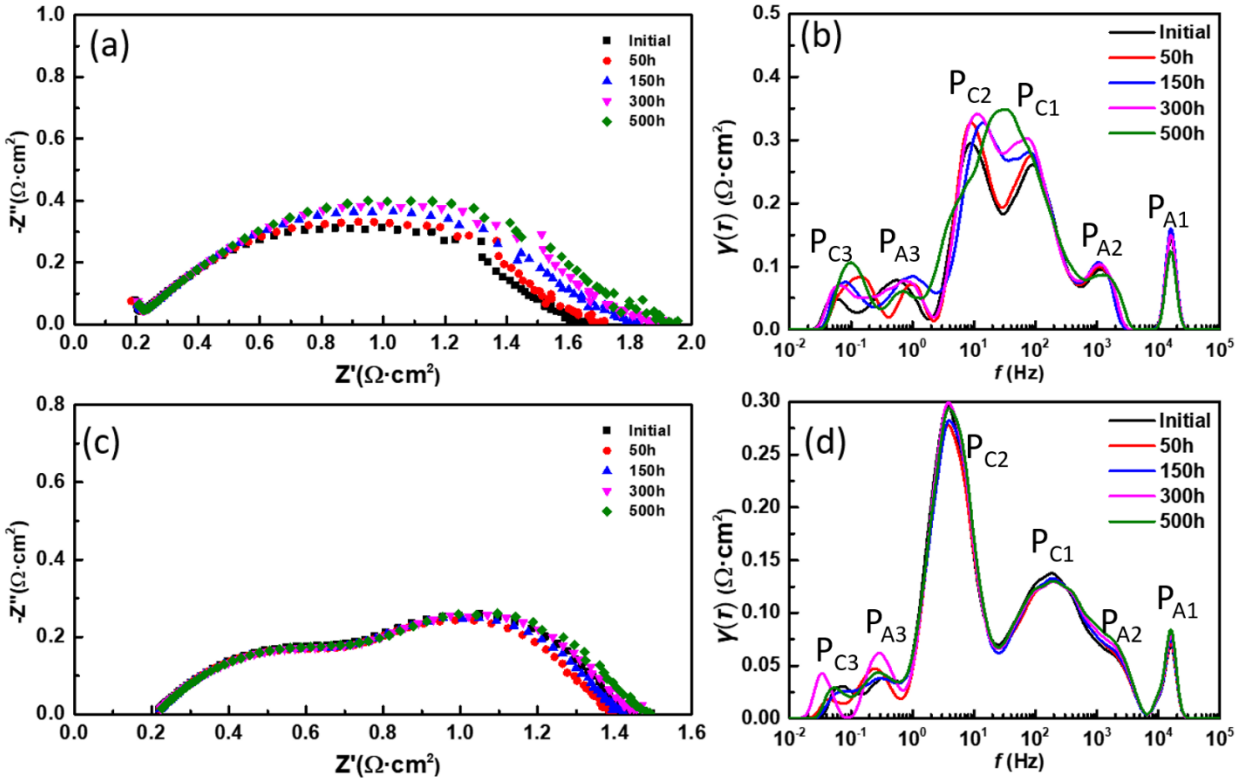

Figure 167 (a, c) EIS and (b, d) the corresponding DRT spectra under OCV during the galvanostatic test at 0.5 A/cm^2 under 800 °C for cell tested with OC11 (a, b) and OC11LZA (c, d).

Figure 165a demonstrates the EIS spectra of ASC tested without alloys under OCV during the galvanostatic test at 0.5 A/cm^2 under 800 °C. It can be seen that the ohmic resistance is almost unchanged during the 500 h test. However, the polarization resistance has a slight increase with the increase of the operation time. The DRT spectra calculated from the EIS spectra are shown in Figure 165b in which six DRT peaks can be observed for the ASCs. Two peaks (P_{A1} and P_{A2}) at 2 - 20 kHz were assigned to gas diffusion coupled with charge-transfer reaction and ionic transport in the Ni/YSZ AFL layer. The peak P_{C1} assigned to migration of oxygen ions from LSCF to YSZ and peak P_{C2} assigned to dissociative adsorption and diffusion of oxygen ions on LSCF are generally observed at 100-2000 Hz and 20-50 Hz, respectively. However, P_{C1} overlapped with P_{A2} at 500-1000 Hz. The gas diffusion within the Ni/YSZ anode substrate observed at 1-10 Hz and gas diffusion losses within the pores of the cathode observed at 0.1-5 Hz is assigned to peak P_{A3} and P_{C3}, respectively. Peaks P_{C1} and P_{C2} slightly change with the prolonged operation time which can be attributed to the change in cathode microstructure by long-term operation. However, the peaks P_{A1} and P_{A2} stay constant with the increase of operation time. The almost unchanged DRT anode peaks observed at high frequency during long-term operation are also reported by Kornely.

Figure 166 shows the EIS curves and DRT spectra under OCV during the galvanostatic test at 0.5 A/cm^2 under 800 °C for 310S and 625. The ohmic resistance almost stays constant, while the polarization resistances increase with the increase of the operation time for both alloys (Figure 166a and b). Six DRT peaks were calculated for the ASCs tested with commercial alloys (Figure 166c and d). The peaks assigned to gas diffusion coupled with charge-transfer reaction and ionic transport in the Ni/YSZ AFL structure (P_{A1} and P_{A2}) was observed to stay constant during the

entire galvanostatic test. However, the peak assigned to the migration of oxygen ions from LSCF to YSZ (P_{C1})and the peak assigned to the dissociative adsorption and diffusion of oxygen ions on LSCF (P_{C2}) were observed to increase during the test which could be attributed to the Cr poisoning. Moreover, some oscillation for the peaks assigned to the gas diffusion processes (P_{A3} and P_{C3}) during the test could be also observed.

Figure 167 shows the EIS curves and DRT spectra under OCV during the galvanostatic test at 0.5 A/cm^2 under 800 °C for OC11 and OC11LZA. Same as baseline and commercial alloys, the ohmic resistance of OC11 and OC11LZA almost stayed constant as well. However, the polarization resistances of OC11 and OC11LZA had a smaller increase than that of commercial alloys (Figure 167a and b). Six peaks can also be observed for the AFA alloys in the calculated DRT spectra (Figure 167c and d). Likewise, the peaks P_{A1} and P_{A2} had a minor change during the entire galvanostatic test. Moreover, P_{C1} and P_{C2} were also observed to increase during the test which could be also assigned to the Cr poisoning whose increase was much lower than the commercial alloys.

Subtask 4.3 Post-Mortem Analysis

Cross-sectional images of cells tested with alloys

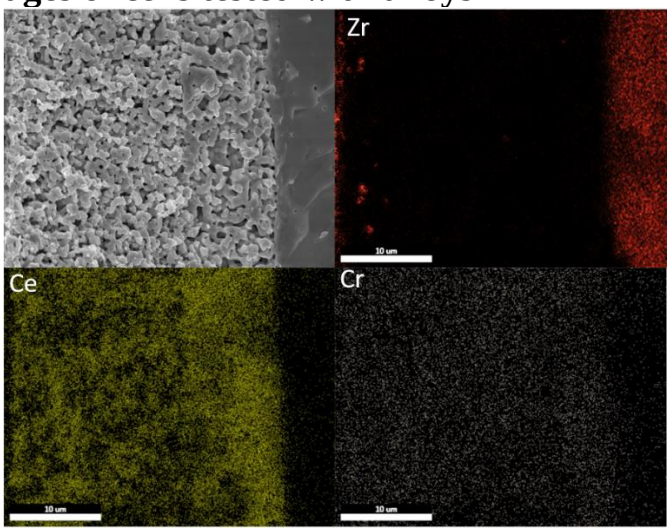

Figure 168 SEM/EDX mapping of the cross-sectional of the anode-supported cell under a constant current density of 0.5 A cm^{-2} at 800 °C with 310S.

In order to analyze the microstructures and Cr distribution at cathode/electrolyte interfaces, cross-sectional images of anode-supported cells tested with 310S, 625, OC11 and OC11LZA under a constant current density of 0.5 A cm^{-2} at 800 °C was characterized by SEM/EDS mapping. It can be seen from Figure 168-171 that the LSCF-GDC composite cathode has a porous structure with small grains (1-3 microns) on a barrier GDC layer and a dense YSZ electrolyte. As shown in Figure 168, different from the deposition of Cr gaseous species at LSM cathode/electrolyte interface, the deposition of Cr species distributed on all the cathode region and the interface region which is attributed to the different sites where oxygen reduction reaction takes place. Distinct deposition of Cr species on the cathodes could be obviously observed for 310S(Figure 168) and 625 (Figure 169). However, there is just slight Cr deposition near the interface could be observed for OC11 (Figure 170) and OC11LZA which is much less than 310S and 625 (Figure 171). And all these SEM mapping results are consistent with the electrochemical results that discussed before.

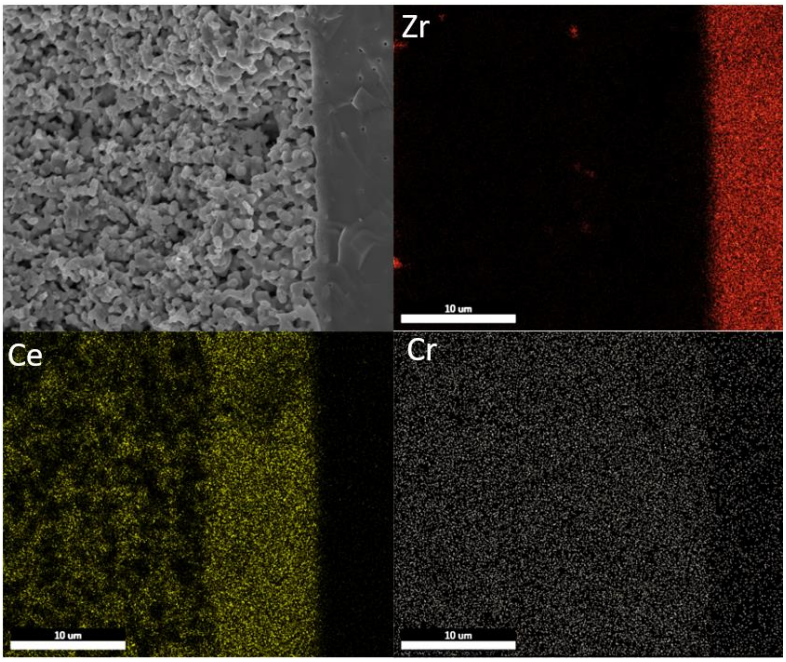

Figure 169 SEM/EDX mapping of the cross-sectional of the anode-supported cell under a constant current density of 0.5 A cm^{-2} at 800 °C with 625.

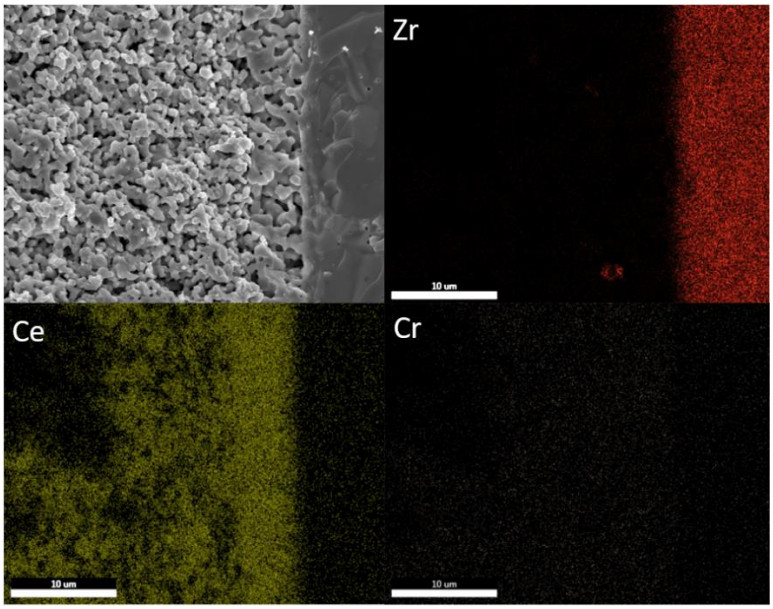

Figure 170 SEM/EDX mapping of the cross-sectional of the anode-supported cell under a constant current density of 0.5 A cm^{-2} at 800 °C with OC11.

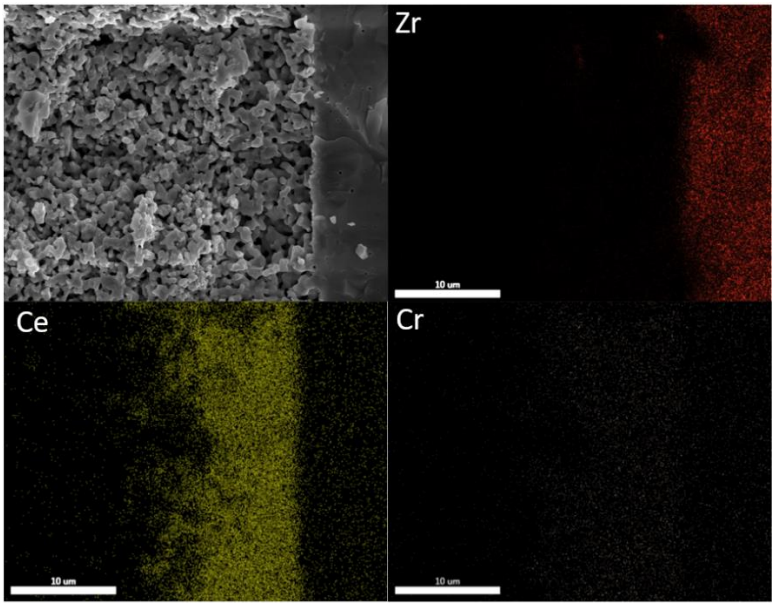

Figure 171 SEM/EDX mapping of the cross-sectional of the anode-supported cell under a constant current density of 0.5 A cm^{-2} at 800 °C with OC11LZA.

Xrd profiles of alloys after cell test

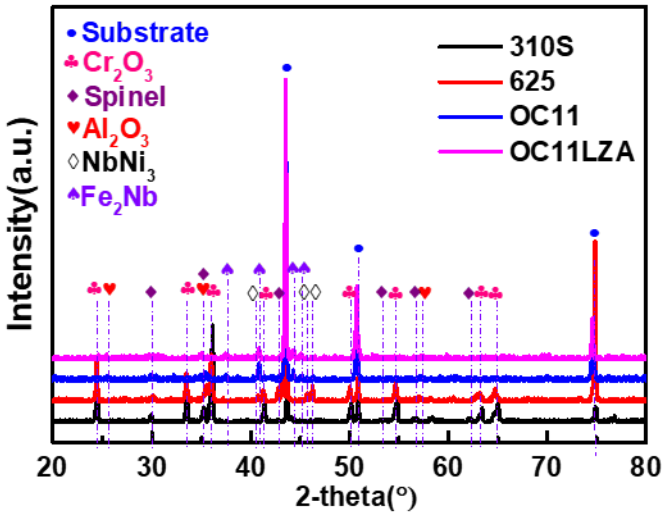

Figure 172 XRD patterns of 310S, 625, OC11 and OC11LZA samples after 500h operation with cell.

Figure 172 shows XRD patterns of 310S, 625, OC11 and OC11LZA alloy after tested with cells for 500h. The results reveal that $(Mn, Cr)_3O_4$ spinel and Cr_2O_3 are the two major phases formed during cell operation for 310S and 625 sample at 800°C. One can notice that the main difference of XRD patterns of 310S from 625 is the formation of $NbNi_3$. However, the main peaks for OC11 and OC11LZA after the 500h cell operation are the substrate and Fe_2Nb Laves phases which demonstrates that the oxide scales formed on the AFAs could be thinner than 10 microns. For AFA alloys, substrate peaks can be observed as the main peak couple with some small peaks of alumina.

No spinel and Cr_2O_3 peaks could be observed after only 500h cell operation. It could be deduced that AFA alloys exhibited significantly greater oxidation resistance than the chromia-forming 310S and 625 in cathode regions environments which indicates of great interest for the BoP application in SOFC industry.

Cross-sectional images of alloys after cell test

Figure 173 shows the surface morphology of alloys after 500h operation with cell. After operation for 500h (Figure 173a), plate-like oxides and some diamond-like oxides covered the entire surface. According to the corresponding XRD pattern (Figure 172), these two phases can be identified as Cr_2O_3 and $(Cr, Mn)_3O_4$, respectively. Spinel grains with different sizes can be observed at higher magnification (Figure 173b). For the 625 alloy tested after 500 h operation (Figure 173c), diamond-like oxides with different sizes uniformly covered the whole surface which can be attributed to the $(Cr, Mn)_3O_4$. For the OC11 alloy, numerous oxide nodules are formed and cover the entire surface after the cell operation (Figure 173e). Moreover, the size of these particles is about 0.3μm which could be assigned to the Fe-Al-Cr-Mn-rich oxides (Figure 173f). The morphology of OC11LZA is similar to that of OC11. However, there are oxides with bigger sizes formed on the surface of OC11LZA than OC11 which could be attributed to the Nb-rich oxides(Figure 173g).

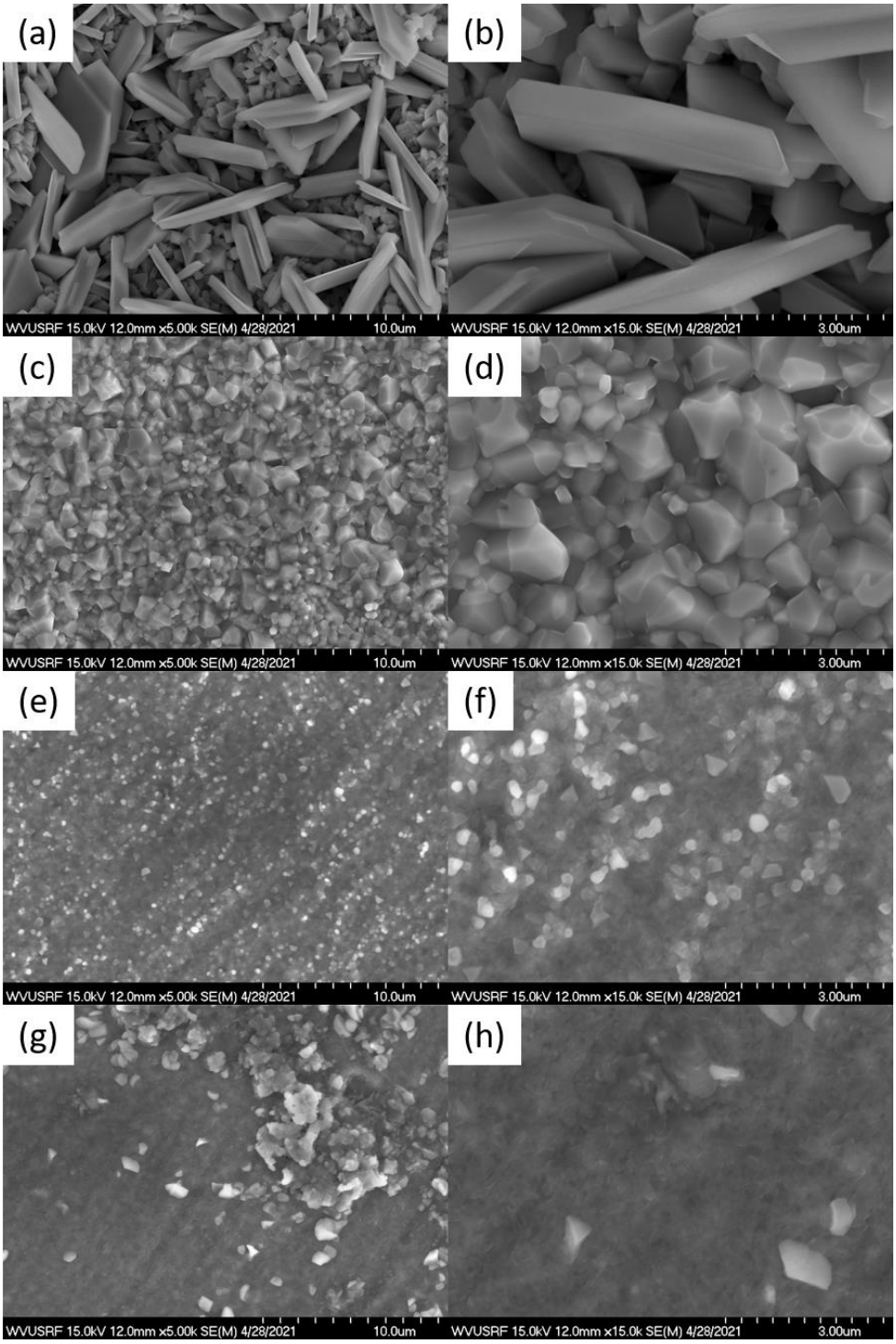

Figure 173 SEM surface morphologies of (a, b) 310S, (c, d) 625, (e, f) OC11 and (g, h) OC11LZA samples after 500h operation with cell.

Comparison between commercial alloys and AFA alloys

To further demonstrate the superior properties of AFA alloys to commercial alloys, the formed oxide scales on each alloy and how they affect the evaporated Cr species from each alloy. At the initial stage, taking the diffusion rate of the each element and the growth rates of different oxides,

$(Fe, Cr)_2O_3$ oxide forms earliest on the surface of 310S (NiO and Cr_2O_3 oxide forms earliest on the surface of 625). In addition, it has a high oxidation resistance which can decrease both the Cr outward diffusion and the O inward diffusion. However, $(Fe, Cr, Mn)_3O_4$ spinel will form on the earliest formed oxide which can be attributed to the high solubility and mobility of Mn ions. With the cell test operating, the evaporated Cr vapor species which is caused by the reaction between chromium oxide and oxygen at the cathode region can be brought with air to the cathode, thus contributing to the severe degradation of cell. However, compared with the commercial alloys, the formed outmost oxide layer is mainly consisted of Cr_2O_3 with minor Fe_2O_3, MnO_2 and Al_2O_3 which can greatly decrease the oxygen partial pressure at the oxide scale/substrate interface, thus facilitating the selective oxidation of aluminum. In addition, the third-element effect of Cr also significantly contributes to the formation of continuous alumina layer beneath the Cr_2O_3. Wagner reported that Cr can play a role as oxygen getter in alloys, the outward diffusion of aluminum is largely reduced when these chromium oxides form which also prevents the internal oxidation of aluminum and decreased the critical level of aluminum to form a continuous layer. Therefore, outward diffusion of Cr from the alloy matrix to the scale surface are vastly prevented that caused much less Cr deposition on the cathode which doesn't lead to a precipitous degradation of the cells.

Task 5.0 Investigation of AFA's Key Properties for BOP Applications – ORNL & BE
Subtask 5.1 Long-term Oxidation Kinetics

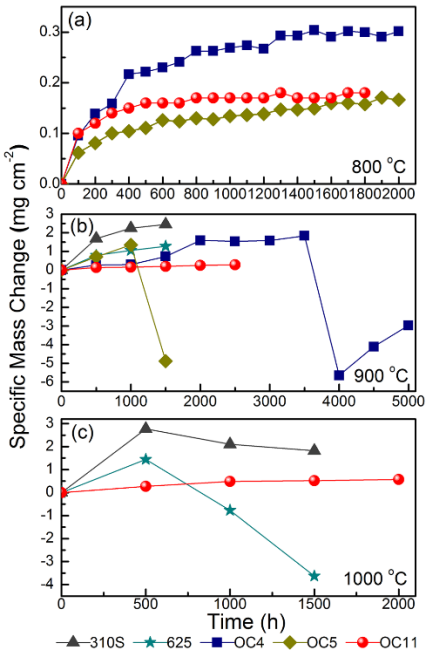

Figure 174 Specific mass change for commercial alloys (310S and 625) and AFA alloys under different temperatures.

As shown in Figure 174, for the AFA alloys tested at 800 ºC, low oxidation rates were exhibited by these three kinds of AFA alloys. OC5 and OC11 showed comparative oxidation rate about 0.15 mg/cm^{-2}, whereas OC4 exhibited two times higher oxidation behavior than OC5 and OC11. However, there is a different story for the samples tested at 900 ºC, the oxidation rates are much higher than that under 800 ºC. OC11 demonstrated a little higher oxidation rate than OC4, however, OC11 exhibited lower oxidation rate than OC4 at 800 ºC because OC11 is designed to work at temperature above 850 ºC. 310S exhibited the highest oxidation rate under 900 ºC. OC4 and OC5 transitioned to mass loss after operation for 1000h and 3500h, respectively. This should be attributed to the scale spallation. At 1000 ºC, the 310S and 625 transitioned to mass loss after only 500h operation, whereas the OC11 exhibited low rates of oxidation which was related to the protective alumina scale formation.

The results to date of ongoing oxidation studies conducted at ORNL at 900 and 1000°C in air + 10% H_2O are shown in Figures 175 and 176. Most of the exploratory AFA compositions exhibited superior oxidation resistance to the chromia-forming commercial alloys 310S stainless steel and Ni-base alloy 625, which suffered from oxide scale spallation and exhibited substantial mass losses. Testing at 1000°C (Figure 175 a, b) as an accelerated condition revealed excellent oxidation resistance for the original OC11 and 35Ni AFA variations. Replacement of costly Hf in the original OC11 formulation with Zr ± Y (OC11LZ alloy variations) has yielded moderately reduced, but still promising oxidation resistance. Most of the initial Bloom Energy alloy producer partner small scale trial AFA sheet products (OBH alloys) are exhibiting promising oxidation resistance at 1000°C thus far, although several variants experienced local oxidation nodules and a transition to rapid oxidation (Figure 175 c). At 900°C (Figure 176 a, b), multiple variations of ORNL AFA alloys are showing promising oxidation resistance. Similar to the oxidation trends observed at 1000°C, the OBH alloys are exhibiting promising levels of oxidation resistance at 900°C, with the exception of several variants (Figure 176 c). Cross-sectioning of alloys after

1000°C and 900°C exposures are planned once target oxidation test times are reached, typically 5000 to 10,000 hours.

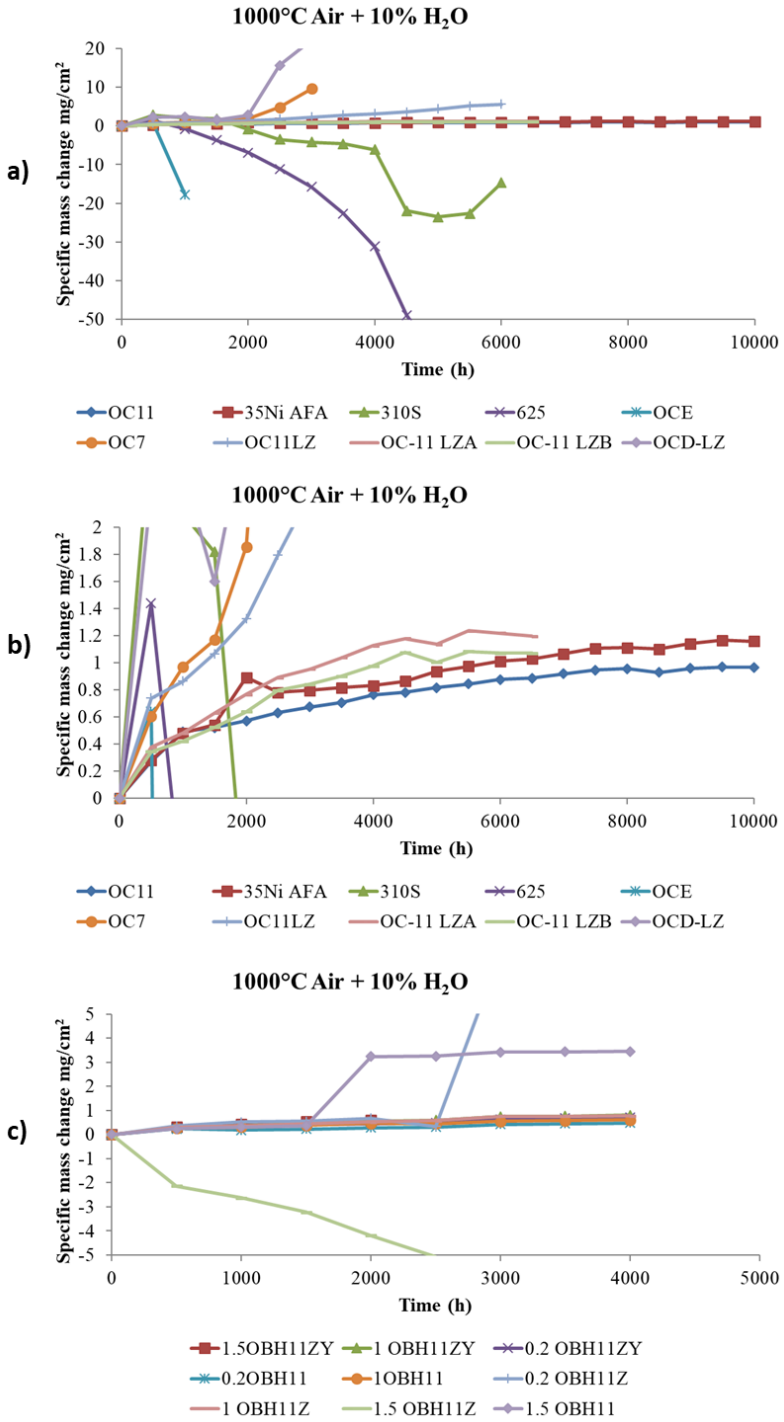

Figure 175 Specific mass change at 1000°C in air with 10% H_2O (500 h cycles). a) exploratory ORNL AFA alloys compared to 310S and 625; b) same data as a) at a different mass change scale; c) initial Bloom Energy alloy producer partner AFA alloy sheet (OBH alloys, details proprietary)

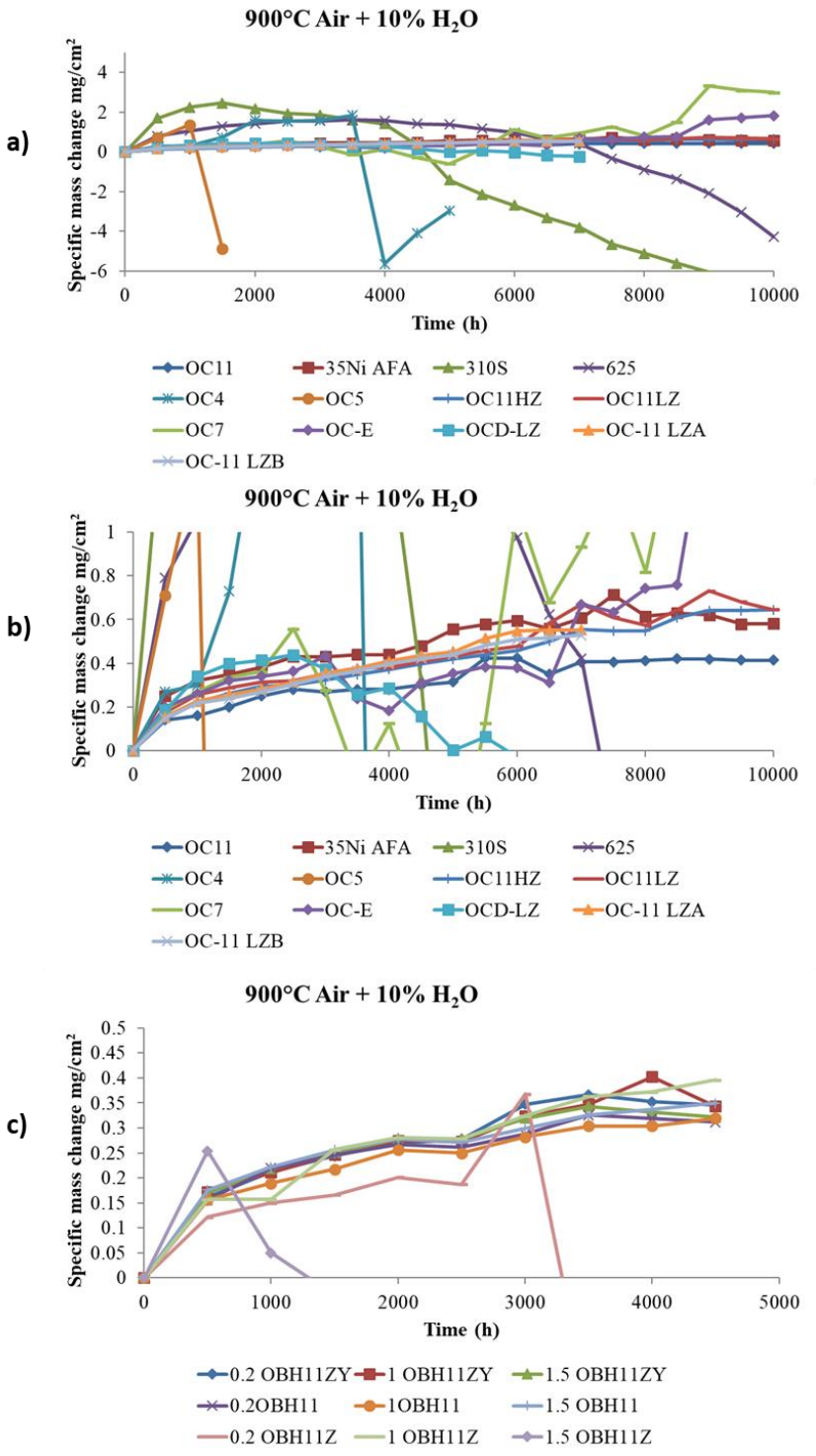

Figure 176 Specific mass change at 900°C in air with 10% H_2O (500 h cycles). a) exploratory ORNL AFA alloys compared to 310S and 625; b) same data as a) at a different mass change scale; c) initial Bloom Energy alloy producer partner AFA alloy sheet (OBH alloys, details proprietary).

Long-term oxidation exposures at 900 and 1000°C in air + 10% H_2O continued at ORNL for several sets of AFA alloys modified for improved manufacturability and reduced raw element cost (primarily replacement of Hf with Zr, and reduction in Nb levels). Several of these alloys have

now reached 8000 h of exposure, with cross-sectioning planned at 10,000 h. Two new alloy sets were added to the oxidation testing in FY2020 Q1 and Q2 and have accumulated 1500 to 2000 h of exposures to date (Figure 177). The first set, OBH11-Z1, Z2, and Z3 was supplied by Bloom Energy via their alloy producer partner(s) and is designed to aid in understanding specification range sensitivity to oxidation resistance of a key element impacting manufacturability for thin sheet product needed for some balance of plant components. The second set of alloys were manufactured at ORNL (OC11LZB series) to assess specification range sensitivity of an additional key element for oxidation resistance, with select corresponding creep tests also to be initiated. Compositional details of these alloys are currently considered confidential. All these new alloys are exhibiting low mass gains and promising oxidation resistance consistent with protective alumina scale formation at 900°C in air + 10% H_2O. At 1000°C, which is being used as an accelerated test protocol and is above targeted use temperatures, several alloys have exhibited transitions to non-protective oxidation behavior as evidenced by sudden large mass gains or mass losses.

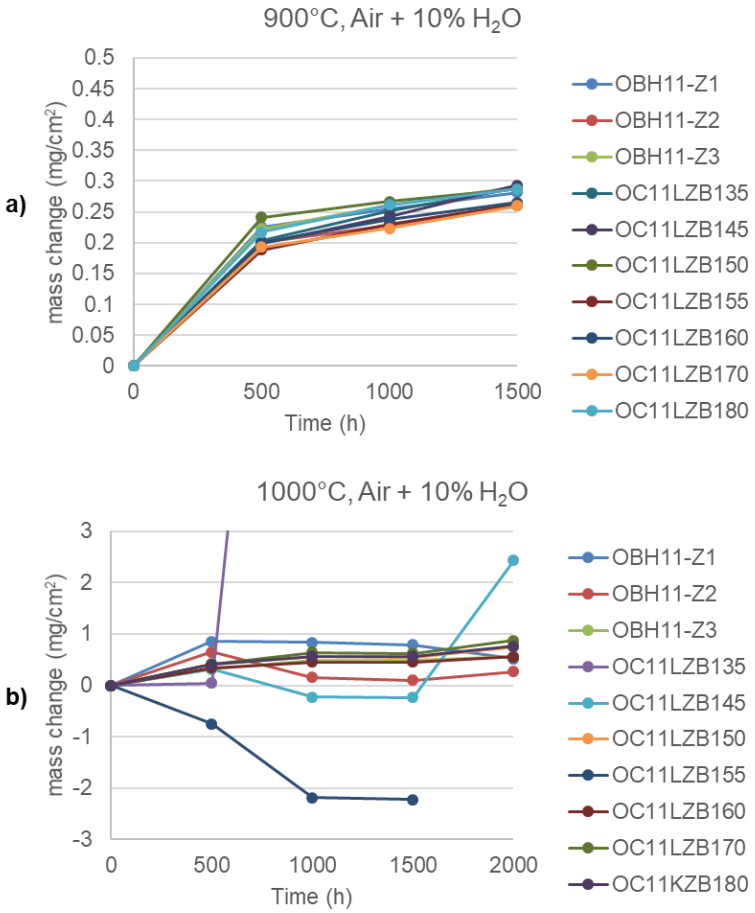

Figure 177 Specific mass change data at 900 and 1000°C in air with 10% H_2O (500 h cycles).

Long-term oxidation exposures at 900 and 1000°C in air + 10% H_2O continued at ORNL for several sets of AFA alloys modified for improved manufacturability and reduced raw element cost (primarily replacement of Hf with Zr, and reduction in Nb levels). 1000°C condition is being used as an accelerated test protocol. Two of these alloys have now reached 9500 h of exposure. The

cross-sectioning analysis will be conducted at 10,000 h. Figure 178a shows oxidation at 1000°C in air with 10% H_2O for baseline chromia-forming 310S and 625 alloys, baseline AFA alloy OC11 which uses Hf and Y, the modified AFA alloy OC11LZA which uses Zr instead of Hf along with no Y, and a further variation OC11LZB which also lowers the Nb content. The chromia-forming alloys exhibited a transition to spallation and mass loss after 1000 to 2000 h of exposure under this aggressive condition (previously reported). The mass change for the AFA alloys are very similar, which suggests that alloy modifications for improved manufacturability can be achieved without a significant detriment in oxidation resistance. Bloom Energy and their alloy producer partner are currently performing scale up evaluations of variations of the OC11LZA and B compositions. A second set of alloys to further assess variations of OC11LZB were manufactured at ORNL and put to testing in Q1 FY20 (compositional details of these alloys are currently considered confidential). These new alloys have thus far exhibited low mass gains consistent with good oxidation resistance at 900°C in air + 10% H_2O after 2500 h of exposure. At 1000°C in air + 10% H_2O (Figure 178b), several alloys have exhibited transitions to non-protective oxidation behavior as evidenced by sudden large mass gains or mass losses, with the remainder continuing to show promising oxidation resistance.

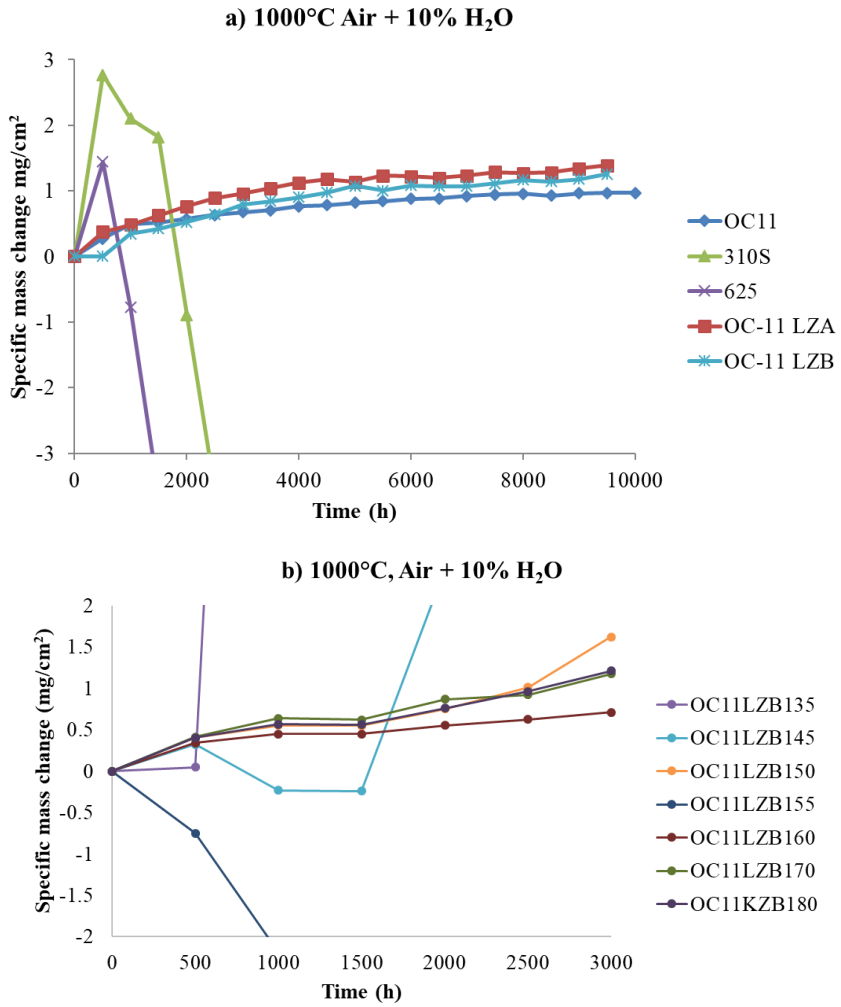

Figure 178 Specific mass change data at 1000°C in air with 10% H_2O (500 h cycles).

Subtask 5.2 Characterization of oxide scales – ORNL

In Phase I, more samples had been characterized using STEM/EDS and XPS and the results are listed below.

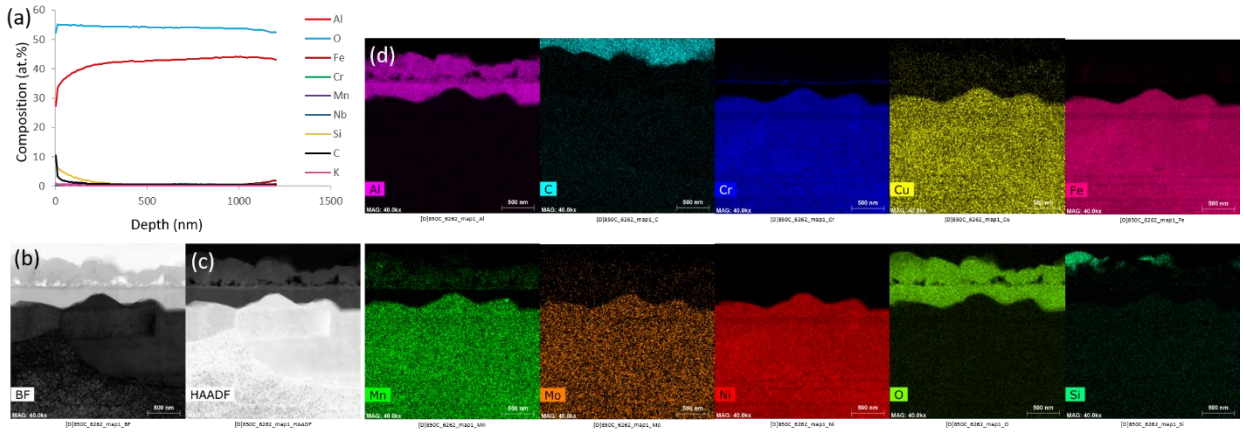

Figure 179 Oxide scales formed on AFA OC5 alloy after 500 h oxidation at 850 ºC in air + 10% H_2O. (a) XPS sputter depth profiles, (b) STEM Bright-field (BF) image, (c) STEM High-angle annular dark-field (HADDF) image, (d) corresponding EDX elemental maps.

Figure 179 presented the STEM-EDX mapping of the oxide scale formed on AFA OC5 alloy after 500 h oxidation at 850 ºC in air + 10% H_2O. XPS sputter depth profile data showed that the oxide was rich in Al, but also contained a small amount of Si. Cross-sectional STEM/EDS analysis showed that the scale consisted of a 40- to 50-nm inner region of columnar a-Al_2O_3 adjacent to the alloy and an overlying 60- to 100-nm-thick, intermixed layer of transition Al_2O_3 + Cr_2O_3 + porosity. In some scale regions, a 0.05- to 0.5-µm columnar-grained surface layer of intermixed Al-Cr-Mn-Fe-Cu-Mo-O–rich phase was also observed, and SiO_2 was observed formed on the top of the oxide scale.

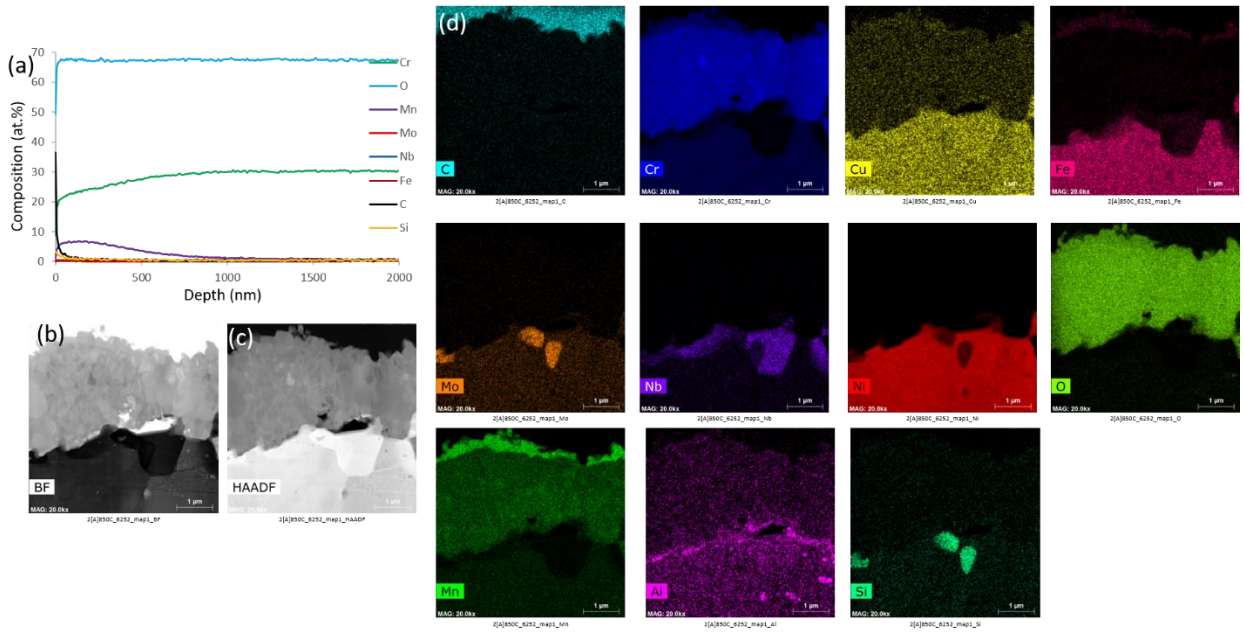

Figure 180 Oxide scales formed on 625 alloy after 500 h oxidation at 850 °C in air + 10% H_2O. (a) XPS sputter depth profiles, (b) STEM Bright-field (BF) image, (c) STEM High-angle annular dark-field (HADDF) image, (d) corresponding EDX elemental maps.

Figure 180 presented the STEM-EDX mapping of the oxide scale formed on AFA OC5 alloy after 500 h oxidation at 850 °C in air + 10% H_2O. XPS sputter depth profile data showed that the oxide was rich in Cr, but also contained a small amount of Mn. Cross-sectional STEM/EDS analysis showed that the scale consisted of an inner region of Si-Nb-Mo-Al precipitation adjacent to the alloy and an overlying 1- to 1.5-µm-thick, intermixed layer of transition Cr-Mn-Cu-Al-O-rich phase. In the top of the scale regions, a surface layer of intermixed Cr-Mn-Fe–rich phase was also observed.

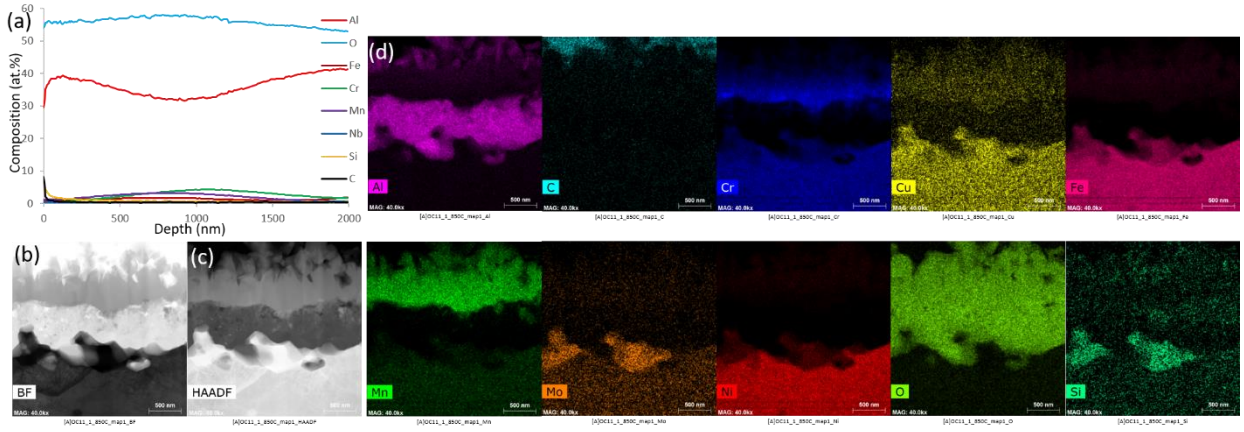

Figure 181 Oxide scales formed on AFA OC11 alloy after 500 h oxidation at 850 °C in air + 10% H_2O. (a) XPS sputter depth profiles, (b) STEM Bright-field (BF) image, (c) STEM High-angle annular dark-field (HADDF) image, (d) corresponding EDX elemental maps.

Figure 181 presented the STEM-EDX mapping of the oxide scale formed on AFA OC11 alloy after 500 h oxidation at 850 °C in air + 10% H_2O. Similar as OC5, XPS sputter depth profile data showed that the oxide was rich in Al, however, OC11 contained a small amount of Cr and Mn. Cross-sectional STEM/EDS analysis showed that the scale consisted of a 300- to 500-nm inner

region of columnar a-Al_2O_3 adjacent to the alloy and an overlying 60- to 100-nm-thick, intermixed layer of transition Al_2O_3 + Cr_2O_3 + SiO_2+porosity. In some scale regions, a 0.05- to 0.5-mm columnar-grained surface layer of intermixed Al-Cr-Mn-Fe-Cu-Ni-O–rich phase was also observed.

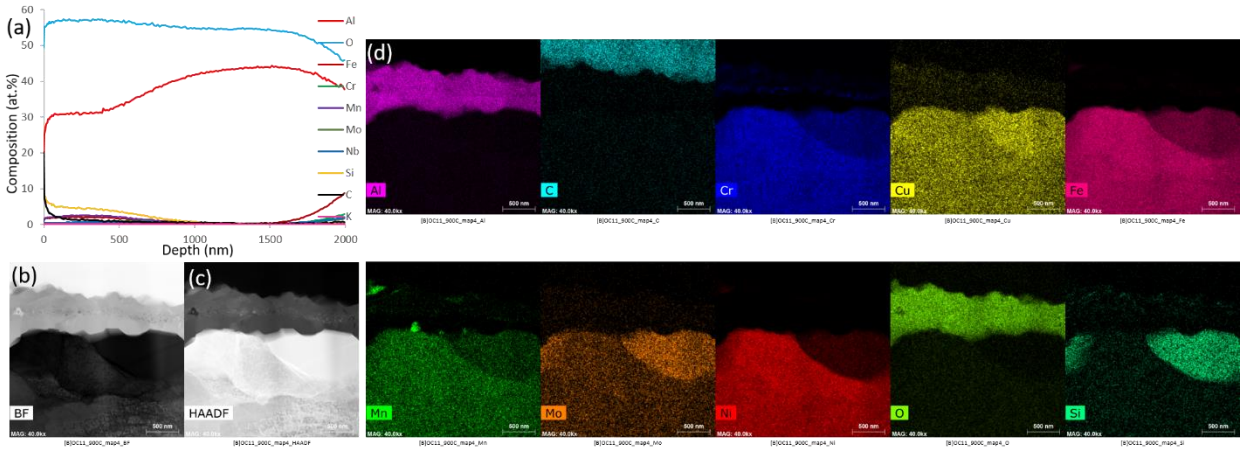

Figure 182 Oxide scales formed on AFA OC11 alloy after 500 h oxidation at 900 ºC in air + 10% H_2O. (a) XPS sputter depth profiles, (b) STEM Bright-field (BF) image, (c) STEM High-angle annular dark-field (HADDF) image, (d) corresponding EDX elemental maps.

Figure 182 presented the STEM-EDX mapping of the oxide scale formed on AFA OC11 alloy after 500 h oxidation at 900 ºC in air + 10% H_2O. Similar as OC11 tested under 850 ºC, XPS sputter depth profile data showed that the oxide was rich in Al, however, OC11 tested under 900 ºC contained a small amount of Si. Cross-sectional STEM/EDS analysis showed that the scale consisted of a 200- to 300-nm inner region of columnar a-Al_2O_3 adjacent to the alloy and an overlying 40- to 60-nm-thick, intermixed layer of transition Al_2O_3 + Cr_2O_3 + porosity. In some scale regions, a 0.05- to 0.5-mm columnar-grained surface layer of intermixed Al-Cr-Mn-Cu-O–rich phase was also observed, and SiO_2 was also observed formed on the top of the oxide scale.

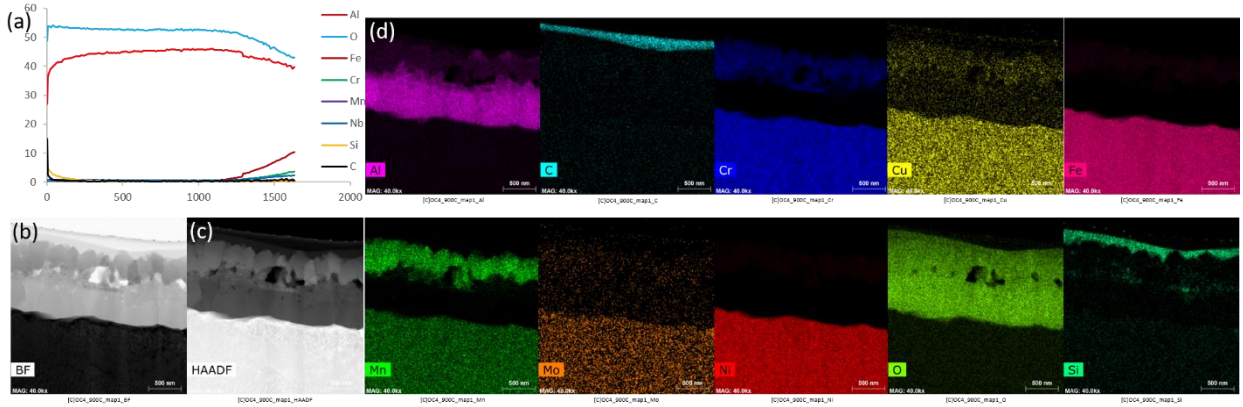

Figure 183 Oxide scales formed on AFA OC4 alloy after 500 h oxidation at 900 ºC in air + 10% H_2O. (a) XPS sputter depth profiles, (b) STEM Bright-field (BF) image, (c) STEM High-angle annular dark-field (HADDF) image, (d) corresponding EDX elemental maps.

Figure 183 presented the STEM-EDX mapping of the oxide scale formed on AFA OC4 alloy after 500 h oxidation at 900 °C in air + 10% H_2O. XPS sputter depth profile data showed that the oxide was rich in Al, but also contained a small amount of Fe and Si. Cross-sectional STEM/EDS analysis showed that the scale consisted of a 400- to 600-nm inner region of columnar a-Al_2O_3 adjacent to the alloy. In upper scale regions, a 0.05- to 0.5-mm columnar-grained surface layer of intermixed Al-Cr-Mn-Fe-Cu-Mo-O–rich phase was also observed, and SiO_2 was observed formed on the top of the oxide scale.

Cross-sectional morphology of commercial alloys and AFA alloys under different temperature after tested for different time are shown in Figure 184-186. For the first 500 h, the thickness of the oxide scales formed on AFA specimens is about 0.7-1 μm (Figure 185b and 186a), while the thickness of alloy 310S is about 2 μm (Figure 184a). After 500 h test (Figure 184a), the oxide scales on alloy 310S display an outer (Cr, Mn)-rich oxide layer, which coincides with the results of XRD. In addition, parallel cracks formed at the oxide/alloy interface are evident. However, for the AFA alloys, there is no cracks observed, three different oxide layers are well arranged, including continuous inner Al_2O_3 layer, duplex transient scale of intermediate Cr_2O_3 layer and outer Cr-Mn-Al rich oxide layer. With continuing the oxidation test to 1000 h, for alloy 310S the thickness of the oxide scale increases to about 3 μm, and it is observed that cracks merge together and form big gaps, and consequently decrease the mechanical stability of oxide (Figure 184c). In the case of AFA alloys, not only there is absence of pores, also the formation of uniform oxides at the oxide/alloy interface characterizes the oxidation performance of AFA alloys compared to the alloy 310S (Figure 185c and 186c).Moreover, the thickness of the oxide scale formed on AFA alloys almost remained the same. Comparing the Fe and Cr line scans (Figure 184d and 185d), it is clearly shown that alloy 310S suffers from Fe and Cr depletion in the sub-scale regions after 1000 h oxidation which could result in the spallation of oxide scales. After 2000 h test, the development of holes and cracks results in the spallation of the oxide scale on specific surface sites (Figure 184e) and furtherly results in the formation of uneven and non-uniform oxide layers which thickness is about 4.5 μm for alloys 310S. In contrast, no cracks can be observed for the AFA alloys and the thickness remained the same. Formation of peg-like oxides could be observed on OC4 other than OC5. Obviously, inward diffusion of oxygen along the grain boundaries leads to the formation of peg-like oxides which can increase the adherence of the scale to the alloy, thus avoiding initial oxide spallation. After 5000 h test, more spallation areas could be obviously observed for alloys 310S, both line scans and cross-section morphology reveals that the Fe and Cr depletion beneath the oxide layer corresponds to the spallation area. In contrast, AFA alloy still possess a more uniform oxide scale and no defects could be observed (Figure 185g and 186g). One thing that should be bear in mind that after exposures (more than 1000 h), the outmost and the intermediate oxide layer on AFA alloys disappear which is assigned to the spallation of outmost layer and the evaporation of Cr gaseous species from the intermediate layer.

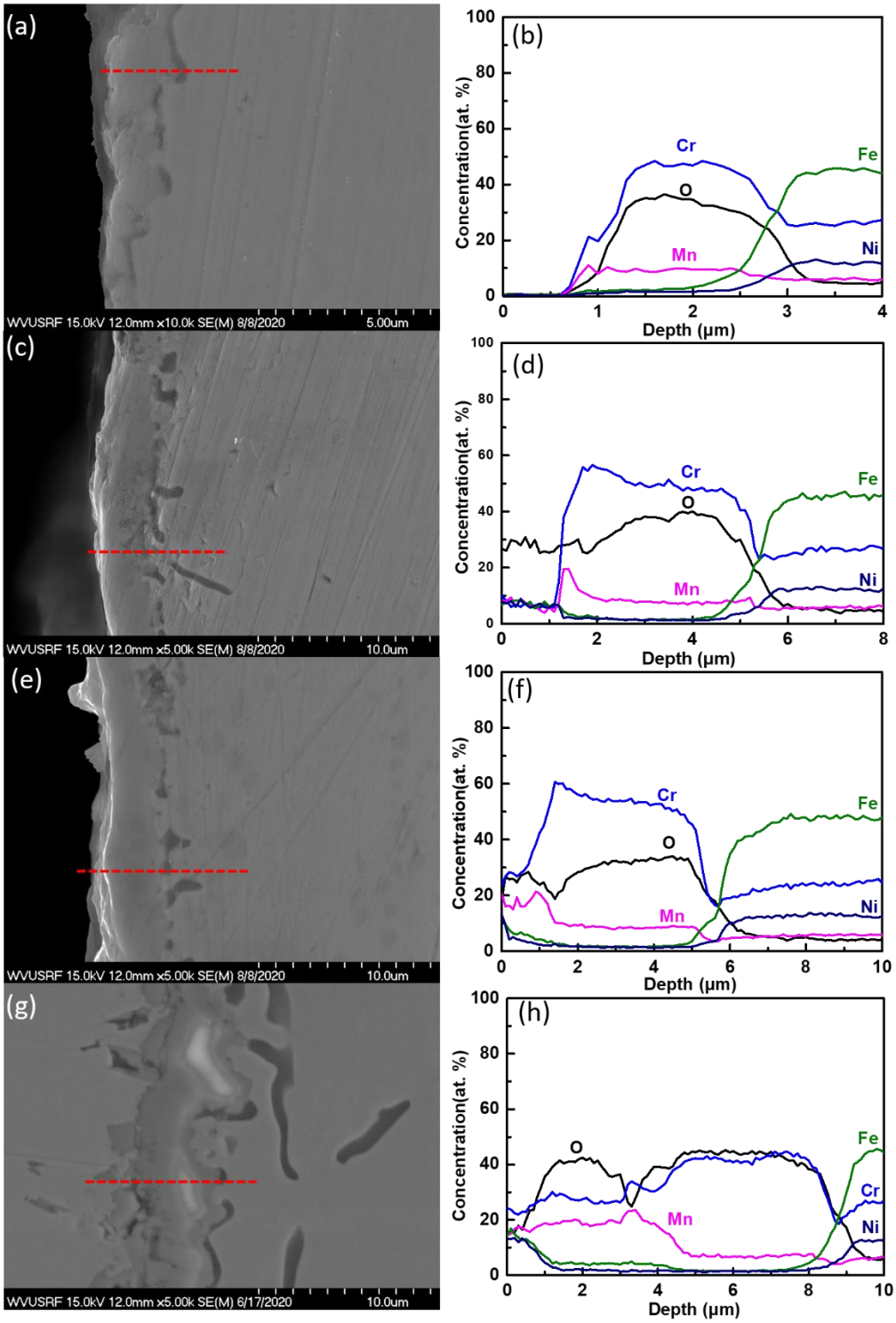

Figure 184 Cross-section profiles of oxide scales formed on alloy 310S tested for different durations: (a, b) 500 h, (c, d) 1000 h, (e, f) 2000 h, and (g, h) 5000 h.

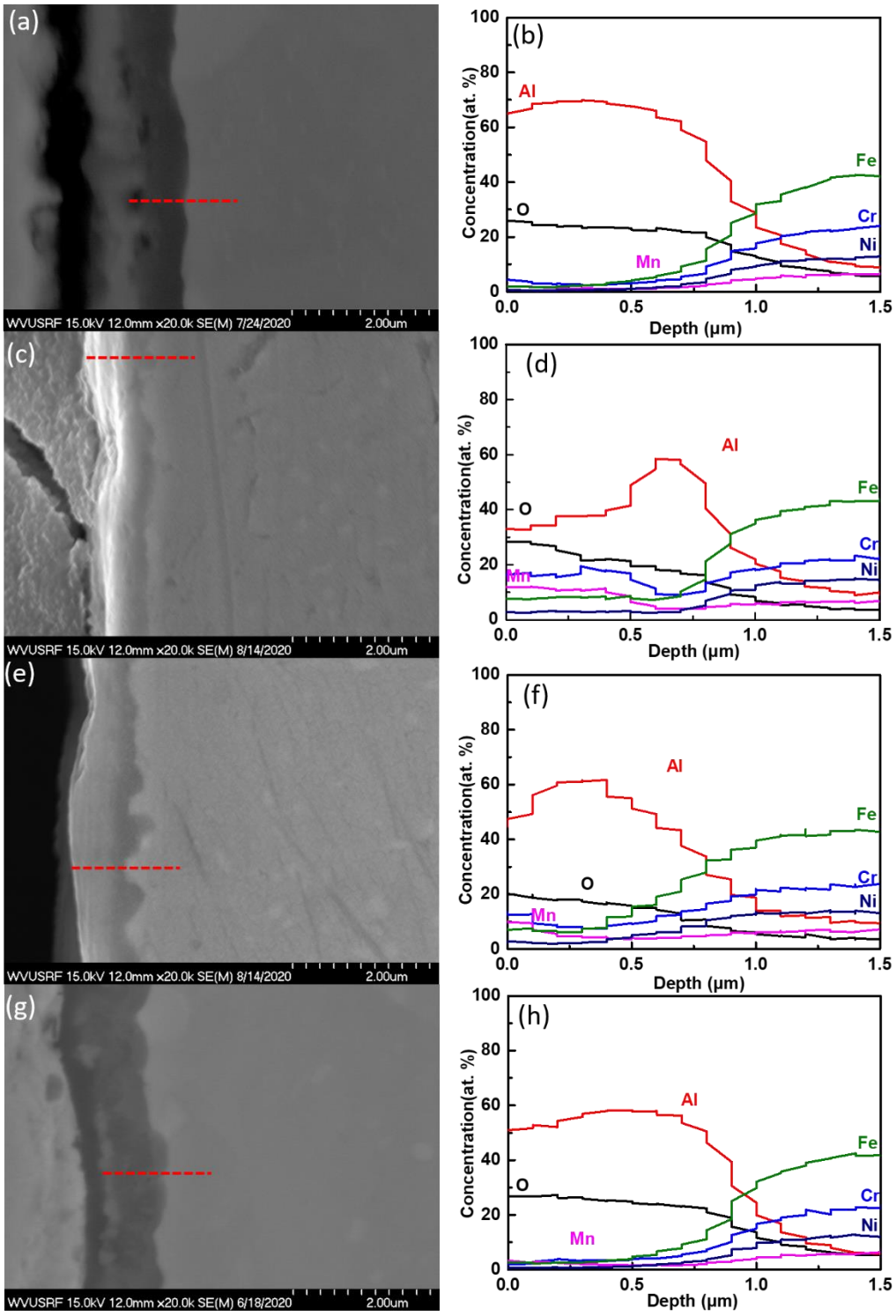

Figure 185 Cross-section profiles of oxide scales formed on alloy OC4 tested for different durations: (a, b) 500 h, (c, d) 1000 h, (e, f) 2000 h, and (g, h) 5000 h.

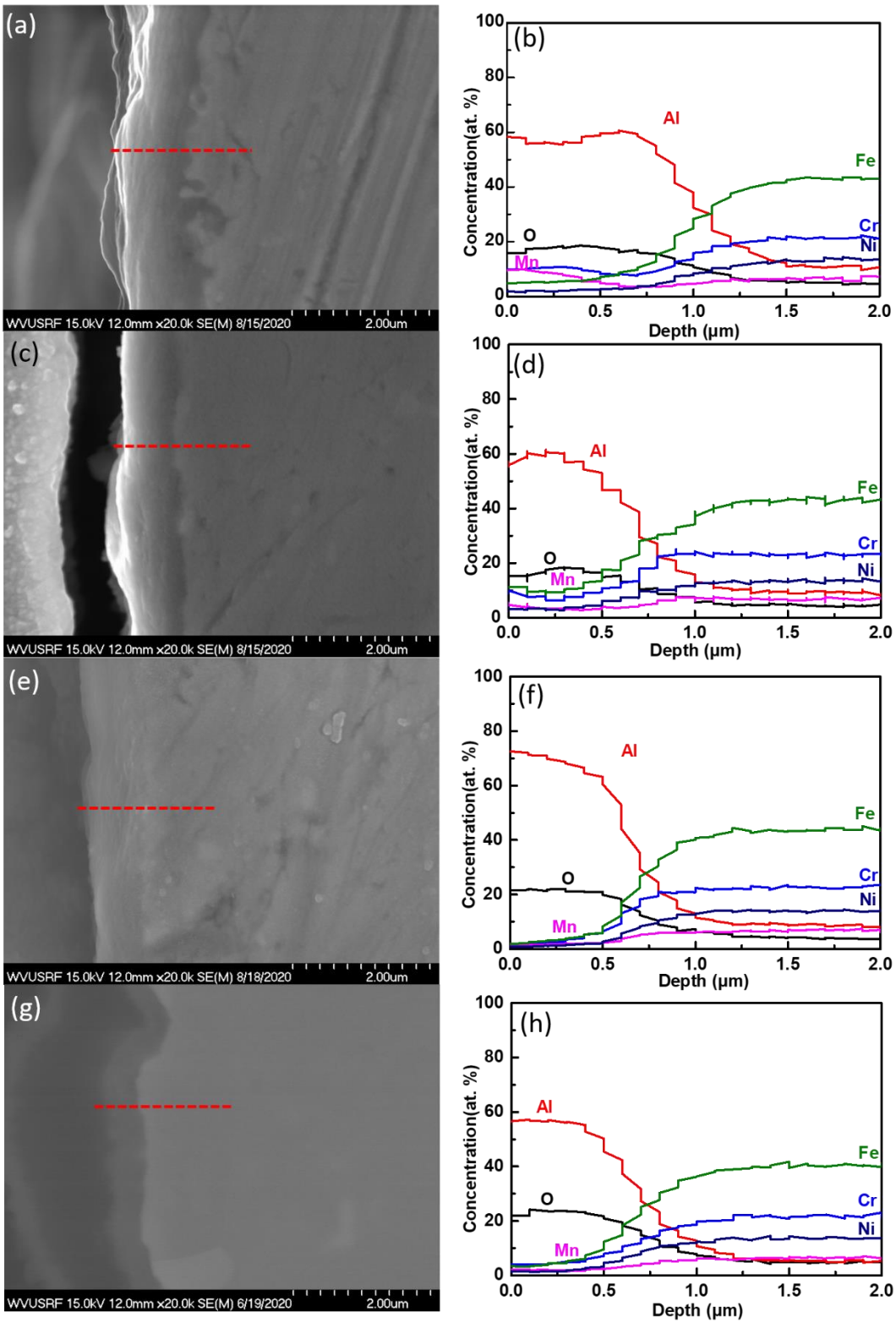

Figure 186 Cross-section profiles of oxide scales formed on alloy OC5 tested for different durations: (a, b) 500 h, (c, d) 1000 h, (e, f) 2000 h, and (g, h) 5000 h.

Subtask 5.3 High Temperature Mechanical Properties of AFA

Evaluation of creep properties of AFA alloy OC11 (Fe-15Cr-4Al-25Ni-2Mo-2.5Nb-C base) with variations of minor alloy additions (Zr, Y, and Hf) has been conducted at ORNL (Figure 187). The initial small scale trial AFA sheet materials produced by Bloom Energy's alloy producer partner, designated as "OBH", consisted of relatively small grain size (average: 10 -16 μm) in the as-received condition and no significant differences in the grain structure was observed among the variations of minor alloying additions. The as-received OBH alloys showed a significant reduction of the creep strength compared to the original OC11 type series (OC11-LZ, -HZ, and OC4 in the plot). However, the creep-rupture performance was improved significantly in the same alloys with coarse grain structure (average: 52um, after applying additional annealing). This indicates that the creep-rupture performance in the OC11 composition range under these conditions is sensitive to the grain size, and the coarser grains the better creep performance, as expected. The upper limit grain size would be limited by the target thickness of the components (e.g. target more than 10 grains in the thickness) and needs to be coordinated with the final design of the products. A lab-scale OC11 base alloy variation (designated as "OC11-LZB") with a lower Nb addition (1.5 wt.%) also showed longer creep-rupture life than the as-received OBH alloys, even with a relatively small grain size (17 μm), suggesting an avenue to creep performance improvement. Although the oxidation resistance at elevated temperatures may be degraded by lowering the Nb content, oxidation testing thus far (Figures 185 and 186) indicates good behavior by OC11-LZB. Additional, very low Nb and high Cr containing exploratory AFA alloys, designated "SVA", exhibited very low creep resistance.

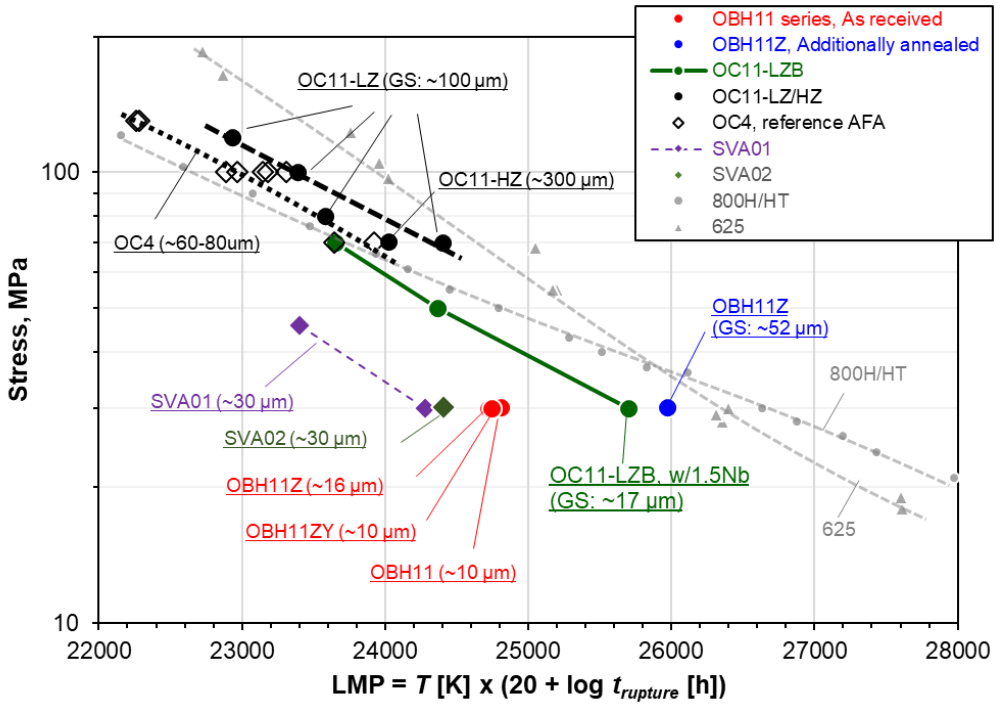

Figure 187 Larson Miller Parameter (LMP) creep data from high-load, short-term exploratory testing (typically 50 to 1000 h rupture lifetime range) for developmental AFA alloys and initial Bloom Energy alloy producer partner AFA alloy sheet OBH alloys (details proprietary). Comparisons with commercial alloy 800 and 625 creep data should be considered semi-quantitative and preliminary due to the short-term nature of the AFA creep rupture data.

Task 6.0 Manufacturing and Testing BOP Components in Industrial SOFC Systems - All
Subtask 6.1 Investigation of Manufacturability of AFA for the BOP Components

With our alloy supplier partner, we have made three (3) heats of developmental AFA alloys of size 10 Kg. Full chemical, metallographic and thermochemical characterization led us to down select two of the compositions for making 600 Kg heats each in Cycle 1B. Selected characteristics of the Cycle 1 alloy are present in Figure 188.

The alloys made in Phase 1B with 600 Kg each heats were fully processed using production machinery to make 300 mm wide sheets and foils of following four thicknesses 1.5, 1.0, 0.5 and 0.2mm. Unfortunately, several issues occurred with the processing of these large heats. Of which the most important issue was edge cracking. Examples of these cracks are shown in Figure 189.

One of the alloys from Cycle 1B has been selected to fabricate actual SOFC components for engineering evaluation in the first and second quarter of this year.

Cycle 1C of the project that is currently underway is essentially a repeat of Cycle 1B with the exception of slight changes in the chemistry and some changes in the processing that are hoped to address the cracking issue.

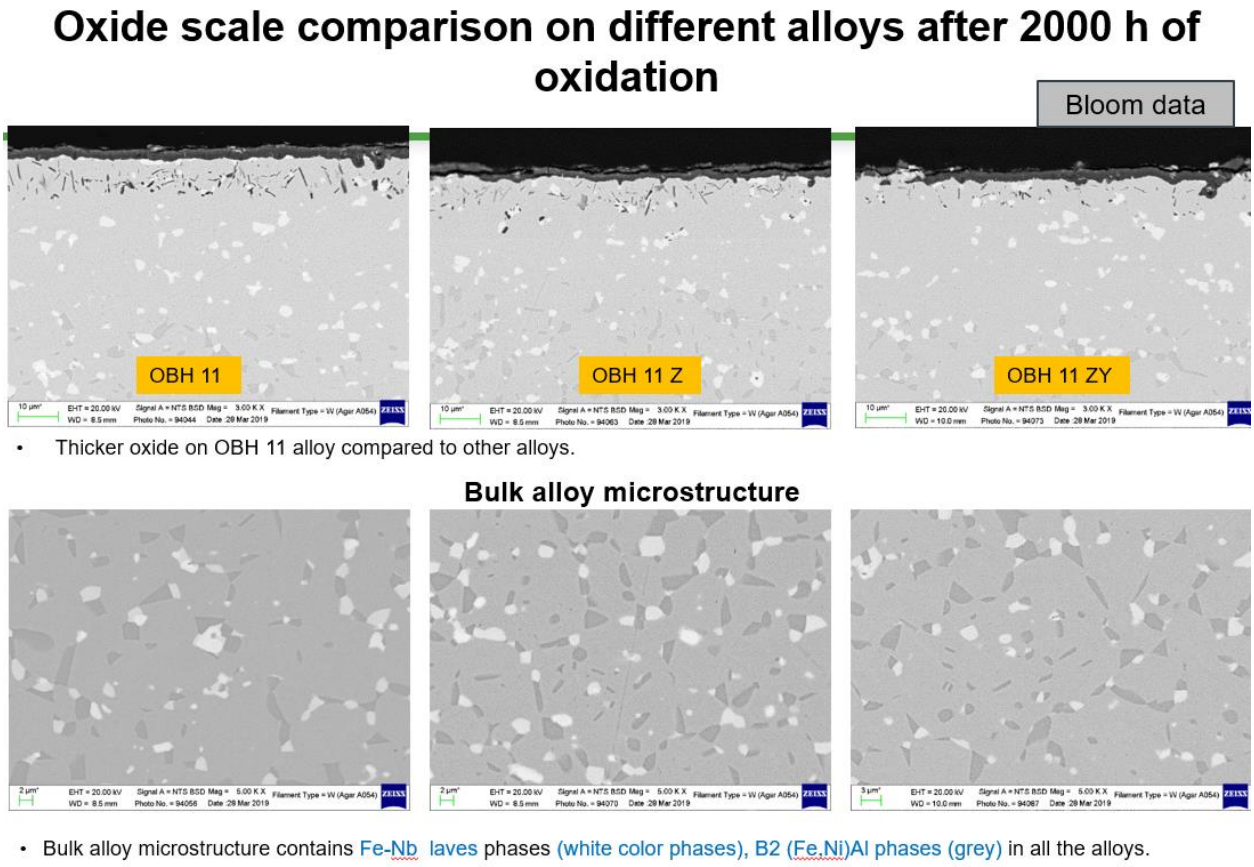

Figure 188 Alumina Scale Development on three AFA alloys in a 2000 Hrs. testing conducted in simulated SOFC environment at 850 C.

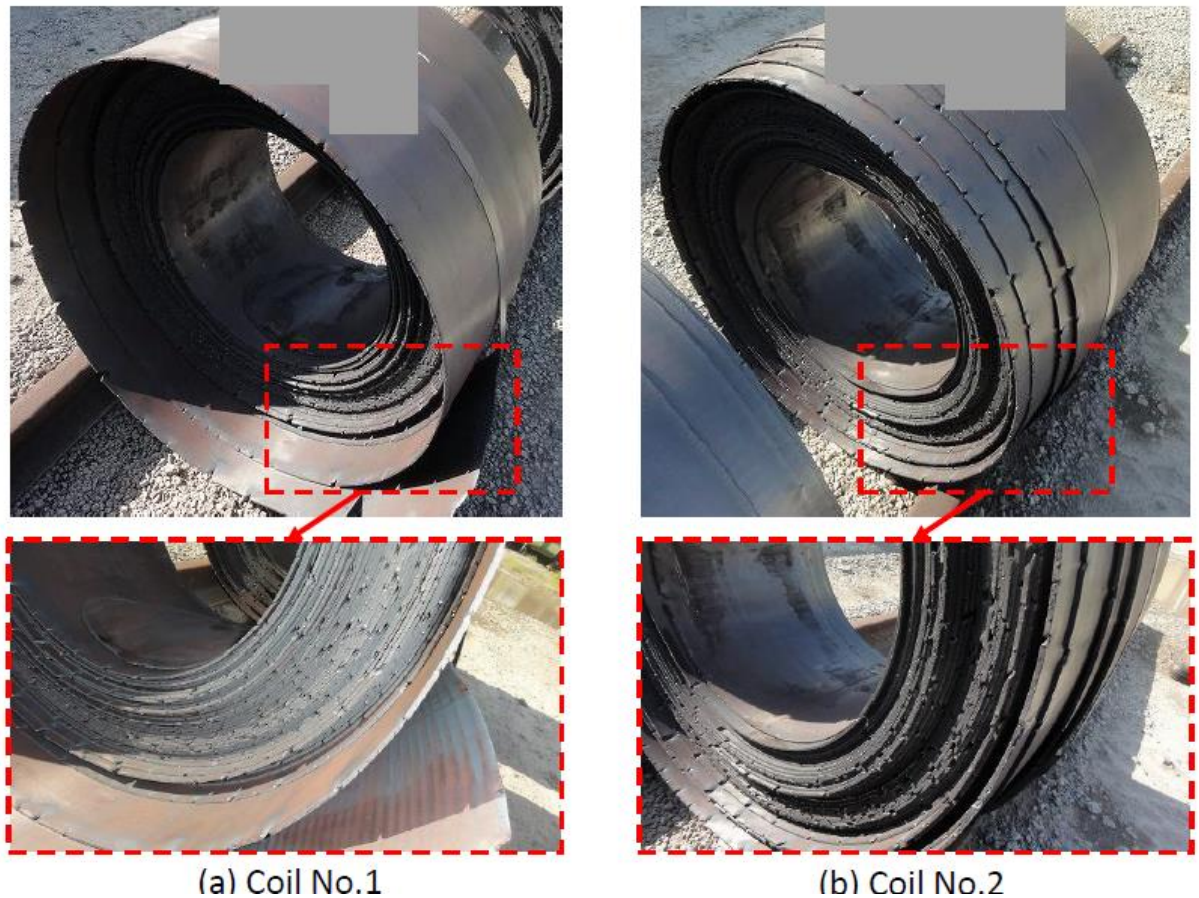

Figure 189 After hot rolling at the alloy maker, severe cracks at both edges of the sheet coils. The affected area is about 10 to 30mm from the edge.

The commercial development of AFA alloys in cooperation with a commercial alloy maker is based on the original composition proposed by ORNL.

During the Phase 1C of the development that ended in Q2 of this year, Hitachi Metals has produced two slightly different versions of the AFA alloys in 250 mm widths. This material has now been delivered to our supplier in Taiwan.

Two each hotbox worth of components have been fabricated from the materials that was produced in Phase 1B of the development. These hotboxes are being assembled with SOFC columns at BE and will go for testing at full power at the end of Q3. These systems will run at least one full quarter before autopsied for evaluation of material performance and any degradation. The two major subassemblies for one of the hotbox mentioned above are shown in Figure 190.

Currently we are planning to start the Phase II of the development. In this phase, one or both versions of alloys will be produced with 5000 Kg melts. The final sheet metal width will be up to 800 mm. Which will be adequate for making hotboxes without weld joining the strips. Per the plan, we will have the fully processed material by the end of this year.

Figure 190 two major subassemblies for one of the hotbox

3. Conclusions

The evolving oxidation behavior of alumina-forming austenitic (AFA) stainless steel and commercial alloys in Air + 10% H_2O at 800 °C and 900 °C is comprehensively studied. Commercial alloys suffered from breakaway oxidation and scale spallation after only one cycle exposure, while the AFAs exhibits higher oxidation resistance in the long-term oxidation process (5000 h). After exposed for one cycle, oxide scale formed on the 310S alloy is consisted of an outmost (Fe, Cr, Mn)$_3O_4$ layer and an inner (Fe, Cr)$_2O_3$ layer. While for the AFAs, its oxide scale is consisted of the outer Fe-Cr-Mn-Al-rich oxides, an intermediate (Fe, Cr)$_2O_3$ layer and an inner continuous alumina layer. Commercial alloys severely suffered from the spallation which caused by evaporation of chromium oxyhydroxide that results in the formation of hole in the oxide scale, while there are no voids observed for AFAs during the long-term oxidation process (5000 h). The inner continuous alumina layer formed on the AFA alloy significantly reduces and prevents the diffusion of Cr and Mn which can immensely alleviate the evaporation of chromium oxyhydroxide and the scale spallation.

An optimal method is invented to accurately evaluate the Cr evaporation rates of BoP components. In this project, problems of these methods have been discussed. Cr evaporation rates of AFA alloys were lower than Cr_2O_3 forming 310S and 625 alloys at 800-900 °C operation with all four methods. Surface Si contamination on all samples was observed after 500 h operation at 800-900 °C in air with 10% H2O using quartz furnace (method 1) tube in our previous study. Although it did not appear to significantly impact Cr evaporation behavior for short-term exposure, however, a great number of Si deposits could be observed after 4500 h operation using quartz tube in this paper which could significantly alter the evaporated Cr species quantities. Surface Na pollution on all samples (method 4) and chemical interaction between gaseous Cr species and alumina tube (method 2) which could result in the lower Cr evaporation rates of alloys were observed after 500 h exposure. Si contamination, Na pollution and the chemical interaction were solved using the sodium carbonate coated thin alumina tubes (method 3) which could accurately evaluate the Cr evaporation rates of alloys.

Based on the Cr evaporation rates results, we had investigated the Cr deposition of anode-supported cell under a constant current density of 0.5 A cm^{-2} at 800 °C with AFA alloys commercial alloys compared with commercial alloys. It is found that during the galvanostatic test the cell voltage decreases about 4.42% in the absence of alloys. However, a considerable decrease of 22.14 % and 12.06 % was determined in the presence of 310S and 625 alloy, respectively, which can be attributed to the gaseous Cr species evaporated from chromia-forming 310S and 625 that vastly deteriorate the performance of the ASC cells. However, slight decrease of 5.09 % and 1.54 % was determined in the presence of OC11 and OC11LZA alloy, respectively. Cr deposition distributions on the cathode region were also more severe of commercial alloys than AFA alloys which verified the potential of AFA alloys on the application of SOFC BoP components.

4. Future work

1) Optimizing the alloy additions of AFA alloys to improve the long-term stability of oxide scales in environment containing water vapor.

2) Conducting long-term operation of anode-supported cells in the presence of AFA alloys to evaluate the practical application at SOFC BoP components.

3) More comprehensive researches on the effect of reactive elements on the long-term stability of oxide scales formed on AFA alloys.

Supplementary materials

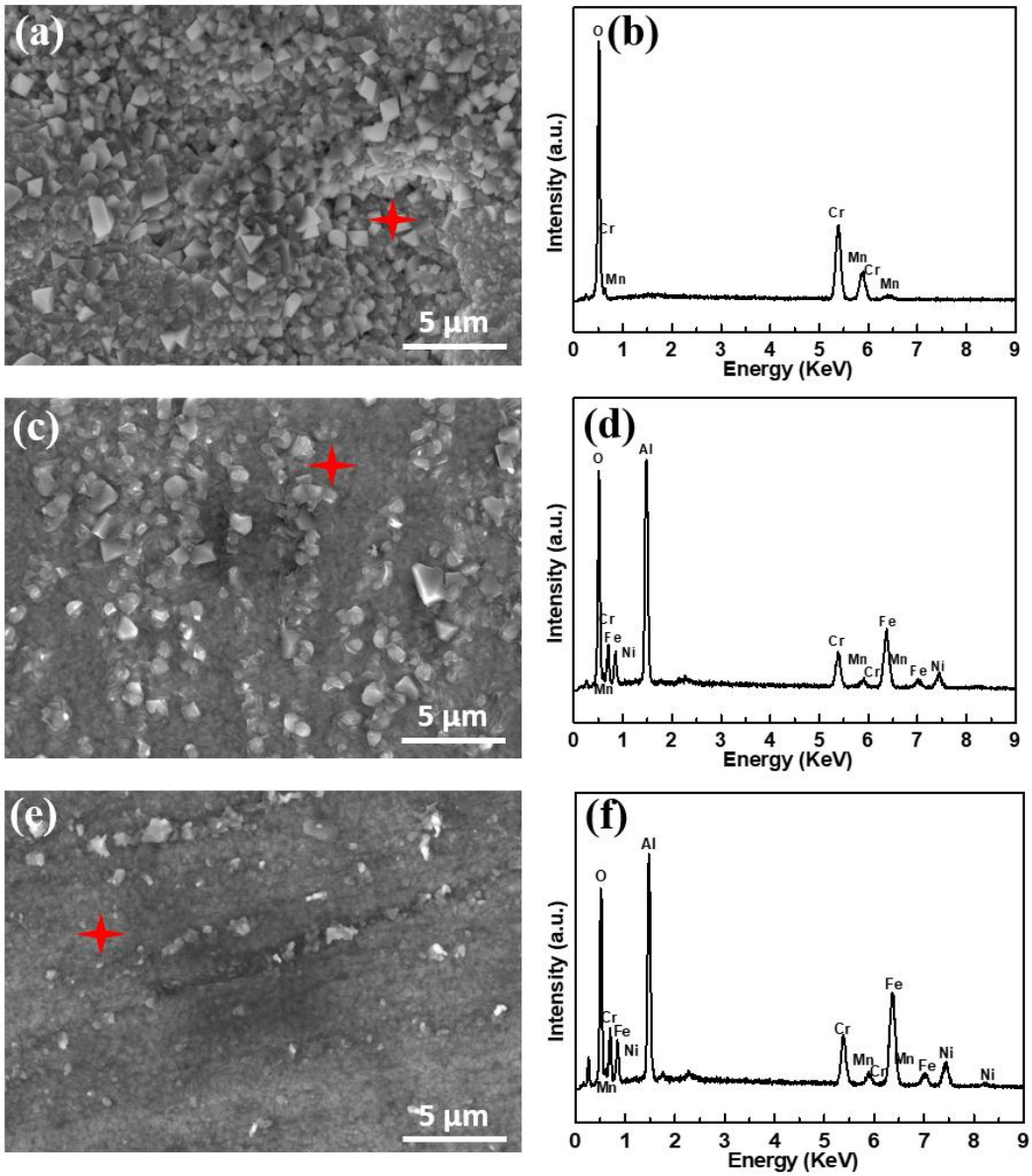

Fig. S1. SEM surface images of a) 310S, b) OC4 and c) OC5 and corresponding EDS analysis of b) 310S, d) OC4 and f) OC5 after 500 h chromium evaporation test at 800 °C in Na_2CO_3 coated thin alumina tube.

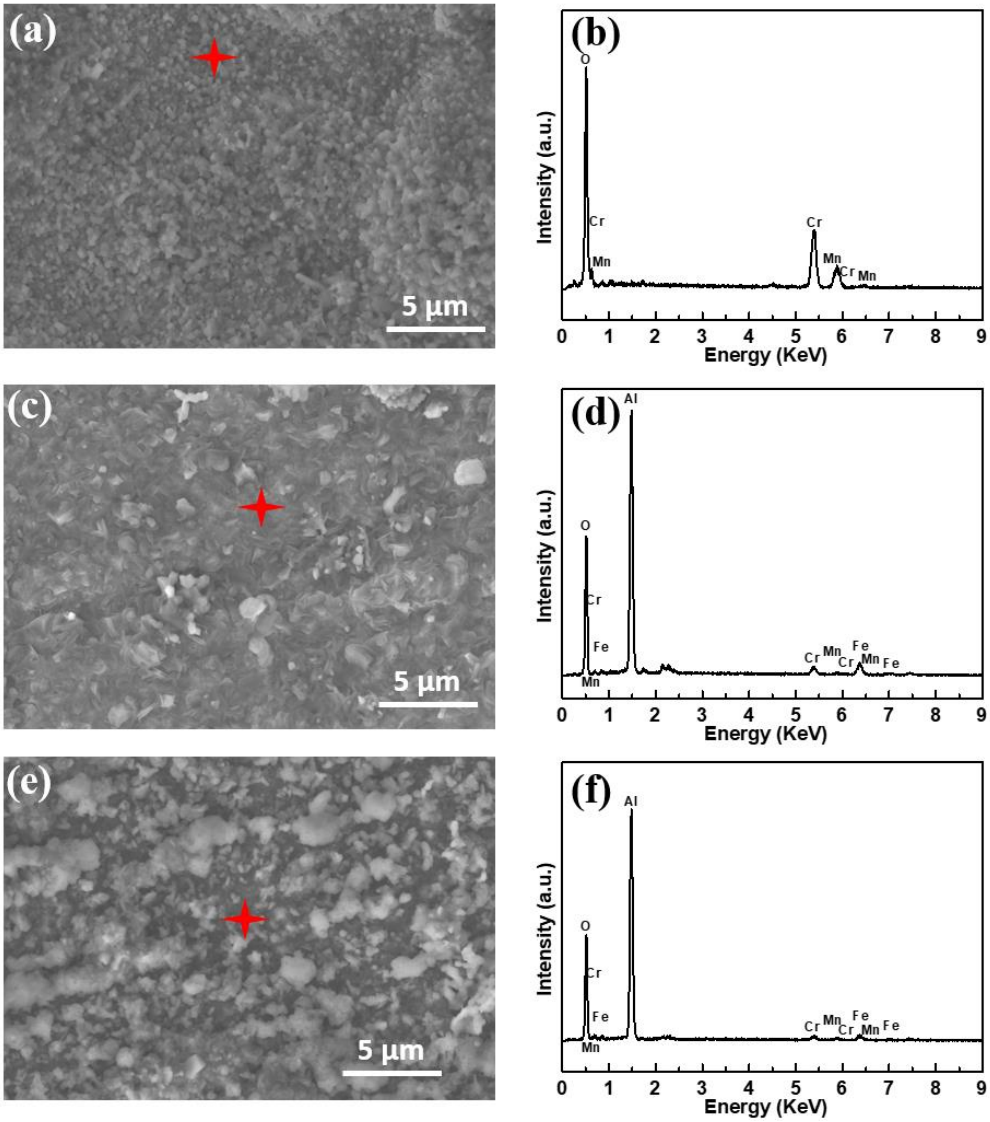

Fig. S2. SEM surface images of a) 625, b) OC11 and c) OC11LZ and corresponding EDS analysis of b) 625, d) OC11 and f) OC11LZ after 500 h chromium evaporation test at 900 °C in Na_2CO_3 coated thin alumina tube.

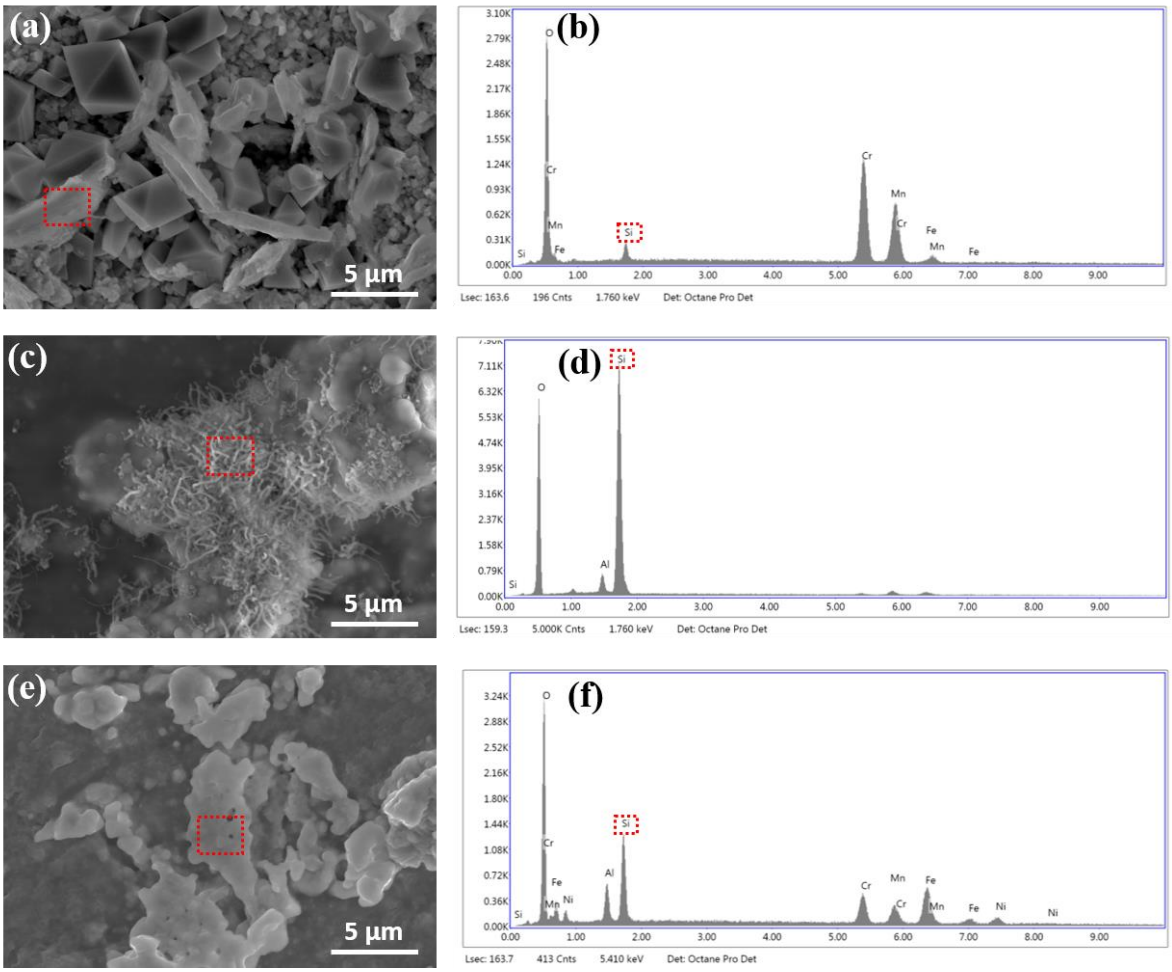

Fig. S3. SEM surface images of (a) 310S, (b) OC4 and (c) OC5 after 4500 h test in quartz tube and corresponding EDS analysis of (b) 310S, (d) OC4 and (f) OC5.

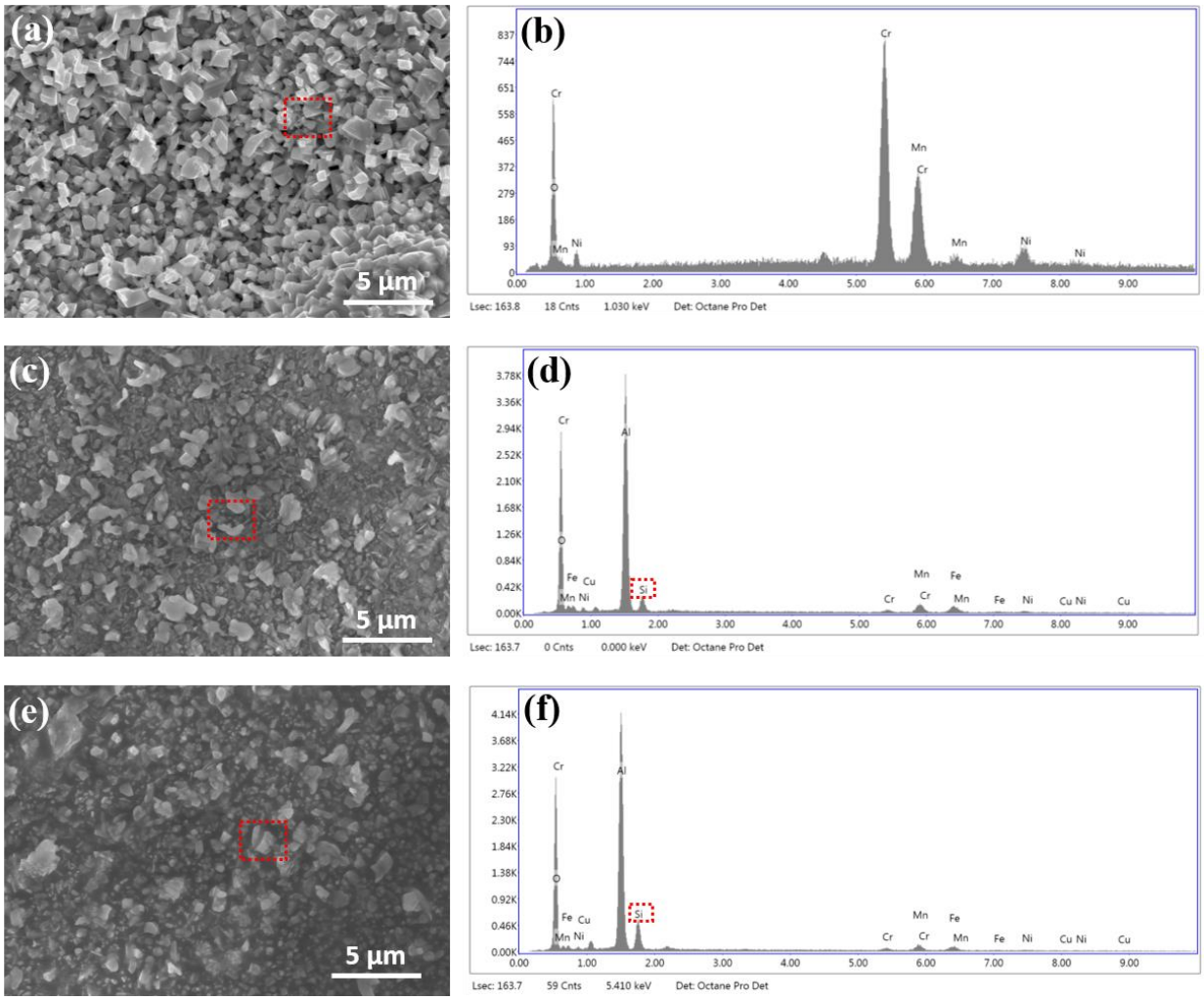

Fig. S4. SEM surface images of (a) 625, (b) OC11 and (c) OC11LZ after 4500 h test in quartz tube and corresponding EDS analysis of (b) 625, (d) OC11 and (f) OC11LZ.

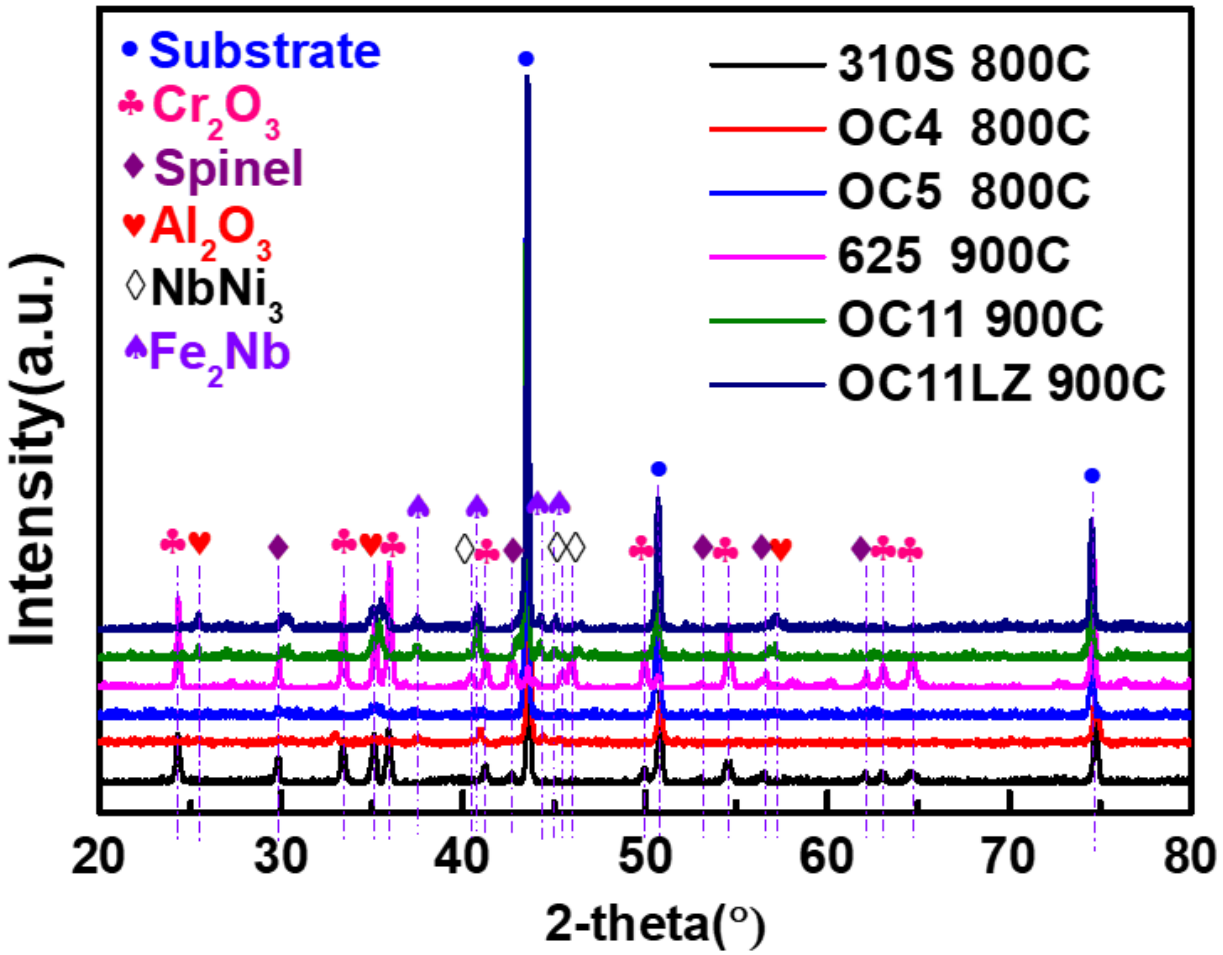

Fig. S5. XRD profiles of the oxide scales developed on 310S, OC4 and OC5 at 800 °C and 625, OC11 and OC11LZ after 500 h chromium evaporation test in alumina tube.

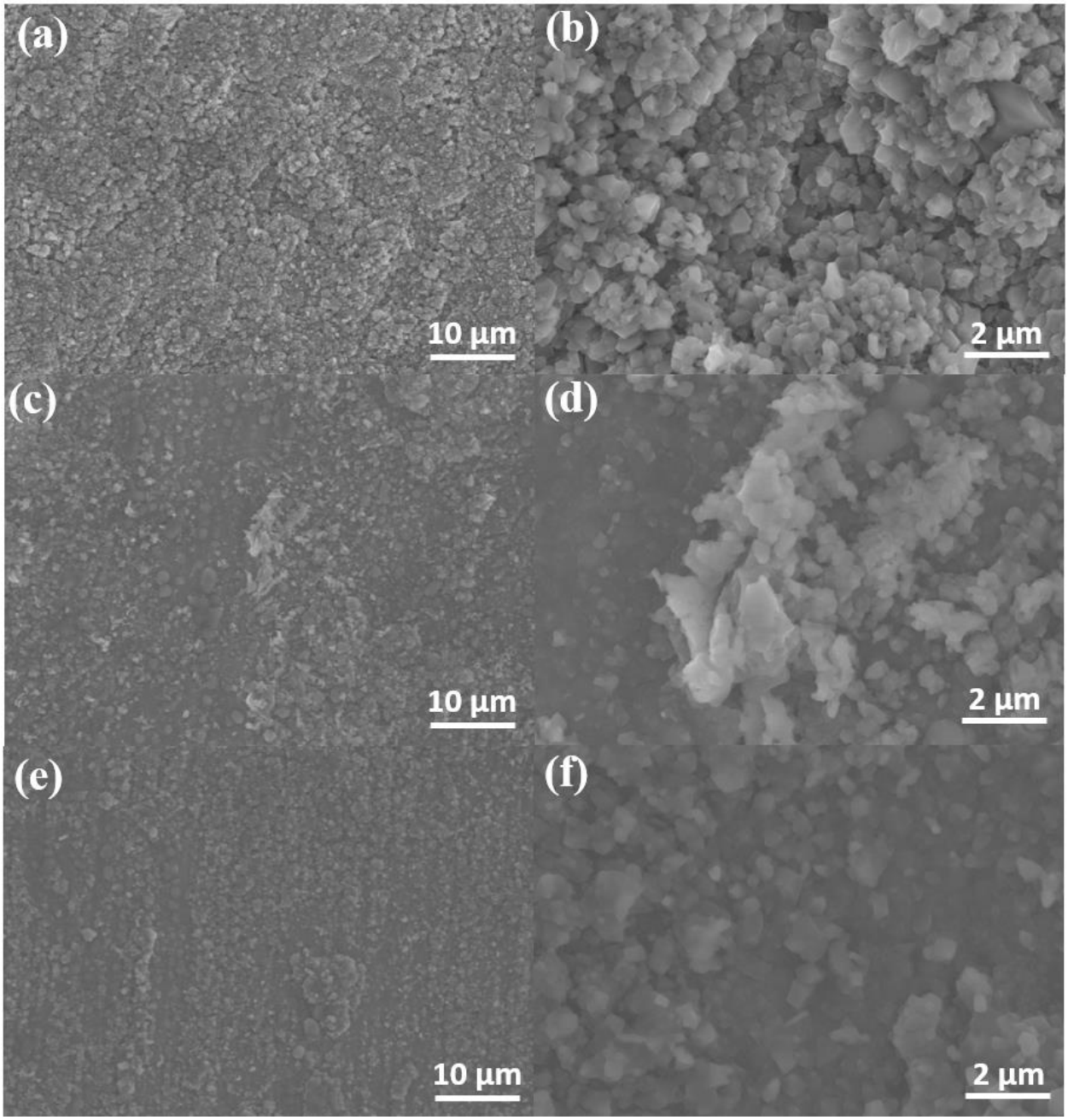

Fig. S6. Oxide scale morphologies developed on (a, b) 310S, (c, d) OC4 and (e, f) OC5 tested for 500 h in air + 10% H_2O at 800 °C in alumina tube.

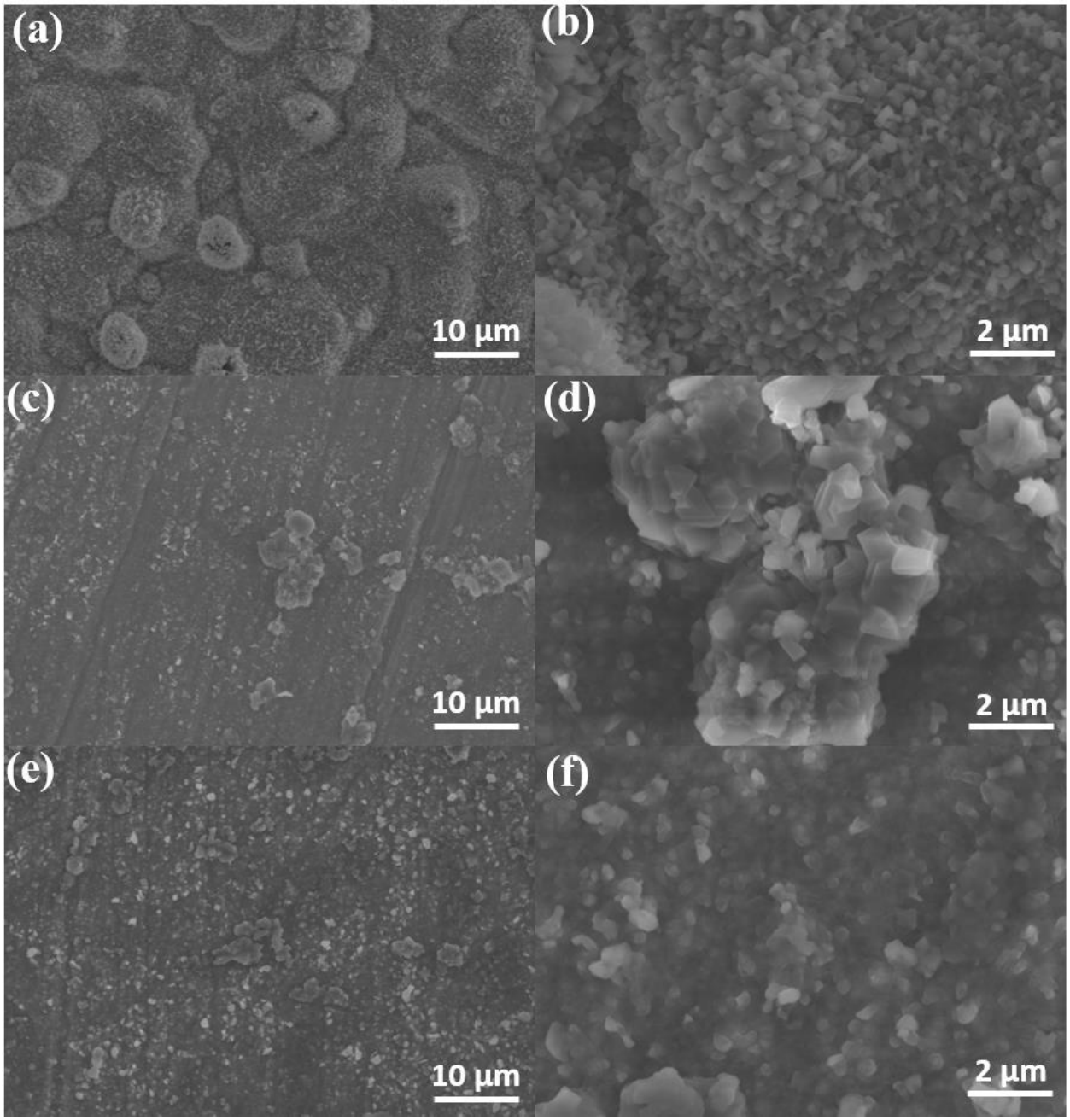

Fig. S7. Oxide scale morphologies developed on (a, b) 625, (c, d) OC11 and (e, f) OC11LZ tested for 500 h in air + 10% H_2O at 900 °C in alumina tube.

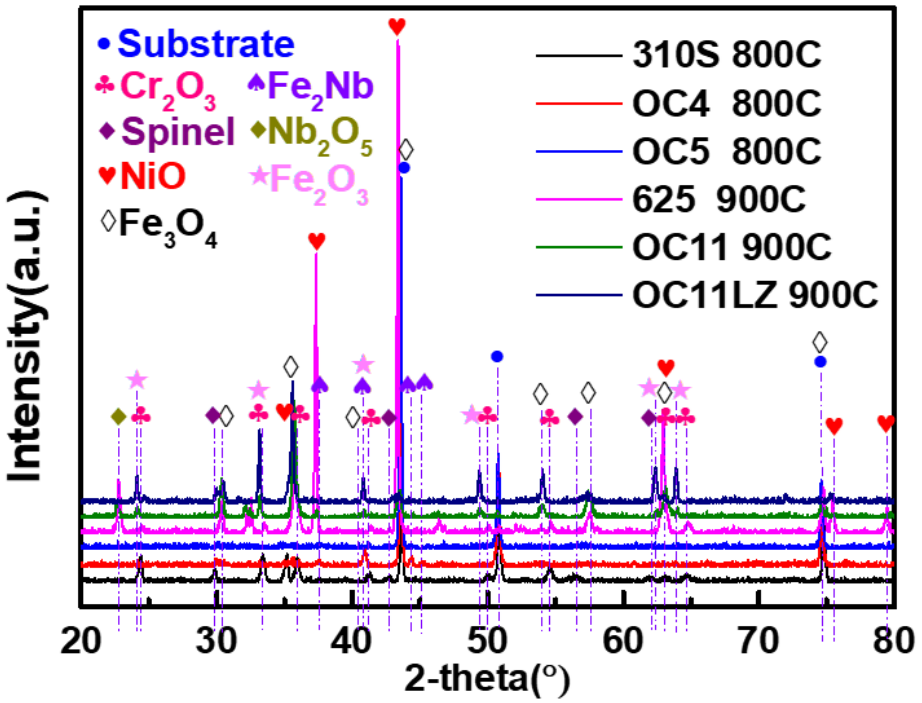

Fig. S8. XRD profiles of the oxide scales developed on 310S, OC4 and OC5 at 800 °C and 625, OC11 and OC11LZ after 500 h chromium evaporation test in sodium carbonate coated alumina tube.

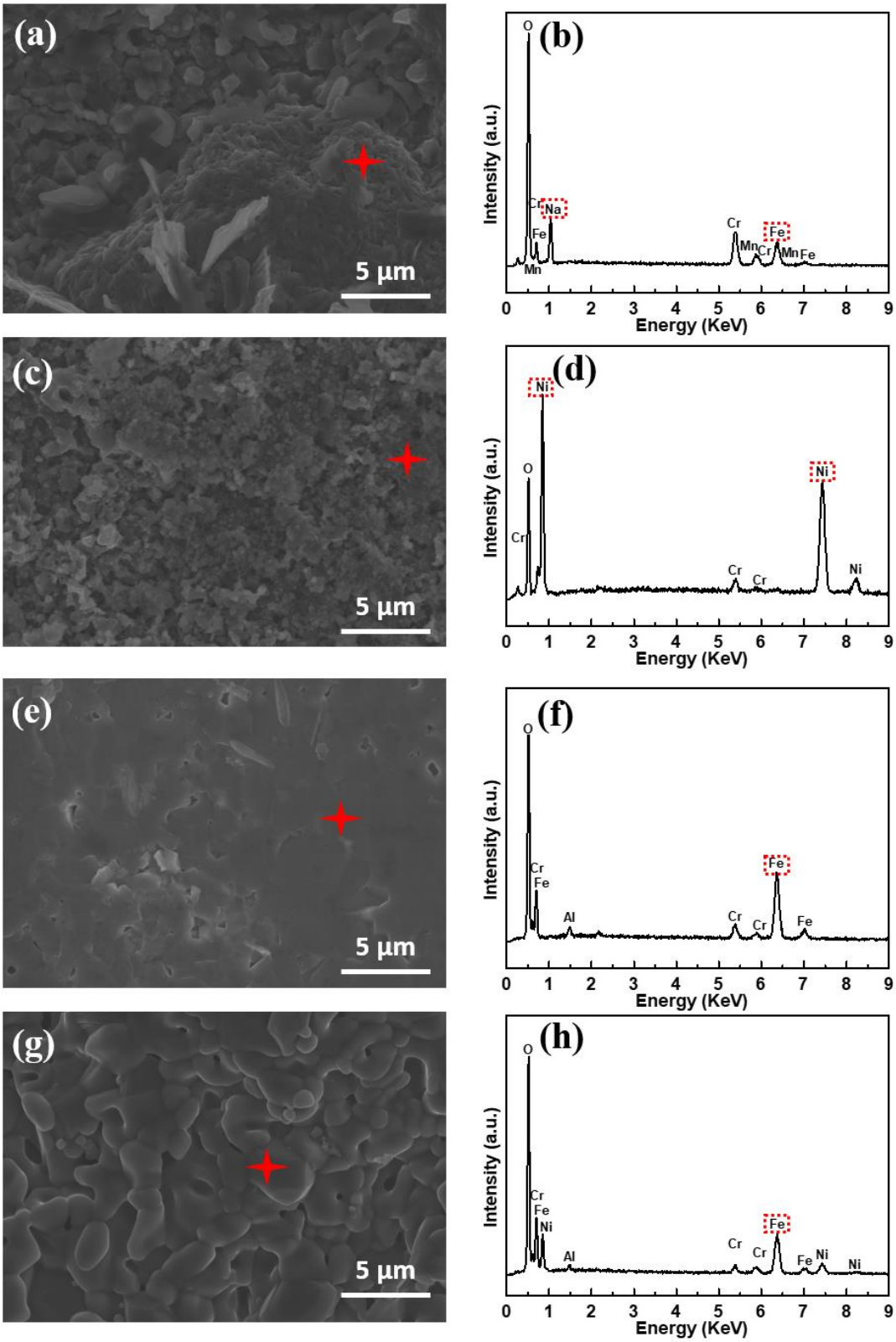

Fig. S9. SEM surface images of a) 310S, c) 625, e) OC11 and g) OC11LZ and corresponding EDS analysis of b) 310S, d) 625, f) OC11 and h) OC11LZ after 500 h chromium evaporation test at 800 °C in Na_2CO_3 coated alumina tube.